National Library of Canada
Bibliothèque nationale du Canada

Canadian Theses Service
Service des thèses canadiennes

Ottawa, Canada
K1A 0N4

NOTICE

The quality of this microform is heavily dependent upon the quality of the original thesis submitted for microfilming. Every effort has been made to ensure the highest quality of reproduction possible.

If pages are missing, contact the university which granted the degree.

Some pages may have indistinct print especially if the original pages were typed with a poor typewriter ribbon or if the university sent us an inferior photocopy.

Reproduction in full or in part of this microform is governed by the Canadian Copyright Act, R.S.C. 1970, c. C-30, and subsequent amendments.

AVIS

La qualité de cette microforme dépend grandement de la qualité de la thèse soumise au microfilmage. Nous avons tout fait pour assurer une qualité supérieure de reproduction.

S'il manque des pages, veuillez communiquer avec l'université qui a conféré le grade.

La qualité d'impression de certaines pages peut laisser à désirer, surtout si les pages originales ont été dactylographiées à l'aide d'un ruban usé ou si l'université nous a fait parvenir une photocopie de qualité inférieure.

La reproduction, même partielle, de cette microforme est soumise à la Loi canadienne sur le droit d'auteur, SRC 1970, c. C-30, et ses amendements subséquents.

NL-339 (r. 88/04) c

Canada

THE UNIVERSITY OF ALBERTA

A Constitutive Model for Ice

by

Heng Aik Khoo

A THESIS

SUBMITTED TO THE FACULTY OF GRADUATE STUDIES AND RESEARCH IN PARTIAL FULFILMENT OF THE REQUIREMENTS FOR THE DEGREE OF MASTER OF SCIENCE.

DEPARTMENT OF CIVIL ENGINEERING

EDMONTON, ALBERTA

Spring, 1990

National Library of Canada
Bibliothèque nationale du Canada

Canadian Theses Service
Service des thèses canadiennes

Ottawa, Canada
K1A 0N4

NOTICE

The quality of this microform is heavily dependent upon the quality of the original thesis submitted for microfilming. Every effort has been made to ensure the highest quality of reproduction possible.

If pages are missing, contact the university which granted the degree.

Some pages may have indistinct print especially if the original pages were typed with a poor typewriter ribbon or if the university sent us an inferior photocopy.

Reproduction in full or in part of this microform is governed by the Canadian Copyright Act, R.S.C. 1970, c. C-30, and subsequent amendments.

AVIS

La qualité de cette microforme dépend grandement de la qualité de la thèse soumise au microfilmage. Nous avons tout fait pour assurer une qualité supérieure de reproduction.

S'il manque des pages, veuillez communiquer avec l'université qui a conféré le grade.

La qualité d'impression de certaines pages peut laisser à désirer, surtout si les pages originales ont été dactylographiées à l'aide d'un ruban usé ou si l'université nous a fait parvenir une photocopie de qualité inférieure.

La reproduction, même partielle, de cette microforme est soumise à la Loi canadienne sur le droit d'auteur, SRC 1970, c. C-30, et ses amendements subséquents.

ISBN 0-315-60291-0

NL-339 (r. 88/04) c

Canada

THE UNIVERSITY OF ALBERTA

RELEASE FORM

NAME OF AUTHOR: Heng Aik Khoo

TITLE OF THESIS: A Constitutive Model for Ice

DEGREE: Master of Science

YEAR THIS DEGREE GRANTED 1990

Permission is hereby granted to THE UNIVERSITY OF ALBERTA LIBRARY to reproduce single copies of this thesis and to lend or sell such copies for private, scholarly or scientific research purposes only.

The author reserves other publication rights, and neither the thesis nor extensive extracts from it may be printed or otherwise reproduced without the author's written permission.

(Student's Signature)

42, TAMAN SENTOSA

BAKAR ARANG, SUNGAI PETANI

KEDAH, MALAYSIA.

(Student's Permanent Address)

Date: NOV 6, 87

THE UNIVERSITY OF ALBERTA

FACULTY OF GRADUATE STUDIES AND RESEARCH

The undersigned certify that they have read, and recommend to the Faculty of Graduate Studies and Research for acceptance, a thesis entitled A Constitutive Model for Ice submitted by Heng Aik Khoo in partial fulfilment of the requirements for the degree of Master of Science.

T. Hrudey
(Supervisor: Prof. T. M. Hrudey)

D. W. Murray
(Prof. D. W. Murray)

Gary Faulkner
(Prof. M. G. Faulkner)

Date: NOV/1/89

Abstract

A one dimensional model is developed for ice in compression. It consists of the combination of a Maxwell unit and a Kelvin-Voigt unit. The model includes the effects of loading rate and material damage. It is able to account for the residual strength that exists in ice under a constant strain rate compression by allowing the viscosity of the dashpot in the Maxwell unit to vary. However, the model is restricted to the lower range of deformation rates. It does not repressent compressive brittle fracture.

The one dimensional model is generalized to a plane stress situation using the principles of continuum mechanics and where possible the two dimensional test data from the literature. In the plane stress model, tensile brittle fracture is represented by a simple tensile stress cutoff. The process of implementing the plane stress model into a finite element program is discussed. This includes various assumptions and mathematical treatments that are made and performed to ease the numerical computation.

The plane stress model is then used to solve some indentation problems. Numerical analyses with different indentor shapes are run to predict the peak force on the indentor and the stress distribution in the ice sheet. Some uniaxial and plane strain analyses are also performed to compare the numerical solutions to the actual test results.

Acknowledgements

I am highly indebted to Dr. T. M. Hrudey, supervisor of this project, for his valuable advice and guidance. He has been a source of encouragement and unwavering support.

My grateful thanks to C-FER and NSERC for their financial assistance.

To the two indomitable twins whom I share the office with: Jose Napoleao and Zabi Behin. You have taugth me a lot and put up with my idiosyncracies. Thank you for everything.

My special thanks to my good friend Peter Gaffran. Your encouragement has been inspirational.

I would like to dedicate this thesis to my family in Malaysia. The last eight years in engineering school would not have been possible without your strong support.

And finally to Sam, who just wants to be acknowledged. Thanks for putting me back in tune.

Table of Content

Chapter		Page
1.	Introduction	1
	1.1 Objective of the Thesis	2
	1.2 Organisation of the Thesis	3
2.	Literature Review	5
	2.1 Ice Mechanics	5
	2.1.1 Types of Ice	5
	2.1.2 Material Properties of Ice	6
	2.1.3 Ice Indentation	10
	2.2 Ice Force Prediction in Indentation	10
	2.2.1 Empirical Equations	11
	2.2.2 Ice Modelling	14
	2.2.3 Other Methods	18
3.	Constitutive Model	22
	3.1 One Dimension Model	22
	3.1.1 Instantaneous Elastic Element	23
	3.1.2 Delayed Elastic Element	23
	3.1.3 Viscous Element	24
	3.1.3.1 Initial and Final Value of η	25
	3.1.3.2 Viscous Strain ε_v - As a Controlling Parameter	26
	3.1.3.3 Critical Viscous Strain ε_{vc}	27
	3.1.3.4 The Mathematical Expression for Viscous Element	28
	3.2 Plane Stress	29
	3.2.1 Instantaneous Elastic Element	29

3.2.2 Delayed Elastic Element 29
3.2.3 Viscous Element 31
3.2.4 Brittle Fracture of Ice 38
4. Finite Element Formulation 43
4.1 Overall Formulation. 43
4.2 Implementing the Proposed Ice Model into the Computer Program 48
4.2.1 The Instantaneous Elastic Element 48
4.2.2 Delayed Elastic Element 48
4.2.3 Viscous Element 55
4.2.3.1 Rate of Change of the Viscous Strain Increment 57
4.2.3.2 Change in η_b 58
4.2.4 Tensile Brittle Fracture 61
4.3 Flow Chart for the Finite Element Program. 62
5. Presentation and Discussion of the Analytical Results 65
5.1 Estimation and Calibration of the Parameters Used in the Model 65
5.1.1 Parameters That Do Not Change 66
5.1.2 Parameters Approximated from Test Results..... 66
5.1.2.1 Estimation Using Uniaxial Test Results ... 67
5.1.2.2 Estimation Using Plane Strain Test Results 68
5.1.3 Estimating the Remaining Parameters 74
5.2 Uniaxial and Plane Strain Compression 75
5.2.1 Sinha's Test 75
5.2.2 Mellor and Cole's Test 78

5.2.3 Frederking's Test 80
5.3 Indentation 82
5.3.1 Michel and Toussaint's Test 84
5.3.2 Frederking and Gold's Test 92
5.3.3 Cylinder Indentation 93
6. Summary and Conclusions 156
References 160

List of Figures

Figure		Page
2.1	Typical stress-strain curve of ice under constant strain rate compression.	20
2.2	Relationship between the peak stress and uniaxial strain rate for ice in tension and compression.	20
2.3	Typical strain-time curve of ice under a constant stress loading.	21
2.4	Orientation of c-axis in a hexaganol crystal structure.	21
3.1	Maxwell unit.	40
3.2	Kelvin-Voigt unit.	40
3.3	The proposed constitutive model for ice under uniaxial compressive loading.	40
3.4	The effect of the final value of η on the residual stress under constant strain rate loading.	41
3.5	The orientation of the ice specimen in Frederking's test.	41
3.6	The orientation of the axes for the plane stress formulation.	42
4.1	Flow chart for the finite element program of plane stress ice model.	64
5.1	Relationship between the peak stress and the constant compression strain rate from Sinha's test result.	97
5.2	The analytical peak stress versus strain rate with different η_i, and the experimental results for Sinha's test.	98
5.3	The stress-strain curve of constant strain rate compression for both analytical and Sinha's test results.	98

5.4 The stress-strain curve of constant strain rate compression for both analytical and Sinha's test result. 99

5.5 The stress-strain curve of constant stress rate compression for both analytical and Sinha's test result. 99

5.6 Relationship between the peak stress and the constant compression strain rate from Mellor and Cole's test results. 100

5.7 Relationship between η_f versus the constant comprssion strain rate for Mellor and Cole's test. 101

5.8 The test and analytical strain-time curves for Mellor and Cole's constant stress test. 102

5.9 The test and analytical strain-time curves for Mellor and Cole's constant stress test. 102

5.10 The test and analytical strain-time curves for Mellor and Cole's constant stress test. 103

5.11 The peak stress versus strain rate plot from both the original and modified model together with the best fit curve of the test result for Mellor and Cole's constant strain rate test. 103

5.12 The stress-strain curve of constant strain rate compression for both the analytical and Mellor and Cole's tests. 104

5.13 The stress-strain curves of constant strain rate compression for both the analytical and Mellor and Cole's tests. 104

5.14 The stress-strain curves from the modified model and the experiment for Mellor and Cole's constant strain rate test. ... 105

5.15 Relationship between η_f versus constant comprssion strain rate for Frederking's test. 106

5.16 The analytical and experimental peak stress versus strain rate plot for both Frederking's plane strain and uniaxial tests. 107

5.17 The stress-strain curves of uniaxial constant strain rate compression for both the analytical and Frederking's test. 107

5.18 The stress-strain curves of plane strai compression for both the analytical and Frederking's test. 108

5.19 Boundary condition for modelling Michel and Toussaint's ice indentation. 109

5.20 Boundary condition for modelling Frederking and Gold's ice indentation. 110

5.21 Boundary condition for modelling against a cylindrical indentor. 111

5.22 The numbering system for the finite element mesh in the ice indentation analysis for a cylindrical indentor. 112

5.23 The numbering system for the finite element mesh in the ice indentation analysis for Michel and Toussaint's Test. 113

5.24 The numbering system for the finite element mesh in the ice indentation analysis for Frederking and Gold's Test. 114

5.25 Analytical peak average stress at different v/b for Michel and Toussaint's test. 115

5.26 The peak average stress at different v/b from Michel and Toussaint's test and the best fit curve of the analytical result. 115

5.27 Analytical average stress versus indentor displacement with 50mm indentor for Michel and Toussaint's test. 116

5.28 Analytical average stress versus indentor displacement with 100mm indentor for Michel and Toussaint's test. 116

5.29 Analytical average stress versus indentor displacement with 150mm indentor for Michel and Toussaint's test. 117

5.30 Analytical average stress versus indentor displacement at 5mm/s for Michel and Toussaint's test. 117

5.31 Analytical average stress versus indentor displacement at $5x10^{-1}$mm/s for Michel and Toussaint's test. 118

5.32 Analytical average stress versus indentor displacement at $5x10^{-2}$mm/s for Michel and Toussaint's test. 118

5.33 Analytical average stress versus indentor displacement at $5x10^{-3}$mm/s together with an experimental curve for Michel and Toussaint's test. 119

5.34 Analytical average stress versus indentor displacement at $5x10^{-4}$mm/s for Michel and Toussaint's test. 119

5.35 Normal stress σ_y along the 50mm rectangular indentor at $5x10^{-1}$mm/s with 2x2 Gaussian integration. 120

5.36 Normal stress σ_y along the 50mm rectangular indentor at $5x10^{-2}$mm/s with 2x2 Gaussian integration. 120

5.37 Normal stress σ_y along the 50mm rectangular indentor at $5x10^{-3}$mm/s with 2x2 Gaussian integration. 121

5.38 Normal stress σ_y along the 50mm rectangular indentor at $5x10^{-4}$mm/s with 2x2 Gaussian integration. 121

5.39 Normal stress σ_y along the 150mm rectangular indentor at $5x10^{-1}$mm/s with 2x2 Gaussian integration. 122

5.40 Normal stress σ_y along the 150mm rectangular indentor at $5x10^{-2}$mm/s with 2x2 Gaussian integration. 122

5.41 Normal stress σ_y along the 150mm rectangular indentor at $5x10^{-3}$mm/s with 2x2 Gaussian integration. 123

5.42 Normal stress σ_y along the 150mm rectangular indentor at $5x10^{-4}$mm/s with 2x2 Gaussian integration. 123

5.43 Normal stress σ_y along the 50mm rectangular indentor at 5mm/s with 3x3 Gaussian integration. 124

5.44 Normal stress σ_y along the 50mm rectangular indentor at $5x10^{-1}$mm/s with 3x3 Gaussian integration. 124

5.45 Normal stress σ_y along the 50mm rectangular indentor at $5x10^{-2}$mm/s with 3x3 Gaussian integration. 125

5.46 Normal stress σ_y along the 50mm rectangular indentor at $5x10^{-3}$mm/s with 3x3 Gaussian integration. 125

5.47 Normal stress σ_y along the 50mm rectangular indentor at $5x10^{-4}$mm/s with 3x3 Gaussian integration. 126

5.48 Normal stress σ_y along the 150mm rectangular indentor at $5x10^{-4}$mm/s with 3x3 Gaussian integration. 126

5.49 Comparison of the normal stress σ_y along the 150mm rectangular indentor at $5x10^{-4}$mm/s with different Gaussian integration at initial loading. 127

5.50 Comparison of the normal stress σ_y along the 150mm rectangular indentor at $5x10^{-4}$mm/s with different Gaussian integration at peak σ_{avg}. 127

5.51 Comparison of the normal stress σ_y along the 150mm rectangular indentor at $5x10^{-4}$mm/s with different Gaussian integration at steady state. 128

5.52 Comparison of the normal stress σ_y along Y-axis for the 150mm rectangular indentor at $5x10^{-4}$mm/s with different Gaussian integration at peak σ_{avg}. 128

5.53 Comparison of the normal stress σ_y along Y-axis for the 150mm rectangular indentor at $5x10^{-4}$mm/s with different Gaussian integration at steady state. 129

5.54 Comparison of the normal stress σ_y along Y-axis for the 150mm rectangular indentor at $5x10^{-4}$mm/s with different Gaussian integration at131 initial loading. 129

5.55 Normal stress σ_y along Y-axis for the 50mm rectangular indentor at $5x10^{-1}$mm/s with 2x2 Gaussian integration. 130

5.56 Normal stress σ_y along Y-axis for the 50mm rectangular indentor at $5x10^{-2}$mm/s with 2x2 Gaussian integration. 130

5.57 Normal stress σ_y along Y-axis for the 50mm rectangular indentor at $5x10^{-3}$mm/s with 2x2 Gaussian integration. 131

5.58 Normal stress σ_y along Y-axis for the 50mm rectangular indentor at $5x10^{-4}$mm/s with 2x2 Gaussian integration. 131

5.59 Normal stress σ_y along Y-axis for the 150mm rectangular indentor at $5x10^{-1}$mm/s with 2x2 Gaussian integration. 132

5.60 Normal stress σ_y along Y-axis for the 150mm rectangular indentor at $5x10^{-2}$mm/s with 2x2 Gaussian integration. 132

5.61 Normal stress σ_y along Y-axis for the 150mm rectangular indentor at $5x10^{-3}$mm/s with 2x2 Gaussian integration. 133

5.62 Normal stress σ_y along Y-axis for the 150mm rectangular indentor at $5x10^{-4}$mm/s with 2x2 Gaussian integration. 133

5.63 Normal stress σ_y along Y-axis for the 50mm rectangular indentor at $5x10^{-1}$mm/s with 3x3 Gaussian integration. 134

5.64 Normal stress σ_y along Y-axis for the 50mm rectangular indentor at $5x10^{-2}$mm/s with 3x3 Gaussian integration. 134

5.65 Normal stress σ_y along Y-axis for the 50mm rectangular indentor at $5x10^{-3}$mm/s with 3x3 Gaussian integration. 135

5.66 Normal stress σ_y along Y-axis for the 50mm rectangular indentor at $5x10^{-4}$mm/s with 3x3 Gaussian integration. 135

5.67 Normal stress σ_y along Y-axis for the 150mm rectangular indentor at $5x10^{-4}$mm/s with 3x3 Gaussian integration. 136

5.68 Maximum principal stress along Y-axis for the 50mm rectangular indentor at $5x10^{-1}$mm/s with 2x2 Gaussian integration. 137

5.69 The distribution of normal stress on the indentor for Saeki et al's test at b/h=4.14 and $v/4b=0.610x10^{-3}s^{-1}$. 138

5.70 The distribution of normal stress on the indentor for Saeki et al's test at b/h=2.76 and $v/4b=0.667x10^{-3}s^{-1}$. 138

5.71 The distribution of normal stress on the indentor for Saeki et al's test at b/h=1.67 and $v/4b=0.815x10^{-3}s^{-1}$. 139

5.72 The peak average stress at different v/b from Frederking and Gold's test. 140

5.73 The analytical peak average stress at different v/b and the Frederking and Gold's test results. 140

5.74 Position of the ice plate and the indentor at the start of a penetration test. 141

5.75 Position of the ice plate and the indentor at the start of a indentation test. 142

5.76 The analytical peak average stress at different v/b for the cylindrical indentor. 143

5.77 The analytical average stress versus indentor displacement with 100mm cylindrical indentor. 143

5.78 The analytical average stress versus indentor displacement with 150mm cylindrical indentor. 144

5.79 The analytical average stress versus indentor displacement with 200mm cylindrical indentor. 144

5.80 The analytical average stress versus indentor displacement for cylindrical indentor at 5mm/s 145

5.81 The analytical average stress versus indentor displacement cylindrical indentor at $5x10^{-1}$mm/s 145

5.82 The analytical average stress versus indentor displacement cylindrical indentor at $5x10^{-2}$mm/s 146

5.83 The analytical average stress versus indentor displacement cylindrical indentor at $5x10^{-3}$mm/s 146

5.84 The analytical average stress versus indentor displacement cylindrical indentor at $5x10^{-4}$mm/s 147

5.85 Radial stress σ_r along the 100mm cylindrical indentor at $5x10^{-1}$mm/s with 2x2 Gaussian integration. 148

5.86 Radial stress σ_r along the 100mm cylindrical indentor at $5x10^{-2}$mm/s with 2x2 Gaussian integration. 148

5.87 Radial stress σ_r along the 100mm cylindrical indentor at $5x10^{-3}$mm/s with 2x2 Gaussian integration. 149

5.88 Radial stress σ_r along the 100mm cylindrical indentor at $5x10^{-4}$mm/s with 2x2 Gaussian integration. 149

5.89 Radial stress σ_r along the 100mm cylindrical indentor at $5x10^{-1}$mm/s with 3x3 Gaussian integration. 150

5.90 Radial stress σ_r along the 100mm cylindrical indentor at $5x10^{-2}$mm/s with 3x3 Gaussian integration. 150

5.91 Radial stress σ_r along the 100mm cylindrical indentor at $5x10^{-3}$mm/s with 3x3 Gaussian integration. 151

5.92 Radial stress σ_r along the 100mm cylindrical indentor at $5x10^{-4}$mm/s with 3x3 Gaussian integration. 151

5.93 Radial stress σ_y along Y-axis for the 100mm cylindrical indentor at $5x10^{-1}$mm/s with 2x2 Gaussian integration. 152

5.94 Radial stress σ_y along Y-axis for the 100mm cyiindrical indentor at $5x10^{-2}$mm/s with 2x2 Gaussian integration. 152

5.95 Radial stress σ_y along Y-axis for the 100mm cylindrical indentor at $5x10^{-3}$mm/s with 2x2 Gaussian integration. 153

5.96 Radial stress σ_y along Y-axis for the 100mm cylindrical indentor at $5x10^{-4}$mm/s with 2x2 Gaussian integration. 153

5.97 Radial stress σ_y along Y-axis for the 100mm cylindrical indentor at $5x10^{-1}$mm/s with 3x3 Gaussian integration. 154

5.98 Radial stress σ_y along Y-axis for the 100mm cylindrical indentor at $5x10^{-2}$mm/s with 3x3 Gaussian integration. 154

5.99 Radial stress σ_y along Y-axis for the 100mm cylindrical indentor at $5x10^{-3}$mm/s with 3x3 Gaussian integration. 155

5.100 Radial stress σ_y along Y-axis for the 100mm cylindrical indentor at $5x10^{-4}$mm/s with 3x3 Gaussian integration. 155

List of Symbols

[A]	-	the matrix that relates the stress σ to viscous strain rates.
a_1, a_2, a_3	-	parameters used in calculating τ.
a_4, a_5, a_6	-	parameters used in calculating τ.
b	-	the width (or other appropriate dimension) of the indentor.
B	-	the width of the ice sheet.
[B]	-	the strain interpolation function matrix that includes the differential operators on the displacement.
C	-	the indentation coefficient which takes into account the biaxial stress condition around the structure.
[D]	-	the constitutive matrix for the instantaneous elastic deformation.
E_1	-	the elastic modulus in the instantaneous elastic element.
E_1^f	-	the elastic modulus in the instantaneous elastic element for the failed region.
E_2	-	the elastic modulus in the delayed elastic element.
E_2^f	-	the elastic modulus in the instantaneous elastic element for the failed region.
f	-	the unbalance nodal force.
F	-	the horizontal force exerted by the ice sheet or the nodal force.
h	-	the ice thickness.
I	-	denotes the time step number.
I+θ	-	denotes the intermediate value calculated using θ.
I+θ_1	-	denotes the intermediate value calculated using θ_1.
I+θ_2	-	denotes the intermediate value calculated using θ_2.
J	-	denotes the iteration number in a time step.

k	-	the contact coefficient that accounts for incomplete contact between the structure and the ice.
m	-	a parameter which takes into account the shape of the structure or an exponential constant in the delayed elastic element.
n	-	an exponential constant in the viscous strain element.
[N]	-	the displacement interpolation function matrix.
pl	-	denotes values for plane strain compression.
[P]	-	the matrix that relates σ' to ε_d or σ'' to $\dot{\varepsilon}_d$.
q	-	the nodal displacement.
R	-	the change in creep strain increment with respect to stress.
S	-	the surface area.
T	-	the temperature of the ice or the surface traction.
uni	-	denotes values for uniaxial compression.
v	-	the velocity of the moving ice sheet.
V	-	the volume.
[W]	-	the stiffness matrix.
$\alpha_1, \alpha_2, \alpha_3, \alpha_4$	-	the parameters that control how η changes.
$\alpha_5, \alpha_6, \alpha_7, \alpha_8$	-	the parameters that control how η_b changes.
β_1, β_2	-	the parameters that relate $\dot{\varepsilon}_v$ to η_f.
β_3, β_4	-	the parameters that relate $\dot{\varepsilon}_{vb}$ to η_{bf}.
δq	-	the virtual nodal displacement.
δu	-	the virtual displacement.
$\delta \varepsilon$	-	the virtual strain.
Δ	-	denotes changes that occur in a time step or an iteration.
Δt	-	the time step.
υ	-	the Poisson's ratio.

ζ_1 - the ratio of the elastic modulus of the intact region over the failed region.

ζ_2 - the ratio of η_b^f over η_{bi}.

λ - the error limit.

λ_b - the error limit for checking tensile brittle fracture.

λ_L - the error limit for the overall accuracy of the solution.

μ_1 - the viscosity in the viscous element.

μ_2 - the viscosity in the delayed elastic element.

η - the recipocal of the viscosity in the viscous element.

η_b - the equivalent of η in the plane stress model.

η_f - the final value of η under uniaxial constant strain rate compression.

η_i - the initial value of η.

η_{bf} - the equivalent of η_f in the plane stress model.

η_{bi} - the equivalent of η_i in the plane stress model.

η_b^f - the value of η_b used in the failed region.

σ - the applied stress.

σ_{avg} - the average stress.

σ_{peak} - the peak stress.

σ_r - the radial stress.

$\sigma_{residual}$ - the residual stress.

σ_{tf} - the tensile stress cutoff point.

σ_y - the normal stress in the Y-direction.

σ' - the elastic stress in the delayed elastic element.

σ'' - the stress taken up by the dashpot in the delayed elastic element.

σ''_{eff}	-	the effective value of σ'' in the plane stress model.
σ_0	-	the uniaxial compressive strength of ice corresponding to the reference strain rate.
σ_c	-	the uniaxial crushing strength of the ice.
$\theta, \theta_1, \theta_2$	-	the constants which are used in calculating the intermediate stresses.
ε	-	the strain.
$\dot{\varepsilon}$	-	the strain rate.
ε_c	-	the creep strain.
ε_d	-	the delayed elastic strain.
$\dot{\varepsilon}_d$	-	the delayed elastic strain rate.
ε_e	-	the instantaneous elastic strain.
ε_v	-	the viscous strain.
ε_v^p	-	the principal viscous strain.
$\dot{\varepsilon}_v$	-	the viscous strain rate.
$\dot{\varepsilon}_{vb}$	-	the effective viscous strain rate.
ε_{vb}	-	the effective viscous strain.
ε_{vc}	-	the critical viscous strain.
ε_{vcb}	-	the equivalent of ε_{vc} in the plane stress model.
$\dot{\varepsilon}_0$	-	a reference strain rate.
φ	-	the unbalance stress.
Φ	-	a scalar potential function.
ρ_1	-	a constant used in the calculation of $\dot{\varepsilon}_{vb}$.
ρ_2	-	a constant used in the calculation of ε_{vb}.
τ	-	the effective applied stress in the plane stress model.

1. Introduction

Snow and ice are an integral part of life in the region around the Arctic and the Antarctic. The further away the region is from the equator, the greater the effect of snow and ice is on daily life because the winter is longer. Besides the many inconveniences that may arise, snow and ice can be a financial burden to the society. Blowing snow and icy roads are traffic hazard. Floating ice sheets and ice-bergs constantly threaten the safety of shipping and offshore structures. Structures have to be designed to carry heavier loads due to snow accumulation. Bridge piers have to be designed to withstand the collision with ice floes and ice sheets moving downstream.

Since the oil crisis in the 70's, there has been an increase in the oil exploration and drilling activity in and around the arctic region. Some of this activity occurs at sea. Offshore platforms are built to extract crude oil from beneath the sea floor. Beside the severe weather conditions, the danger created by floating ice sheets and ice-bergs is a major safety concern for the offshore structure operators. The impact force of a huge ice-berg is very large. Fortunately, the collision between a huge ice-bergs and drilling platforms rarely occurs. Thus, it is uneconomical to design the drilling platform to withstand such forces. However, the structure in frozen sea will often experience forces due to ice sheet indentation. This is the force that is exerted by an ice sheet as it advances slowly against a structure. The associated pressure can be as high as 10-20 MPa. This type of loading condition occurs in high Arctic regions such as the Beaufort Sea where offshore platforms are surrounded by ice during the winter months. The ice sheet, driven by wind and wave action, slowly advances against the structure. As a result, the structure has to be designed to withstand this load because it occurs frequently. A more accurate prediction of the magnitude and

the distribution of stress on the indentor will allow the offshore structure to be designed more safely and economically.

However, it is difficult to predict the ice forces because the behaviour of ice is very complicated. Ice encountered in nature normally exists close to its melting temperature. Thus, the strength of ice is sensitive to temperature and loading rate, and as a result, the force exerted by the ice sheet on a structure is also sensitive to these two parameters. Some other factors, such as ice crystal orientation, type of ice etc., also greatly influence the behaviour of ice. There is the lack of a good constitutive model, even in one dimension, that deals with all the factors which influence the ice behaviour. Even with a representative constitutive model, it is difficult to solve a realistic two dimensional and three dimensional problems because the material is not uniform.

1.1 Objective of the Thesis

The objective of this thesis is to develop a simple plane stress ice model to represent the behaviour of the ice sheet. A one dimension model for ice in compression is first developed. The model includes the effects of the loading rate and material damage. It is able to account for the residual strength that exists in ice under a constant strain rate in compression. However, the model is restricted to the lower range of the deformation loading rates where ductile failure in the ice dominates. It does not represent compressive brittle fracture which is experienced by ice at high loading rates. Thus, as the loading rate gets higher, the prediction from the model becomes less reliable. The one dimensional model is later generalized to a plane stress situation using the principles of continuum mechanics and, where possible, two dimensional test data from the literature. In the plane stress model, the tensile brittle fracture is modelled by a simple tensile stress cutoff. This plane stress model is then used in solving some indentation

problems. Numerical analyses with different indentor shapes are run to predict the peak force on the indentor and the stress distribution in the ice sheet. Some uniaxial and plane strain analyses are also performed to compare the numerical solutions to the actual test results.

1.2 Organisation of the Thesis

Chapter 2 consists of a literature review on ice. The review includes a brief discussion of ice mechanics. In addition to ice mechanics, various work done on prediction of the ice force on different shapes of structure and on numerical modelling of ice are also discussed.

Chapter 3 discusses the proposed ice model. It is divided into two parts. The first deals with the proposed model in uniaxial loading. This part lists the various components in the model and explains their roles. The second part describes how the one dimensional model is expanded to a plane stress one.

Chaper 4 deals with the process of implementing the plane stress model into a finite element program. The first section of this chapter explains the solution scheme that is used to solve a general creep problem. The second section deals with special considerations associated with the implementation of the various components of the model, in the finite element program. The considerations include various assumptions and mathematical treatments that are made and performed to ease the numerical computation. The third section in this chapter consists of a flow chart with some explanation to assist in showing the sequence of the numerical operations in the finite element program for the plane stress ice model.

Chapter 5 consists of the presentation and the discussion of the analytical solution. The first part of this chapter gives a brief explanation on how to work out the values of the parameters used in the numerical analysis. This part is

followed by the presentation and the discussion of the numerical results for problems of ice in uniaxial compression, plane strain compression, and indentation. Where possible the numerical predictions are compared with actual test results.

Chapter 6 consists of a summary and conclusions.

2. Literature Review

Ice is a very complex material. This is due in part, to the fact that in its natural state it is very close to its melting point. The behaviour of ice depends on its crystal orientation, the loading rate and many other factors. Much work has been done to categorize ice based on its crystal orientation, to determine its response under different load conditions, and to predict the forces that ice may exert on a structure.

2.1 Ice Mechanics

Ice has a hexagonal crystal structure. Its material properties depend on many factors. These include the crystal orientation, crystal size, temperature, and air voids. The behaviour of ice has been investigated considerably under various factors and different types of loading. The two most common load conditions used in testing are indentation and uniaxial loading.

2.1.1 Types of Ice

There are two main categories of ice: granular and columnar. These two groups are differentiated by the ice crystal orientation. The ice crystals in granular ice are randomly orientated and the material can be considered isotropic. For columnar ice, the c-axes of the ice crystals are oriented in the plane perpendicular to the columns (the c-axis of an ice crystal is shown in Figure 2.4). This is due to the preferential growth of the ice crystals in the direction of the columns. Since the c-axes of the columnar ice crystals are randomly distributed within only one plane, the material can be classified as tranverse isotropic. In certain situations, as in a narrow channel, the ice growth may be influenced by the current flow. This creates a unique form of columnar ice where the c-axes of the

ice crystals are aligned in one direction. This type of columnar ice exhibits orthotropic material properties. The subsequent use of the term 'columnar ice' in this thesis refers to the tranverse isotropic type.

2.1.2 Material Properties of Ice

The form of the stress-strain curve that ice exhibits under constant strain rate deformation depends on the strain rate, temperature, loading direction, type of ice, grain size and etc. These factors also influence the peak stress and the type of failure that ice experiences.

Ice encountered in nature normally exists close to its melting temperature. Thus, the strength of ice is sensitive to temperature and loading rate. The strength of ice is defined as the maximum stress that ice experiences under a constant strain rate loading. It can be the peak stress, the asymptotic stress or the maximum stress depending on the shape of stress-strain curve ice as shown in Figure 2.1. Most materials, such as steel, exhibit the same effects near their melting points.

There are two distinct modes of failure for ice: creep mode and brittle mode. Creep failure is governed by the viscous flow of ice and occurs at a low strain rate. The relationship between the applied strain rate and the peak stress for this failure can be represented by power-law creep as illustrated in Figure 2.2. The brittle failure which occurs at high strain rates is characterized by a sudden complete material failure. For the creep mode type of failure, Haynes (1979) has shown that for the same deformation loading rate, the strength of ice increases as the temperature decreases. As the temperature is reduced, ice becomes more viscous, consequently a higher stress is required to generate the same deformation rate at a lower temperature. A similar occurrence is found for

compressive brittle fracture. The compressive brittle fracture strength increases with the reduction in temperature (Carter,1972).

Under constant strain rate compression, the shape of the stress-strain curve depends on the strain rate. These stress-strain curves of ice are shown in Figure 2.1. At a very low strain rate ($1x10^{-8}s^{-1}$), ice reaches an asymptotic stress value without peaking. For higher strain rates ($1x10^{-5}s^{-1}$), the stress reaches a peak value and then decreases. At an even higher strain rate ($1x10^{-1}s^{-1}$), ice fails abruptly once the peak (maximum) stress is achieved. As a result, there is no descending branch on the stress-strain curve.

The failure mechanism governing ice varies with strain rate. At very low strain rates, the failure mechanism is governed by the creep process. Material deterioration does not occur for this mode of failure. In this situation, the deformation of the ice consists primarily of viscous flow. The viscous deformation rate is equal to the applied deformation rate. The stress that is required to produce a viscous deformation rate equal to the imposed deformation rate is considered as the strength of the ice. For very low strain rates, the stress in the ice reaches an asymptotic value and remains at that level unless there is a change in the loading condition. However, at very high strain rates, the strength is controlled by brittle fracture. In this case, the failure stress does not change with strain rate. For intermediate strain rates, the failure mechanism is a combination of both creep and brittle fracture.

Ice has a quite different response under tensile loading (Figure 2.2). At low strain rates, the response in tension and compression are similar. At higher strain rate, ice exhibits a greater capacity to carry the compressive load. As illustrated in Figure 2.2, the strength for tensile brittle facture is only slightly lower than the maximum peak tensile stress, but the strength for compressive brittle fracture is much lower than the maximum peak compressive stress.

Under constant stress loading, the deformation of the ice can be divided into four main stages: i) instantaneous elastic deformation, ii) primary creep , iii) secondary creep , iv) tertiary (accelerating) creep and failure. These four stages are shown on Figure 2.3. At very low stresses (0.1MPa), the deformation does not pass beyond the secondary creep stage. At higher stresses (2.0MPa), ice progresses to the tertiary creep stage and eventually fails. At even higher stresses (4.0MPa), the secondary creep stage is bypassed and the tertiary stage occurs immediately after the primary stage.

The behaviour of ice under multiaxial loading is naturally more complicated than under uniaxial loading. Most work done on ice under multiaxial load has been for compression. Frederking (1977), and Timco and Frederking (1984 and 1986) have done some plane strain tests on ice. The plane strain confinement is found not to affect the strength of granular ice very significantly (Frederking,1977). In the plane strain tests done on columnar ice with load application in the direction perpendicular to the long direction of the columnar grains, two different confinements have been used: confinement in the long direction of the column and confinement in the plane perpendicular to the long direction. The observed strength for the former case is almost the same as uniaxial situation. However, the failure strength for the latter plane strain case is three to four times that of the uniaxial situation. Columnar ice can carry more load in the direction along the columns than in the plane orthogonal to the columns (horizontal direction). In triaxial tests, the peak compressive deviatoric stress of granular ice increases with the confining pressure up a certain point only (Jones,1982). After that, the peak deviatoric stress decreases. However, the tensile strength of ice does not increase with increasing confining pressure. Instead, the tensile strength drops off dramatically (Haynes,1973).

In addition to the temperature and the loading rate, there are other factors that affect the strength of ice. Air voids and salt inclusions can cause a significant reduction in strength. In the situation where the brine volume is much greater than the air void volume, Weeks and Assur (1967) have suggested that the strength of ice varies according to $\sigma_f = (1 - cv_b^k)\sigma_o$, where σ_f is the reduced strength, v_b is the brine volume, σ_o is the strength with zero air void and brine volume, and c and k are constants that vary with the shape of the brine pockets. One may expect the crystal size to have some effect on the strength since an ice specimen is usually made up of many individual crystals. However, there is no consensus as to whether this is true or not. Schulson and Cannon (1984) claim that the compressive strength of the ice decreases by approximately 1.5 MPa as the grain size increases from 1 to 8 mm. On the other hand, Jones and Chew (1983) have found that there is no grain size dependency for the compressive strength within the size range of 0.6 to 2.0 mm.

Vittoratos and Kry (1979) have found that the strengths of large scale and small scale ice specimens are the same at small strain rates. The large scale specimen measures 0.3m wide 0.5 deep and 1.5m long while the small scale specimen has the corresponding dimension of 0.101m, 0.101m and 0.2m. At high strain rates, the strength of the small specimens is found to be bigger than that of the large specimens. This behaviour is attributed to the type of failure mode. Ductile failure at a low strain rate is found to be size independent, but brittle fracture at a high strain rate is found to be size dependent. Sanderson (1986) and Ashby et al. (1986) suggest that the reason for the reduction in strength, is the non-simultaneous failure in the ice rather than the increase in the flaw size due to the size increase of the specimen. Schwarz et al. (1974) suggest that the compressive strength of ice depends on the ratio of the sample size to the crystal size rather than on the sample size itself. In the experiment done by

Schwarz et al., with a large ice sample width to crystal size ratio, the uniaxial compressive strength is relatively constant for all samples ranging from 1 to 100 cm^2.

2.1.3 Ice Indentation

The interaction between ice and an indentor is very complicated. All the factors mentioned in the previous section which govern the strength of ice, have some influence on the ice indentation force. The indentation velocity, the ice thickness, and the size and shape of the indentor also influence the load the ice sheet exerts on the indentor. The effective indentation stress can be two to four times the uniaxial strength of the ice. There has been much discussion on the dependency of the indentation force on the ice thickness and the indentor width. Afanasev et al. (1971) has pointed out that the effective indentation stress is very much influenced by ratio of the thickness to the indentor width. The effective stress increases with increasing value of this ratio. Sodhi and Morris (1984), Ponter et al. (1983), and Ralston (1978) also consider this ratio as an important factor in determining the effective indentation stress. They have stated that as the ratio increases, the loading condition shifts from plane stress to plane strain. However, Frederking and Gold (1975), Michel and Toussaint (1977) and Saeki et al. (1977) have disputed that claim. Their findings show that the effective indentation stress is only dependent on the width of the indentor.

2.2 Ice Force Prediction in Indentation

Indentation problems are closely related to actual field situations. When a moving ice sheet advances slowly against a structure, only a portion of the ice sheet is in contact with the structure. This is similar to an indentation test where

the indentor moves slowly against an ice sheet. An offshore structure in a frozen sea or a bridge pier in a frozen river experiences the indentation type of loading. In winter, the offshore structure is surrounded by the ice sheet. Driven by the sea current as well as the wind, the ice sheet moves slowly against the stucture. The same situation occurs in a frozen river when the ice sheet advances against the bridge pier. Consequently, extensive studies made on ice indentation have been carried out so that the forces exerted on these structures can be better understood.

There are two main approaches to predicting indentation ice forces: 1) prediction based on empirical equations, or 2) prediction based on the numerical analysis using an appropriate two or three dimension material model for ice.

2.2.1 Empirical Equations

The simplest approach to predict the force exerted on a structure by a floating ice sheet is to use empirical equations based on experimental results. The general form of the equation of this type is:

$$F = f\left(C, v, \frac{\dot{\varepsilon}}{\dot{\varepsilon}_0}, m, k, b, h, \sigma_c \text{ or } \sigma_0, B, T \right)$$

where F = the horizontal force exerted by the ice sheet,

C = the indentation coefficient which takes into account the biaxial stress condition around the structure,

m = a parameter which takes into account the shape of the structure,

k = the contact coefficient that accounts for incomplete contact between the structure and the ice,

v = the velocity of the moving ice sheet,

b = the width (or other appropriate dimension) of the indentor,

h = the ice thickness,

B = the width of the ice sheet,

$\dot{\varepsilon}$ = the strain rate,

$\dot{\varepsilon}_0$ = a reference strain rate,

σ_0 = the uniaxial compressive strength of the ice corresponding to the reference strain rate,

σ_c = the uniaxial crushing strength of the ice, and

T = the temperature of the ice.

Various equations of this form have been proposed.

Korzhavin (1962) has proposed an equation of the form:

$$F = bhCmk\sigma_c\left(\frac{1}{v}\right)^{0.33}.$$

For $B/b \geq 15$, C is suggested to be 2.5. In the equation, the force generated by the ice is a function of the velocity. However, the effect of either b or h on the strength of the ice was not included.

Afanasev et al. (1971) has suggested that:

$$F = bhCmk\sigma_c$$

The strength of the ice is affected by the width of the structure and the ice thickness. The value of C in the equation varies with b/h as follows:

for $1 \leq \frac{b}{h} \leq 6$ $\quad C = \sqrt{5\frac{h}{b}+1}$, and

for $0.1 \leq \frac{b}{h} < 1$ $\quad C = \frac{1}{6}\left(25\frac{h}{b} - 10\right)$.

Thus, for the same contact area, the ice force decreases as b/h increases.

Schwarz et al. (1974) have proposed the equation:

$$F = 3.57\sqrt{b}\,h^{1.1}\sigma_c = 3.57\,bh\sigma_c\frac{h^{0.1}}{\sqrt{b}}.$$

This equation is limited to circular piles and the penetration type of ice-pile interaction. No velocity is included in his equation because the numerical constant and the crushing stress used are supposed to produce the upper bound load.

Saeki et al. (1977) have proposed a function that is quite similar to the one proposed by Schwarz et al. Their function is:

$$F = C_I h\sigma_c\sqrt{b} = bh\sigma_c\frac{C_I}{\sqrt{b}},$$

where C_I = a coefficient that varies with the shape of the pile.

The constant $3.57h^{0.1}/\sqrt{b}$ from Schwarz et al. and $C_I/\sqrt{b}$ from Saeki et al. play the same role as the product Cm in both the equations of Korzhavin and Afanasev et al. Both Schwarz et al. and Saeki et al. claim that the failure in the ice sheet is due to horizontal cracking and the strength of the ice is proportional to $h^{0.1}/\sqrt{b}$ and $1/\sqrt{b}$ respectively. In both cases, the influence of the ice thickness on the strength is very small or none.

Michel and Toussaint (1977) have presented a set of equations for a whole range of ice deformation rates. Their equations also do not consider the ice thickness as a factor in the strength. The indentor width b is used to calculate the effective strain rate $\dot{\varepsilon} = v/4b$ which in turn is used to determine the type of failure and the magnitude of the force. The set of equations proposed are:

i) In the pure ductile zone.

$$F = bhCmk\sigma_0\left(\frac{\dot{\varepsilon}}{\dot{\varepsilon}_0}\right)^{0.32}$$

ii) In the transition zone.

$$F = bhCmk\sigma_0\left(\frac{\dot{\varepsilon}}{\dot{\varepsilon}_0}\right)^{-0.126}$$

iii) In the brittle zone.

$F = bhCmk\sigma_b$

where σ_b = the uniaxial crushing strength of the ice under brittle condition.

The parameters C and k are different for each zone.

2.2.2 Ice Modelling

Another approach in the ice load prediction is through a numerical analysis using a suitable ice material model. The material model used has to be two or three dimensional to represent ice indentation. Even though one dimensional models are not suitable for indentation analyses, they can be a useful guide for forming two dimensional or three dimensional models. Therefore, a discussion on one dimension models is included in this section.

Glen (1955) has observed that at low stress, there are transient and continuous components of creep. At higher stresses, an accelerating stage of creep occurs. The minimum creep rate is found to be closely represented by $\dot{\varepsilon} = B\sigma^n \exp(-Q/RT)$, where T is the temperature in degrees Kelvin, R is the gas constant, and B, n, and Q are constants with the value of 3.2, 32 kcal/mole and 7×10^{24} (1/(bar^n.year)) respectively.

Karlsson (1971) has proposed a viscoelastic-plastic model for sea ice. The pre-yield ice response is modelled by the combination of a Kelvin-Voigt unit and a Maxwell unit. For plastic deformation, an assumed yield surface is used. The shape of the yield surface is constant, but its size increases with strain rate.

The strain rate dependence of the yield surface size only occurs at the pre-yield stage. Once the ice has yielded, the size of the yield surface stays constant.

Sinha (1978a, 1978b and 1981) has proposed a rheological model for ice under uniaxial loading based on his experimental results. It is made up of three components.

1) Elastic strain $\varepsilon_e = \sigma / E_0$.

2) Delayed elastic strain (recoverable) $\varepsilon_d = (c\sigma/E_0)(1-\exp(-(a_t t)^b))$.

3) Viscous strain $\varepsilon_v = \dot{\varepsilon}_{v_1} |\sigma|^n t$

where σ = applied stress,

E_0 = Young's modulus which is almost temperature independent,

$\dot{\varepsilon}_{v_1}$ = steady state strain rate for one unit stress (temperature dependent),

n = 3,

c = a constant that varies with the grain size, and

a_t = a constant that varies with temperature.

The viscous strain proposed by Sinha is very similar to the minimum strain rate equation proposed by Glen (1955). However, this model is unable to represent the post peak behaviour of the ice.

Michel (1977) has proposed a two dimensional creep model that takes into account the elastic and plastic deformation of each ice crystal. The plastic deformation expression in this model is based on Glen's law and the increase in number of mobile dislocations. Only the shearing stress acting in the direction of the basal plane of the ice crystal causes the plastic deformation.

A constitutive relation for the non-elastic deformation of polycrystalline ice has been proposed by Le Gac and Duval (1979). Their model contains two forms of hardening (isotropic and directional). Both are affected by two opposite

processes of strain hardening and softening. Scalar and tensor state variables that change with time and deformation are used. The tensor state variable allows the model to represent creep recovery. This situation occurs when the tensor state variable is larger than the applied deviatoric stress (as in the case of a load removal or reduction).

Wang (1982) has proposed a simple one dimensional model to describe the mechanical behaviour of sea ice. This model has the form:

$$\frac{\sigma}{\sigma_0} = \frac{\left(\frac{\dot{\varepsilon}}{\dot{\varepsilon}_0}\right)^n \frac{\varepsilon}{\varepsilon_0}}{\left(\left(\frac{\varepsilon}{\varepsilon_0}\right)^2 + \left(1 + A\left(\frac{\dot{\varepsilon}}{\dot{\varepsilon}_0}\right)^n \frac{\varepsilon}{\varepsilon_0}\right)^2\right)^{\frac{1}{2}}}$$

where A = constant,

n = constant,

ε = strain,

$\dot{\varepsilon}$ = strain rate,

ε_0 = reference strain,

$\dot{\varepsilon}_0$ = reference strain rate,

σ = stress, and

σ_0 = reference stress.

The parameters A, n, σ_0, ε_0 and $\dot{\varepsilon}_0$ are five temperature dependent material constants of which only four are independent. Under constant strain rate loading, the stress-strain curve has a peak stress:

$$\sigma_{max} = (\dot{\varepsilon}/\dot{\varepsilon}_0)^n \sigma_0.$$

The strain at peak stress is given by:

$$\varepsilon/\varepsilon_0 = [A\,(\dot{\varepsilon}/\dot{\varepsilon}_0)^n]^{-1}.$$

At very large strain, the model gives an asymptotic stress of

$$\sigma_{asymp} = (\dot{\varepsilon}/\dot{\varepsilon}_0)^n [1 + A^2 (\dot{\varepsilon}/\dot{\varepsilon}_0)^{2n}]^{-0.5}.$$

Chen et al (1985) have proposed a hypoelastic model for high strain rates that includes the confining pressure and post peak softening. At small strains, the model is almost linear elastic; at large strains, it displays a Mohr-Coulomb type behaviour where the residual strength is dependent on the confining pressure. However, there are some limitations in the application of this model. One is its inability to simulate unloading and cyclic loading. Another is the restriction to only imposed incremental displacement loading. This restriction is imposed because the stress-strain relationship is not unique, as there can be two values of strain for one stress.

Szyszkowski and Glockner (1985) use the combination of a modified Maxwell unit and a modified Kelvin-Voigt unit in series, to describe the uniaxial stress-strain behaviour of the ice. The spring stiffness in the Kelvin-Voigt unit varies with the state of stress and strain in the unit. The dashpots in both the Kelvin-Voigt and Maxwell units have non-linear stress-strain rate relationships. These takes the form of $\dot{\varepsilon} \propto \sigma^n$, with each unit having a different n. To account for the post peak behaviour, the viscosity for the dashpot in the Maxwell unit decreases with strain after the strain in that unit exceeds a specific value.

Ting and Sunder (1985) have proposed a constitutive model for the sea ice. It covers both ductile and brittle behaviours of ice from uniaxial to triaxial state of stress. The model is made up of two parts: one part accounts for the continuum behaviour and the other, for brittle fracture. The continuum behaviour is modelled by using the combination of a rate-dependent spring and a non-linear dashpot in series. A damage parameter, which is a function of the strain and strain rate, is also included to describe the ice response in the ductile to brittle transition zone. This parameter reduces the spring stiffness and the

dashpot viscosity. The yield/fracture behaviour of the ice is governed by a rate sensitive and isotropic Drucker-Prager failure surface.

Karr (1984,1985a,1985b) has proposed a constitutive equation for ice under uniaxial compression that is based on the theory of continuum damage mechanics. The model attempts to represent the changes in the microstructure of the ice caused by the the internal cracking and the plastic flow. The formation of the internal cracks in the ice sample is related to its acoustic emission response.

2.2.3 Other Methods

There are some other lesser known approaches to predicting indentation ice forces beside the two main one mentioned in the preceeding sections. Some of these lesser known procedures are dealt with in this section.

Reinicke and Ralston (1977) , and Ralston (1978) calculate the upper bound and lower bound force on a flat indentor using a plastic limit analysis approach. A generalized Von Mises yield function is used to take into account the difference of the ice strength in tension and compression. To find the lower bound solution, the ice sheet is divided into ten zones of constant stress. For the upper bound solution, the ice sheet is divided into five distinct rigid bodies. Both solutions are then solved numerically.

Mellor and Cole (1983) use a different approach from other researchers to describe the stress-strain-time relationship of ice. Instead of representing the behaviour of ice mathematically as most other researchers do, they construct the response of the ice from experimental results from creep tests and constant strain rate tests. Creep test results are used to construct the stress-strain curve for the constant strain rate loading and the constant strain rate test results are used to construct the creep curve for the constant stress loading.

Ponter et al (1983) use the reference stress method to estimate the ice sheet indentation force. This procedure utilizes a number of related numerical and analytical solutions, together with some assumptions, to estimate the indention force. The two basic assumptions are:

1) $PU = \sigma_0 V_0 F_{\dot{\varepsilon}}(\sigma_0)$, and

2) $\frac{\sigma_0}{P} = \frac{Y}{P_L}$ where

$F_{\dot{\varepsilon}}(\sigma_0)$ = strain rate corresponding to the reference stress,

V_0 = reference volume,

σ_0 = reference stress,

P = the load on the structure,

U = the velocity at the point of loading,

P_L = the plastic collapse load of the structure, and

Y = the yield stress corresponding to P_L.

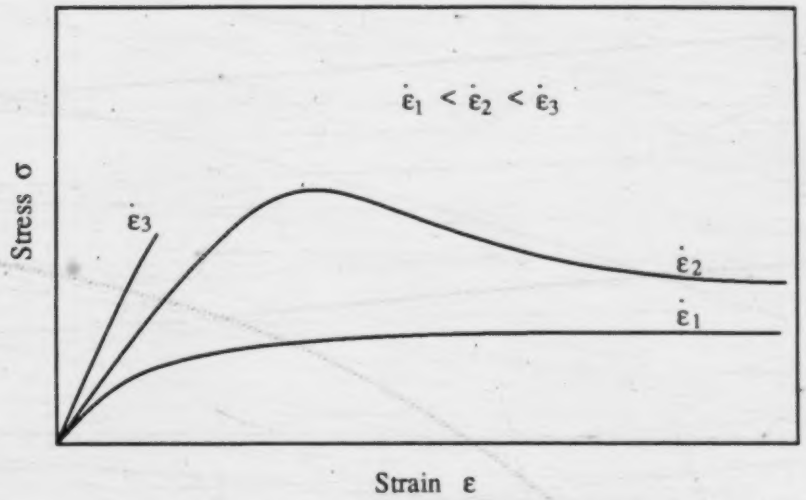

Figure 2.1 Typical stress strain curve of ice under constant strain rate compression.

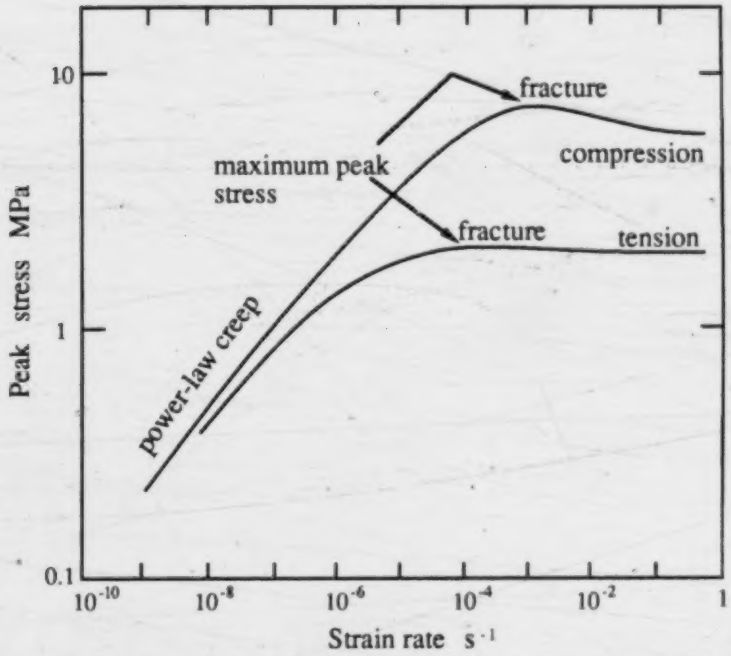

Figure 2.2 Relationship between the peak stress and uniaxial strain rate for ice in tension and compression. (Modified from Palmer et al., 1983)

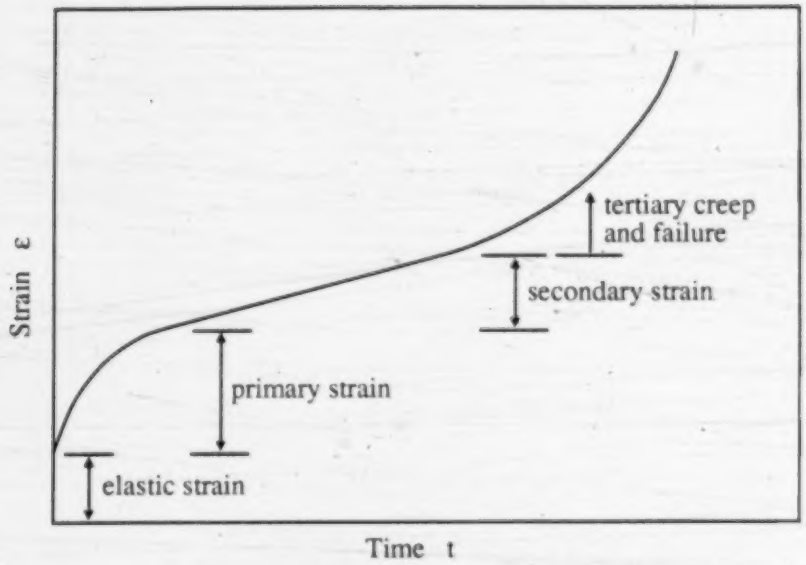

Figure 2.3 Typical strain-time curve of ice under constant stress loading.

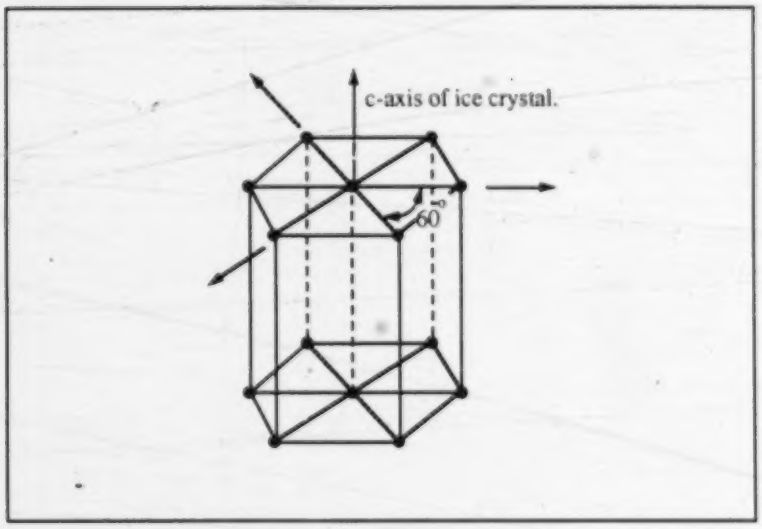

Figure 2.4 Orientation of c-axis in a hexaganol crystal structure. (Modified from Vlack, 1980)

3 Constitutive Model

The proposed constitutive model for ice is formulated on a semi-empirical basis. It is based on the results of ice tests reported in the literature. The model is first formed for uniaxial loading and expanded to include the plane stress condition. The model divides the deformation of ice into three components: instantaneous elastic, delayed elastic and viscous flow. These components are discussed in the following sections. The instantaneous elastic and viscous deformations are represented by a Maxwell unit (Figure 3.1), and the delayed elastic deformation is represented by a Kelvin-Voigt unit (Figure 3.2). Softening of ice is treated by allowing the viscosity of the Maxwell unit to change. In the plane stress model, a tensile stress cutoff is used to simulate tensile brittle fracture. The proposed model can, however, only be used in the range of loading where the peak stress of ice is governed by power-law creep (viscous flow). The range varies with temperature, type of loading, type of ice etc. Figure 2.2 gives an illustrative intrepretation of the loading range governed by power-law creep for a uniaxial condition.

3.1 One Dimension Model

The proposed one dimensional model for ice in compression consists of the combination of a Maxwell unit (Figure 3.1) and a Kelvin-Voigt unit (Figure 3.2) in series. The dashpots in both units are non-linear. In addition, the dashpot in the Maxwell unit is damage sensitive. Figure 3.3 gives a graphical representation of the model.

In Figure 3.3, the applied stress is represented by σ. This is the normal stress that is experienced by ice. The model can be divided into three elements: instantaneous elastic, viscous and delayed elastic. The elastic member in the

Maxwell unit represents the instantaneous elastic response of ice. It has an elastic modulus of E_1 and a corresponding elastic strain ε_e. The dashpot in the Maxwell unit represents the non-recoverable viscous deformation. It has the viscosity of μ_1 or $1/\eta$ and a viscous strain of ε_v. The delayed elastic response of ice is represented by the Kelvin-Voigt unit. This is the non-instantaneous elastic deformation which does not manifest itself immediately after loading or unloading. This unit has an elastic modulus E_2, a viscosity μ_2 and a delayed elastic strain ε_d. The stress in the elastic member is denoted with σ' and the remaining stress that has to be taken up by the dashpot is denoted by σ''. These three elements are discussed in detail in the following subsections.

3.1.1 Instantaneous Elastic Element

The instantaneous elastic response of ice is represented by an elastic element with the modulus E_1. Creep tests done by Brill and Camp (1961) have shown that ice experiences instantaneous deformation and recovery upon the application and removal of the load. The instantaneous deformation is found to be almost equal to the instantaneous recovery. Sinha (1978b) has observed that at -40^0C and for a compressive stress in the range of 0-2.5MPa, columnar ice has a linear stress to instantaneous strain relationship. Consequently, the instantaneous elastic strain is assumed to change linearly with the applied stress in the form of $\varepsilon_e = \sigma / E_1$. The Young's modulus also remains quite stable over a wide range of temperature (Sinha,1978a and Mellor,1983). Thus, the modulus E_1 for the proposed model is assumed to be loading rate and temperature independent.

3.1.2 Delayed Elastic Element

A Kelvin-Voigt unit is used to represent the delayed elastic deformation. This unit can accommodate the non-instantaneous elastic response such as the

creep recovery during unloading. The strain rate in the dashpot is assumed to be proportional to $(\sigma'')^m$ where m is a constant. As a result, the delayed elastic strain rate is:

$$\dot{\varepsilon}_d = (\sigma'')^m / \mu_2 \ .$$

In reverse, the stress σ'' can be expressed as:

$$\sigma'' = (\mu_2 \dot{\varepsilon}_d)^{1/m} \ .$$

The relationship between σ' and ε_d is assumed to be linear. Therefore, the stress σ' can be written as:

$$\sigma' = E_2 \varepsilon_d \ .$$

The applied stress which is the sum of σ' and σ'' can be written in terms of delayed viscous strain and strain rate as follow:

$$\sigma = \sigma' + \sigma''$$
$$= E_2 \varepsilon_d + (\mu_2 \dot{\varepsilon}_d)^{1/m} \ .$$

Both the elastic modulus E_2 and the viscosity μ_2 are independent of time and deformation. The Kelvin-Voigt model proposed is quite similar to the one proposed by Szyszkowski and Glockner (1985) except that their model has an elastic modulus that varies with the deformation.

3.1.3 Viscous Element

The viscous element is a non-linear dashpot based on Glen's power law (Glen,1955). The viscous strain rate $\dot{\varepsilon}_v$ is given by $\eta\sigma^n$ where n is constant. To accommodate the post peak softening of the ice under uniaxial constant strain rate loading, the value of η is allowed to vary. A higher η value allows ice to deform faster with the same stress or to deform at the same rate with a lower stress. The changing value of η takes into account the structural deterioration in the ice. However, η cannot decrease in value because the damage process is irreversible.

There are five important parameters that influence η. They are η_i, η_f, $\dot{\varepsilon}_v$, ε_v and ε_{vc} where η_i is the initial η, η_f is the final η under constant strain rate compression, $\dot{\varepsilon}_v$ is the viscous strain rate, ε_v is the viscous strain and ε_{vc} is the critical viscous strain. The following subsections explain the role of these five parameters and how η must change to duplicate the experimental results.

3.1.3.1 Initial and Final Value of η

For low strain rate compression, the peak stress of ice is governed by power-law creep as shown in Figure 2.2. Consequently, the viscous element is used to control the peak stress. In constant strain rate compression, the peak stress is influenced by the initial η value of η_i. The peak stress can be approximated by:

$$\sigma_{peak} \approx \left(\frac{\dot{\varepsilon}}{\eta_i}\right)^{\frac{1}{n}} .$$

Various experiments (Sinha,1983, Mellor and Cole,1982, Cox et al., 1984 and 1985) have shown that ice possesses some residual strength when tested under constant uniaxial compressive strain rate. This is exemplified in Figure 3.4. The residual strength seems to depend on the deformation rate. At the later stage of loading under constant strain rate, almost all the deformation is due to viscous flow. This suggests that the residual strength is controlled by the value of η. In order to model this characteristic, the final value of η has to be a function of the viscous strain rate ($\eta_f = f[\dot{\varepsilon}_v]$). Therefore, the residual strength is assumed to be:

$$\sigma_{residual} = \left(\frac{\dot{\varepsilon}}{\eta_f}\right)^{\frac{1}{n}} .$$

At strain rates less than $5x10^{-7}s^{-1}$ in Sinha's (1982) tests and at stresses less than 0.5MPa in Gold's (1972) tests, ice does not seem to undergo any structural deterioration with time. For example, curve 1 in Figure 3.4 shows the stress approaching an asymptotic value without showing a peak value. In this case, the value of η_f cannot be greater than the initial value η_i. Since η cannot decrease, it follows that η_f must be equal to η_i. For curve 2 and 3, σ_{peak} is greater than $\sigma_{residual}$. Therefore, η_f for these two cases must be greater than η_i.

3.1.3.2 **Viscous Strain ε_v - As a Controlling Parameter**

Saeki et al. (1977) and Schwarz et al. (1974) observed that the failure of ice in their indentation tests occurred with the formation of cleavage cracks perpendicular to the thickness of the ice sheet. In tests done on columnar ice, Frederking (1977) noticed that the pattern in which initial cracking occurs is the same for uniaxial compression and plane strain compression. Figure 3.5 gives the loading direction with respect to the orientation of the ice specimens for both cases of loading. In the uniaxial test, the loading is in X direction. In the plane strain test, the free surface is parallel to the X-Y plane. Cracks form in a plane parallel to the direction of the loading and the long axis of the grains. These cracks then coalesce to form shear bands. The maximum stress in the uniaxial compression tests occurs with the appearance of the shear band. For the plane strain case, the stress continues to increase until extensive cleavage cracks are formed parallel to the X-Y plane. Sinha (1982 and 1985) and Gold (1972) have noticed a similar cracking pattern. From the observations made by Saeki et al., Schwarz et al., Frederking, Sinha and Gold, the cracking activity seems to be governed by the tensile strain. For columnar ice loaded uniaxially in the X direction, the strain rate is much lower along the Z axis than in the other two directions (Wang,1981). Thus, the tensile strain is bigger in the Y direction than

Z direction. This explains why cracks first form on a plane perpendicular to the Y direction. In plane strain tests, the tensile deformation is confined to the Z direction. As a result, the cleavage cracks form in the X-Y plane. However, this does not explain why the initial crack pattern in the plane strain tests is similar to that in the uniaxial tests. In the plane strain tests, the initial cracking pattern does not seem to be influenced by the total strain. For this reason, the total strain should not be used as a parameter to control η. The total strain is made up of the instantaneous elastic strain, the delayed elastic strain and the viscous strain. Among these three strains, only the viscous strain can increase indefinately while the other two are limited by the applied stress. Therefore, the viscous strain is a more suitable parameter to be used to control η than the instantaneous elastic or the delayed elastic strain. In plane strain tests, the total strain is zero in the direction of the confinement (Y direction), but this does not mean that the viscous strain is also zero. Thus, the initial cracking pattern in the plane strain tests can possibly be accounted for by using the viscous strain as the controlling parameter, because it is not zero in the Y direction. As a result, the viscous strain is used to control η. In uniaxial compression, the viscous strains in Y and Z directions are tensile. Since cracks are assumed to be caused by tensile strain, only these two strains influence the value of η. Assuming that there is no volume change in viscous flow, the sum of normal viscous strains can be written as $\varepsilon_{vX}+\varepsilon_{vY}+\varepsilon_{vZ}= 0$. This gives $\varepsilon_{vX}= -\varepsilon_{vY}-\varepsilon_{vZ}$, and so ε_{vX} is a measure of ε_{vY} and ε_{vZ}. Consequently, the viscous strain in X direction is used to represent the effect of the tensile viscous strain in Y and Z directions in the one dimension model.

3.1.3.3 Critical Viscous Strain ε_{vc}

The constant ε_{vc} is used to control the strain at peak stress. The parameter ε_{vc} is the viscous strain at which the value of η starts to increase.

Mellor and Cole (1982) have found that the peak stress for most of the uniaxial strain rate tests occurs at almost the same strain. Tests done on fresh water columnar ice by Sinha (1983) over the strain rate range of $.5\times10^{-7}s^{-1}$ to $3\times10^{-5}s^{-1}$ have showed that the strain at peak stress increases only slightly with the strain rate, varying over the range from 4.5×10^{-4} to 11×10^{-4}. On this basis, ε_{vc} is assumed to be constant.

3.1.3.4 The Mathematical Expression for Viscous Element

The assumed mathematical expression for the viscous element is listed below.

The viscous strain rate is $\dot{\varepsilon}_v = \eta\sigma^n$.

For $\varepsilon_v \le \varepsilon_{vc}$, $\eta = \eta_i$.

For $\varepsilon_v > \varepsilon_{vc}$,

$$\frac{d\eta}{d\varepsilon_v} = (\eta_f - \eta)\alpha_1\left(\frac{\alpha_2|\varepsilon_v| - \varepsilon_{vc}}{\alpha_3}\right)^{\alpha_4} \qquad (3.1)$$

and $$\frac{d\eta}{d\varepsilon_v} = 0 \quad \text{if} \quad \alpha_2|\varepsilon_v| - \varepsilon_{vc} \le 0 \quad \text{or} \quad \eta_f - \eta \le 0$$

where $\eta_f = \beta_1(\dot{\varepsilon}_v)^{\beta_2}$,

n, ε_{vc}, β_1, β_2, α_1, α_2, α_3 and α_4 are constants,

η_i is the initial value of η, and

η_f is the final value of η under a constant strain rate loading.

Equation 3.1 controls how η changes with respect to the viscous strain ε_v. However, when $\alpha_2|\varepsilon_v| - \varepsilon_{vc}$ or η_f-η is less than zero, $d\eta/d\varepsilon_v$ is set to zero. The criterion η_f-η less than zero takes into account the irreversibility of the damage

process. The other condition, $\alpha_2|\varepsilon_v| - \varepsilon_{vc}$ less than zero is introduced because equation 3.1 is undefined in this case.

3.2 Plane Stress

The indentation of an ice sheet whose thickness is small relative to the lateral dimensions can be assumed to be a plane stress condition. This assumption is valid except when the indentor width to ice thickness ratio is small. Referring to the coordinate system in Figure 3.6, and assuming columnar ice with the columns in the X_3 direction, the ice is taken to be isotropic in the X_1, X_2 plane. In the following, the one dimension model for compression from the previous section, is generalized to the plane stress situation. Each of the three element is considered in turn.

3.2.1 Instantaneous Elastic Element

The stress-strain relationship for a linear elastic material is well-known. For plane stress loading, it is:

$$\begin{Bmatrix} \varepsilon_{e11} \\ \varepsilon_{e22} \\ \varepsilon_{e12} \end{Bmatrix} = \frac{1}{E_1} \begin{bmatrix} 1 & -\upsilon & 0 \\ -\upsilon & 1 & 0 \\ 0 & 0 & 2(1+\upsilon) \end{bmatrix} \begin{Bmatrix} \sigma_{11} \\ \sigma_{22} \\ \sigma_{12} \end{Bmatrix}$$

or

$$\begin{Bmatrix} \sigma_{11} \\ \sigma_{22} \\ \sigma_{12} \end{Bmatrix} = \frac{E_1}{(1-\upsilon^2)} \begin{bmatrix} 1 & \upsilon & 0 \\ \upsilon & 1 & 0 \\ 0 & 0 & (1-\upsilon)/2 \end{bmatrix} \begin{Bmatrix} \varepsilon_{e11} \\ \varepsilon_{e22} \\ \varepsilon_{e12} \end{Bmatrix}.$$

3.2.2 Delayed Elastic Element

The generalization of the delayed elastic term is more complicated. One of the difficulties encountered is to make the term coordinate invariant in the X_1,

X_2 plane because columnar ice is isotropic in that plane. The elastic component is assumed to have a similar stress-strain relationship of a linear elastic material. It follows that:

$$\begin{Bmatrix} \varepsilon_{d11} \\ \varepsilon_{d22} \\ \varepsilon_{d12} \end{Bmatrix} = \frac{1}{E_2} \begin{bmatrix} 1 & -\upsilon & 0 \\ -\upsilon & 1 & 0 \\ 0 & 0 & 2(1+\upsilon) \end{bmatrix} \begin{Bmatrix} \sigma'_{11} \\ \sigma'_{22} \\ \sigma'_{12} \end{Bmatrix}$$

or $$\begin{Bmatrix} \varepsilon_{d11} \\ \varepsilon_{d22} \\ \varepsilon_{d12} \end{Bmatrix} = \frac{1}{E_2} [P] \begin{Bmatrix} \sigma'_{11} \\ \sigma'_{22} \\ \sigma'_{12} \end{Bmatrix}$$ where

$$[P] = \begin{bmatrix} 1 & -\upsilon & 0 \\ -\upsilon & 1 & 0 \\ 0 & 0 & 2(1+\upsilon) \end{bmatrix}.$$

Consequently, the stress that has to be taken up by the viscous component σ'' is:

$$\begin{Bmatrix} \sigma''_{11} \\ \sigma''_{22} \\ \sigma''_{12} \end{Bmatrix} = \begin{Bmatrix} \sigma_{11} \\ \sigma_{22} \\ \sigma_{12} \end{Bmatrix} - \begin{Bmatrix} \sigma'_{11} \\ \sigma'_{22} \\ \sigma'_{12} \end{Bmatrix}.$$

Similar to the one dimension model, the delayed elastic strain rate is assumed to depend on only σ''. The assumed expression for the delayed elastic strain rates is:

$$\frac{d}{dt} \begin{Bmatrix} \varepsilon_{d11} \\ \varepsilon_{d22} \\ \varepsilon_{d12} \end{Bmatrix} = \frac{(\sigma''_{eff})^{m-1}}{\mu_2} \begin{bmatrix} 1 & -\upsilon & 0 \\ -\upsilon & 1 & 0 \\ 0 & 0 & 2(1+\upsilon) \end{bmatrix} \begin{Bmatrix} \sigma''_{11} \\ \sigma''_{22} \\ \sigma''_{12} \end{Bmatrix}$$

or $$\frac{d}{dt} \begin{Bmatrix} \varepsilon_{d11} \\ \varepsilon_{d22} \\ \varepsilon_{d12} \end{Bmatrix} = \frac{(\sigma''_{eff})^{m-1}}{\mu_2} [p] \begin{Bmatrix} \sigma''_{11} \\ \sigma''_{22} \\ \sigma''_{12} \end{Bmatrix}$$

where $\sigma''_{eff} = \sqrt{\sigma''^2_{11} + \sigma''^2_{22} + 2\sigma''^2_{12}}$.

The parameter σ''_{eff} takes into account the effect of biaxial stress on the strain rate. The influence of each component of σ'' on the rate is related by the matrix

[P]. In the elastic part of the delayed elastic element, the delayed elastic strain ε_e is also related to each component of σ' by the matrix [P]. The use of [P] in both elastic and viscous parts makes the delayed elastic term coordinate invariant.

3.2.3 Viscous Element

The multiaxial viscous strain model is based on the constitutive equations suggested by Sanderson (1984). This model reduces to the one dimension viscous strain model in section 3.13 in the undamaged state. The viscous strain rates for the multiaxial case are determined from a potential function. For an anisotropic material, the viscous strain rates are given by:

$$\dot{\varepsilon}_{vij} = \frac{\partial \Phi}{\partial \sigma_{ij}} \tag{3.2}$$

where $\Phi = \dfrac{2\eta_b \tau^{n+1}}{n+1}$ is a scalar potential function,

$$2\tau^2 = a_1(\sigma_{11} - \sigma_{22})^2 + a_2(\sigma_{22} - \sigma_{33})^2 + a_3(\sigma_{33} - \sigma_{11})^2 + 6(a_4\sigma_{12}^2 + a_5\sigma_{23}^2 + a_6\sigma_{31}^2),$$

a_1 to a_6 are constants, and η_b is similar to η in the one dimension model. Substituting for Φ in equation 3.2 gives:

$$\dot{\varepsilon}_{vij} = 2\eta_b \tau^n \frac{\partial \tau}{\partial \sigma_{ij}}$$

with

$$\frac{\partial \tau}{\partial \sigma_{11}} = \frac{1}{2\tau}\left(a_1(\sigma_{11} - \sigma_{22}) - a_3(\sigma_{33} - \sigma_{11})\right),$$

$$\frac{\partial \tau}{\partial \sigma_{22}} = \frac{1}{2\tau}\left(-a_1(\sigma_{11} - \sigma_{22}) + a_2(\sigma_{22} - \sigma_{33})\right),$$

$$\frac{\partial \tau}{\partial \sigma_{33}} = \frac{1}{2\tau}\left(-a_2(\sigma_{22} - \sigma_{33}) + a_3(\sigma_{33} - \sigma_{11})\right),$$

$$\frac{\partial \tau}{\partial \sigma_{12}} = \frac{1}{2\tau}(6a_4\sigma_{12}),$$

$$\frac{\partial \tau}{\partial \sigma_{23}} = \frac{1}{2\tau}(6a_5\sigma_{23}), \text{ and}$$

$$\frac{\partial \tau}{\partial \sigma_{31}} = \frac{1}{2\tau}(6a_6\sigma_{31}).$$

For a transversely isotropic material in plane stress loading, Hill (1948) shows that:

$$a_1 = a_3,$$
$$6a_4 = 2(2a_1 + a_2),$$
$$\sigma_{31} = \sigma_{23} = \sigma_{33} = 0, \text{ and}$$
$$2\tau^2 = a_1(\sigma_{11} - \sigma_{22})^2 + a_2(\sigma_{11}^2 + \sigma_{22})^2 + 2(2a_1 + a_2)\sigma_{12}^2.$$

The viscous strain rates are then:

$$\dot{\varepsilon}_{v11} = \eta_b \tau^{n-1} \left((a_1 + a_2)\sigma_{11} - a_1\sigma_{22}\right),$$

$$\dot{\varepsilon}_{v22} = \eta_b \tau^{n-1} \left((a_1 + a_2)\sigma_{22} - a_1\sigma_{11}\right),$$

$$\dot{\varepsilon}_{v33} = \eta_b \tau^{n-1} \left(-a_2(\sigma_{11} + \sigma_{22})\right), \text{ and}$$

$$\dot{\varepsilon}_{v12} = \eta_b \tau^{n-1} 2(2a_1 + a_2)\sigma_{12}.$$

Summing $\dot{\varepsilon}_{v11}$ and $\dot{\varepsilon}_{v22}$ gives:

$$\dot{\varepsilon}_{v11} + \dot{\varepsilon}_{v22} = \eta_b \tau^{n-1} \left((a_1 + a_2)\sigma_{11} - a_1\sigma_{22} + (a_1 + a_2)\sigma_{22} - a_1\sigma_{11}\right)$$

$$= \eta_b \tau^{n-1} \left(a_2(\sigma_{11} + \sigma_{22})\right).$$

From the assumption that there is no viscous volume change, $\dot{\varepsilon}_{v33}$ can be written in terms of $\dot{\varepsilon}_{v11}$ and $\dot{\varepsilon}_{v22}$ as:

$$\dot{\varepsilon}_{v33} = -\dot{\varepsilon}_{v11} - \dot{\varepsilon}_{v22}.$$

As for η in the one dimension model, the value of η_b is allowed to change. This modification is made to Sanderson's constitutive equations in order to model the post peak behaviour of ice. In the plane stress case, the effective viscous strain and strain rate are utilised in order to control the change in η_b. The following is the discussion on how η_b is allowed to change.

The effective viscous strain rate is defined as:

$$\dot{\varepsilon}_{vb} = \sqrt{\dot{\varepsilon}_{v11}^2 + \dot{\varepsilon}_{v22}^2 + 0.5\dot{\varepsilon}_{v12}^2 + \rho_1 \dot{\varepsilon}_{v33}^2}$$

where ρ_1 is a constant.

The effective viscous strain is assumed to be:

$$\varepsilon_{vb} = g(\sigma)\, h(\varepsilon_v)$$

where

$$h(\varepsilon_v) = \varepsilon_{v11}^p + \varepsilon_{v22}^p + \rho_2 \varepsilon_{v33}^p ,$$

$$g(\sigma) = \frac{\sqrt{\frac{1}{2}\left(a_1(\sigma_{11}-\sigma_{22})^2 + a_2\left(\sigma_{11}^2+\sigma_{22}^2\right) + 2(2a_1+a_2)\sigma_{12}^2\right)}}{\sqrt{\frac{1}{2}(a_1+a_2)\left(\sigma_{11}^2+\sigma_{22}^2+2\sigma_{12}^2\right)}}$$

$$= \frac{\tau}{\sqrt{\frac{1}{2}(a_1+a_2)\left(\sigma_{11}^2+\sigma_{22}^2+2\sigma_{12}^2\right)}} ,$$

ρ_2 is a constant and ε_{vii}^p (no sum) are the principal viscous strains.

Since columnar ice is transversely isotropic, the effect of $\dot{\varepsilon}_{v33}^2$ on $\dot{\varepsilon}_{vb}$ may be different from the effects of $\dot{\varepsilon}_{v11}^2$ or $\dot{\varepsilon}_{v22}^2$. For this reason, ρ_1 is introduced to the effective strain rate expression. In the function $h(\varepsilon_v)$, ρ_2 serves the same purpose as ρ_1 in $\dot{\varepsilon}_{vb}$. The effective viscous strain is made up of $g(\sigma)$ and $h(\varepsilon_v)$. In section 3.1.3.2, cracks are assumed to be influenced by the tensile viscous strain.

Therefore, $h(\varepsilon_v)$ being a measure of the tensile viscous strain's effect on cracks, only includes the tensile principal viscous strain in the summation. Consequently, ε^p_{vii} (no sum) is considered to be zero if it is compressive. However, even with the same $h(\varepsilon_v)$, the effect of viscous strain on cracks is not expected to be the same for uniaxial and biaxial stress conditions. To account for the difference, $h(\varepsilon_v)$ is modified by $g(\sigma)$ to give the effective viscous strain. The effective viscous strain is equivalent to the viscous strain used to control η in the one dimension model. In $g(\sigma)$, the uniaxial state of stress is used as the reference state. Therefore, $g(\sigma)$ is unity for uniaxial loading. For plane strain condition, $g(\sigma)$ is less than one. This implies that the effect of $h(\varepsilon_v)$ is less critical in plane strain compression than uniaxial compression. In tests done by Frederking (1977), the strain at peak stress is found to be considerably smaller in a uniaxial condition than for plane strain conditions. On the other hand, the post peak stress reduction in uniaxial tests is much faster than in plane strain. These two behaviours are indirectly represented by $g(\sigma)$ which makes the viscous strain less critical in causing ice deterioration for plane strain than uniaxial compression.

The mathematical expressions for η_b are patterned after the corresponding expressions in the one dimension model. Under constant strain rate loading, the final value of η_b reaches η_{bf}.

$$\eta_{bf} = \beta_3 \left(\dot{\varepsilon}_{vb}\right)^{\beta_4}$$

where β_3 and β_4 are constants.

For $\varepsilon_{vb} \le \varepsilon_{vcb}$, $\eta_b = \eta_{bi}$.

For $\varepsilon_{vb} > \varepsilon_{vcb}$,

$$\frac{d\,\eta_b}{d\,\varepsilon_{vb}} = \left(\eta_{bf} - \eta_b\right) \alpha_5 \left(\frac{\alpha_6 \varepsilon_{vb} - \varepsilon_{vcb}}{\alpha_7} \right)^{\alpha_8}, \qquad (3.3)$$

and $$\frac{d\eta_b}{d\varepsilon_{vb}} = 0 \quad \text{if} \quad \alpha_6\varepsilon_{vb} - \varepsilon_{vcb} \le 0 \quad \text{or} \quad \eta_{bf} - \eta_b \le 0 \,.$$

The parameters α_5 to α_8 are constants and ε_{vcb} is similar to ε_{vc} in the one dimension model.

Similar to equation 3.1 in the one dimensional model, equation 3.3 controls how η_b changes with respect to the effective viscous strain ε_{vb}. However, when $\alpha_6\varepsilon_{vb} - \varepsilon_{vcb}$ or $\eta_{bf}-\eta_b$ is less than zero, $d\eta_b/d\varepsilon_{vbc}$ is set to zero. The criterion $\eta_{bf}-\eta_b$ less than zero takes into account the irreversibility of the damage process. The other criterion, $\alpha_6\varepsilon_{vb} - \varepsilon_{vcb}$ less than zero is introduced because equation 3.3 is undefined for this condition.

Most of the constants for the plane stress model can be related to those in the uniaxial model.. Under uniaxial loading, the plane stress model reduces to:

$$\tau = \sigma_{11}\sqrt{\frac{1}{2}(a_1+a_2)} \,,$$

$$\dot{\varepsilon}_{v11} = \eta_b\left(\frac{1}{2}(a_1+a_2)\right)^{\frac{n-1}{2}}(a_1+a_2)\,\sigma_{11}^n \,, \tag{3.4}$$

$$\dot{\varepsilon}_{v22} = \eta_b\left(\frac{1}{2}(a_1+a_2)\right)^{\frac{n-1}{2}}(-a_1)\,\sigma_{11}^n \,, \tag{3.5}$$

$$\dot{\varepsilon}_{v33} = \eta_b\left(\frac{1}{2}(a_1+a_2)\right)^{\frac{n-1}{2}}(-a_2)\,\sigma_{11}^n \,. \tag{3.6}$$

Dividing equation 3.5 and 3.6 by equation 3.4, the following equations are obtained:

$$\frac{\dot{\varepsilon}_{v22}}{\dot{\varepsilon}_{v11}} = \frac{-a_1}{a_1+a_2} \tag{3.7}$$

and $$\frac{\dot{\varepsilon}_{v33}}{\dot{\varepsilon}_{v11}} = \frac{-a_2}{a_1+a_2} . \qquad (3.8)$$

From the uniaxial model,

$$\dot{\varepsilon}_{v11} = \eta\, \sigma_{11}^{n} . \qquad (3.9)$$

Comparing equation 3.4 and 3.9, it follows that:

$$\eta = \eta_b \left(\frac{1}{2}\right)^{\frac{n-1}{2}} (a_1+a_2)^{\frac{n+1}{2}} = K\eta_b \qquad (3.10)$$

where

$$K = \left(\frac{1}{2}\right)^{\frac{n-1}{2}} (a_1+a_2)^{\frac{n+1}{2}} .$$

For the uniaxial case:

$$g(\sigma) = 1 \quad \text{and} \quad h(\varepsilon_v) = \varepsilon_{v22}^{p} + \rho_2 \varepsilon_{v33}^{p} ,$$

so that using equations 3.7 and 3.8, the effective viscous strain is given by:

$$\begin{aligned} \varepsilon_{vb} &= g(\sigma)\, h(\varepsilon_v) \\ &= -L\, \varepsilon_{v11} \end{aligned} \qquad (3.11)$$

where $$L = \frac{a_1+a_2\rho_2}{a_1+a_2} .$$

The effective viscous strain rate is given by:

$$\dot{\varepsilon}_{vb} = \sqrt{\dot{\varepsilon}_{v11}^{2} + \dot{\varepsilon}_{v22}^{2} + \rho_1 \dot{\varepsilon}_{v33}^{2}} .$$

Substituting equation 3.7 and 3.8 in the above equation, the effective viscous strain rate becomes:

$$\dot{\varepsilon}_{vb} = \left(\dot{\varepsilon}_{v11}^{2} \left(1 + \left(\frac{-a_1}{a_1+a_2}\right)^{2} + 1 + \rho_1 \left(\frac{-a_2}{a_1+a_2}\right)^{2} \right) \right)^{0.5}$$

$$= \dot{\varepsilon}_{v11}\left(1+\left(\frac{a_1^2+\rho_1 a_2^2}{(a_1+a_2)^2}\right)\right)^{0.5}$$

$$= M\dot{\varepsilon}_{v11} \qquad (3.12)$$

where $$M = \left(1+\left(\frac{a_1^2+\rho_1 a_2^2}{(a_1+a_2)^2}\right)\right)^{0.5} .$$

In the uniaxial model, it is assumed that:

$$\eta_f = \beta_1\left(\dot{\varepsilon}_{v11}\right)^{\beta_2} . \qquad (3.13)$$

For the plane stress model in uniaxial loading, a similar expression, in terms of the effective viscous strain rate is used.

$$\eta_{bf} = \beta_3\left(\dot{\varepsilon}_{vb}\right)^{\beta_4} . \qquad (3.14)$$

Substituting equation 3.12 into 3.14 gives:

$$\eta_{bf} = \beta_3\left(M\,\dot{\varepsilon}_{v11}\right)^{\beta_4} . \qquad (3.15)$$

From equation 3.10, this relationship is obtained:

$$\eta_{bf} = \frac{\eta_f}{K} . \qquad (3.16)$$

Substituting equation 3.16 into 3.15 gives:

$$\eta_f = K\beta_3\left(M\,\dot{\varepsilon}_{v11}\right)^{\beta_4} . \qquad (3.17)$$

Comparing equations 3.13 and 3.17, it follows that:

$$\beta_2 = \beta_4 \quad \beta_1 = K M^{\beta_4}\beta_3 .$$

Substituting equations 3.10 and 3.11, $\frac{d\eta_b}{d\varepsilon_{vb}}$ can be expressed as:

$$\frac{d\eta_b}{d\varepsilon_{vb}} = \frac{1}{KL}\frac{d\eta}{d\varepsilon_{v11}} .$$

Substituting equation 3.1 gives: $$\frac{d\eta_b}{d\varepsilon_{vb}} = \frac{1}{KL}(\eta_f - \eta)\alpha_1\left(\frac{\alpha_2|\varepsilon_{v11}| - \varepsilon_{vc}}{\alpha_3}\right)^{\alpha_4} .$$

Substituting equation 3.10 gives: $$\frac{d\eta_b}{d\varepsilon_{vb}} = \frac{1}{L}(\eta_{bf} - \eta_b)\alpha_1\left(\frac{\alpha_2|\varepsilon_{v11}| - \varepsilon_{vc}}{\alpha_3}\right)^{\alpha_4} .$$

Substituting equation 3.11 gives: $$\frac{d\eta_b}{d\varepsilon_{vb}} = \frac{1}{L}(\eta_{bf} - \eta_b)\alpha_1\left(\frac{\alpha_2\frac{\varepsilon_{vb}}{L} - \frac{\varepsilon_{vcb}}{L}}{\alpha_3}\right)^{\alpha_4}$$

$$= \frac{1}{L}(\eta_{bf} - \eta_b)\alpha_1\left(\frac{\alpha_2\varepsilon_{vb} - \varepsilon_{vcb}}{L\alpha_3}\right)^{\alpha_4} . \quad (3.18)$$

Therefore, by comparing equation 3.18 and 3.3, it follows that

$$\alpha_5 = \alpha_1/L,\ \alpha_6 = \alpha_2,\ \alpha_7 = L\alpha_3,\ \alpha_8 = \alpha_4 \text{ and } \varepsilon_{vcb} = \varepsilon_{vc} .$$

3.2.4 **Brittle Fracture of Ice**

Ice is much weaker in tension than in compression when it is deformed at a high strain rate. Hawkes and Mellor (1972) have done some uniaxial tensile and compressive tests on polycrystalline ice at -7°C. In these tests, the highest tensile stress attained is around 2MPa. The brittle failure strength of the ice in tension is found to be almost the same as the maximum peak tensile strength. But in compression, the maximum peak strength is much larger than the compressive brittle fracture strength (Figure 2.2). The maximum peak strength is defined as the maximum peak stress that can be attained in ice under uniaxial constant strain

rate loading as shown in Figure 2.2. The brittle failure strength is the peak stress or the maximum stress of ice under high constant strain rate loading where the failure mode is brittle fracture. The brittle facture of ice under biaxial stress condition is very complicated. Under compression-compression stress conditions, ice is not expected to fail in a brittle manner in the range of 'strain rate' where the peak stress can be approximate by power-law creep. In plane strain tests done by Frederking (1977), brittle fracture does not occur even at the loading rate of $1x10^{-4}s^{-1}$. Frederking suggests that the strain rate at which brittle fracture occurs falls between $1x10^{-4}s^{-1}$ and $1x10^{-3}s^{-1}$. But in the same range of strain rate, brittle fracture may occur under compression-tension and tension-tension stress conditions. As shown in Figure 2.2 for the uniaxial case, brittle fracture in tension occurs at a lower strain rate than compression. The tests done by Haynes (1973) have shown that the tensile fracture strength of polycrystalline ice decreases with increasing confining pressure. However, no experimental results on the brittle fracture of ice where the principal stress in more than one direction is tensile can be found. However for brittle materials such as concrete, the principal stresses that are required to cause failure in a biaxial stress state are always less than the uniaxial tensile strength. It is assumed here that ice has this same characteristic. This means that brittle fracture may occur when at least one of the principal stresses is tensile but its value is less than the uniaxial tensile brittle fracture strength. Consequently, a tensile stress cutoff is used to approximate brittle fracture of ice in tension-tension and tension-compression state of stress. In the proposed model, if the maximum principal stress in a region reaches the tensile stress cutoff point σ_{tf}, the ice at that particular region is considered to have failed and it is unable to carry any load.

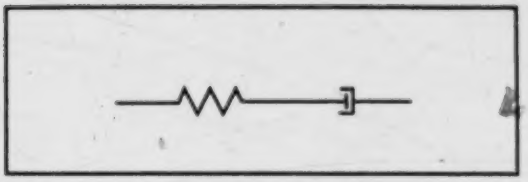

Figure 3.1 Maxwell unit.

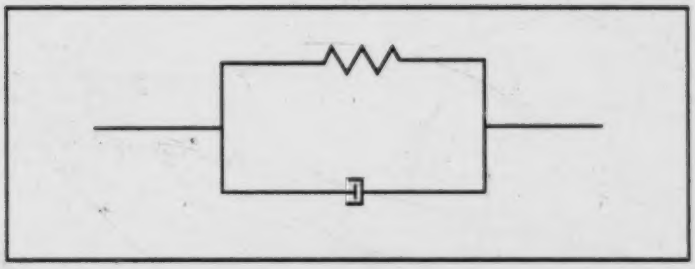

Figure 3.2 Kelvin-Voigt unit.

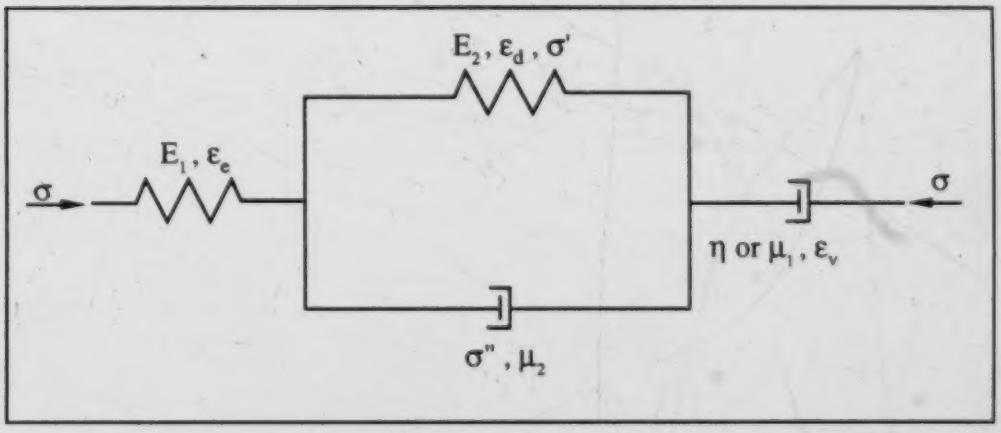

Figure 3.3 The proposed constitutive model for ice under uniaxial compressive loading.

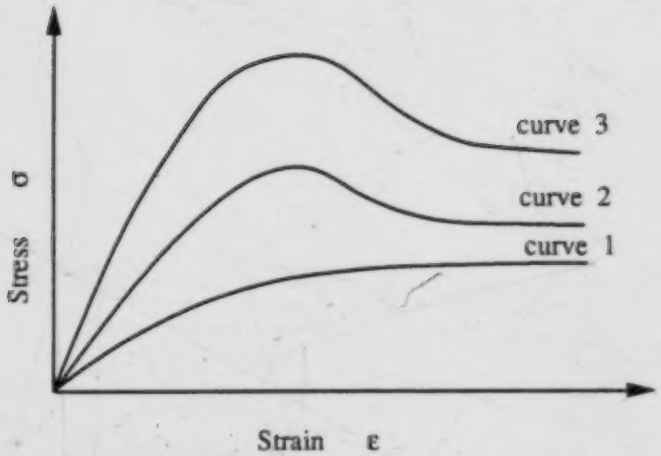

Figure 3.4 The effect of the final value of η on the residual stress under constant strain rate loading.

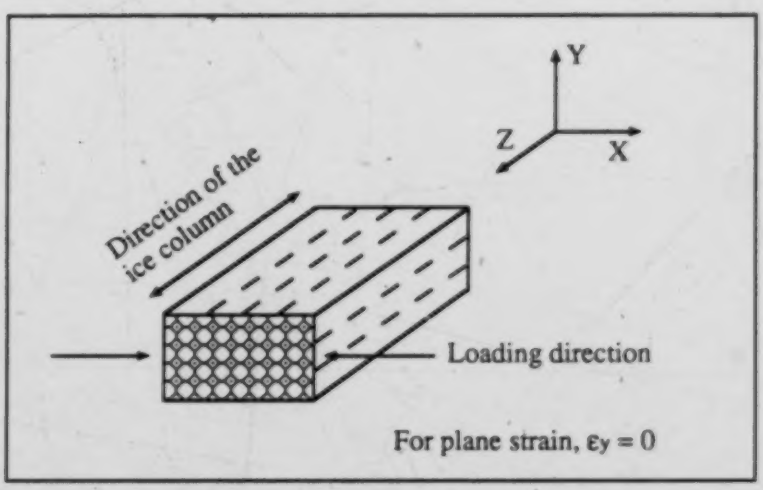

Figure 3.5 The orientation of the ice specimen in Frederking's tests. (Modified from Frederking, 1977)

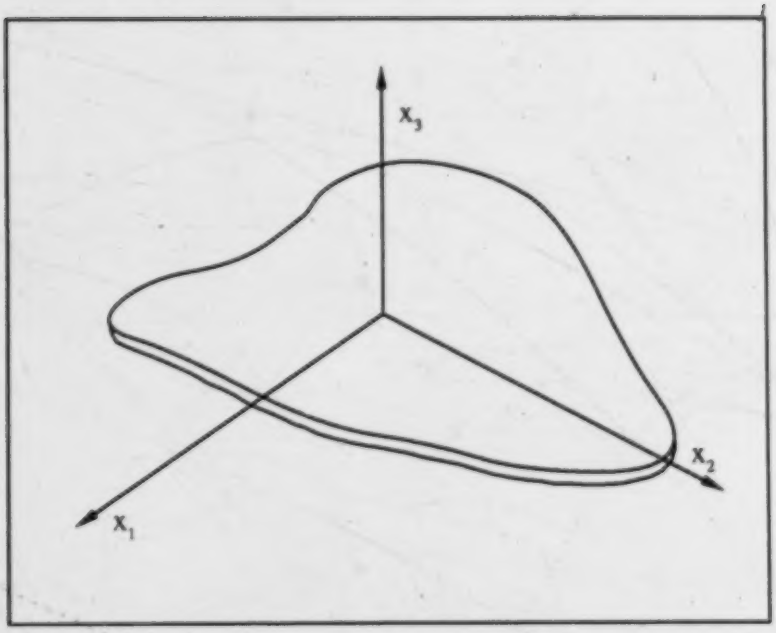

Figure 3.6 The orientation of the axes for the plane stress formulation.

4. Finite Element Formulation

The finite element method is used to model the indentation of an ice sheet. The procedure is based on the modified Euler's method for creep problem discussed by Zienkiewicz (1977). The creep strain increment is calculated from an intermediate value of stress and strain within a time step. Since the stress and strain at the end of the time step, and the creep strain increment are inter-dependent, there is no direct way of solving the problem. An iterative solution scheme, as suggested by Zienkiewicz, is needed to estimate the stress and strain at the end of each time step. This process is incorporated into a finite element program. The computer program is modified from a finite element program for a two dimension linear elastic problem, (developed by Murray at The University of Alberta.) This program uses the isoparametric serendipity family of elements. The Gaussian elimination method, for symmetric banded matrices, is used to solve the system of equations at each time step.

4.1 Overall Formulation

The strain response of an ice sheet under load, can be divided into an instantaneous elastic strain (ε_e) and a time dependent creep strain (ε_c). The total strain can be written as:

$$\varepsilon = \varepsilon_e + \varepsilon_c \ .$$

It is not possible to calculate directly the creep strain increment that occurs in a time step because it depends on stress, strain, and time. One way of obtaining a good approximation of the exact creep strain increment is to use a simplified calculation involving an intermediate stress value. An iterative process is used to arrive at a solution at the end of the time step, that is within the desired accuracy.

The Principle of Virtual Work is used to obtain the equilibrium equations for the finite element model. Assuming no body forces, the virtual work expression can be written as:

$$\int_V \sigma_{ij}\,\delta\varepsilon_{ij}\,dV = \int_S T_i\,\delta u_i\,dS. \tag{4.1}$$

The virtual strains and the virtual displacements are interpolated from the virtual nodal displacements, as follows:

$$\{\delta\varepsilon\} = [B]\{\delta q\}, \text{ and} \tag{3.2}$$

$$\{\delta u\} = [N]\{\delta q\}. \tag{3.3}$$

Substituting equations 3.2 and 3.3 into 3.1, the virtual work expression becomes:

$$\int_V \langle\delta q\rangle[B]^T\{\sigma\}\,dV = \int_S \langle\delta q\rangle[N]^T\{T\}\,dS.$$

Therefore, under arbitrary <δq>, it follows that:

$$\int_V [B]^T\{\sigma\}\,dV = \int_S [N]^T\{T\}\,dS,$$

or

$$\int_V [B]^T\{\sigma\}\,dV = \{F\},$$

with

$$\{F\} = \int_S [N]^T\{T\}\,dS,$$

- V = the volume,
- S = the surface area,
- {T} = the surface traction,
- [B] = the strain interpolation function matrix that includes the differential operators on the displacement,
- [N] = the displacement interpolation function matrix,
- [F] = the nodal forces.

For the rest of this section, the discussion is centered on the method of solving the general form of equations that has been developed. In the following formulation, the subscript 'I' denotes the time step number and the superscript 'J' denotes the iteration number in a time step. For the sake of simplicity, the matrices and vectors are shown without brackets.

The intermediate stress used to calculate the creep strains is given by:

$$\sigma_{I+\theta} = (1-\theta)\sigma_I + \theta\sigma_{I+1}$$

where θ is a constant with a value between 0 to 1.

The increment of the creep strain is assumed to be a function of the intermediate stress, the creep strain at the beginning of the time step and the size of the time step. That is:

$$\Delta\varepsilon_c = \omega\left(\sigma_{I+\theta},\ \varepsilon_{cI},\ \Delta t\right).$$

There are two conditions that have to be satisfied at the end of the time step:

1) $$\sigma_{I+1} - \sigma_I - DB(q_{I+1} - q_I) + D\omega_{I+\theta} = 0 \qquad (4.4)$$

where D is the constitutive matrix for the instantaneous elastic deformation and the subscript $I+\theta$ denotes the value calculated from the intermediate stress $\sigma_{I+\theta}$, and

2) $$\int_V B^T \sigma_{I+1}\, dV - F_{I+1} = 0\ . \qquad (4.5)$$

The first condition is the linear elastic relationship between the stress increment and the instantaneous elastic strain increment. The second condition represents the overall system equilibrium. Since the solution scheme starts with guesses for the stress and strain at the end of the time step, it is unlikely that these two conditions can be met on the first try. Thus, an iterative process, as suggested by

Zienkiewicz, is used to arrive at the state of stress and strain that does satisfy these conditions. The following is a detailed description of the iterative procedure.

Equation 4.4 can be written as:

$$\varphi_{i+1}^{J} = \sigma_{i+1}^{J} - \sigma_i - DB\left(q_{i+1}^{J} - q_i\right) + D\omega_{i+\theta}^{J}$$

where φ is the difference between the predicted stress increment and the stress corresponding to the predicted instantaneous elastic strain increment.

A first order approximation for the error at the start of the next iteration can be written in terms of changes in the stress and strain during the current iteration. That is:

$$\varphi_{i+1}^{J+1} = \varphi_{i+1}^{J} + \Delta\sigma_{i+1}^{J} - DB\,\Delta q_{i+1}^{J} + DR_{i+\theta}^{J}\theta\,\Delta\sigma_{i+1}^{J} \qquad (4.6)$$

where $R_{i+\theta}^{J} = \dfrac{\partial \omega_{i+\theta}^{J}}{\partial \sigma_{i+1}}$,

$\Delta\sigma_{i+1}^{J}$ = the change in stress in the J^{th} iteration, and

Δq_{i+1}^{J} = the change in the nodal displacement in the J^{th} iteration.

In order to minimize the error at the end of the iteration, equation (4.6) is set to zero, giving:

$$\varphi_{i+1}^{J} + \Delta\sigma_{i+1}^{J} - DB\,\Delta q_{i+1}^{J} + DR_{i+\theta}^{J}\theta\,\Delta\sigma_{i+1}^{J} = 0 .$$

After some manipulation, this can be written as:

$$\left(I + DR_{i+\theta}^{J}\theta\right)\Delta\sigma_{i+1}^{J} = DB\,\Delta q_{i+1}^{J} - \varphi_{i+1}^{J} .$$

Multiplying both sides by D^{-1} gives:

$$\left(D^{-1} + R_{i+\theta}^{J}\theta\right)\Delta\sigma_{i+1}^{J} = B\,\Delta q_{i+1}^{J} - D^{-1}\varphi_{i+1}^{J} .$$

Solving for the stress increment at the iteration J gives:

$$\Delta\sigma^{J}_{I+1} = \bar{D}^{J} B \Delta q^{J}_{I+1} - \bar{D}^{J} D^{-1} \varphi^{J}_{I+1} \tag{4.7}$$

where $\bar{D}^{J} = \left(D^{-1} + R^{J}_{I+\theta}\theta\right)^{-1}$.

Thus after the (J+1)st iteration, the predicted stresses and displacements at the time t_{I+1} are:

$$\sigma^{J+1}_{I+1} = \sigma^{J}_{I+1} + \Delta\sigma^{J}_{I+1} \tag{4.8}$$

and $q^{J+1}_{I+1} = q^{J}_{I+1} + \Delta q^{J}_{I+1}$.

To solve the creep problem, the iterative scheme is incorporated into the equilibrium equation. Assuming equilibrium is achieved at iteration J+1, equation 4.5 can be rewritten as:

$$\int_V B^T \dot{\sigma}^{J+1}_{I+1} dV - F_{I+1} = 0 . \tag{4.9}$$

Substituting equations 4.7 and 4.8 into 4.9 gives:

$$\int_V B^T \left(\sigma^{J}_{I+1} + \bar{D}^{J} B \Delta q^{J}_{I+1} - \bar{D}^{J} D^{-1} \varphi^{J}_{I+1}\right) dV = F_{I+1} .$$

Rearranging the equation gives:

$$\int_V B^T \bar{D}^{J} B \Delta q^{J}_{I+1} dV = F_{I+1} - \int_V B^T \left(\sigma^{J}_{I+1} - \bar{D}^{J} D^{-1} \varphi^{J}_{I+1}\right) dV .$$

This can be further simplified to:

$$\left[W^{J}_{I+1}\right]\left\{\Delta q^{J}_{I+1}\right\} = \left\{f_{I+1}\right\}$$

where $f_{I+1} = F_{I+1} - \int_V B^T \left(\sigma^{J}_{I+1} - \bar{D}^{J} D^{-1} \varphi^{J}_{I+1}\right) dV$,

and $W^{J}_{I+1} = \int_V B^T \bar{D}^{J} B \, dV$.

The following criterion is used to measure the magnitude of the error after each iteration, so that a decision can be made as to when to proceed to the next time step.

$$\text{Maximum} \left| \sigma_{i+1}^{j+1} - \sigma_{i+1}^{j} \right| \leq \lambda \text{ , where } \lambda \text{ is the error limit.}$$

If this condition is satisfied, the iteration process for the current time step is stopped. The criterion utilizes the infinity vector norm of the stress vector.

4.2 Implementing the Proposed Ice Model into the Computer Program

There are some special considerations that have to be made in order to apply the algorithm just described to the constitutive model of ice. These considerations are discussed in the following subsections.

4.2.1 The Instantaneous Elastic Element

The implementation of the instantaneous elastic element into the finite element method is straight forward. That is:

$$\begin{Bmatrix} \sigma_{11} \\ \sigma_{22} \\ \sigma_{12} \end{Bmatrix} = \frac{E_1}{(1-\upsilon^2)} \begin{bmatrix} 1 & \upsilon & 0 \\ \upsilon & 1 & 0 \\ 0 & 0 & (1-\upsilon)/2 \end{bmatrix} \begin{Bmatrix} \varepsilon_{e11} \\ \varepsilon_{e22} \\ \varepsilon_{e12} \end{Bmatrix}, \text{ or } \sigma = D\varepsilon_e,$$

where $$D = \frac{E_1}{(1-\upsilon^2)} \begin{bmatrix} 1 & \upsilon & 0 \\ \upsilon & 1 & 0 \\ 0 & 0 & (1-\upsilon)/2 \end{bmatrix}.$$

4.2.2 Delayed Elastic Element

From the previous chapter, the delayed elastic strain rate is defined as:

$$\frac{d}{dt}\begin{Bmatrix}\varepsilon_{d11}\\ \varepsilon_{d22}\\ \varepsilon_{d12}\end{Bmatrix} = \frac{(\sigma''_{eff})^{m-1}}{\mu_2}\begin{bmatrix}1 & -\upsilon & 0\\ -\upsilon & 1 & 0\\ 0 & 0 & 2(1+\upsilon)\end{bmatrix}\begin{Bmatrix}\sigma''_{11}\\ \sigma''_{22}\\ \sigma''_{12}\end{Bmatrix}.$$

Therefore the increment in the delayed elastic strain is:

$$\{\Delta\varepsilon_d\} = \int_0^{\Delta t} \frac{(\sigma''_{eff})^{m-1}}{\mu_2}[P]\{\sigma''\}dt$$

$$= \int_0^{\Delta t} \frac{(\sigma''_{eff})^{m-1}}{\mu_2}[P]\{\{\sigma\}-\{\sigma'\}\}dt, \qquad (4.10)$$

where $$[P] = \begin{bmatrix}1 & -\upsilon & 0\\ -\upsilon & 1 & 0\\ 0 & 0 & 2(1+\upsilon)\end{bmatrix}$$, and

$\{\Delta\varepsilon_d\}$ = the delayed elastic strain increment for one time step.

Direct integration of equation 4.10 is not possible because $\{\sigma\}$, $\{\sigma'\}$ and σ''_{eff} all vary with time within a time step and are not known explicitly. Two assumptions are made so that the right hand side of equation 4.10 may be evaluated.

1) The stress $\{\sigma\}$ is assumed to be constant within a time step. However, an intermediate value of the stress is used so that it may give a better approximation of the exact integration.

$$\{\sigma_{1+\theta_1}\} = \{\sigma_1\} + \theta_1\{\{\sigma_{1+1}\}-\{\sigma_1\}\}$$

$$= \theta_1\{\sigma_{1+1}\} + (1-\theta_1)\{\sigma_1\}. \qquad (4.11)$$

2) Similarly, σ''_{eff} is assumed to remain constant within a time step. It is as follow:

$$\sigma''_{eff_{1+\theta_2}} = \sqrt{\sigma''^{2}_{11_{1+\theta_2}} + \sigma''^{2}_{22_{1+\theta_2}} + 2\sigma''^{2}_{12_{1+\theta_2}}} \qquad (4.12)$$

where $\{\sigma''_{1+\theta_2}\} = \{\sigma_1\} + \theta_2(\{\sigma_{1+1}\} - \{\sigma_1\}) - \{\sigma'_1\}$

$$= \theta_2\{\sigma_{1+1}\} + (1 - \theta_2)\{\sigma_1\} - \{\sigma'_1\}. \quad (4.13)$$

The values of both θ_1 and θ_2 are between 0 to 1. These values are chosen and stay fixed for the entire analysis. Following these assumptions, the delayed elastic strain rate expression can be written as:

$$\frac{d}{dt}\{\varepsilon_d\} = \frac{\left(\sigma''_{eff_{1+\theta_2}}\right)^{m-1}}{\mu_2}[P]\left(\{\sigma_{1+\theta_1}\} - \{\sigma'\}\right) \quad (4.14)$$

where $$\{\sigma'\} = E_2[P]^{-1}\{\varepsilon_d\}. \quad (4.15)$$

Substituting equation 4.15 into 4.14 gives:

$$\frac{d}{dt}\{\varepsilon_d\} = \frac{\left(\sigma''_{eff_{1+\theta_2}}\right)^{m-1}}{\mu_2}[P]\left(\{\sigma_{1+\theta_1}\} - E_2[P]^{-1}\{\varepsilon_d\}\right)$$

$$= \frac{\left(\sigma''_{eff_{1+\theta_2}}\right)^{m-1}}{\mu_2}[P]\{\sigma_{1+\theta_1}\} - \frac{E_2\left(\sigma''_{eff_{1+\theta_2}}\right)^{m-1}}{\mu_2}\{\varepsilon_d\}. \quad (4.16)$$

Since $\sigma''_{eff_{1+\theta_2}}$ and $\sigma_{1+\theta_1}$ are assumed not to change within the time step, equation 4.16 takes the form:

$$\frac{d}{dt}\{\varepsilon_d\} = \{c_1\} - c_0\{\varepsilon_d\}$$

where $$\{c_1\} = \frac{\left(\sigma''_{eff_{1+\theta_2}}\right)^{m-1}}{\mu_2}[P]\{\sigma_{1+\theta_1}\}, \text{ and}$$

$$c_0 = \frac{E_2\left(\sigma''_{eff_{1+\theta_2}}\right)^{m-1}}{\mu_2} \quad \text{are constant.}$$

Each component of the delayed elastic strain rate and the delayed elastic strain increment can be determined as explained in the following. However, to simplify matters, only a single component is used to illustrate the process.

$$\frac{d\varepsilon_d}{dt} = c_1 - c_0\varepsilon_d$$

$$= c_0\left(\frac{c_1}{c_0} - \varepsilon_d\right). \qquad (4.17)$$

Rearranging (4.17) gives:

$$\frac{d\varepsilon_d}{\frac{c_1}{c_0} - \varepsilon_d} = c_0 dt\,. \qquad (4.18)$$

To calculate the change in the delayed elastic strain during one time step, equation 4.18 is integrated from the beginning to the end of that time step. That is:

$$\int_{\varepsilon_{d_1}}^{\varepsilon_{d_{1+1}}} \frac{d\varepsilon_d}{\frac{c_1}{c_0} - \varepsilon_d} = \int_0^{\Delta t} c_0 dt$$

$$\left[-\ln\left(\frac{c_1}{c_0} - \varepsilon_d\right)\right]_{\varepsilon_{d_1}}^{\varepsilon_{d_{1+1}}} = \left[c_0 t\right]_0^{\Delta t}$$

$$\ln\left(\frac{\frac{c_1}{c_0} - \varepsilon_{d_{1+1}}}{\frac{c_1}{c_0} - \varepsilon_{d_1}}\right) = -c_0\Delta t$$

After some manipulation, this is rearranged to give:

$$c_1 - c_0\varepsilon_{d_{1+1}} = \left(c_1 - c_0\varepsilon_{d_1}\right)\exp\left(-c_0\Delta t\right). \qquad (4.19)$$

Adding $-\left(c_1 - c_0\varepsilon_{d_1}\right)$ to both sides of the equation 4.19 gives:

$$c_0\left(\varepsilon_{d_{1+1}} - \varepsilon_{d_1}\right) = c_1 - c_0\varepsilon_{d_1} - \left(c_1 - c_0\varepsilon_{d_1}\right)\exp\left(-c_0\Delta t\right),$$

or
$$c_0\,\Delta\varepsilon_{d_1} = \left(c_1 - c_0\varepsilon_{d_1}\right)\left(1 - \exp\left(-c_0\Delta t\right)\right), \qquad (4.20)$$

where the change in delayed elastic strain is $\Delta\varepsilon_{d_1} = \left(\varepsilon_{d_{1+1}} - \varepsilon_{d_1}\right)$.

Dividing equation 4.20 by c_0 gives:

$$\Delta\varepsilon_{d_1} = \left(\frac{c_1}{c_0} - \varepsilon_{d_1}\right)\left(1 - \exp\left(-c_0\Delta t\right)\right).$$

Therefore, the delayed elatic strain increment over a time step can be written in a general notation as:

$$\left\{\Delta\varepsilon_{d_1}\right\} = \left(\frac{1}{c_0}\left\{c_1\right\} - \left\{\varepsilon_{d_1}\right\}\right)\left(1 - \exp\left(-c_0\Delta t\right)\right)$$

$$= \left(\frac{1}{E_2}[P]\left\{\sigma_{1+\theta_1}\right\} - \left\{\varepsilon_{d_1}\right\}\right)\left(1 - \exp\left(-\frac{E_2\left(\sigma''_{\mathrm{eff}_{1+\theta_2}}\right)^{m-1}}{\mu_2}\Delta t\right)\right).$$

In addition to the strain increment, the partial derivatives of the elements of $\{\Delta\varepsilon_{dI}\}$, with respect to the change in the stress at the end of the time step, are needed in the iterative procedure to calculate the term $R^{j}_{I+\theta}$ in equation 4.6. These derivatives can be written as:

$$\frac{\partial\Delta\varepsilon_{d_{1\,r}}}{\partial\sigma_{1+1\,s}} = \frac{\partial\left(\left(\frac{1}{E_2}P_{rt}\,\sigma_{1+\theta_{1\,t}} - \varepsilon_{d_{1\,r}}\right)\left(1 - \exp\left(-c_0\Delta t\right)\right)\right)}{\partial\sigma_{1+1\,s}}$$

$$= \frac{P_{rt}}{E_2} \frac{\partial \sigma_{1+\theta_1 t}}{\partial \sigma_{1+1 s}} \left(1 - \exp\left(- c_0 \Delta t\right)\right)$$

$$+ \left(\frac{1}{E_2} P_{rt}\, \sigma_{1+\theta_1 t} - \varepsilon_{d_1 r}\right) \exp\left(- c_0 \Delta t\right) \frac{\partial \left(c_0 \Delta t\right)}{\partial \sigma_{1+1 s}}. \qquad (4.21)$$

To simplify the process of expanding the differentiation, the two terms in equation 4.21 are dealt with separately.

1) In the first term, use of equation 4.11 gives:

$$\frac{\partial \sigma_{1+\theta_1 t}}{\partial \sigma_{1+1 s}} = \frac{\partial \left(\theta_1 \sigma_{1+1 t} + \left(1 - \theta_1\right) \sigma_{1 t}\right)}{\partial \sigma_{1+1 s}}$$

$$= \theta_1 \delta_{ts}.$$

Therefore the first term reduces to:

$$\frac{\theta_1 P_{rs}}{E_2} \left(1 - \exp\left(- c_0 \Delta t\right)\right).$$

2) In the second term of equation 4.21,

$$\frac{\partial \left(c_0 \Delta t\right)}{\partial \sigma_{1+1 s}} = \frac{\partial \left(\dfrac{E_2 \left(\sigma''_{eff_{1+\theta_2}} \right)^{m-1}}{\mu_2} \Delta t \right)}{\partial \sigma_{1+1 s}}$$

$$= \frac{(m-1) E_2 \left(\sigma''_{eff_{1+\theta_2}}\right)^{m-2} \Delta t}{\mu_2} \frac{\partial \left(\sigma''_{eff_{1+\theta_2}} \right)}{\partial \sigma_{1+1 s}}. \qquad (4.22)$$

Substituting for $\sigma''_{eff_{1+\theta_2}}$ from equation 4.12 gives:

$$\frac{\partial \left(\sigma''_{eff_{1+\theta_2}} \right)}{\partial \sigma_{1+1 s}} = \frac{\partial \left(\sigma''^{2}_{11_{1+\theta_2}} + \sigma''^{2}_{22_{1+\theta_2}} + 2\, \sigma''^{2}_{12_{1+\theta_2}} \right)^{\frac{1}{2}}}{\partial \sigma_{1+1 s}}$$

$$= \frac{1}{2\sigma''_{\text{eff}_{1+\theta_2}}} \frac{\partial\left(\sigma''^{2}_{11_{1+\theta_2}} + \sigma''^{2}_{z_{1+\theta_2}} + 2\sigma''^{2}_{12_{1+\theta_2}}\right)}{\partial \sigma_{1+1\,s}} \qquad (4.23)$$

From equation 4.13, it follows that:

$$\frac{\partial\{\sigma_{1+\theta_2}\}}{\partial \sigma_{1+1}} = \frac{\partial\left(\theta_2\{\sigma_{1+1}\} + (1-\theta_2)\{\sigma_1\} - \{\sigma'_1\}\right)}{\partial \sigma_{1+1}}$$

$$= \theta_2. \qquad (4.24)$$

Thus setting the free index s in equation 4.23 to correspond to the 11 component, this gives:

$$\frac{\partial\left(\sigma''_{\text{eff}_{1+\theta_2}}\right)}{\partial \sigma_{11_{1+1}}} = \frac{1}{2\sigma''_{\text{eff}_{1+\theta_2}}} \frac{\partial\left(\sigma''^{2}_{11_{1+\theta_2}} + \sigma''^{2}_{z_{1+\theta_2}} + 2\sigma''^{2}_{12_{1+\theta_2}}\right)}{\partial \sigma_{11_{1+1}}}$$

$$= \frac{2\,\sigma''_{11_{1+\theta_2}}}{2\sigma''_{\text{eff}_{1+\theta_2}}} \frac{\partial \sigma''_{11_{1+\theta_2}}}{\partial \sigma_{11_{1+1}}}$$

$$= \frac{\theta_2\,\sigma''_{11_{1+\theta_2}}}{\sigma''_{\text{eff}_{1+\theta_2}}}.$$

Similarly for the other two components:

$$\frac{\partial\left(\sigma''_{\text{eff}_{1+\theta_2}}\right)}{\partial \sigma_{z_{1+1}}} = \frac{\theta_2\,\sigma''_{z_{1+\theta_2}}}{\sigma''_{\text{eff}_{1+\theta_2}}}, \text{ and}$$

$$\frac{\partial\left(\sigma''_{\text{eff}_{1+\theta_2}}\right)}{\partial \sigma_{12_{1+1}}} = \frac{2\,\theta_2\,\sigma''_{12_{1+\theta_2}}}{\sigma''_{\text{eff}_{1+\theta_2}}}.$$

Therefore, this gives:

$$\frac{\partial\left(\sigma''_{\text{eff}_{1+\theta_2}}\right)}{\partial \sigma_{1+1\,s}} = \frac{\theta_2\,Q_s}{\sigma''_{\text{eff}_{1+\theta_2}}}$$

where Q_s are the elements of the vector or

$$\{Q\} = \begin{Bmatrix} \sigma''_{11_{t+\theta_2}} \\ \sigma''_{22_{t+\theta_2}} \\ 2\sigma''_{12_{t+\theta_2}} \end{Bmatrix}.$$

Thus combining these results, the partial derivatives defined in equation 4.21 can be written as the elements of a matrix as follows:

$$\left[\frac{\partial \Delta \varepsilon_{d_t}}{\partial \sigma_{t+1}}\right] = \frac{\theta_1 [P]}{E_2}\left(1 - \exp(-c_0 \Delta t)\right)$$

$$+ \theta_2 \frac{(m-1)E_2\left(\sigma''_{eff_{t+\theta_2}}\right)^{m-3}\Delta t}{\mu_2}\left(\frac{1}{E_2}[P]\{\sigma_{t+\theta_1}\} - \{\varepsilon_{d_t}\}\right)\langle Q\rangle \exp(-c_0 \Delta t).$$

The first term of the equation is a symmetrical matrix, but the second term is non-symmetrical. This means that, if both terms are used, the matrix $[W^J_{t+1}]$ in section 4.1 becomes asymmetrical. Since the computer program used can only solve a symmetrical matrix, only the first term of the equation is included in the computer program. Furthermore the partial derivatives are only used as part of the iterative scheme, which means that they can be approximated to any values so long as ultimately, equations 4.4 and 4.5 are satisfied. Thus, the rate of change of the delayed elastic strain increment is approximated by:

$$\left[\frac{\partial \Delta \varepsilon_{d_t}}{\partial \sigma_{t+1}}\right] = \frac{\theta_1 [P]}{E_2}\left(1 - \exp(-c_0 \Delta t)\right).$$

4.2.3 Viscous Element

The viscous strain rate components for transversely isotropic ice, as derived in chapter 3, are:

$$\begin{Bmatrix} \dot{\varepsilon}_{v11} \\ \dot{\varepsilon}_{v22} \\ \dot{\varepsilon}_{v12} \end{Bmatrix} = \eta_b \tau^{n-1} [A] \begin{Bmatrix} \sigma_{11} \\ \sigma_{22} \\ \sigma_{12} \end{Bmatrix} \quad \text{or} \quad \{\dot{\varepsilon}_v\} = \eta_b \tau^{n-1} [A] \{\sigma\},$$

$$\dot{\varepsilon}_{v33} = -\dot{\varepsilon}_{v11} - \dot{\varepsilon}_{v22},$$

where $$[A] = \begin{bmatrix} a_1 + a_2 & -a_1 & 0 \\ -a_1 & a_1 + a_2 & 0 \\ 0 & 0 & 2(2a_1 + a_2) \end{bmatrix},$$

$$2\tau^2 = a_1(\sigma_{11} - \sigma_{22})^2 + a_2(\sigma_{11}^2 + \sigma_{22})^2 + 2(2a_1 + a_2)\sigma_{12}^2,$$

and all other components are zero.

Similar to the treatment of the delayed elastic strain, an intermediate value of stress is used to calculate the viscous strain rate within the time step. The intermediate stress is defined as:

$$\{\sigma_{t+\theta_1}\} = \{\sigma_t\} + \theta_1(\{\sigma_{t+1}\} - \{\sigma_t\})$$

$$= \theta_1\{\sigma_{t+1}\} + (1 - \theta_1)\{\sigma_t\} \qquad (4.25)$$

where the parameter θ_1 has the same value as that used in the delayed elastic strain formulation.

The new viscous strain rates corresponding to the intermediate stress can be written as:

$$\{\dot{\varepsilon}_{vt+\theta_1}\} = \eta_{bt} \tau_{t+\theta_1}^{n-1} [A] \{\sigma_{t+\theta_1}\}$$

where $$2\tau_{t+\theta_1}^2 = a_1(\sigma_{11_{t+\theta_1}} - \sigma_{22_{t+\theta_1}})^2 + a_2(\sigma_{11_{t+\theta_1}}^2 + \sigma_{22_{t+\theta_1}}^2) + 2(2a_1 + a_2)\sigma_{12_{t+\theta_1}}^2.$$

The viscous strain increment over one time step is approximated by the product of the viscous strain rate and the time step as:

$$\{\Delta\varepsilon_{vt}\} = \eta_{bt} \tau_{t+\theta_1}^{n-1} [A] \{\sigma_{t+\theta_1}\} \Delta t.$$

4.2.3.1 Rate of Change of the Viscous Strain Increment

Similar to the delayed elastic strain, the partial derivative of the elements of $\{\Delta\varepsilon_{vl}\}$ with respect to the change in the stress at the end of the time step are needed in the iterative procedure to calculate the term $R^{J}_{l+\theta}$ in equation 4.6. The partial derivatives are:

$$\frac{\partial \Delta\varepsilon_{vl\,r}}{\partial \sigma_{l+1\,s}} = \frac{\partial\left(\eta_{bl}\,\tau^{n-1}_{l+\theta_l}\,A_{rt}\,\sigma_{l+\theta_l\,t}\Delta t\right)}{\partial \sigma_{l+1\,s}}$$

$$= \eta_{bl}\,\tau^{n-1}_{l+\theta_l}\,A_{rt}\,\Delta t\,\frac{\partial\left(\sigma_{l+\theta_l\,t}\right)}{\partial \sigma_{l+1\,s}} + \eta_{bl}\,\sigma_{l+\theta_l\,t}A_{rt}\,\Delta t\,\frac{\partial\left(\tau^{n-1}_{l+\theta_l}\right)}{\partial \sigma_{l+1\,s}}. \quad (4.26)$$

Substituting equation 4.25 gives:

$$\frac{\partial \sigma_{l+\theta_l\,t}}{\partial \sigma_{l+1\,s}} = \frac{\partial\left(\theta_l\sigma_{l+1\,t} + (1-\theta_l)\sigma_{l\,t}\right)}{\partial \sigma_{l+1\,s}}$$

$$= \theta_l\delta_{ts}.$$

Therefore, the first term in equation 4.26 becomes:

$$\eta_{bl}\,\tau^{n-1}_{l+\theta_l}\,A_{rs}\theta_l\Delta t. \quad (4.27)$$

From chapter 3,

$$\begin{Bmatrix} \frac{\partial\tau}{\partial\sigma_{11}} \\ \frac{\partial\tau}{\partial\sigma_{22}} \\ \frac{\partial\tau}{\partial\sigma_{12}} \end{Bmatrix} = \frac{1}{2\tau}\begin{bmatrix} a_1+a_2 & -a_1 & 0 \\ -a_1 & a_1+a_2 & 0 \\ 0 & 0 & 2(2a_1+a_2) \end{bmatrix}\begin{Bmatrix} \sigma_{11} \\ \sigma_{22} \\ \sigma_{12} \end{Bmatrix}$$

or $\left\{\frac{\partial\tau}{\partial\sigma}\right\} = \frac{1}{2\tau}[A]\{\sigma\}$.

Thus, considering the partial derivative in the second term of equation 4.26, it follows that:

$$\frac{\partial\left(\tau_{1+\theta_1}^{n-1}\right)}{\partial\sigma_{1+1\,s}} = (n-1)\,\tau_{1+\theta_1}^{n-2}\,\frac{\partial\left(\tau_{1+\theta_1}\right)}{\partial\sigma_{1+1\,s}}$$

$$= (n-1)\,\tau_{1+\theta_1}^{n-2}\,\frac{\partial\left(\tau_{1+\theta_1}\right)}{\partial\sigma_{1+\theta_1\,u}}\,\frac{\partial\left(\sigma_{1+\theta_1\,u}\right)}{\partial\sigma_{1+1\,s}}$$

$$= (n-1)\,\tau_{1+\theta_1}^{n-2}\,\frac{\partial\left(\tau_{1+\theta_1}\right)}{\partial\sigma_{1+\theta_1\,u}}\,\delta_{us}\theta_1$$

$$= (n-1)\,\tau_{1+\theta_1}^{n-2}\,\frac{\partial\left(\tau_{1+\theta_1}\right)}{\partial\sigma_{1+\theta_1\,s}}\,\theta_1 = \frac{\theta_1(n-1)\,\tau_{1+\theta_1}^{n-3}}{2}A_{sv}\sigma_{1+\theta_1\,v}.$$

Therefore, equation 4.26 becomes:

$$\frac{\partial\Delta\varepsilon_{v1\,r}}{\partial\sigma_{1+1\,s}} = \eta_{b1}\,\tau_{1+\theta_1}^{n-1}\,A_{rs}\theta_1\Delta t + \eta_{b1}\,\sigma_{1+\theta_1\,t}A_{rt}\,\Delta t\,\frac{\theta_1(n-1)\,\tau_{1+\theta_1}^{n-3}}{2}A_{sv}\sigma_{1+\theta_1\,v}$$

$$= \eta_{b1}\theta_1\Delta t\left(\tau_{1+\theta_1}^{n-1}\,A_{rs} + \frac{(n-1)\,\tau_{1+\theta_1}^{n-3}}{2}A_{rt}\sigma_{1+\theta_1\,t}A_{sv}\sigma_{1+\theta_1\,v}\right)$$

or in matrix form

$$\left[\frac{\partial\Delta\varepsilon_{v1}}{\partial\sigma_{1+1}}\right] = \eta_{b1}\theta_1\Delta t\left(\tau_{1+\theta_1}^{n-1}\,[A] + \frac{(n-1)\,\tau_{1+\theta_1}^{n-3}}{2}[A]\left\{\sigma_{1+\theta_1}\right\}\left\langle\sigma_{1+\theta_1}\right\rangle[A]^T\right).$$

4.2.3.2 **Change in η_b**

The function η_b and how it is changes are discussed in section 3.1.3. In the early stage of loading, the value of η_b remains constant. However, as the effective viscous strain increases and eventually exceeds ε_{vcb}, the value of η_b

starts to increase in order to model the structural deterioration in ice. The rate of change of η_b with respect to the effective viscous strain, as defined in chapter 3, is:

$$\frac{d\eta_b}{d\varepsilon_{vb}} = (\eta_{bf} - \eta_b)\alpha_5\left(\frac{\alpha_6\varepsilon_{vb} - \varepsilon_{vcb}}{\alpha_7}\right)^{\alpha_8}. \qquad (4.27)$$

The following discussion deals with how the change in η_b is incorporated into the finite element program.

During each time step, η_b is assumed to remain constant. Changes to η_b can occur only at the end of the time step. This assumption is made to simplify the calculation. Therefore, the value of η_b at the end of time step 'I', denoted by η_{bI}, affects only the viscous strain rate for the time step 'I +1'. The change in η_b over one time step can be calculated by integrating the rate of change with respect to the effective viscous strain ε_{vc}. Writing equation 4.27 in the differential form gives:

$$\frac{d\eta_b}{(\eta_{bf} - \eta_b)} = \alpha_5\left(\frac{\alpha_6\varepsilon_{vb} - \varepsilon_{vcb}}{\alpha_7}\right)^{\alpha_8} d\varepsilon_{vb}$$

or $$-\frac{d\eta_b}{(\eta_{bf} - \eta_b)} = -\alpha_5\left(\frac{\alpha_6\varepsilon_{vb} - \varepsilon_{vcb}}{\alpha_7}\right)^{\alpha_8} d\varepsilon_{vb}.$$

This is now integrated over one time step, giving:

$$\int_{\eta_{bI}}^{\eta_{bI+1}} -\frac{d\eta_b}{(\eta_{bf} - \eta_b)} = \int_{\varepsilon_{vbI}}^{\varepsilon_{vbI+1}} -\alpha_5\left(\frac{\alpha_6\varepsilon_{vb} - \varepsilon_{vcb}}{\alpha_7}\right)^{\alpha_8} d\varepsilon_{vb}$$

$$\left[\ln(\eta_{bf} - \eta_b)\right]_{\eta_{bI}}^{\eta_{bI+1}} = \left[-\frac{\alpha_7\alpha_5}{\alpha_6(\alpha_8+1)}\left(\frac{\alpha_6\varepsilon_{vb} - \varepsilon_{vcb}}{\alpha_7}\right)^{\alpha_8+1}\right]_{\varepsilon_{vbI}}^{\varepsilon_{vbI+1}}$$

$$\frac{\eta_{bf} - \eta_{bt+1}}{\eta_{bf} - \eta_{bt}} = \exp\left(\frac{\alpha_7 \alpha_5}{\alpha_6(\alpha_5+1)} \left(\left(\frac{\alpha_6 \varepsilon_{vbt} - \varepsilon_{vcb}}{\alpha_7} \right)^{\alpha_5+1} - \left(\frac{\alpha_6 \varepsilon_{vbt+1} - \varepsilon_{vcb}}{\alpha_7} \right)^{\alpha_5+1} \right) \right)$$

$$= A_e, \tag{4.28}$$

where $$A_e = \exp\left(\frac{\alpha_7 \alpha_5}{\alpha_6(\alpha_5+1)} \left(\left(\frac{\alpha_6 \varepsilon_{vbt} - \varepsilon_{vcb}}{\alpha_7} \right)^{\alpha_5+1} - \left(\frac{\alpha_6 \varepsilon_{vbt+1} - \varepsilon_{vcb}}{\alpha_7} \right)^{\alpha_5+1} \right) \right).$$

$\varepsilon_{vbt+1} = g(\sigma_{t+1})\, h(\varepsilon_{v\,t+1})$ is the effective viscous strain at the end of the time step,

$\varepsilon_{vbt} = g(\sigma_t)\, h(\varepsilon_{v\,t})$ is the effective viscous strain at the beginning of the time step, and

$\eta_{bf} = \beta_3 \left(\dot{\varepsilon}_{vbt+e_1} \right)^{\beta_4}$ is the final value of η_b if $\dot{\varepsilon}_{vbt+e_1}$ remains unchanged.

Multiplying both sides of equation 4.28 with $\eta_{bf} - \eta_{bt}$ gives:

$$\eta_{bf} - \eta_{bt+1} = A_e(\eta_{bf} - \eta_{bt}). \tag{4.29}$$

Multiplying by -1 and then adding $\eta_{bf} - \eta_{bt}$ to both sides of the equation 4.29 gives:

$$\eta_{bt+1} - \eta_{bt} = \eta_{bf} - \eta_{bt} - A_e(\eta_{bf} - \eta_{bt}).$$

$$= (\eta_{bf} - \eta_{bt})(1 - A_e).$$

Therefore, the change in η_b is given by:

$$\Delta\eta_{bt} = (\eta_{bf} - \eta_{bt})(1 - A_e). \tag{4.30}$$

There are a few situations that may require some special treatment in dealing with equation 4.30. In section 3.1.3, η_b is assumed to be unable to decrease in value due to the irreversible nature of the damage process. As a result $\Delta\eta_{bt}$ cannot be

less than zero. Therefore, $\Delta\eta_{bI}$ is set to zero for the two following cases in which the value of $\Delta\eta_{bI}$ is negative:

$$\Delta\eta_{bI} = 0 \quad \text{if} \quad \eta_{bf} \le \eta_{bI} \quad \text{or} \quad \varepsilon_{vbI+1} \le \varepsilon_{vbI}.$$

When $\alpha_6\varepsilon_{vbI+1} - \varepsilon_{vcb}$ or $\alpha_6\varepsilon_{vbI} - \varepsilon_{vcb}$ is less than zero, A_e is undefined. To overcome this problem, they are respectively set to zero if their values are negative:

$$\alpha_6\varepsilon_{vbI+1} - \varepsilon_{vcb} = 0 \text{ if } \alpha_6\varepsilon_{vbI+1} - \varepsilon_{vcb} \le 0, \text{ and}$$

$$\alpha_6\varepsilon_{vbI} - \varepsilon_{vcb} = 0 \text{ if } \alpha_6\varepsilon_{vbI} - \varepsilon_{vcb} \le 0.$$

4.2.4 **Tensile Brittle Fracture**

The treatment of tensile brittle fracture is greatly simplified in the present model in order to make the formulation and calculations easier. When the principal stress at a Gauss point exceeds the tensile stress cutoff point (σ_{tf}), the ice at that particular region is considered to have failed completely and is unable to carry any load. There is no contribution to the overall stiffness from that Gauss point. However, ill conditioning in the numerical procedure may arise if zero stiffness is used for the failed region. To overcome this problem, a small stiffness value is used. Thus, the constants E_1 and E_2 are reduced by a factor of approximately 10^4 and η_b is increased by a factor of approximately 10^{13}. This makes the failed region very soft compared to the surrounding regions of intact ice. As a result, the effect of the brittle fracture can be represented without having numerical problems.

The new parameters for the failed region are expressed as follows:

$$E_1^f = \frac{E_1}{\zeta_1},$$

$$E_2^f = \frac{E_2}{\zeta_1},$$

and $\eta_b^f = \zeta_2 \eta_{bi}$,

with $\zeta_1 \approx 10^4$ and $\zeta_2 \approx 10^{13}$.

These values for ζ_1 and ζ_2 are chosen after some trial runs with different values of ζ_1 and ζ_2. From the results of the trial runs, it is found that if they are too big, the computing time becomes longer and ill-conditioning may occur. The bigger these values are, the more accurately the problem has to be solved. The increased accuracy in the solution is achieved by setting the error limit λ to a very small value. As a result, the computing time increases because more iterations are required to obtain a more accurate solution. There is also a limit to the number of significant figures the computer can handle. If the ζ_1 and ζ_2 are too big, the solution may require an accuracy that exceeds the capability of the computer. Consequently, numerical ill-conditioning may occur if the capability of the computer is exceeded.

4.3 Flow Chart for the Finite Element Program

The flow chart of the computer program is shown in Figure 4.1. All the symbols in the flow chart have been defined before except λ_b and λ_L. They are the two error limits used in the program. The first limit, λ_b, is not a requirement in the computer program. It is introduced in order to save the computing time. However, the second limit, λ_L, is essential to the program because it controls the accuracy of the solution and prevents numerical ill-conditioning.

From the simplification made in section 4.2.4, once the ice at a particular region has undergone brittle failure, a new set of material properties is used for that region. The stress at that place is also reduced corresponding to the

new material properties but the strain remains unchange. As a result, the calculation has to restart from the beginning of the time step if there are additional Gauss points that experience brittle fracture. Therefore, some computing time may be saved by reducing the number of iterations that have to be performed before the Gauss point is checked for brittle fracture. This is done by checking the Gauss point for brittle fracture once the accuracy of the solution meets the limit λ_b, and adopting a value for λ_b which is larger than λ_L. A larger λ_b allows the Gauss point to be checked for brittle fracture at an early stage of the operation before more iterations are performed to calculate for a more refined stress and strain.

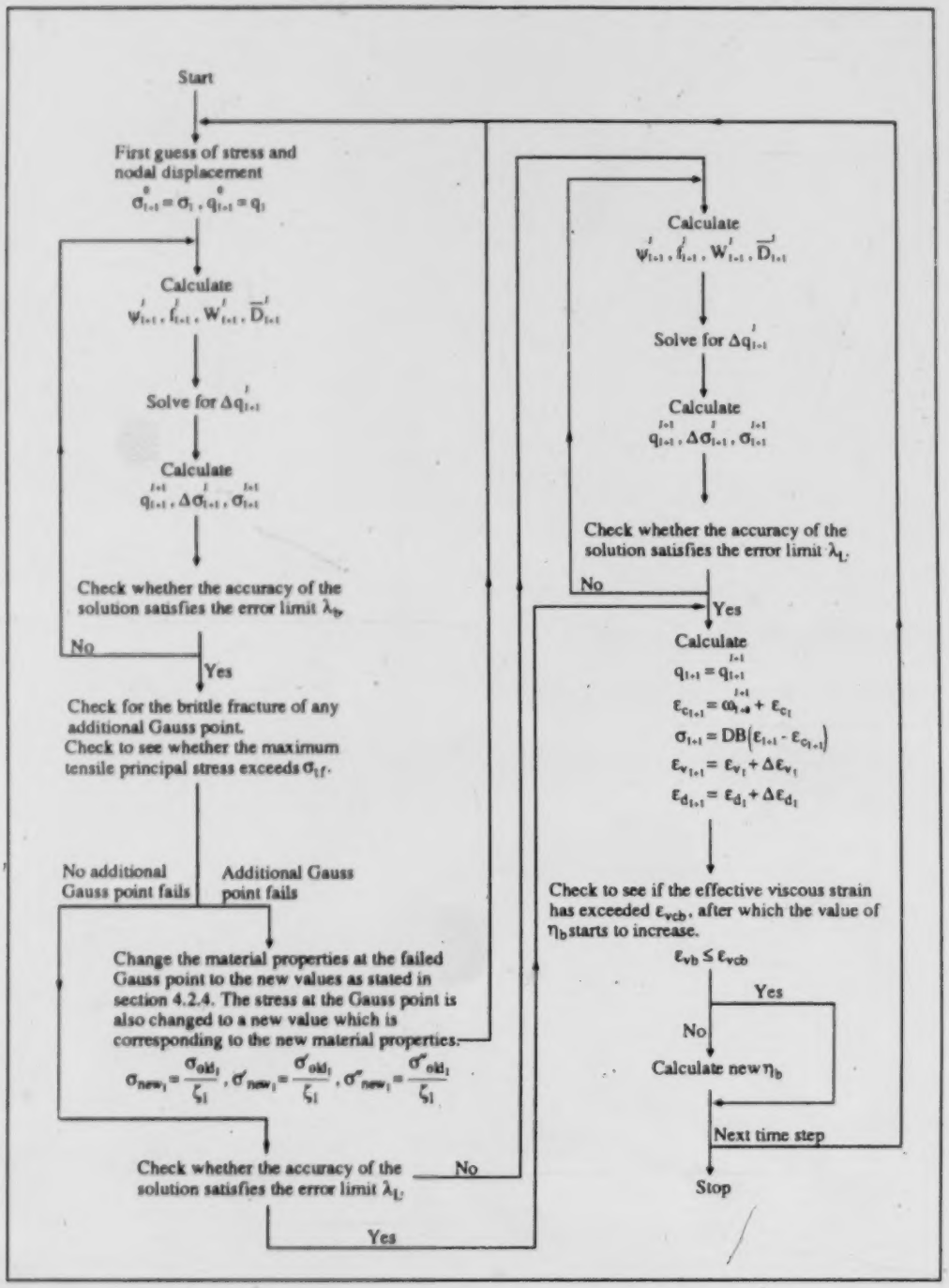
Start
First guess of stress and nodal displacement
$\sigma^0_{i+1} = \sigma_i$, $q^0_{i+1} = q_i$
Calculate
ψ^j_{i+1} , f^j_{i+1} , W^j_{i+1} , $\overline{D}^j_{i+1}$
Solve for Δq^j_{i+1}
Calculate
q^{j+1}_{i+1} , $\Delta\sigma^j_{i+1}$, σ^{j+1}_{i+1}
Check whether the accuracy of the solution satisfies the error limit λ_b
No
Yes
Check for the brittle fracture of any additional Gauss point.
Check to see whether the maximum tensile principal stress exceeds σ_{tf}.
No additional Gauss point fails
Additional Gauss point fails
Change the material properties at the failed Gauss point to the new values as stated in section 4.2.4. The stress at the Gauss point is also changed to a new value which is corresponding to the new material properties.
$\sigma_{new_1} = \frac{\sigma_{old_1}}{\zeta_1}$, $\sigma'_{new_1} = \frac{\sigma'_{old_1}}{\zeta_1}$, $\sigma''_{new_1} = \frac{\sigma''_{old_1}}{\zeta_1}$
Check whether the accuracy of the solution satisfies the error limit λ_L
No
Yes
Calculate
ψ^j_{i+1} , f^j_{i+1} , W^j_{i+1} , $\overline{D}^j_{i+1}$
Solve for Δq^j_{i+1}
Calculate
q^{j+1}_{i+1} , $\Delta\sigma^j_{i+1}$, σ^{j+1}_{i+1}
Check whether the accuracy of the solution satisfies the error limit λ_L
No
Yes
Calculate
$q_{i+1} = q^{j+1}_{i+1}$
$\varepsilon_{c_{i+1}} = \omega^{j+1}_{i+1} + \varepsilon_{c_i}$
$\sigma_{i+1} = DB\left(\varepsilon_{i+1} - \varepsilon_{c_{i+1}}\right)$
$\varepsilon_{v_{i+1}} = \varepsilon_{v_i} + \Delta\varepsilon_{v_i}$
$\varepsilon_{d_{i+1}} = \varepsilon_{d_i} + \Delta\varepsilon_{d_i}$
Check to see if the effective viscous strain has exceeded ε_{vcb}, after which the value of η_b starts to increase.
$\varepsilon_{vb} \le \varepsilon_{vcb}$
Yes
No
Calculate new η_b
Next time step
Stop

Figure 4.1 Flow chart for the finite element program of plane stress ice model.

5. Presentation and Discussion of the Analytical Results

Numerical analyses are performed using the proposed model from Chapter 3 and its finite element implementation described in Chapter 4. Three types of loading condition are investigated in the analyses: uniaxial, plane strain and plane stress indentation. The numerical solutions are then compared with the experimental results from the literature to check the accuracy of the modelling. Since the behaviour of ice depends on many factors, most of the parameters have to be altered to match the test results of different researchers. Some of the parameters can be easily estimated from the test results. The following sections show the procedure for finding those parameters, the presentation and the discussion of the analytical results.

5.1 Estimation and Calibration of the Parameters Used in the Model

Most of the parameters used in the numerical calculation can be easily approximated from the experimental results. Some of them remain unchanged or vary only a little for different tests. With the exception of ρ_1, ρ_2, θ_1 and θ_2, the rest of the parameters have to be fine tuned after their crude estimates have been obtained. The fine tuning is done by adjusting the parameters to obtain the analytical stress-strain curve that matches the one from the test. As mentioned in Chapter 3, the parameters for the uniaxial model are related to their multiaxial counterparts. It is easier to determine the parameters for the uniaxial model than for the plane stress model. Thus, the following subsections only discuss how the values for the parameters in the uniaxial model are determined. The values for the uniaxial model can be easily converted to their equivalent for the plane stress model in order to be used in the finite element program. The rough values of

these parameters should be estimated in the sequence in which they are discussed in section 5.1: E_1, υ, η_i, n, a_1, a_2, β_1, β_2, μ_2, E_2, m, α_1, α_2, α_3, α_4 and ε_{vc}. In uniaxial loading, a_1, a_2 and υ can take any value because they are only in effect in multiaxial loading. They are only found in the plane stress model and have no equivalent counterparts in the uniaxial model.

5.1.1 Parameters That Do Not Change

Parameters, ρ_1, ρ_2, θ_1 and θ_2, remain unchanged for all the analyses. The values of ρ_1 and ρ_2 are set to 1, and θ_1 and θ_2 are set to 0.8. By choosing 1 for both ρ_1 and ρ_2, it is directly assumed that the contribution of the viscous strain and the viscous strain rate from all the directions has the same importance. This may be true for isotropic ice, but not for columnar ice. For simplicity and for the lack of values for columnar ice, the assumption is extended to columnar ice.

For the solution scheme to be unconditionally stable, θ_1 and θ_2 have to be greater than or equal to 0.5 (Zienkiewicz, 1977). A value of 0.8 for θ_1 and θ_2 is found to give a satisfactory performance to the numerical procedure, and so these values are adopted for all analyses.

5.1.2 Parameters Approximated from Test Results

The approximate values of some of the parameters can be obtained easily from experiment results. For example, the value of the elastic modulus E_1 can be determined from the initial slope of the stress-strain curve for uniaxial constant strain rate compression. The values of n and η_i can be approximated from the peak stress and the applied strain rate. The parameters a_1 and a_2 can be approximated from the ratio of the peak stress for the uniaxial and plane strain constant strain rate compression tests. The parameters β_1 and β_2 that control η_f are estimated from the residual strength of ice at different applied strain rates.

These estimations are easier to make using the results from the uniaxial rather than the plane strain tests.

5.1.2.1 Estimation Using Uniaxial Test Results

Among the three sets of parameters, E_i is the easiest to determine. It can be approximated from the intial slope of the stress-strain curve for high strain rate compression. The initial deformation of ice is mostly elastic. A higher applied strain rate reduces the length of time to reach a specific value of strain. This means that the fraction of the strain due to the viscous flow is less. Thus, the initial slope of the stress-strain curve for high strain rate loading is more suitable for calculating E_i than the slope from low strain rate tests.

The values of n and η_i have significant influence on the strength of ice under constant strain rate compression. The peak stress σ_{peak} can be approxiamated from the loading rate $\dot{\varepsilon}$, n and η_i by:

$$\sigma_{peak} \approx \left(\frac{\dot{\varepsilon}}{\eta_i}\right)^{\frac{1}{n}}$$

or
$$\log(\sigma_{peak}) \approx \frac{1}{n}\left(\log(\dot{\varepsilon}) - \log(\eta_i)\right).$$

If the $\log(\sigma_{peak})$ and $\log(\dot{\varepsilon})$ data pairs are plotted, the best fit line gives the approximate values of n and η_i for use in the numerical model.

The values of β_1 and β_2 are calculated from the residual strength of ice under constant compressive strain rate loading. The deformation of ice occurring at the later stage of loading is mainly due to the viscous flow. Thus, the applied strain rate is almost equal to the viscous flow rate. As a result, β_1 and β_2 which control the value of η_f, also control the residual strength of ice. As time

approaches infinity, the relationship between the residual strength $\sigma_{residual}$ and the applied strain rate $\dot{\varepsilon}$ is that shown below:

$$\dot{\varepsilon}_v = \dot{\varepsilon} = \eta_f(\sigma_{residual})^n .$$

Rearranging the equation gives:

$$\sigma_{residual} = \left(\frac{\dot{\varepsilon}}{\eta_f}\right)^{\frac{1}{n}} .$$

The best fit line for $\log(\eta_f)$ and $\log(\dot{\varepsilon})$ provides a means of determining β_1 and β_2 using $\eta_f = \beta_1(\dot{\varepsilon}_v)^{\beta_2}$

5.1.2.2 Estimation Using Plane Strain Test Results

In Chapter 4, the parameters η_i, β_1 and β_2, for the uniaxial model, are shown to be related to their multiaxial counterparts η_{bi}, β_3 and β_4. Thus it is possible to estimate the values of η_i, β_1 and β_2 using the plane strain test results. The plane strain case under consideration is that in which both loading and confinement occurs in the X_1, X_2 plane,using a coordinate system adopted in section 3.2. To simplify the calculation, the ice is assumed to be loaded in the X_1 and confined in the X_2 direction. Thus, the normal strain in the X_2 direction is zero (ε_{22}=0).

To estimate E_1, assume that the ice deforms only elastically at the start of loading. This gives:

$$\varepsilon_{e11} = \frac{1}{E_1}\left(\sigma_{11} - \upsilon\,\sigma_{22}\right), \tag{5.1}$$

and

$$\varepsilon_{e22} = \frac{1}{E_1}\left(\sigma_{22} - \upsilon\,\sigma_{11}\right) = 0. \tag{5.2}$$

Multiplying equation 5.2 by υ and summing with equation 5.1 gives:

$$\varepsilon_{e^{11}} = \frac{1}{E_1}\left(\sigma_{11} - \upsilon^2 \sigma_{11}\right)$$

$$= \frac{\sigma_{11}}{E_1}\left(1 - \upsilon^2\right). \qquad (5.3)$$

Rearranging equation 5.3 gives:

$$\frac{E_1}{\left(1 - \upsilon^2\right)} = \frac{\sigma_{11}}{\varepsilon_{e^{11}}} . \qquad (5.4)$$

The right side of equation 5.4 is the slope of the stress-strain curve in the loading direction if the deformation at the beginning of the loading is purely elastic. Thus, E_1 can be calculated from the slope of the stress-strain curve using equation 5.4. A rough estimate of υ can also be made using equation 5.4 if the value of E_1 is determined from the uniaxial test results.

In the following formulation to estimate η_i, n, β_1 and β_2, the deformation is assumed to consist of only viscous flow. In addition to this, the subscript 'uni' denotes the value from uniaxial compression and the subscript 'pl' denotes the value from plane strain compression. The procedure for estimating η_i and n is discussed first, then it is followed by the one for β_1 and β_2.

For the approximation of η_i and n, the peak stress in plane strain loading is converted to its uniaxial equivalent, which is the peak stress in uniaxial compression under the same loading rate. From Chapter 3, the strain rate in uniaxial compression is given by equation 3.4, which is:

$$\dot{\varepsilon}_{11uni} = \eta_b \left(\frac{1}{2}\right)^{\frac{n-1}{2}} \left(a_1 + a_2\right)^{\frac{n+1}{2}} \sigma_{11uni}^{n} . \qquad (5.5)$$

In plane strain loading, the expressions for the strain rate in X_1 and X_2 are as follow:

$$\dot{\varepsilon}_{11pl} = \eta_b \tau^{n-1} \left((a_1 + a_2)\sigma_{11pl} - a_1\sigma_{22pl} \right), \text{ and} \tag{5.6}$$

$$\dot{\varepsilon}_{22pl} = 0 = \eta_b \tau^{n-1} \left((a_1 + a_2)\sigma_{22pl} - a_1\sigma_{11pl} \right). \tag{5.7}$$

Rearranging equation 5.7 gives:

$$\sigma_{22pl} = \frac{a_1}{a_1 + a_2}\sigma_{11pl}. \tag{5.8}$$

Substituting equation 5.8 into 5.6 gives:

$$\dot{\varepsilon}_{11pl} = \eta_b \tau^{n-1} \sigma_{11pl}\left(a_1 + a_2 - \frac{a_1^2}{a_1 + a_2} \right)$$

$$= \eta_b \tau^{n-1} \sigma_{11pl} \frac{a_1^2 + 2a_1a_2 + a_2^2 - a_1^2}{a_1 + a_2}$$

$$= \eta_b \tau^{n-1} \sigma_{11pl} \frac{a_2(2a_1 + a_2)}{a_1 + a_2}. \tag{5.9}$$

For plane stress and plane strain conditions, from chapter 3, τ can be written as:

$$\tau^2 = \frac{1}{2}\left(a_1(\sigma_{11pl} - \sigma_{22pl})^2 + a_2\left(\sigma_{11pl}^2 + \sigma_{22pl}^2 \right) \right). \tag{5.10}$$

Substituting equation 5.8, 5.10 can be simplified to:

$$\tau^2 = \frac{1}{2}\left(a_1\left(\sigma_{11pl} - \frac{a_1}{a_1 + a_2}\sigma_{11pl} \right)^2 + a_2\left(\sigma_{11pl}^2 + \left(\frac{a_1}{a_1 + a_2} \right)^2 \sigma_{11pl}^2 \right) \right)$$

$$= \frac{1}{2}\left(\frac{\sigma_{11pl}}{a_1 + a_2} \right)^2 \left(a_1(a_1 + a_2 - a_1)^2 + a_2\left((a_1 + a_2)^2 + a_1^2 \right) \right)$$

$$= \frac{1}{2}\left(\frac{\sigma_{11pl}}{a_1 + a_2} \right)^2 \left(a_1a_2^2 + a_2\left(a_1^2 + 2a_1a_2 + a_2^2 + a_1^2 \right) \right)$$

$$= \frac{a_2}{2}\left(\frac{\sigma_{11pl}}{a_1 + a_2} \right)^2 \left(2a_1^2 + 3a_1a_2 + a_2^2 \right)$$

$$= \frac{a_2}{2}\left(\frac{\sigma_{11pl}}{a_1 + a_2}\right)^2 (2a_1 + a_2)(a_1 + a_2)$$

$$= \frac{a_2 \sigma_{11pl}^2 (2a_1 + a_2)}{2(a_1 + a_2)}.$$

Therefore, for plane stress and plane strain, τ is given by:

$$\tau = \left(\frac{a_2 (2a_1 + a_2)}{2(a_1 + a_2)}\right)^{0.5} \sigma_{11pl}. \qquad (5.11)$$

Substituting equation 5.11 into 5.9 gives:

$$\dot{\varepsilon}_{11pl} = \eta_b \sigma_{11pl}^n \left(\frac{a_2 (2a_1 + a_2)}{2(a_1 + a_2)}\right)^{\frac{n-1}{2}} \frac{a_2 (2a_1 + a_2)}{a_1 + a_2}$$

$$= \eta_b \sigma_{11pl}^n \left(\frac{1}{2}\right)^{\frac{n-1}{2}} \left(\frac{a_2 (2a_1 + a_2)}{a_1 + a_2}\right)^{\frac{n+1}{2}}. \qquad (5.12)$$

If the uniaxial and plane strain compression rates are equal, that is $\dot{\varepsilon}_{11uni}$ equal to $\dot{\varepsilon}_{11pl}$, then the right hand side of equations 5.5 and 5.12 must be equal. Equating the right hand sides of these two equations gives:

$$\eta_b \left(\frac{1}{2}\right)^{\frac{n-1}{2}} (a_1 + a_2)^{\frac{n+1}{2}} \sigma_{11uni}^n = \eta_b \sigma_{11pl}^n \left(\frac{1}{2}\right)^{\frac{n-1}{2}} \left(\frac{a_2 (2a_1 + a_2)}{a_1 + a_2}\right)^{\frac{n+1}{2}}.$$

Rearranging this equation gives:

$$\sigma_{11uni}^n = \sigma_{11pl}^n \left(\frac{a_2 (2a_1 + a_2)}{(a_1 + a_2)^2}\right)^{\frac{n+1}{2}}$$

or

$$\frac{\sigma_{11uni}}{\sigma_{11pl}} = \left(\frac{a_2 (2a_1 + a_2)}{(a_1 + a_2)^2}\right)^{\frac{n+1}{2n}}. \qquad (5.13)$$

After converting the peak σ_{11pl} to its uniaxial equivalent by multiplying σ_{11pl} by the right hand side of equation 5.13, the procedure mentioned in section 5.1.2.1

is then used to approximate η_i and n. A rough estimate of a_1 and a_2 can also be calculated by using equation 5.13. If η_i and n are estimated from the uniaxial test results, then a_1 and a_2 can be manipulated to give the desired peak stress for plane strain tests based on the peak stress from the uniaxial compression.

The parameter η_f is a function of viscous strain rate. Thus, in order to calculate β_1 and β_2 from the plane strain test results, the effective viscous strain rate in the plane strain test has to be converted to its uniaxial equivalent, that is the viscous strain rate which gives an appropriate value for η_f. From section 3.2.3, it is shown that η_f is related to η_{bf} in the plane stress model. The appropriate value of η_f is the value that corresponds to η_{bf} calculated using the equation $\eta_{bf} = \beta_3(\dot{\varepsilon}_{vb})^{\beta_4}$ from section 3.2.3. Similar to the process for calculating η_i and n, the residual strength from the plane strain test has to be expressed in terms of its uniaxial equivalent using equation 5.13. To calculate the equivalent effective viscous strain rate for plane strain compression, it is required to know the ratio of the effective viscous strain rate of uniaxial and plane strain compression under the same loading rate. The process of calculating this ratio is discussed below.

For plane strain compression, the effective viscous strain rate is given by:

$$\dot{\varepsilon}_{vbpl} = \left(\dot{\varepsilon}_{11pl}^{2} + \rho_1 \dot{\varepsilon}_{33pl}^{2} \right)^{0.5} . \qquad (5.14)$$

From section 3.2.3, $\dot{\varepsilon}_{33pl}$ is shown to be equal to $-\dot{\varepsilon}_{11pl} - \dot{\varepsilon}_{22pl}$. Together with the previous assumptions that $\dot{\varepsilon}_{22pl}$ is zero for plane strain compression, equation 5.14 can be written in terms of $\dot{\varepsilon}_{11pl}$ as:

$$\dot{\varepsilon}_{vbpl} = \left(1 + \rho_1 \right)^{0.5} \dot{\varepsilon}_{11pl} . \qquad (5.15)$$

For uniaxial compression, the effective viscous strain rate is given by equation 3.12 as follows:

$$\dot{\varepsilon}_{vbuni} = \left(1+\left(\frac{a_1^2+\rho_1 a_2^2}{(a_1+a_2)^2}\right)\right)^{0.5} \dot{\varepsilon}_{11uni}$$

$$= \left(2a_1^2+2a_2a_1^2+(1+\rho_1)a_2^2\right)^{0.5} \frac{\dot{\varepsilon}_{11uni}}{a_1+a_2}. \qquad (5.16)$$

From the assumption made in section 5.1.1, ρ_1 is taken to be 1. Equation 5.15 and 5.16 can be simplified to:

$$\dot{\varepsilon}_{vbpl} = 2^{0.5}\dot{\varepsilon}_{11pl}, \text{ and} \qquad (5.17)$$

$$\dot{\varepsilon}_{vbuni} = \left(2\left(a_1^2+a_2a_1^2+a_2^2\right)\right)^{0.5} \frac{\dot{\varepsilon}_{11uni}}{a_1+a_2}. \qquad (5.18)$$

Dividing each side of equation 5.17 by the respective sides of equation 5.18 gives:

$$\frac{\dot{\varepsilon}_{vbpl}}{\dot{\varepsilon}_{vbuni}} = \frac{a_1+a_2}{\left(a_1^2+a_2a_1^2+a_2^2\right)^{0.5}}. \qquad (5.19)$$

Equation 5.19 gives the ratio of the effective viscous strain rate of uniaxial and plane strain compression under the same loading rate. This means that with the same strain rate, the equivalent effective viscous strain rate for plane strain, at steady state, is just the product of the right hand side of equation 5.19 with the applied loading rate $\dot{\varepsilon}_{11pl}$. To calculate the value of η_f, the residual strength from the plane strain test is expressed in terms of its uniaxial equivalent using equation 5.13. The value of η_f is given by:

$$\eta_f = \frac{\dot{\varepsilon}_{11pl}}{\sigma_{eq}^n}$$

where σ^n_{eq} is the product of the residual strength of ice for plane strain compression $\sigma^n_{1ipl.\ residual}$ and the right hand side of equation 5.13.

The best fit line for $\log(\eta_f)$ versus $\log(\dot{\varepsilon}_{eq})$ gives a means to approximate β_1 and β_2 where $\dot{\varepsilon}_{eq}$ is the product of $\dot{\varepsilon}_{1ipl}$ and the right hand side of equation 5.19.

5.1.3 Estimating the Remaining Parameters

The parameters μ_2, E_2, m, α_1, α_2, α_3, α_4 and ε_{vc} are determined by trial and error. They can be put into two groups based on their influence on the stress-strain curve. The parameters μ_2, E_2 and m are placed in one group, and α_1, α_2, α_3, α_4 and ε_{vc} in another. The parameters in the latter group affect only the stress-strain curve at the later stage of loading when the ice starts to deteriorate. It is easier to first obtain a crude estimation for μ_2, E_2 and m using the ascending branch of the stress-strain curve from the constant strain rate compression test before working out the values for α_1, α_2, α_3, α_4 and ε_{vc}. The parameters α_1, α_2, α_3, α_4 and ε_{vc} dictate the rate at which the stress descends from the peak value. They also determine the strain at which peak stress occurs. The process for finding these values involves making some trial analyses using various values of these parameters to see which one can present the best reproduction of the experimental stress-strain curve. From various trial runs, the value of 1 for α_2 is found to produce a satisfactory result. The values of α_4 and ε_{vc} can be estimated using the analytical and experimental results. The sum of α_4 and ε_{vc} is roughly equal to the analytical viscous strain value at the time when the total strain is equal to the strain at peak stress on the experimental stress-strain curve.

Another parameter that has to be mentioned is the tensile stress cutoff point σ_{tf}. This parameter is required for indentation or tensile loading where tensile stresses exist. In the uniaxial tests of isotropic polycrystalline ice at -7°C

done by Hawkes and Mellor (1972), the tensile fracture strength is found to be around 2MPa. With confining pressure, the tensile strength is found to drop dramatically (Haynes,1973). Due to the lack of information on the tensile strength of ice in multiaxial loading, a value of 1.5MPa is adopted for σ_{tf} in the analyses for ice indentation. This value is chosen on the basis that for indentation, ice may experience a tension-compression state of stress. The tensile fracture strength of ice in this situation is less than the uniaxial tensile fracture strength. However, it is important to remember that the fracture strength of ice is greatly influenced by the state of stress and temperature. Thus the choice of σ_{tf}=1.5MPa could be questionable, but in the absence of further experimental data, is unavoidable.

5.2 Uniaxial and Plane Strain Compression

Several analyses are done for uniaxial and plane strain compression. The results are compared to some of the test results from Frederking (1977), Sinha (1982), and Mellor and Cole (1982). Since the ice, temperature and test setup are different for each of these tests, the parameters used in the various analyses are also different. The process mentioned in section 5.1 is used to help in finding suitable values for the parameters. In the following subsections, the comparison between the analytical results and the results from Frederking, Sinha, and Mellor and Cole, are made and discussed.

5.2.1 Sinha's Test

Sinha (1982) has performed uniaxial compression tests on columnar ice at -10^{o}C. Two types of loading conditioned are used: constant strain rate and constant stress rate. The columnar ice used has an average grain diameter of 4 to

5mm and is loaded in the direction perpendicular to the long direction of the ice column.

In constant strain rate compression, the test is terminated a short while after reaching the peak stress. Therefore, no information is available on the residual strength of the ice specimen. As a result, only E_1, η_i and n can be approximated from the stress-strain curve of constant strain rate compression. From the initial slope of the stress-strain curve, E_1 is calculated to be around 6000MPa. The least square fit line for $\log(\sigma_{peak})$ versus $\log(\dot{\varepsilon})$, in Figure 5.1, gives an approxiamte value of n=2.73 and $\eta_i = 2.24\times10^{-7}(MPa)^{-n}s^{-1}$. The only way to work out values for β_1 and β_2 is to use the stress-strain curve of constant stress rate compression and a trial and error procedure. After several trial analyses, the following parameters were obtained.

$E_1 = 7000MPa$	$E_2 = 3500MPa$	
$n = 2.7$	$m = 1.2$	
$\eta_i = 1.4\times10^{-7}(MPa)^{-n}s^{-1}$	$\mu_2 = 1.667\times10^{6}(MPa)^{m}s$	
$\alpha_1 = 200$	$\alpha_2 = 1$	
$\alpha_3 = 0.00005$	$\alpha_4 = 1$	
$\varepsilon_{vc} = 0.00005$		
For $\dot{\varepsilon}_v < 5.0\times10^{-5}s^{-1}$	$\beta_1 = 9.6824\times10^{-6}(MPa)^{-n}s^{-1-\beta_2}$	$\beta_2 = 0.23$
For $\dot{\varepsilon}_v \geq 5.0\times10^{-5}s^{-1}$	$\beta_1 = 3.7789\times10^{-4}(MPa)^{-n}s^{-1-\beta_2}$	$\beta_2 = 0.6$

The analytical results are shown in Figures 5.2 to 5.5. To show the effect of η_i, the analytical peak stresses with $\eta_i = 1.76\times10^{-7}(MPa)^{-n}s^{-1}$ for constant strain rate compression are also plotted in Figure 5.2.

In Figure 5.2, it can be seen that the reduction of η_i shifts the peak stress upwards. As mentioned in section 5.12, η_i and n have a significant influence on the peak stress. Even though it is not shown, lower n is expected to increase the rate of increment of $\log(\sigma_{peak})$ versus $\log(\dot{\varepsilon})$. Since η_i and n are chosen to

produce the same σ_{peak} obtained in the test, it is not surprising that the $\log(\sigma_{peak})$-$\log(\dot{\varepsilon})$ data in Figure 5.2 for $\eta_i = 1.4\text{x}10^{-7}(\text{MPa})^{-n}\text{s}^{-1}$, closely matches the least square fit line for the test result.

In Figures 5.3 to 5.5, comparisons are made between the stress-strain curves generated by the numerical model and the experimental curves. In constant strain rate compression, the model predicts the behaviour of ice fairly well. It is not possible to compare the descending branch of the stress-strain curve because the tests were stopped immediately after reaching the peak stress. The strain at peak stress from the analytical solution is slightly higher than in Sinha's tests. The difference becomes bigger as the loading rate gets smaller. As for the peak stress, the difference between the analytical and test results is small except for $\dot{\varepsilon} = 1.4\text{x}10^{-6}\text{s}^{-1}$.

In constant stress rate compression, the model predicts the load-deformation behaviour of ice very well at the early stage of the loading as can be seen in Figure 5.5. At low stress rates, $4\text{x}10^{-3}$ and $1\text{x}10^{-3}\text{MPas}^{-1}$, the model overpredicts the stress in ice. This means that that strain rate predicted by the model is lower than in real situation. As a result, the experimental curves for these two loading rates are flatter than the experimental curves. At loading rates of $8\text{x}10^{-2}$, $2\text{x}10^{-2}$ and $8\text{x}10^{-3}\text{MPas}^{-1}$, the ice specimen fails in a brittle manner at a strain around 0.002 to 0.003. The numerical model is not able to predict this failure since compressive brittle fracture is not included in the proposed model. Thus, even though the stress and strain rate in the ice specimen are large enough to cause compressive brittle fracture, the analytical stress-strain curves extend beyond the strain values of 0.002 to 0.003 for the three high stress rate cases.

5.2.2 Mellor and Cole's Test

A series of constant strain rate and constant stress (creep) tests on fine-grained isotropic ice at -5°C have been performed by Mellor and Cole (1982). The average grain size of the ice used is 1.2mm. The initial slope of the stress-strain curve for constant strain rate compression gives an approximate E_1 of 7000MPa. In Figure 5.6, it can be seen that the relationship between $\log(\sigma_{peak})$ versus $\log(\dot{\varepsilon})$ is quite linear at low strain rates. At strain rates greater than $1.0\times10^{-5}s^{-1}$, the $\log(\sigma_{peak})$ data fall below the initial linear prediction. The values of n=3 and $\eta_i = 2.9\times10^{-7}(MPa)^{-n}s^{-1}$ are approximated from the straight line drawn through those points at low strain rates. The two lines drawn in Figure 5.6 are the best fit lines and not the least square fit lines. Figure 5.7 shows the relationship of $\log(\eta_f)$ versus $\log(\dot{\varepsilon})$ where η_f is calculated using the equation $\dot{\varepsilon} = \eta_f \sigma_{residual}^{n}$ mentioned in section 5.1.1 and the residual strength $\sigma_{residual}$ is measured from the test results. The values of η_f from the test results are calculated based on n=3. The solid curve in Figure 5.7 represents the values of η_f used in the numerical analyses.

The parameters used for the numerical analyses are listed below.

$E_1 = 9500MPa$ $\quad$ $E_2 = 1267MPa$

$n = 3$ $\quad$ $m = 3$

$\eta_i = 3.2\times10^{-7}(MPa)^{-n}s^{-1}$ $\quad$ $\mu_2 = 3.333\times10^{5}(MPa)^{m}s$

$\alpha_1 = 6.5$ $\quad$ $\alpha_2 = 1$

$\alpha_3 = 0.007$ $\quad$ $\alpha_4 = 1$

$\varepsilon_{vc} = 0.007$

For $\dot{\varepsilon}_v < 7.0\times10^{-7}s^{-1}$ $\quad$ $\beta_1 = 2.18\times10^{-4}(MPa)^{-n}s^{-1-\beta_2}$ $\quad$ $\beta_2 = 0.3562$

For $7.0\times10^{-7}s^{-1} \le \dot{\varepsilon}_v < 1.25\times10^{-5}s^{-1}$ $\quad$ $\beta_1 = 1.4\times10^{-6}(MPa)^{-n}s^{-1-\beta_2}$

$\beta_2 = 0.3562$

For $\dot{\varepsilon}_v \geq 1.25\times10^{-5}\,s^{-1}$ $\beta_1 = 1.3972\times10^{-4}(MPa)^{-n}s^{-1-\beta_2}$ $\beta_2 = 0.6117$

The analytical results are plotted together with the test results in Figures 5.8 to 5.14. As shown in Figures 5.8, 5.9 and 5.10, the analytical strain-time curves are very close to the experimental curves for constant stress loading. There is a general trend observed in these figures. The strain rate predicted by the analytical solution is generally higher than the experimental rate at strains in excess of around 0.04. This can be attributed to the values of β_1 and β_2 which control the viscous strain rate ($\dot{\varepsilon}_v$). At a large strain, the viscous strain rate is essentially equal to the total strain rate for constant stress loading.

For constant strain rate compression, the model gives a fairly good prediction of the stress-strain curves at low strain rate (Figures 5.11 and 5.12). However at high strain rates, the model overestimates the peak stress and the strain at peak stress, as shown in Figures 5.11 and 5.13. If η_i is allowed to change with $\dot{\varepsilon}_v$, the analytical peak stress can be reduced significantly for high compression strain rate. By using the following values for η_i:

$\eta_i = 3.2\times10^{-7}(MPa)^{-n}s^{-1}$ for $\dot{\varepsilon}_v < 7.4\times10^{-6}\,s^{-1}$,

and $\eta_i = 6.448\times10^{-6}\dot{\varepsilon}_v^{\,0.254}(MPa)^{-n}s^{-1.254}$ for $\dot{\varepsilon}_v \geq 7.4\times10^{-6}\,s^{-1}$,

the peak stress for high strain rates has been reduced close to the test result (Figures 5.11 and 5.14). However, this modification only allows for a better prediction of the peak stress, the strain at which the peak stress occurs remains much higher than the test values. Ice behaves in a more brittle manner as the strain rate increases. It can be seen that for strain rates of $8.32\times10^{-5}\,s^{-1}$ and $1.14\times10^{-3}\,s^{-1}$, the strain at peak stress is significantly lower than the values at low strain rates. Since the analytical model is formulated following the assumption that the strain at peak stress does not change or varies very little with respect to the compression strain rate, the model is unable to simulate the observed reduction of the strain at peak stress for high loading rates. Although, as

demonstrated in Figure 5.11, the prediction of peak stress can be made more accurate by allowing η_i to vary with $\dot{\varepsilon}_v$, this has not been incorporated in the model for several reasons. First, it is difficult to implement in the two-dimension model and finite element program. As well, even with the modification, the model is still unable to predict the reduction in the strain at which the peak stress for high strain rate compression occurs.

5.2.3 Frederking's Test

Frederking (1977) has done some tests on columnar ice at -10°C. The columnar ice used in the test has an average grain size of 5mm. Even though the ice type and the temperature in Frederking's tests are similar to those in the tests performed by Sinha (1982), their result, however, differ significantly. Consequently, the parameters used in the model to simulate Sinha's test cannot be used for Frederking's test. Frederking's test results, for the constant strain rate compression loaded perpendicular to the long direction of the column, are compared with the analytical solutions. There are two types of loading condition that are investigated: uniaxial and plane strain. The direction of confinement in the plane strain compression test follows the orientation shown in Figure 3.5. The values of η_i and n are approximated from the peak stress in uniaxial compression. However, E_i, β_1 and β_2 are approximated from the stress-strain curves of plane strain compression because only one stress-strain curve for uniaxial compression is available in Frederking's article. Assuming υ=0.3, the estimate for E_i is 3600MPa. From the equation of the least square fit line calculated by Frederking for $\log(\sigma_{peak})$ versus $\log(\dot{\varepsilon})$, the estimated values of η_i and n are found to be 2.322×10^{-7} $(MPa)^{-n}s^{-1}$ and 3.34 respectively. In Frederking's test, the peak stress in plane strain compression is roughly 2 to 5 times the peak stress in uniaxial compression under the same loading rate. Taking the average of

the minimum and the maximum values of the magnification and using n=3, a_1/a_2 is found to be around 10.3, using equation 5.13. After some fine-tuning, the following values are found to give a satisfactory representation of Frederking's tests.

$E_1 = 4500MPa$	$E_2 = 9000MPa$	
$n = 3.1$	$m = 1.0$	
$\eta_i = 2.1x10^{-7}(MPa)^{-n}s^{-1}$	$\mu_2 = 1.25x10^{6}(MPa)^{m}s$	
$\alpha_1 = 150$	$\alpha_2 = 1$	
$\alpha_3 = 0.0011$	$\alpha_4 = 0.9$	
$\varepsilon_{vc} = 0.0018$	$\upsilon = 0.35$	
$a_1 = 12$	$a_2 = 1$	
For $\dot{\varepsilon}_v < 2.36x10^{-5}s^{-1}$	$\beta_1 = 3.52x10^{-3}(MPa)^{-n}s^{-1-\beta_2}$	$\beta_2 = 0.6364$
For $\dot{\varepsilon}_v \geq 2.36x10^{-5}s^{-1}$	$\beta_1 = 9.884x10^{-5}(MPa)^{-n}s^{-1-\beta_2}$	$\beta_2 = 0.301$

Figure 5.15 shows the plot of η_f, calculated from the procedure in section 5.122 using n=3.1 and a_1/a_2=12, and the actual values of η_f used in the numerical solution which is represented by a solid curve.

Based on the above values, the model gives a fairly accurate prediction of the peak stress for both uniaxial and plane strain compression. In Figure 5.16, the analytical peak stress falls very close to the least square fit line for the experimental data. The analytical stress-strain curve for uniaxial compression at $1.67x10^{-5}s^{-1}$ compares well with the experimental curve except for the peak stress. As shown in Figure 5.17, the curves exhibit a close resemblance in their general shape and trend except the analytical peak stress is slightly higher. Both curves peak at almost the same strain (0.002) and their residual strengths are almost equal.

The analytical and experimental stress-strain curves for plane strain compression are shown in Figure 5.18. In general, the model is able to give a

good representation of the behaviour of ice in plane strain compression. The model captures the overall shape of the stress strain curve except for the curve at the loading rate of $1.67 \times 10^{-5} s^{-1}$. The test result for this loading rate shows a much higher initial stress reduction rate on the descending branch of the stress-strain curve than is predicted by the model. By comparing the experimental results with each other, the curve for loading rate $1.67 \times 10^{-5} s^{-1}$ does seem to have a considerably high initial stress reduction rate immediately after reaching the peak stress. This suggests the possibility that some irregularities may have occurred in the test for strain rate of $1.67 \times 10^{-5} s^{-1}$.

5.3 Indentation

When a moving ice sheet interacts with an offshore structure, the stress distribution in the ice sheet is far more complicated than what occurs in either the uniaxial or plane strain compression tests. For certain conditions, the interaction between the ice sheet and the structure can be described as an indentation process. This may occur, for example, in mid-winter, when the ice slowly advances against the structure.

Two shapes of indentor are investigated using the proposed plane stress ice model. These are the rectangular and cylindrical indentors. The indentation with a rectangular structure is analysed using two different sets of boundary conditions whereas only one set of boundary conditions is used for a cylindrical structure. The boundary conditions for the rectangular structure are designed specifically to match the tests of Michel and Toussaint (1977), and Frederking and Gold (1975). The geometry of the finite element meshes are also adjusted to match the size of their ice plates. For the cylindrical structure, the finite element mesh is designed to approximate an infinite ice sheet. This is done by using a mesh that is relatively large compared to the size of the indentor. The boundary

conditions for these three cases are shown respectively in Figures 5.19, 5.20 and 5.21. The numbering system for the finite element meshes are shown in Figures 5.22, 5.23 and 5.24. Since the effects of bonding and friction between the ice and the structure are beyond the scope of this study, normal stress only is assumed between the ice and the structure. Thus, in the finite element mesh, all the boundary nodes that are in contact with any external object are assumed to be on rollers. For the cylindrical indentor, a fictitious outer boundary is assumed in order to limit the size of the grid. At a further distance from the indentor, the movement of the ice sheet is virtually unaffected by the indentor. Therefore, the nodes at the fictitious boundary are considered fixed to the region outside the mesh so that at this boundary, the ice on both sides of the boundary is in contact and have the same displacement at all time.

The tests of both Michel and Toussaint, and Frederking and Gold, are performed using columnar ice at -10^{0}C. Thus, it is logical to use the same parameters that are used in section 5.3 for Frederking's tests which have also been performed on columnar ice at -10^{0}C. In addition to these parameters, the tensile stress cutoff point of σ_{tf} =1.5MPa is used. The selection of σ_{tf}=1.5MPa has been discussed in section 5.1.3.

In Chapter 2, various empirical equations for predicting the force exerted on a structure by a floating ice sheet were discussed. For example, there are the equations which have been proposed by Korzhavin (1962), Afanasev et al. (1971), Schwarz et al. (1974) and Saeki et al. (1977). It might appear appropriate to compare the predictions of those equations with the results of the indentation simulations presented in this chapter. However, it must be pointed out that those empirical results are only valid for high deformation rates where compressive brittle fracture occurs. The present model is limited to lower strain rates and for this reason no direct comparison is made.

5.3.1 Michel and Toussaint's Test

To simulate Michel and Toussaint's test, numerical analyses have been performed for a rectangular indentor with the boundary condition shown in Figure 5.19. Three indentor sizes of 50mm, 100mm and 150mm have been used. Each indentor has been analysed under five displacement rates: $5x10^{-4}$, $5x10^{-3}$, $5x10^{-2}$, $5x10^{-1}$ and 5 mm/s. The analyses are divided into 100 time steps with an applied deformation of 0.04mm for each step. This means that the time step sizes are different for different indentation rates. The analytical peak average stress, load-deformation curve, and the stress distribution are examined and compared to the test results. Figures 5.25 to 5.68 show some of the results of the analyses. The analytical peak average stresses and load-deformation curves are obtained from the solution with 3x3 Gauss point integration, whereas, the stress distributions are obtained from both 2x2 and 3x3 Gauss point integration. To facilitate the discussion, three ranges of dimensionless displacement rates (v/b) are defined where v is the deformation rate of the indentor and b is the width of the indentor. The low range is defined roughly for v/b of less $1.0x10^{-4}s^{-1}$, the intermediate range as $1.0x10^{-4}s^{-1}$ to $1.0x10^{-2}s^{-1}$, and the high range as larger than $1.0x10^{-2}s^{-1}$.

In Figure 5.26, the analytical and experimental peak average stress (σ_{avg}) are plotted against the dimensionless deformation rate (v/b). The stress σ_{avg} is the normal force on the indentor divided by the contact area which is the product of b and h where b is the width of the indentor and h is the thickness of the ice. For the analytical result, h is taken to be unity. A best fit curve is drawn through the data points from the analyses. At low to intermediate v/b, the curve shows a linear relationship between log(peak σ_{avg}) and log(v/b). At v/b greater than $3.0x10^{-2}s^{-1}$, the peak average stress appears to decrease with v/b. This

behaviour also shows up in Michel and Toussaint's tests where the last experimental point suggests a drop in σ_{avg} versus v/b. However, it is not possible to conclude that this trend continues for higher v/b because all three data points for v/b greater than $3.0x10^{-2}s^{-1}$ come from the analyses with the same deformation rate v but different indentor width. Therefore, to conclude that the experimental peak average stress is decreasing with v/b in the high v/b range, further analyses with different deformation rates are required. But further analyses have not been performed because the proposed model is unable to predict the behaviour of ice at high v/b range. This limitation is explained in the following discussions.

The comparison of the analytical and experimental peak σ_{avg} shows that at low v/b, the experimental peak σ_{avg} is slightly lower than that predicted by the numerical model. On the other hand, the analytical log(peak σ_{avg}) increases at a lower rate with log(v/b). It is possible to adjust the predicted peak σ_{avg} by changing the values of η_i and n. At low v/b, smaller n makes the best fit curve steeper and higher η_i shifts the curve downward. Thus with some adjustments to η_i and n, the numerical model should be able to produce a better prediction of the peak σ_{avg}. At high v/b, the model overestimates the peak σ_{avg} by a large margin. This can be explained by the deficiency inherent in the model in describing the behaviour of ice at high compression rates. In tension, a tensile cutoff stress is used for tensile brittle fracture, but there is no similar consideration for compressive brittle fracture. Thus, at high v/b the ice may in fact experience compressive brittle fracture whereas the model assumes the ice remains intact. From Frederking's (1977) plane strain test, the peak stress in the loading direction is observed to be around 18MPa for the loading rate of $1.67x10^{-4}s^{-1}$. Frederking speculates that the transition from ductile to brittle failure for plane strain loading to be around $1.0x10^{-4}$ to $1.0x10^{-3}s^{-1}$. Assuming that brittle failure occurs at loading rates of $1.0x10^{-3}s^{-1}$, extrapolation from Frederking's results

gives a peak stress of approximately 26MPa for a strain rate of $1.0 \times 10^{-3} s^{-1}$. Thus, it is safe to assume that, in the indentation tests, by Michel and Toussaint, the stress in the ice plate cannot exceed 26MPa because compressive brittle failure would have occurred before this level of stress is achieved. From the stress distribution predicted by the model for the 50mm indentor at a deformation rate of 5mm/s, shown in Figure 5.43, the normal stress in the Y-direction is found, however, to be much greater than 26MPa. This means that the stress distribution given by the numerical solution is, in fact, unrealistic and compressive brittle fracture should have occurred. Since the model does not include compressive brittle fracture, and it is unable to predict the behaviour of ice for high v/b. It can be concluded that the peak average stress predicted for this loading range is probably not reliable. For intermediate v/b, the tensile principal stress, at locations close to the edge of the indentor is sufficiently large to cause tensile brittle fracture. This type of failure is represented by using a tensile stress cutoff. However, the propagation of brittle fracture is unpredictable. Since at this stage, the failure is not extensive, the model can still give a fairly reasonable estimate of the peak average stress, but the value is time step, loading rate, and mesh sensitive. This is due to the fact that even though the size of the time step only controls the distance the indentor moves per time step, it indirectly controls the stress increment at every time step. Consequently, the bigger the time step size, the bigger the stress increment is. Since the proposed model for tensile brittle fracture is governed by the principal tensile stress, the size of the stress increment influences the pattern of brittle fracture. For instance, a larger stress increment causes the stress at more Gauss points to exceed the tensile stress cutoff point σ_{tf} simultaneously than for a lower stress increment. The influence of the finite element mesh on the peak average stress is caused by the way the effect of tensile brittle failure is incorporated into the finite element formulation. In the

formulation, whenever the tensile principal stress at a Gauss point exceeds σ_{tf}, the contribution of that point, to the overall stiffness of the ice is assumed to be zero. Consequently, the effect of the brittle fracture at a Gauss point in a big element is greater than for a small element. As the deformation increases beyond the peak value of σ_{avg}, for intermediate range of v/b, the region of tensile brittle fracture progresses into the ice plate. At this point, the numerical prediction becomes unrealiable. The validity of the analytical prediction is reflected by the smoothness in the average stress versus displacement curves in Figures 5.27 to 5.34. Any jump on the curve implies that brittle fracture has occurred, and the analytical solution becomes less reliable.

In Figure 5.33, an experimental curve for σ_{avg} versus indentor displacement, is plotted together with the analytical curves. The general shape of the experimental curve can be seen to closely resemble that of the analytical curves except for the value of the indentor displacement at which the peak value of σ_{avg} occurs. From the analytical curves in Figure 5.33, the displacement of the indentor at peak σ_{avg} is seen to decrease with indentor size. Therefore, it is expected that the displacement of the indentor at peak σ_{avg}, for an analysis with an indentor width of 25.4mm, would be less than that with a 50mm indentor. But the displacement at which the experimental curve peaks is bigger than that of the analytical curve with a 50mm indentor. This is probably due to the fact that the parameters used in the analyses are based on Frederking's (1977) test results, and that the appropriate parameters required to model the ice used in Michel and Toussaint's test are different.

The stress distribution across the indentor changes with time. At the beginning of loading, the largest normal stress in the Y-direction is located close to the indentor's edge. This can be explained by the fact that there is a difference in displacement rate for the region under the indentor and outside of the indentor.

To bridge this difference, the ice in the area around the indentor's edge, as a result, has a higher strain rate than the other region under the indentor. Therefore, the stress in the region around the edge of the indentor increases at a faster rate than at any other locations along the indentor face. This pattern of stress distribution occurs for the entire range of deformation rates analysed, as can be seen in Figures 5.35 to 5.48. The following discussion of the stress distribution focuses on the analyses at intermediate and low v/b because the results for high v/b are felt to be unreliable once the deformation gets beyond the initial stage. At peak σ_{avg}, for low v/b, the normal stress σ_y is almost uniform right across the indentor, but the maximum stress no longer occurs close to the edge. The location of maximum stress has moved inward by about 0.15b towards the centre of the indentor. By this time, the normal stress σ_y near the indentor's edge has already fallen from its peak value. Thus, even though the highest strain rate is still near the edge of the indentor, the stress is no longer the largest in that region. For intermediate v/b, the maximum σ_y has also shifted inside from the edge. However, the stress around the indentor's edge is much lower than at other locations along the indentor. This is caused by the loss of confinement around the edge of the indentor due to brittle failure of ice.

At a steady state (large deformation), for low v/b, σ_y is almost uniform across the length of the indentor with the stress at the edge being slightly greater than elsewhere. The situation is somewhat different for intermediate values of v/b. There are two types of stress distribution observed for intermediate values of v/b. At the upper end of the intermediate v/b range, at values greater than $5.0 \times 10^{-3} s^{-1}$, the ice under the indentor has almost entirely failed. There is no common pattern for the distribution of σ_y except that, in most of the region under the indentor, σ_y is zero. At the lower end of the intermediate v/b range, less than $5.0 \times 10^{-3} s^{-1}$, σ_y is close to being uniform across the indentor except at the edge.

The stress at the edge is governed by the progression of the tensile brittle fracture which is sensitive to the finite element mesh, the loading rate, and the time step. But the progression of the tensile brittle fracture is not very predictable, as can be seen in Figures 5.39 and 5.40. The stress distribution shown in Figure 5.39 is from the analysis with the deformation rate that is ten times higher than that for Figure 5.40. In Figure 5.40, the Gauss point near the indentor's edge has σ_y which is close to zero due to tensile brittle fracture. This situation is also expected to occur for the higher loading rate, but as shown in Figure 5.39, this does not occur. This shows that the prediction after the peak σ_{avg} for intermediate v/b is not very reliable.

There is one odd behaviour that shows up on the analyses with the 3x3 Gauss point integration but not in the 2x2 Gauss point integration. This behaviour only appears at steady state of loading. The comparisons of the result from the 2x2 and 3x3 integrations at various stages of loading are shown in Figures 5.49 to 5.54 for the 150mm indentor at 5.0×10^{-4} mm/s. At the early stage and the peak σ_{avg} of loading, the stress distribution for the 2x2 and 3x3 integrations are close to each other. Both methods give stress distributions that do not show any wild fluctuations. At the steady state, the 2x2 integration still gives a smooth distribution of stress across the indentor but not the 3x3 integration. For the 3x3 integration, the value of σ_y fluctuates wildly from one Gauss point to the next. At a low v/b, the average value of stress predicted by the 3x3 integration is very close to the one predicted by the 2x2 integration, as shown in Figures 5.51 to 5.54. Therefore, at steady state, both methods give a similar prediction of the total force on the indentor at low v/b. But at intermediate v/b, the 3x3 integration may overpredict the stress at steady state for certain locations. This overprediction may cause an unnecessary tensile brittle failure in ice. This can be seen in Figures 5.39 and 5.44 or 5.40 and 5.45. As a result, there is some

uncertainty with respect to the σ_{avg} that is predicted by the 3x3 integration at steady state. The wild fluctuation in the stress distribution can be explained by the shift in the dominant mode of deformation from the elastic deformation to the viscous flow. It is well known that as the Poisson's ratio approaches 0.5, in a three dimension analysis for problems such as a sphere under an internal pressure or an elastic foundation under a uniform pressure, the elastic solution with a 3x3 integration gives a stress prediction at the Gauss points that deviates greatly from the actual value. As the Poisson's ratio approaches 0.5, the matrix that relates the stresses to the elastic strains, in a general three dimension formulation, becomes singular. The same thing happens to the matrix [A] in the proposed model as the ratio a_2/a_1 approaches zero or a_1/a_2 approaches infinity. The matrix [A] is defined in Chapter 4 as the matrix that relates the stresses to the viscous strain rates. Therefore, with a_1/a_2=12 and a 3x3 integration, the predicted stress at the Gauss points from the analyses, fluctuates from the actual value. Since the matrix [A] is only involved with the viscous flow, this explains why the deviation only shows up at the steady state where viscous flow is the dominant mode of deformation

The curves for the normal stress (σ_y) distribution along the centreline of the ice plate show a typical reduction of stress as the distance from the indentor increases. The plots for σ_y versus the distance from the indentor along the centreline are shown in Figures 5.55 to 5.67. Close to the indentor, the slope gets steeper as the distance from the indentor increases. This only occurs for a short distance from the indentor. After a certain point, the slope begins to get flatter as the distance increases. Sometimes, at points close to the indentor, the normal stress may even increase before its value starts to go down. This occurs at the initial loading stage in the analyses with the 150mm indentor, which is illustrated in Figures 5.59 to 5.62. It does not show up on the analyses with 50mm indentor probably due to the wide spacing of the stress sampling locations relative to the

indentor width. At peak σ_{avg}, the stress does not show an increase at points close to the indentor. However, it shows up again, at steady state, in the analyses with 150mm indentor at the loading rates of $5.0x10^{-3}$ and $5.0x10^{-4}$ mm/s (Figures 5.61 and 5.62). At the initial stage of loading, the ice near the indentor's edge has the highest stress. The stress starts to redistribute as the distance away from the indentor increases. Thus, the stress at the indentor's edge is redistributed to other regions, such as the centreline of the ice plate, causing the stress at the centreline to initially increase. As the distance increases, the width that is effective in carrying the load also expands. Therefore, the stress σ_y along the centreline only increases for a short distance before starting to decline. This is also the same reason why, at steady state, the stress initially increases in the analyses with 150mm indentor at the loading rates of $5.0x10^{-3}$ and $5.0x10^{-4}$ mm/s.

A major portion (over 80%) of the stress reduction occurs within a distance of 3b from the indentor. The reduction rate goes down significantly at distances greater than 4b for the 50mm indentor and 8b for 50mm indentor. One of the reasons is because there is a width limit to the ice plate. As the distance increases, the width that is effective in carrying the load also expands. However, the finite size of the ice plate limits the maximum effective width that can be achieved. Beyond a certain distance from the indentor, the reduction of σ_y is more a result of stress redistribution than the expansion of the effective width. For loading rate around intermediate v/b and above, the ice plate fractures 1 to 2b away from the indentor. Plotting the highest tensile principal stress (in the situation where there is no tensile principal stress, the minimum compressive principal stress is used) along the centerline, it is observed that the curve peaks at a distance of 1 to 2b away from the indentor. As the ice plate is indented in the Y-direction, the material is squeezed out in X-direction. But since the plate is confined in X-direction, the only place that the ice can move out is through the

space between the containment and the indentor. Figure 5.19 shows the most likely direction of ice movement. The motion of the ice directly under the indentor is restricted by the indentor. Thus, both principal stresses are compressive. Further away from the indentor, the constriction decreases, and as a result, a tensile principal stress is created by the outward movement of the ice. But as the influence of the indentor decreases with greater distance, the influence of the confinement in the X-direction increases. Therefore, after a certain point, the tensile principal stress stops increasing and starts to drop. This can be seen in Figure 5.68. As a result, tensile brittle fracture occurs along the centreline for loading rate around intermediate v/b and above because the tensile principal stress generated is larger than the tensile stress cutoff point σ_{tf}.

Saeki et al. (1984) have performed some indentation tests on a rectangular pile. Some of their stress distributions across the indentor, at peak average stress, are shown in Figures 5.69 to 5.71. The results do not seem to show any characteristic or common stress distribution pattern. On the whole, the stress can be considered to be uniform across the indentor. This is quite similar to the prediction from the numerical analyses for low v/b.

5.3.2 Frederking and Gold's Test

Six analyses have been performed in order to allow a comparison of the analytical and experimental peak σ_{avg} for Frederking and Gold's (1975) indentation tests. The loading rates are from 3.75×10^{-5} to 7.5×10^{-3} mm/s and the indentor width is 75mm. Both analytical and experimental results are plotted on Figure 5.73 for log(peak σ_{avg}) versus log(v/b). A least square fit line is also drawn through the experimental points. The top two data points from the numerical analyses are excluded from the comparison because their loading rates are outside the range of the tests. Leaving these two points out, the analytical

solutions give a fairly good estimate of peak σ_{avg}. At v/b below $5.0x10^{-6}s^{-1}$, the numerical model gives a slightly higher peak σ_{avg} prediction, but at v/b above $5.0x10^{-6}s^{-1}$, the peak σ_{avg} is slighty underestimated. However, as mentioned before, both η_i and n can be adjusted to give a closer estimate of peak σ_{avg}.

5.3.3. Cylinder Indentation

Three indentor of 100, 150 and 200 mm in diameter are used in the analyses. Similar to the analyses performed for Michel and Toussaint's test, each indentor size is analysed under five compression rates: $5x10^{-4}$, $5x10^{-3}$, $5x10^{-2}$, $5x10^{-1}$ and 5 mm/s. The analyses are divided into 100 time steps with an applied deformation of 0.04mm for step. A semi-circular finite element mesh of 1900mm in radius is employed to represent the ice sheet. The analytical results are shown in Figures 5.76 to 5.100. Since most of the tests done on cylindrical indentors involve a penetration type of loading, it is difficult to find any reference on an indentation test with a cylindrical pile. In a penetration test, the advancing edge of the ice sheet is only in contact with the tip of the cylindrical face in the beginning of the test (Figure 5.74). But in indentation, the indentor is already in full contact with the ice sheet at the start (Figure 5.75). Tanaka et al. (1987) have carried out some indentation tests on sea ice at temperatures ranging from -2 to -5^{0}C. Since the parameters used in the analyses are calibrated with Frederking's (1977) test results, it is inappropriate to compare the analytical and Tanaka results. Even though the radial stress distribution around the indentor have been measured by Tanaka et al., their data show such variation that it is not possible to establish a consistent pattern for the radial stress distribution. Thus, a comparison between the analytical and the experimental stress distribution pattern is of questionable value. For this reason, the remainder of this section is focused on the discussion of the analytical results. To facilitate the discussion,

three ranges of the dimensionless defermation rate (v/b) are defined where v is the deformation rate of the indentor and b is the diameter of the indentor. The low range is defined roughly as less than $1.0x10^{-4}s^{-1}$, the intermediate range as between $1.0x10^{-4}s^{-1}$ and $1.0x10^{-3}s^{-1}$, and the high range as larger than $1.0x10^{-3}s^{-1}$. Similar to section 5.3.1, the results for peak σ_{avg}, and σ_{avg} versus deformation are obtained from the 3x3 integration. For the study of the stress distribution, both the 2x2 and 3x3 Gaussian integrations are used. The limitations and effects of the 3x3 integration discussed in section 5.3.1 are applicable here.

The log-log plot of peak σ_{avg} and v/b is shown in Figure 5.76. The average stress σ_{avg} is defined as the force on the indentor in the Y-direction divided by the product of b and h where b is the diameter of the indentor and h is the thickness of the ice. Similar to the analytical results for Michel and Toussaint's test in section 5.3.1, the relationship between log(peak σ_{avg}) and log(v/b) is linear at low to intermediate v/b. In the case of a cylindrical indentor, the relationship is linear until v/b=$5.0x10^{-4}s^{-1}$. Beyond this point, there is no clear dependency between log(peak σ_{avg}) and log(v/b) except in the situation where the indentor size is constant. If the indentor size is constant, the value of log(peak σ_{avg}) continues to increase with the log(v/b). However, the prediction of the model in this range is felt to be unreliable and it is not appropriate to examine the predicted relationship between log(peak σ_{avg}) and log(v/b) for a constant indentor size. The unreliability at high v/b is reflected by the occurrence of high stress and extensive brittle failure in the ice, as shown in Figure 5.85. Similar to the analyses for Michel and Toussaint's test at high v/b, the compressive stress is bigger than what the ice can sustain. The ice plate being indented in the low range of v/b, such as $5.0x10^{-4}$ and $5.0x10^{-3}$mm/s for 100mm indentor, deforms mainly in a ductile manner with very limited brittle fracture. For intermediate v/b, such as $5.0x10^{-2}$mm/s for 100mm indentor, there is no

extensive brittle fracture up to the point of peak σ_{avg}. Following that, the region of brittle fracture expands and becomes widespread as illustrated in Figure 5.86. Since the progression of the brittle fracture is unpredictable, as a result, the calculated stress distribution after σ_{avg} for intermediate v/b is not reliable. As mentioned in section 5.3.1, the validity of the numerical solution can be gauged from the smoothness of the average stress versus displacement curves on Figures 5.77 to 5.84

For low v/b, at initial loading and steady state stages, the radial stress on the indentor is a maximum at the Y-axis and slowly drops to a minimum value at the X-axis. At steady state, the ice at element 7 experiences brittle fracture. As a result, the radial stress on the indentor at that location is close to zero. This may be due to the way the boundary joint is represented in the finite element program and is not representative of the actual situation. The roller joint employed in the finite element program is able to carry both compression and tension loads. The use of roller joints to represent the boundary between the ice sheet and the indentor is consistent with the assumption that there is no bonding or friction between these two objects. However in the real situation, there can be no tensile normal stress at the contact surface whereas the roller boundary condition does allow such stresses. As a result, the ice at element 7, which is moving away from the indentor, is held back by the joint. Consequently, the ice at that region fails in a brittle manner due to the tensile stress that is created. However, this does not affect the value of σ_{avg} since the actual contribution from this region is zero anyway. At peak σ_{avg}, the radial stress is almost constant or even rises slightly from Y-axis up to an angle of 45^0. After this point, the radial stress drops dramatically. The radial stress distribution patterns around the indentor at initial loading stage and at peak σ_{avg}, for intermediate v/b, is similar to that for low v/b. But at steady state, in the intermediate v/b range, extensive brittle fracture occurs

at the regions near both the X and Y axes. The failure around the X-axis is probably due to the roller boundary condition. However, the failure around the Y-axis is a result of the indentor's shape. As the cylindrical indentor moves into the ice sheet, it acts like a wedge, driving the ice sheet apart. The tensile stress created in the X direction causes the ice to fail in a brittle manner. At this stage, the stress and σ_{avg} predicted by the model becomes unreliable because the progression of brittle fracture is unpredictable and is very dependent on the finite element mesh, the loading rate, and the size of the time step.

Along the Y-axis, the radial stress distribution shows a typical stress reduction as one moves further away from the indentor. These curves are shown in Figures 5.93 to 5.100. But unlike the distribution for a rectangular indentor, as in the case for Michel and Toussaint's test, there is no slight increment of radial stress near the indentor. The value of the radial stress, from the analyses with a cylindrical indentor, instead drops off right away. More than 80% of the reduction of the radial stress occurred within the first 3b from the indentor. For intermediate v/b, brittle fracture occurs near the indentor at steady state due to the wedging action of the indentor.

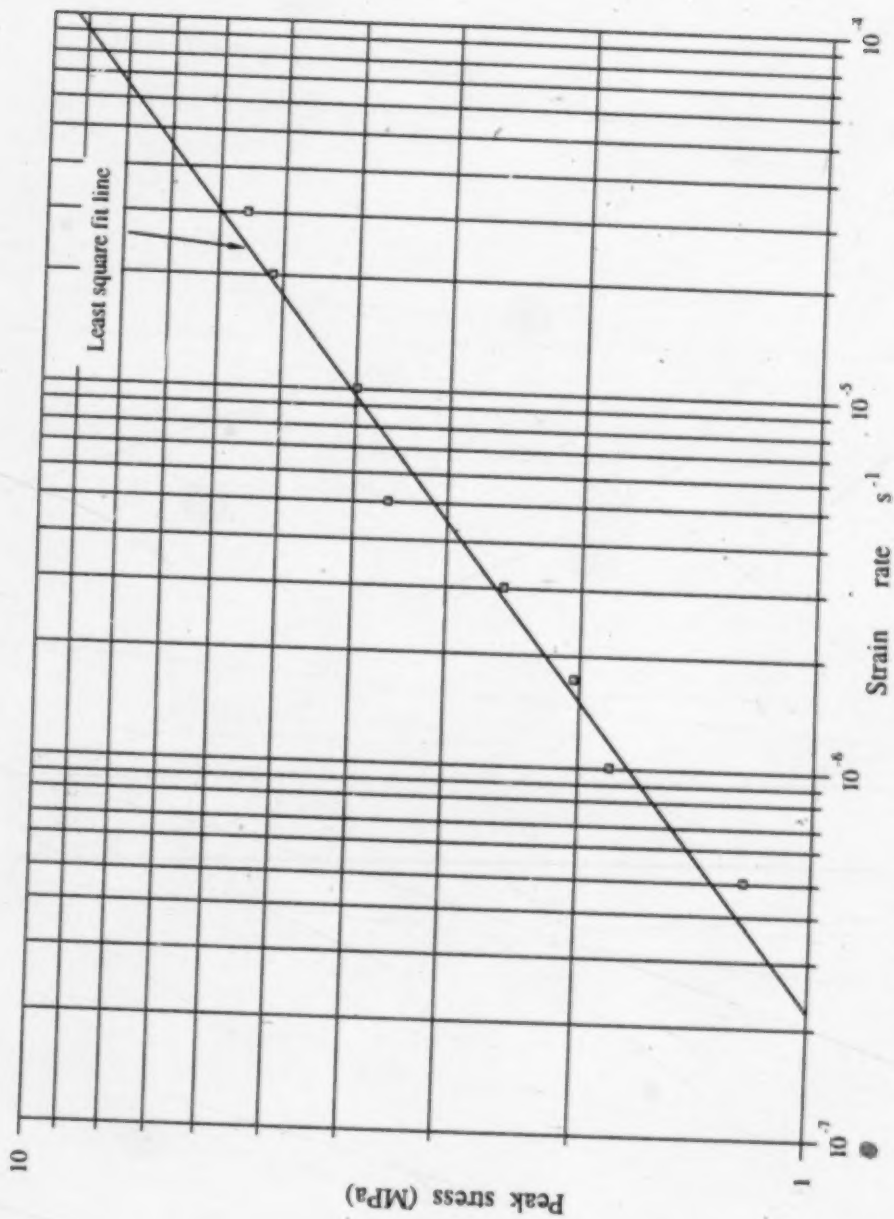

Figure 5.1 Relationship between the peak stress and the constant compression strain rate from Sinha's test.
(Modified from Sinha, 1982)

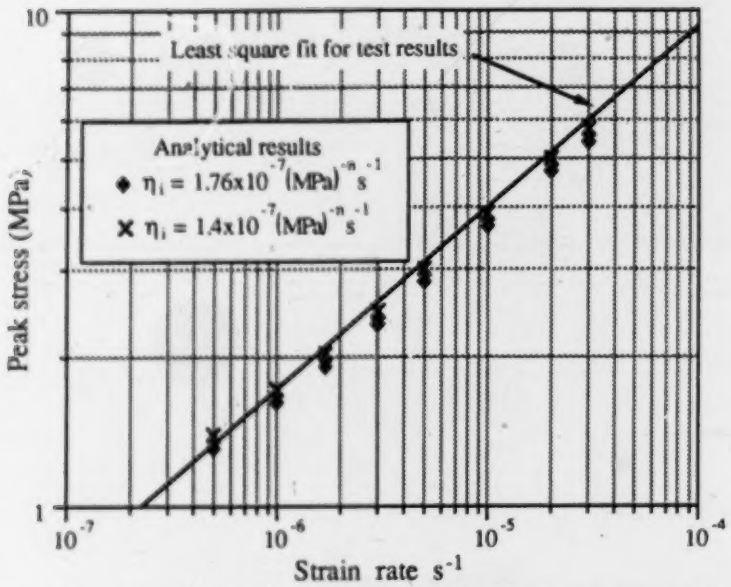

Figure 5.2 The analytical peak stress versus strain rate with different η_i and the experimental results for Sinha's test. (Modified from Sinha, 1982)

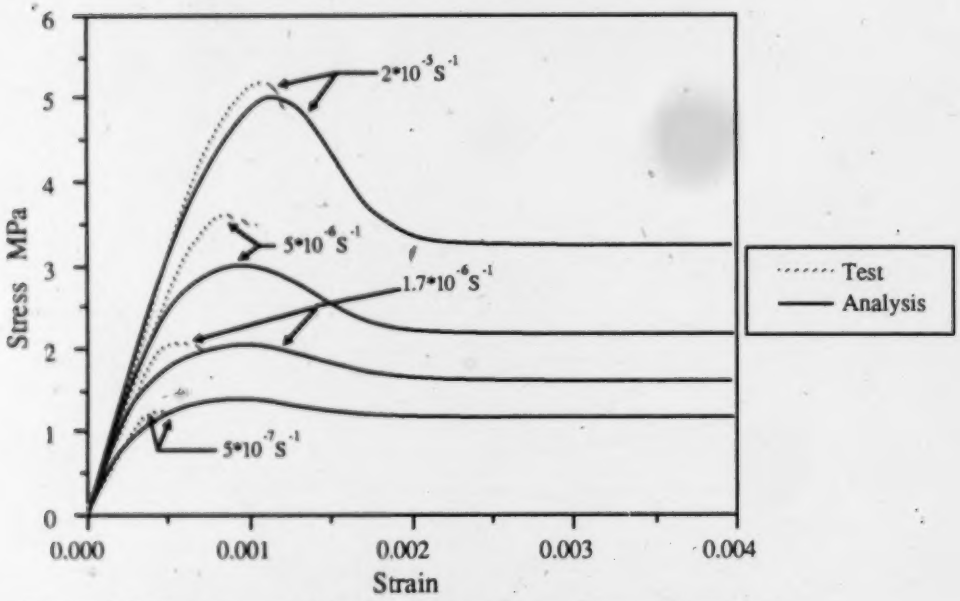

Figure 5.3 The stress-strain curve of constant strain rate compression for both analytical and Sinha's test result. (Modified from Sinha, 1982)

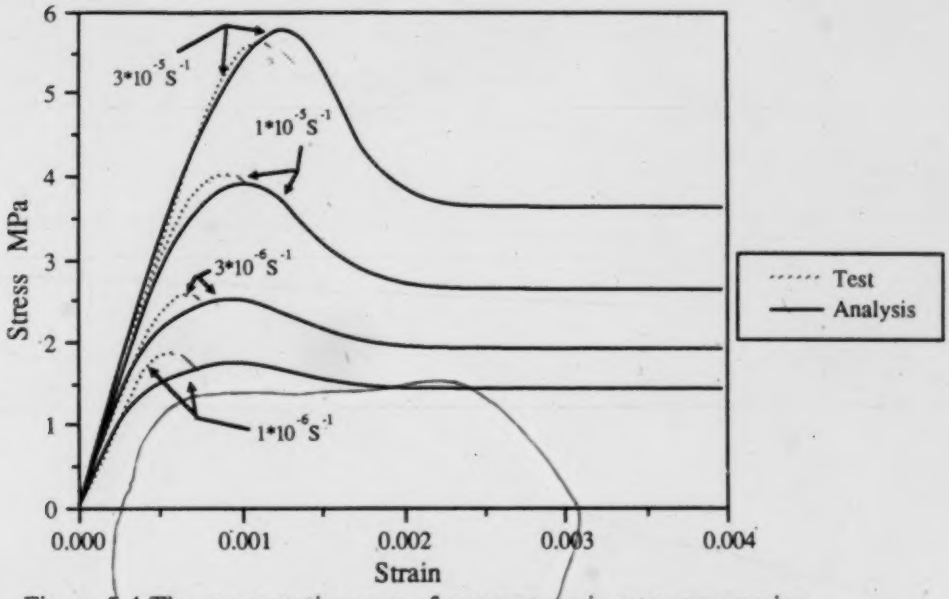

Figure 5.4 The stress-strain curve of constant strain rate compression for both analytical and Sinha's test result. (Modified from Sinha, 1982)

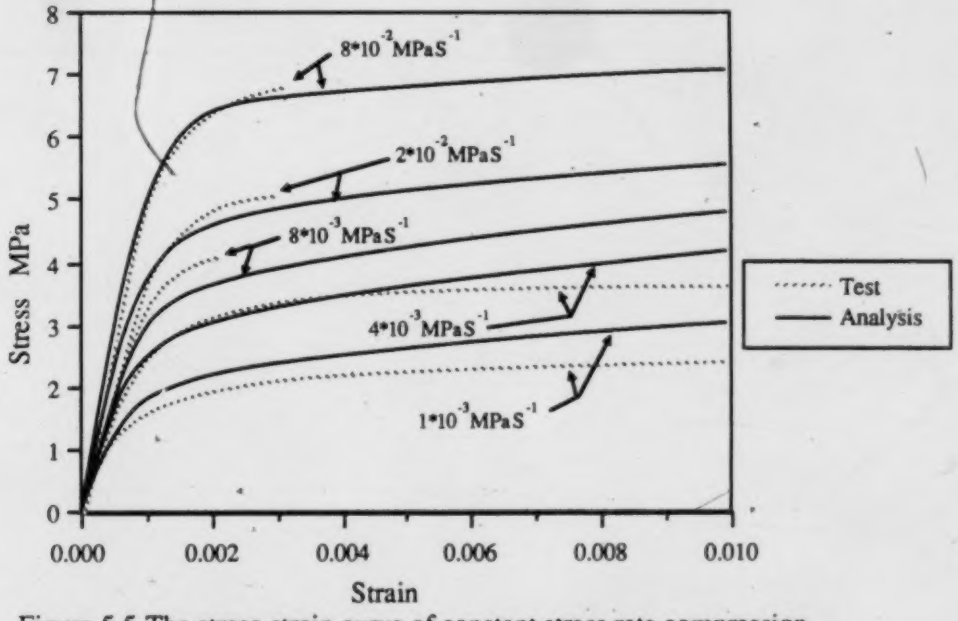

Figure 5.5 The stress-strain curve of constant stress rate compression for both analytical and Sinha's test result. (Modified from Sinha, 1982)

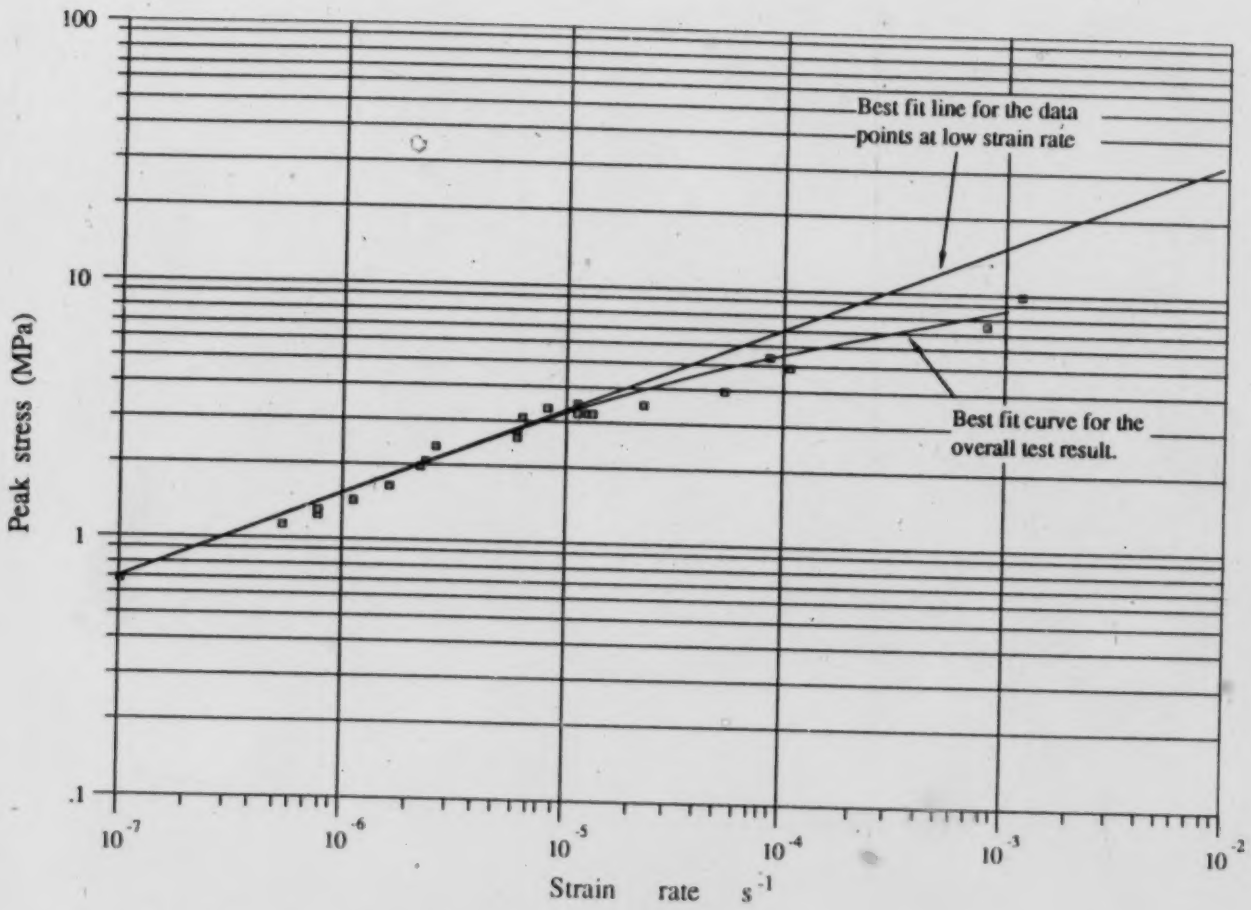

Figure 5.6 Relationship between the peak stress and the constant compression strain rate from Mellor and Cole's test. (Modified from Mellor and Cole, 1982)

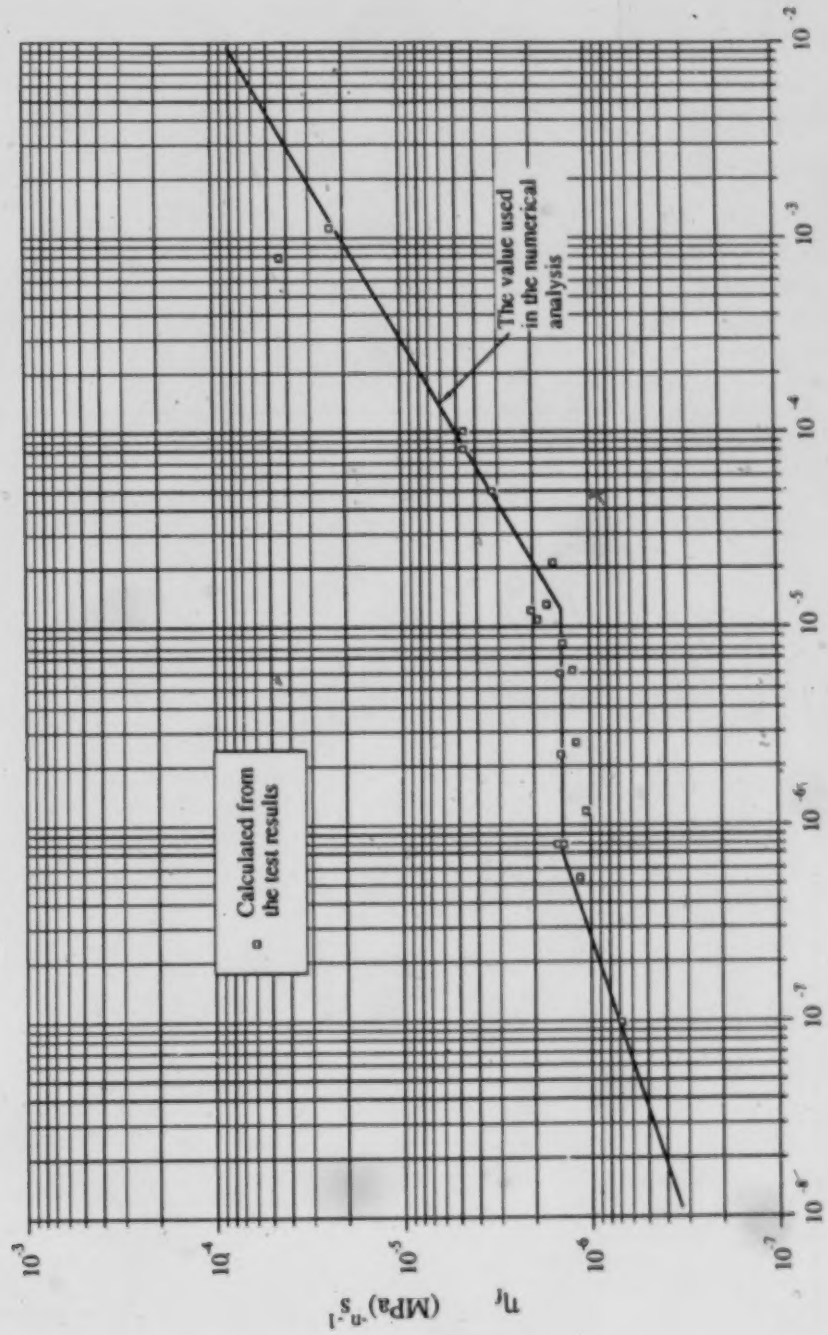

Figure 5.7 Relationship between η_f versus constant compression rate for Mellor and Cole's test. (Modified from Mellor and Cole, 1982)

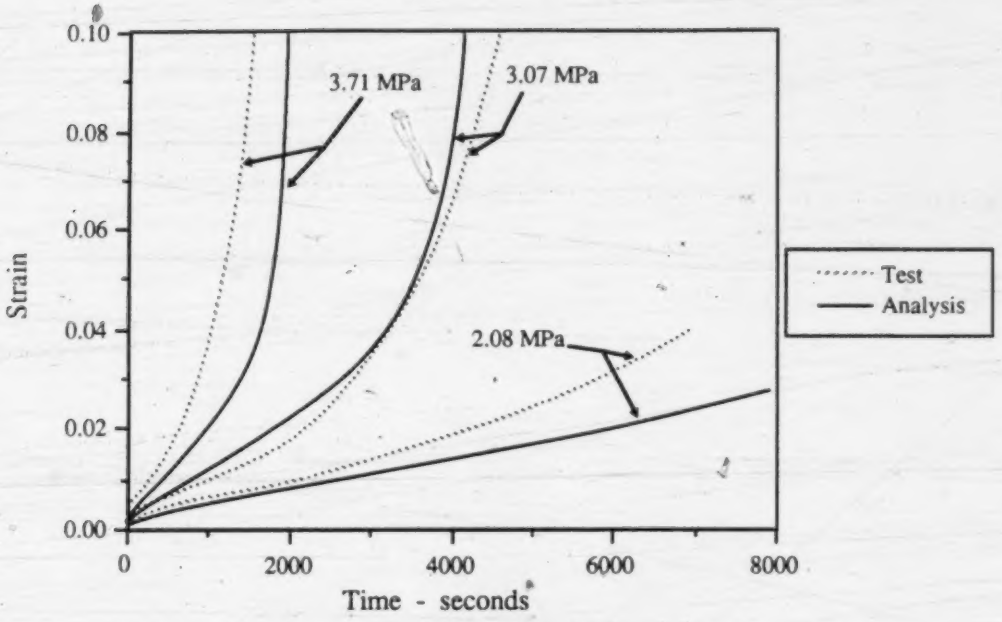

Figure 5.8 The test and analytical strain-time curves for Mellor and Cole's constant stress test. (Modified from Mellor and Cole, 1982)

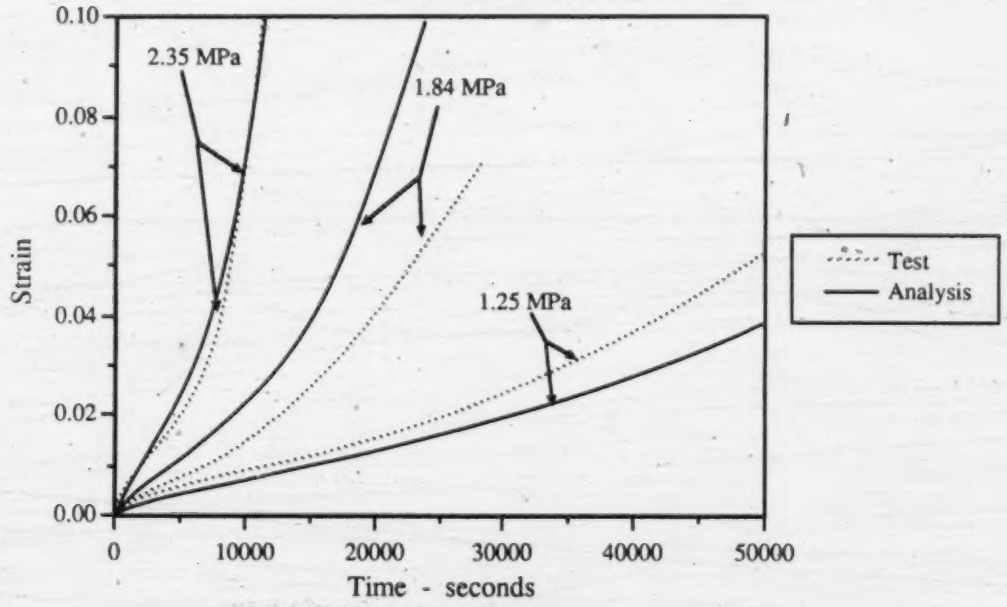

Figure 5.9 The test and analytical strain-time curves for Mellor and Cole's constant stress test. (Modified from Mellor and Cole, 1982)

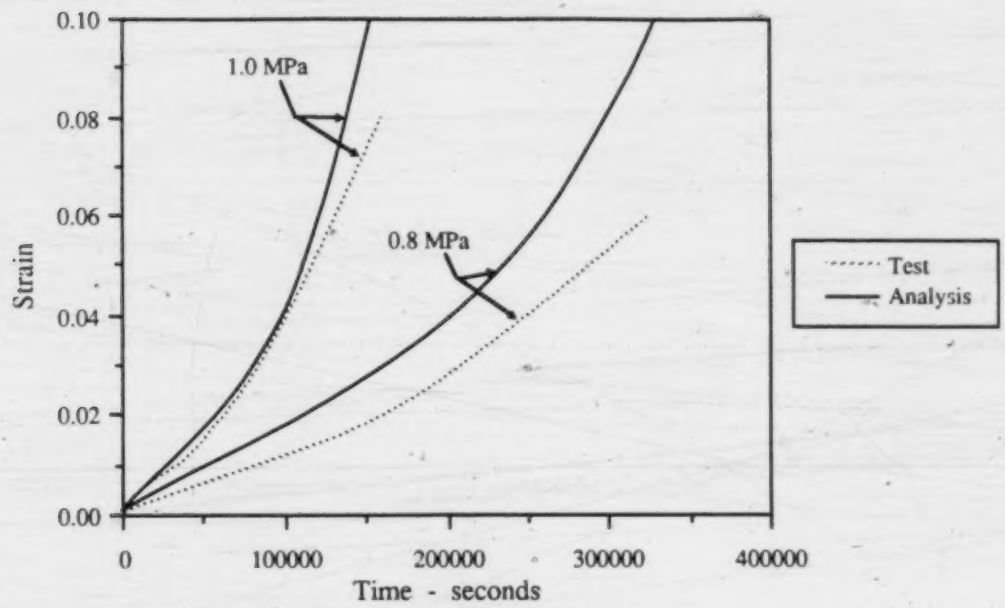

Figure 5.10 The test and analytical strain-time curves for Mellor and Cole's constant stress test. (Modified from Mellor and Cole, 1982)

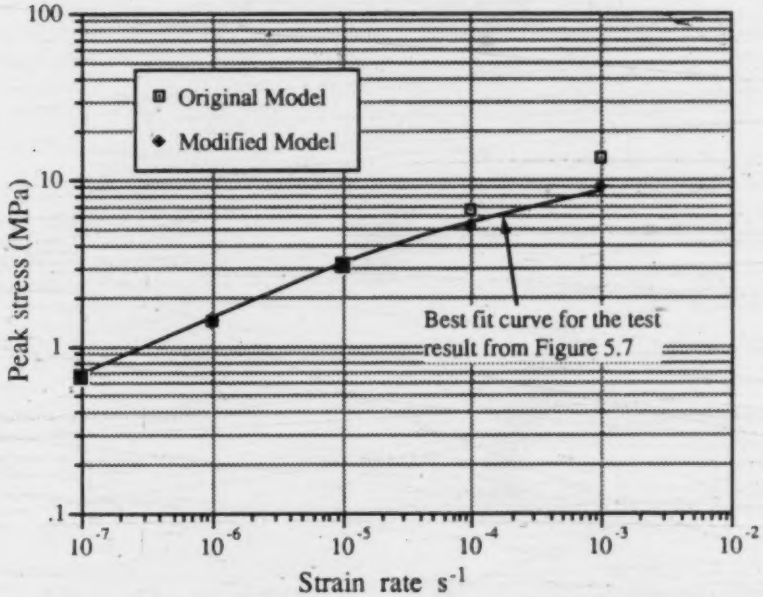

Figure 5.11 The peak stress versus strain rate plot from both the original and the modified model together with the best fit curve of the test result for Mellor and Cole's constant strain rate test. (Modified from Mellor and Cole, 1982)

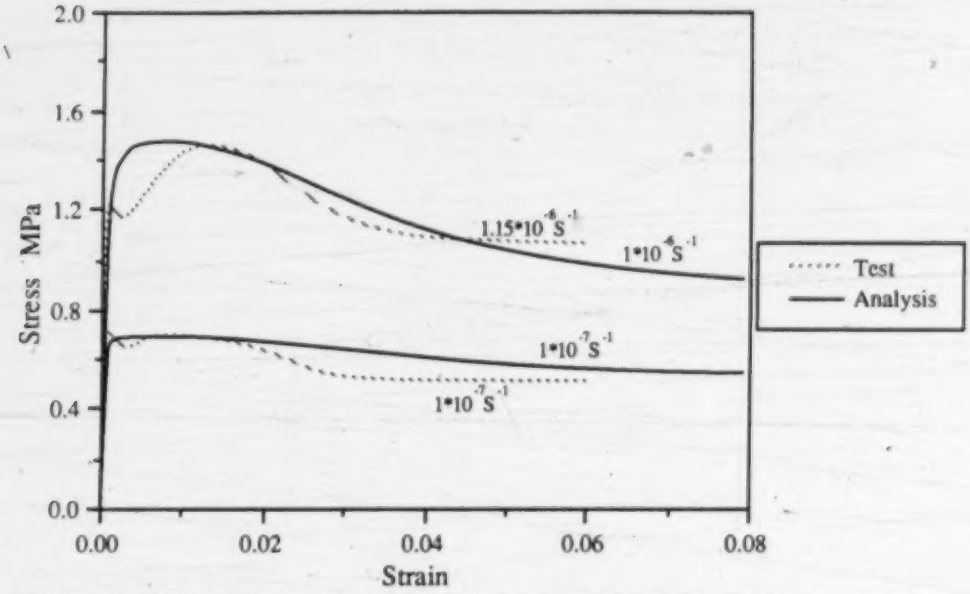

Figure 5.12 The stress-strain curve of constant strain rate compression for both analytical and Mellor and Cole's test result. (Modified from Mellor and Cole, 1982)

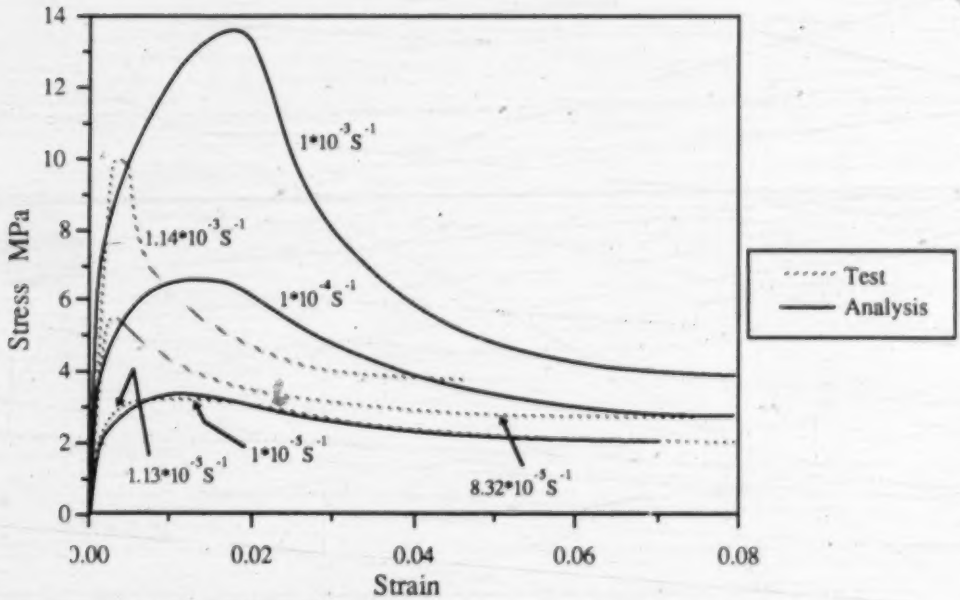

Figure 5.13 The stress-strain curve of constant strain rate compression for both analytical and Mellor and Cole's test result. (Modified from Mellor and Cole, 1982)

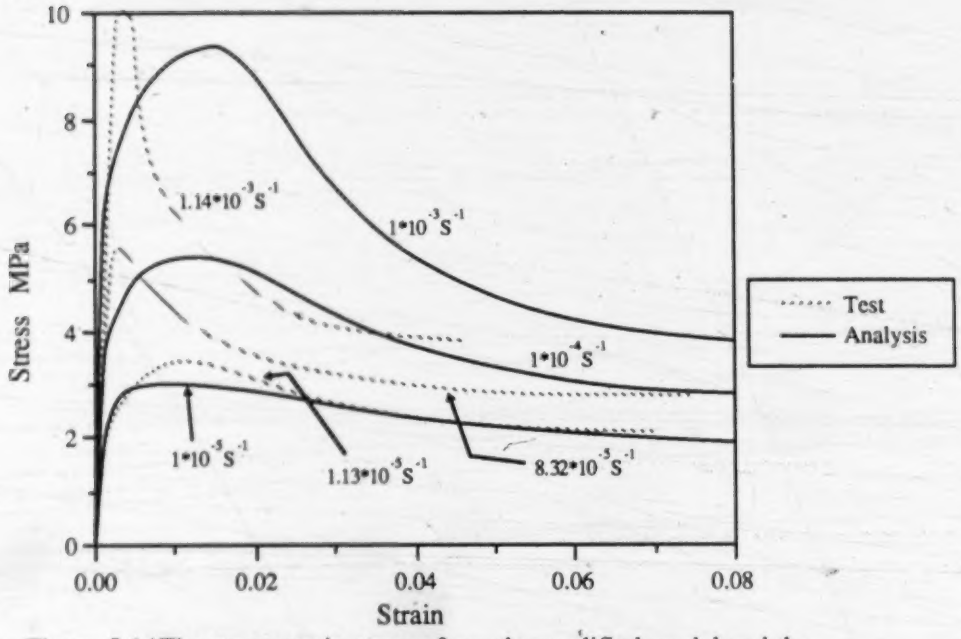

Figure 5.14 The stress-strain curves from the modified model and the experiment for Mellor and Cole's constant strain rate test. (Modified from Mellor and Cole, 1982)

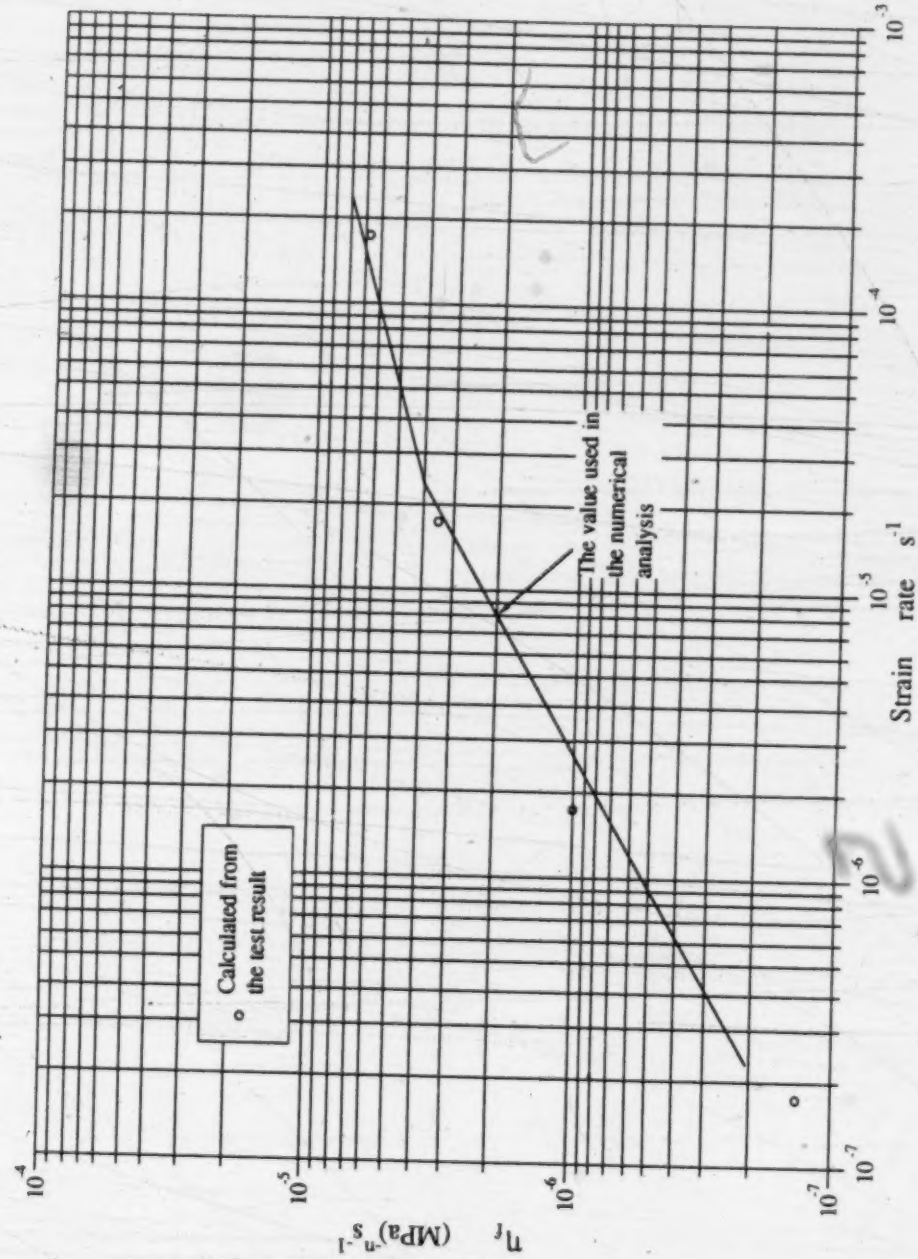

Figure 5.15 Relationship between η_f versus constant strain rate compression for Frederking's test. Modified from Ferderking, 1977)

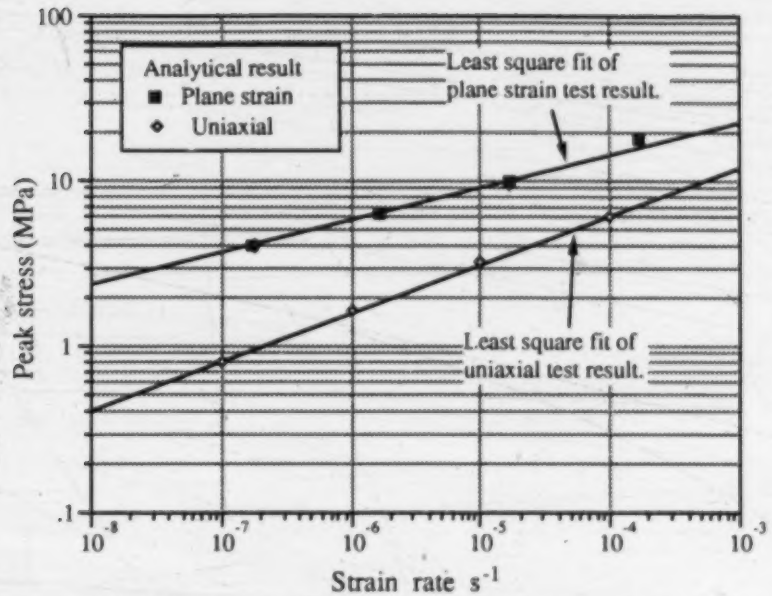

Figure 5.16 The analytical and experimental peak stress versus strain rate plot for both Frederking's plane strain and uniaxial tests. (Modified from Frederking, 1977)

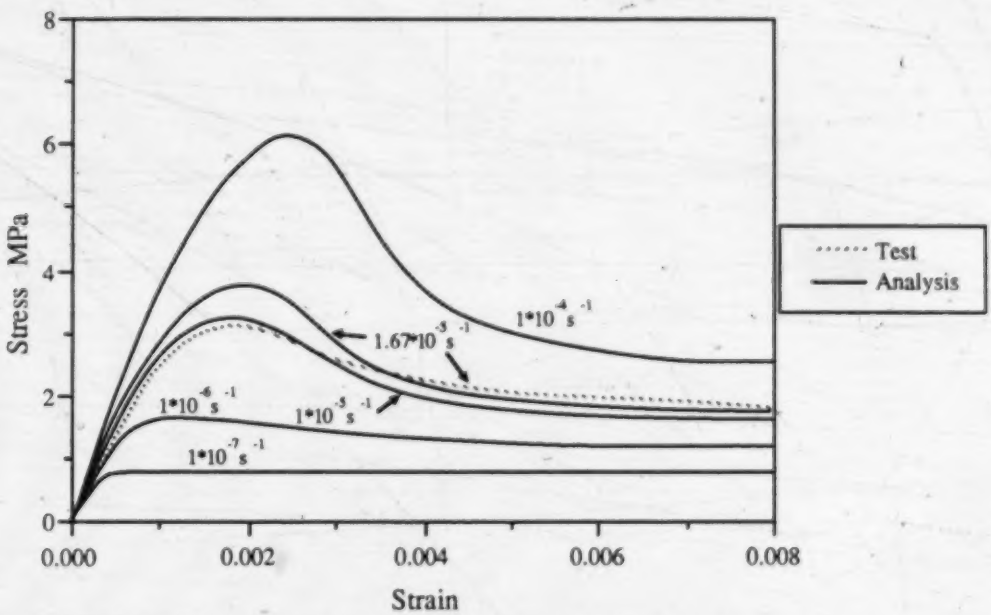

Figure 5.17 The stress-strain curves of uniaxial constant strain rate compression for both the analytical and Frederking's test. (Modified from Frederking, 1977)

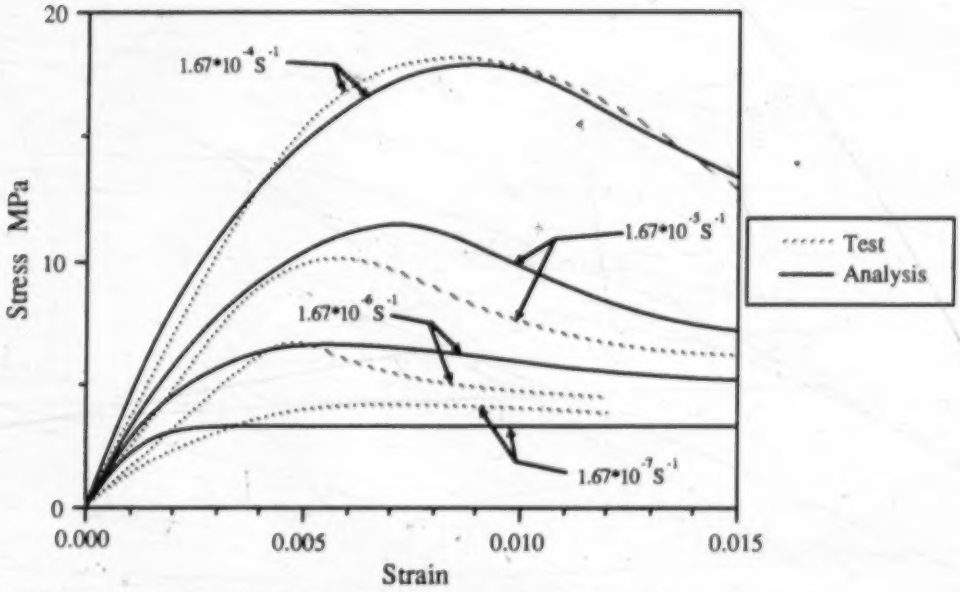

Figure 5.18 The stress-strain curves of plane strain compression for both the analytical and Frederking's test. (Modified from Frederking, 1977)

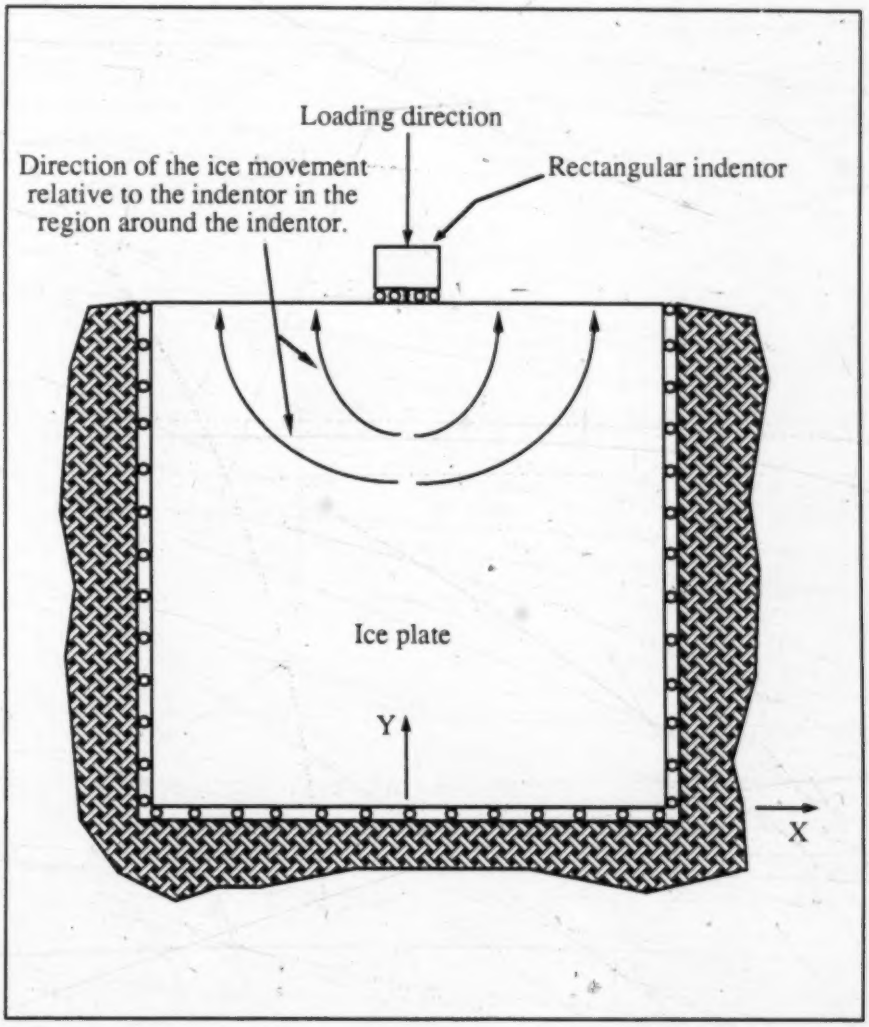

Figure 5.19 Boundary condition for modelling Michel and Toussaint's ice indentation.

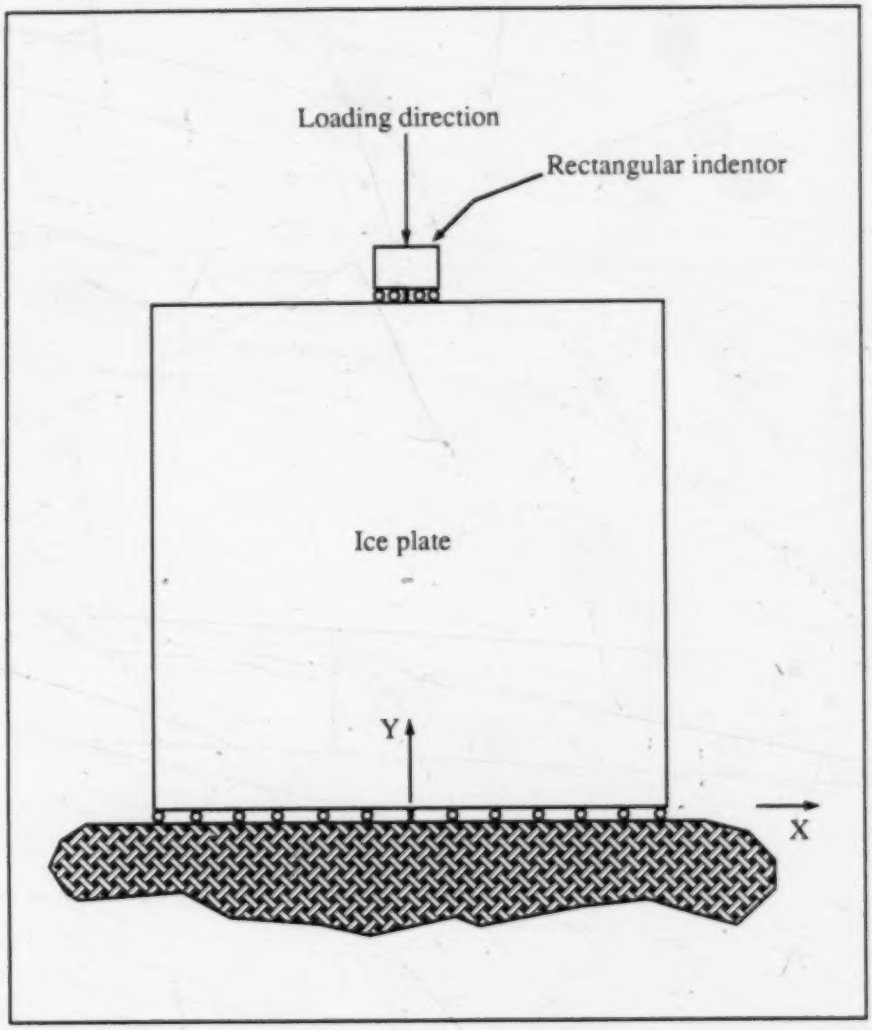

Figure 5.20 Boundary condition for modelling Frederking and Gold's ice indentation.

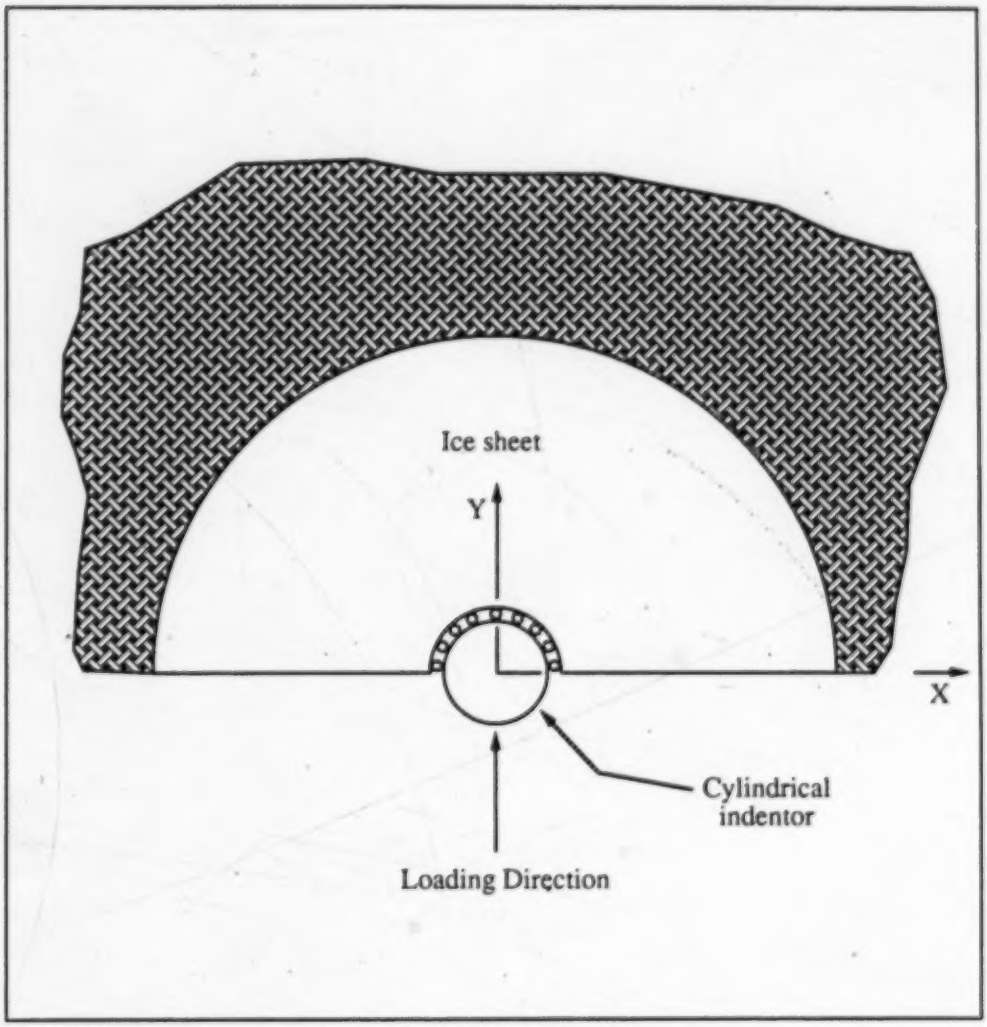

Figure 5.21 Boundary condition for modelling ice indentation against a cylindrical indentor.

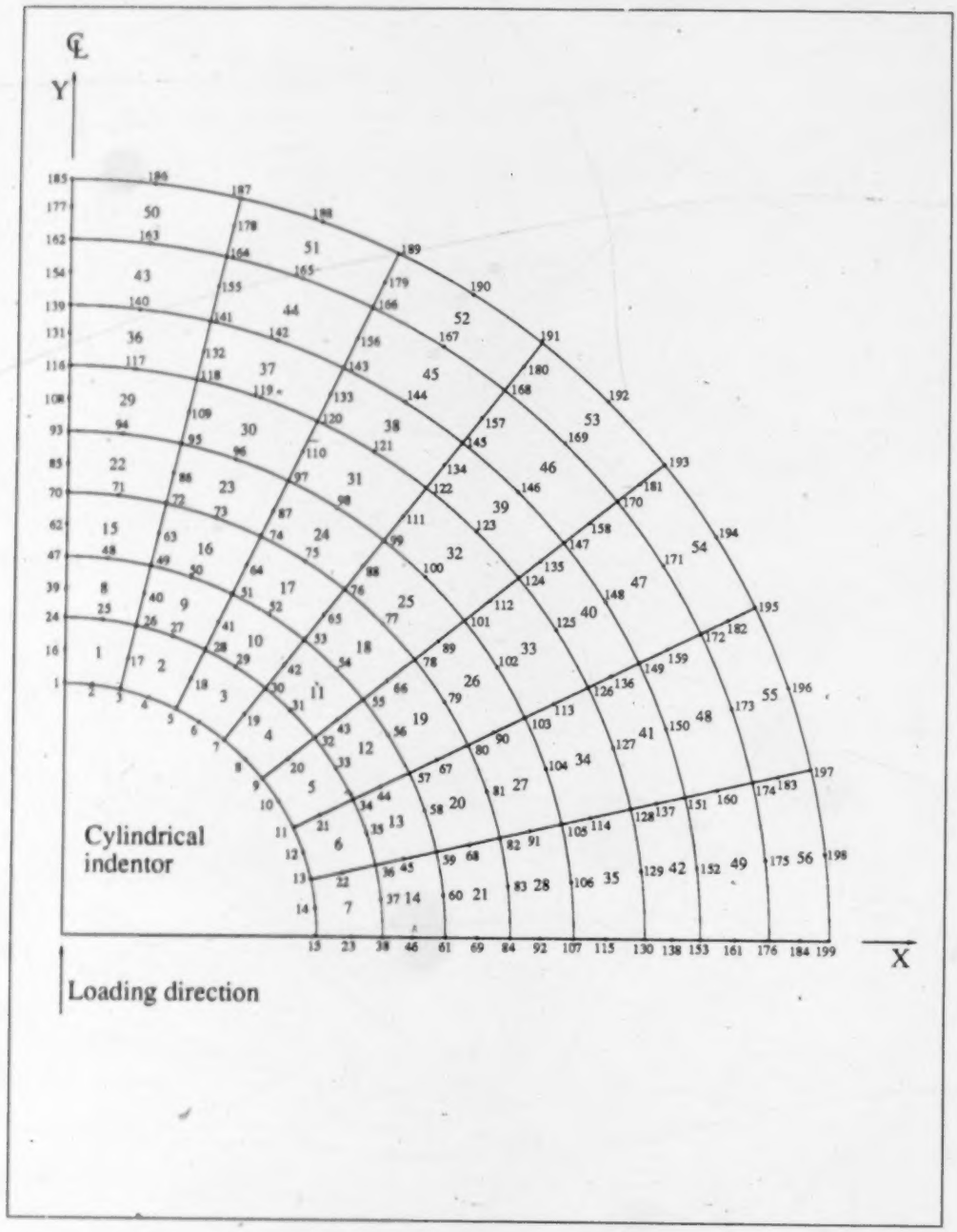

Figure 5.22 The numbering system for the finite element mesh in the ice indentation analysis for a cylindrical indentor.

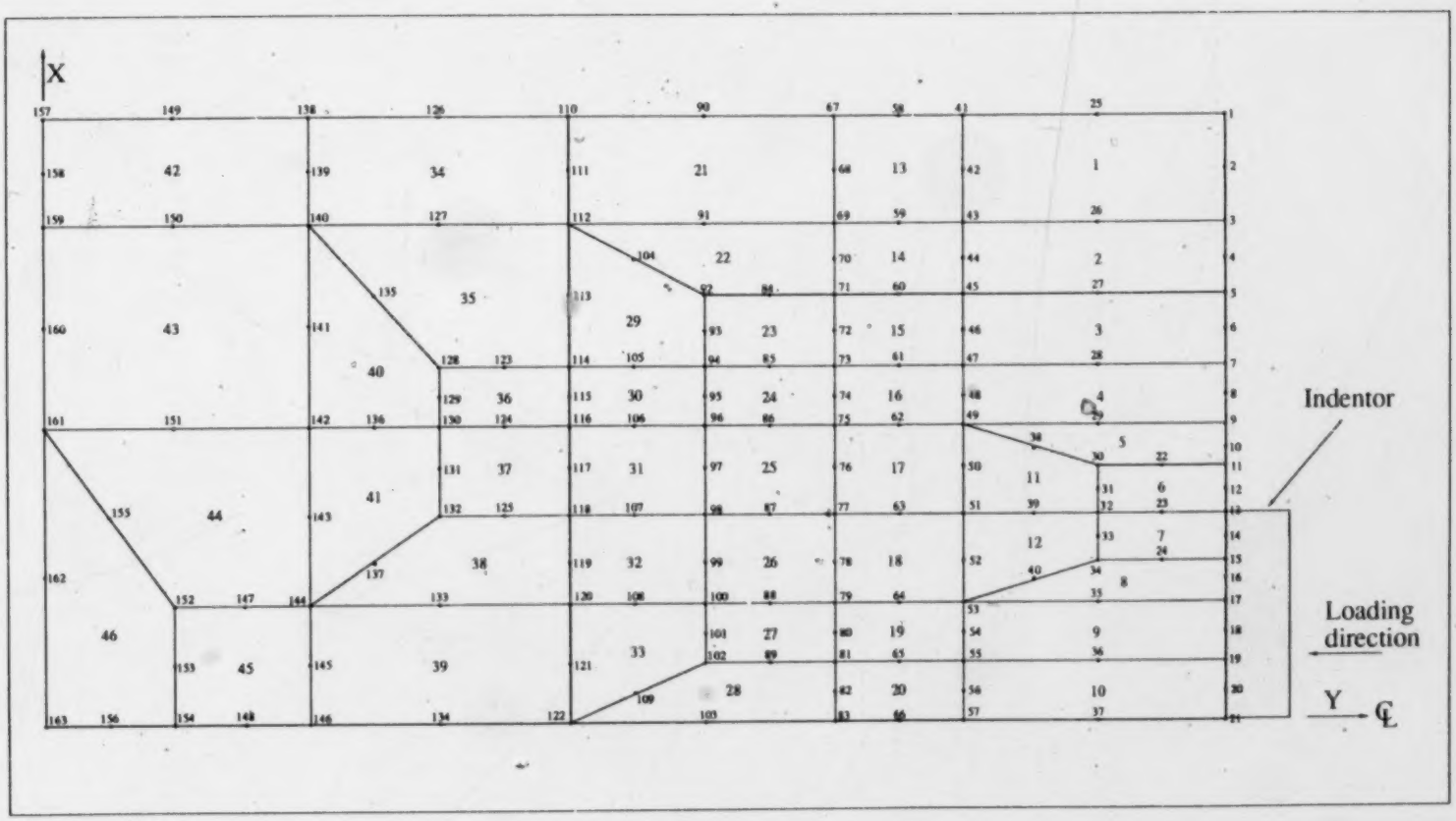

Figure 5.23 The numbering system for the finite element mesh in the ice indentation analysis for Michel and Toussaint's test.

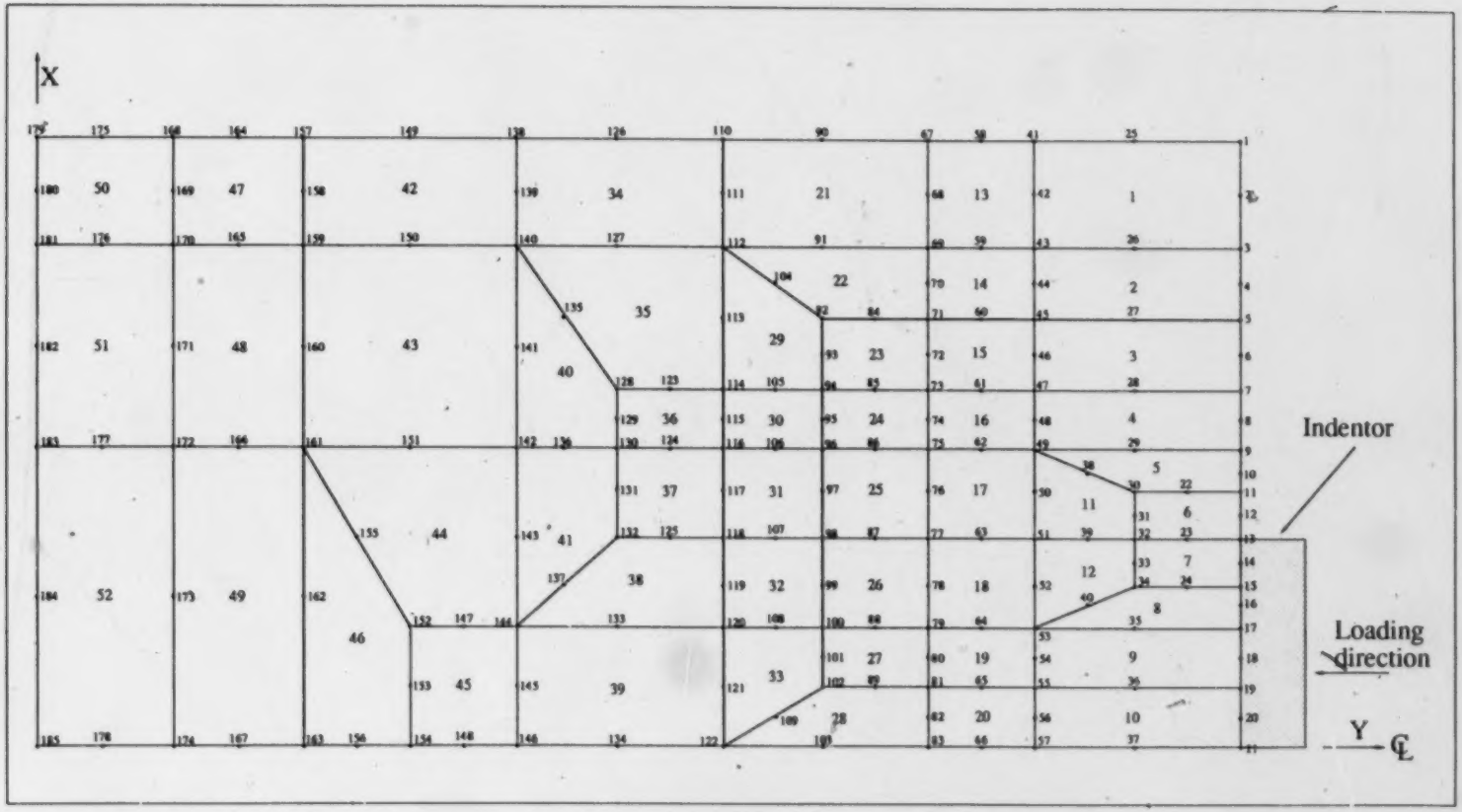

Figure 5.24 The numbering system for the finite element mesh in the ice indentation analysis for Frederking and Gold's test.

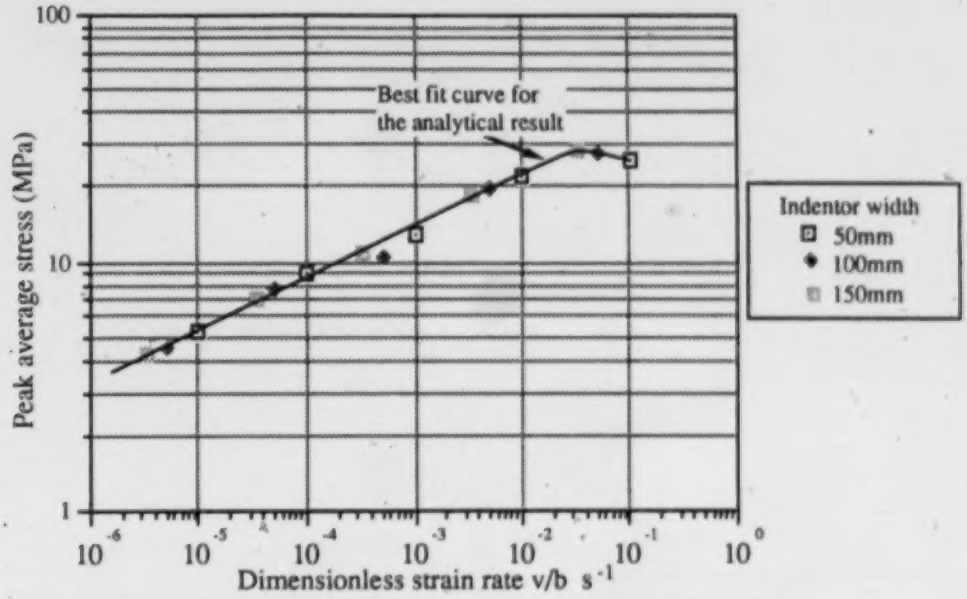

Figure 5.25 Analytical peak average stress at different v/b for Michel and Toussaint's test.

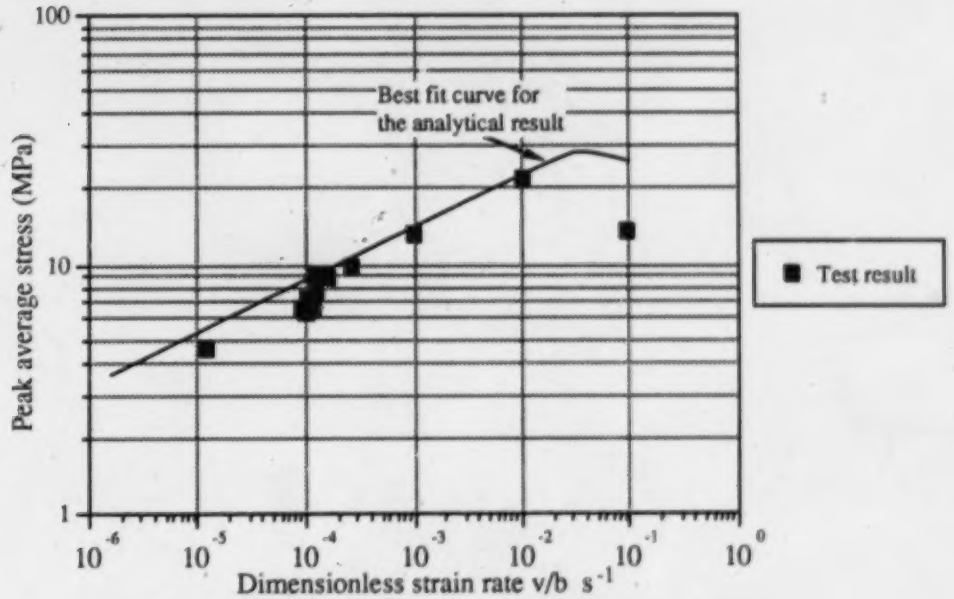

Figure 5.26 The peak average stress at different v/b from Michel and Toussaint's test and the best fit curve of the analytical result.(Modified from Michel and Toussaint, 1977)

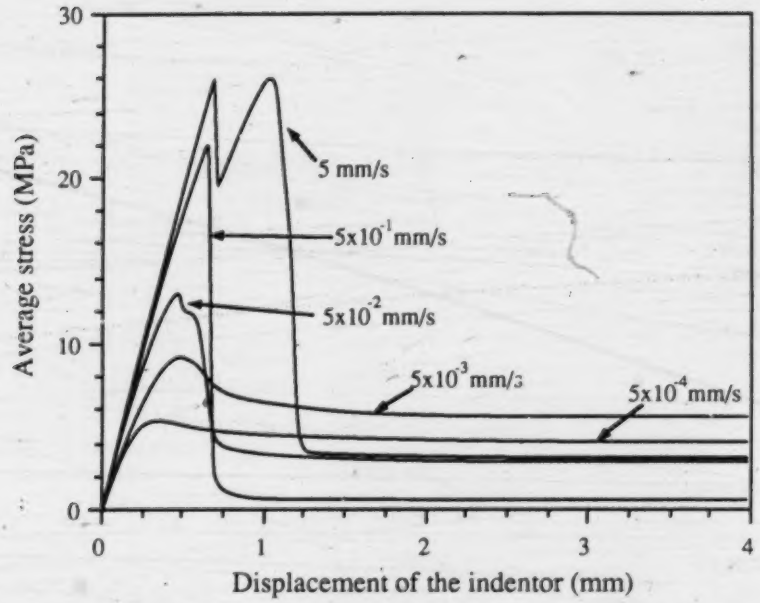

Figure 5.27 Analytical average stress versus indentor displacement with 50mm indentor for Michel and Toussaint's test.

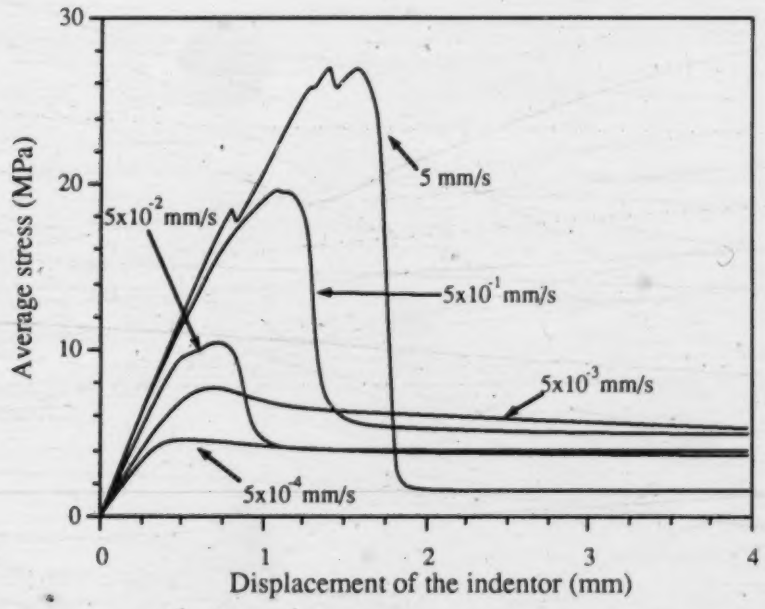

Figure 5.28 Analytical average stress versus indentor displacement with 100mm indentor for Michel and Toussaint's test.

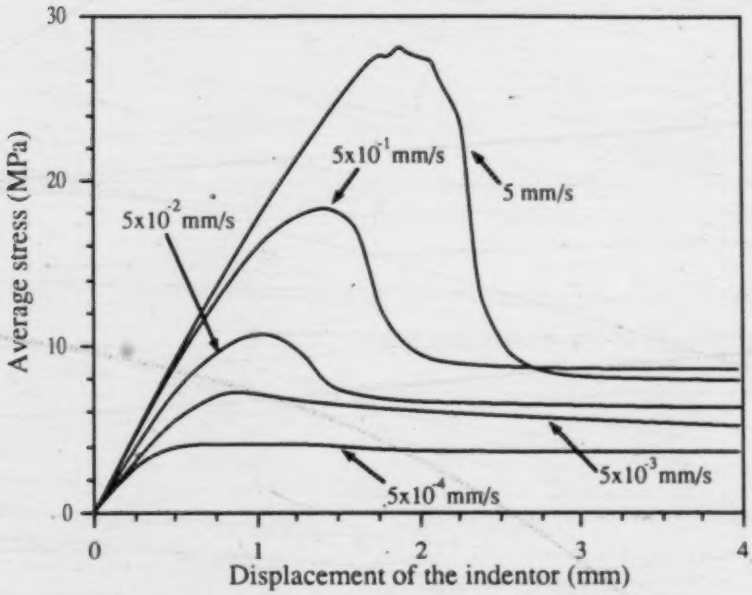

Figure 5.29 Analytical average stress versus indentor displacement with 150mm indentor for Michel and Toussaint's test.

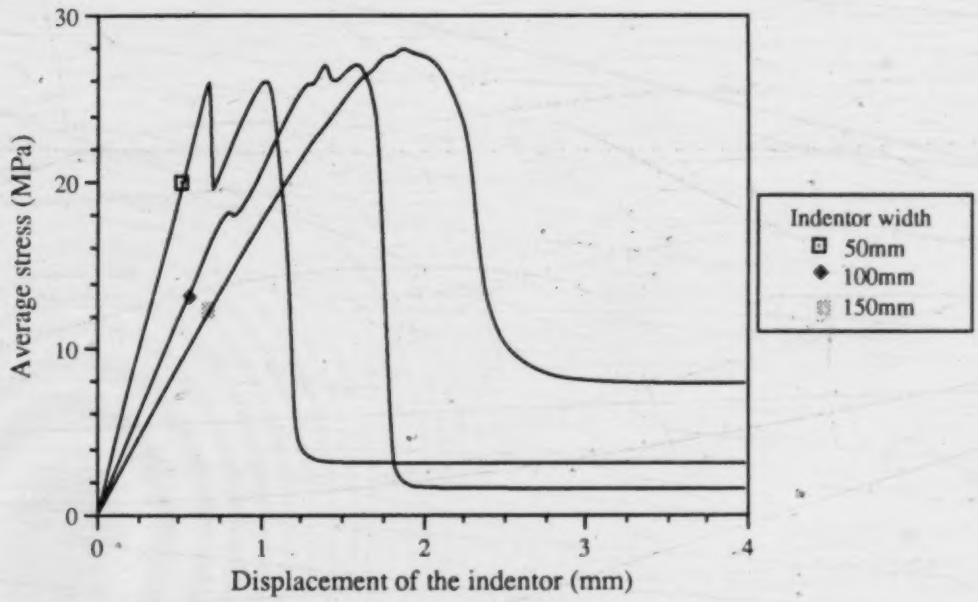

Figure 5.30 Analytical average stress versus indentor displacement at 5mm/s for Michel and Toussaint's test.

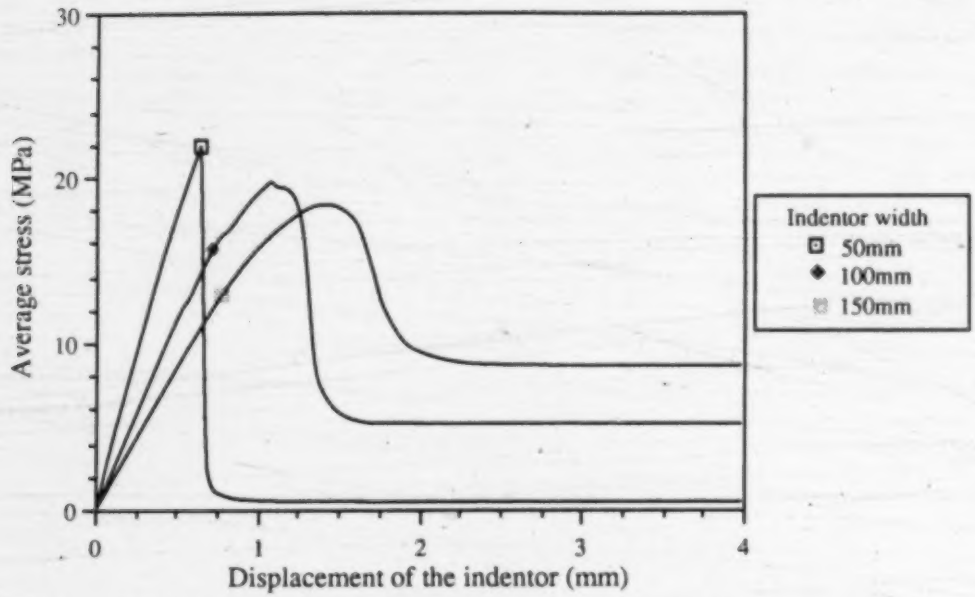

Figure 5.31 Analytical average stress versus indentor displacement at $5x10^{-1}$mm/s for Michel and Toussaint's test.

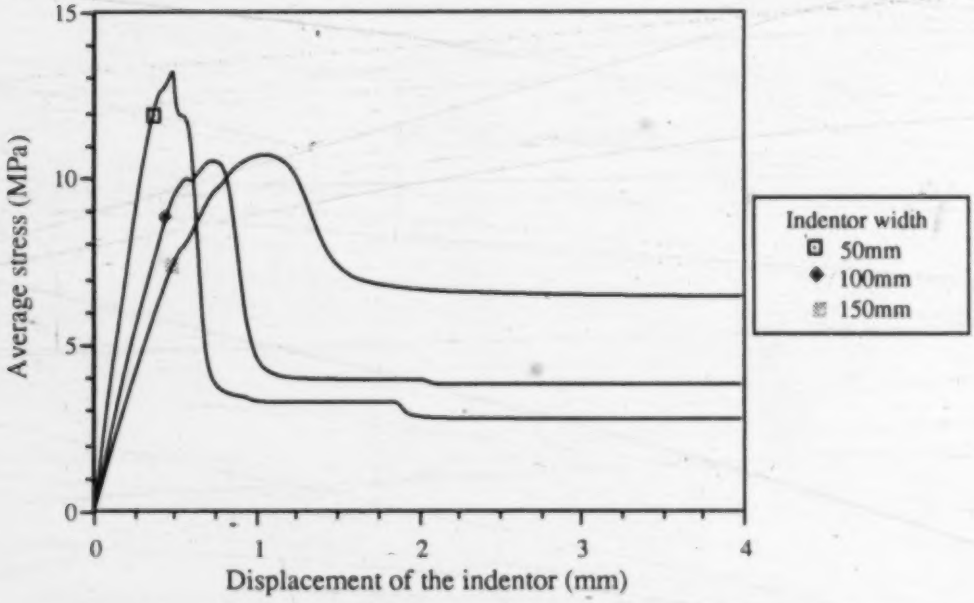

Figure 5.32 Analytical average stress versus indentor displacement at $5x10^{-2}$mm/s for Michel and Toussaint's test.

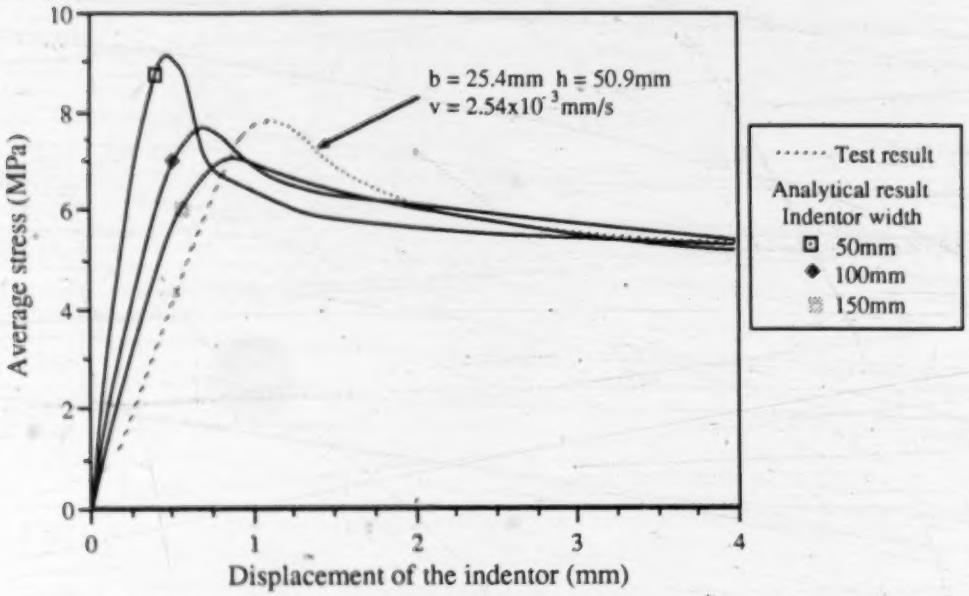

Figure 5.33 Analytical average stress versus indentor dis placement at $5x10^{-3}$mm/s together with an experimental curve for Michel and Toussaint's test. (Modified from Michel and Toussaint, 1977)

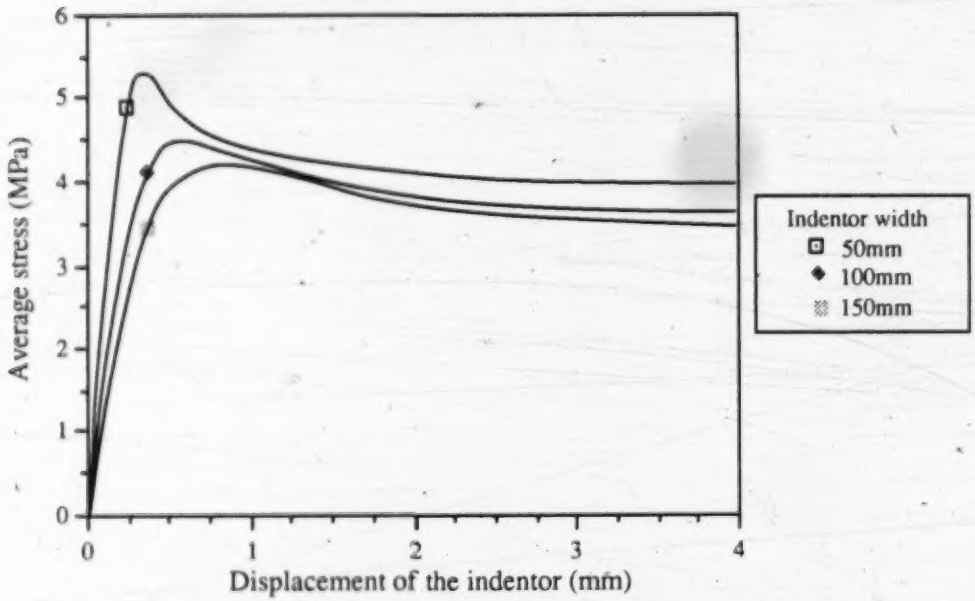

Figure 5.34 Analytical average stress versus indentor displacement at $5x10^{-4}$mm/s for Michel and Toussaint's test.

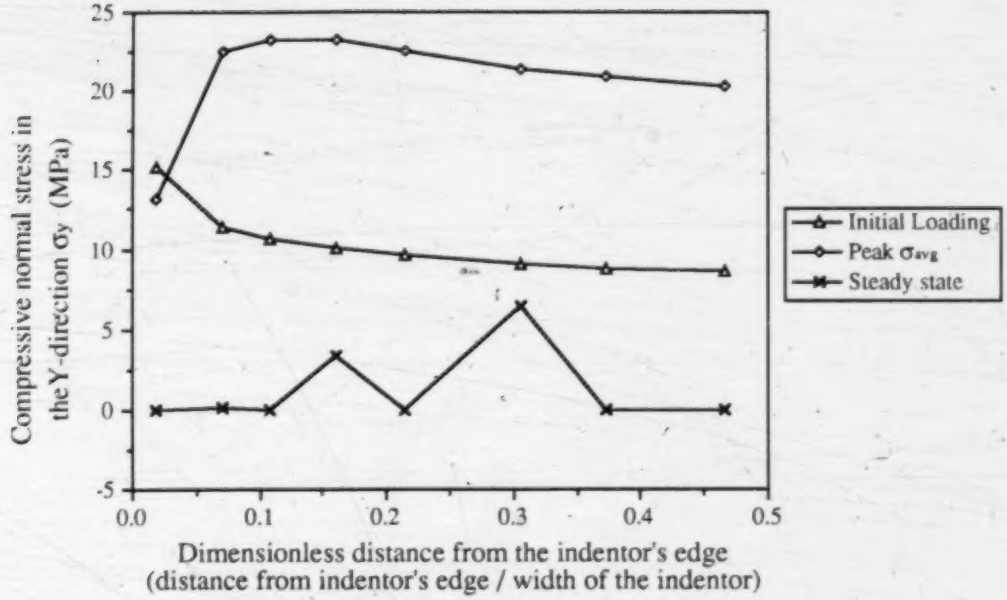

Figure 5.35 Normal stress σ_y along the 50mm rectangular indentor at $5*10^{-1}$ mm/s with 2x2 Gaussian integration.

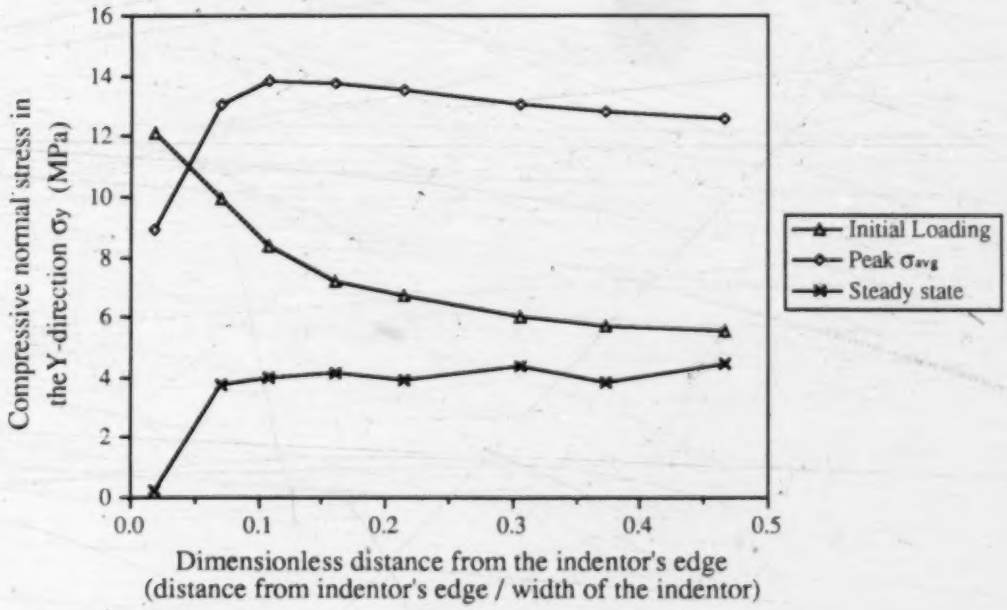

Figure 5.36 Normal stress σ_y along the 50mm rectangular indentor at $5*10^{-2}$ mm/s with 2x2 Gaussian integration.

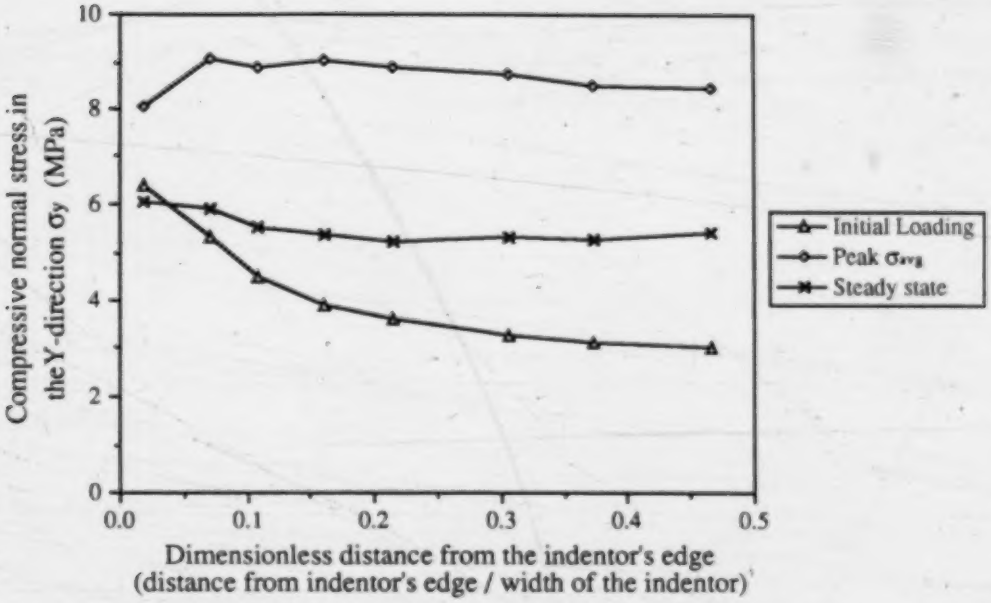
Compressive normal stress in the Y-direction σy (MPa)
Dimensionless distance from the indentor's edge
(distance from indentor's edge / width of the indentor)
Initial Loading
Peak σavg
Steady state

Figure 5.37 Normal stress σ_y along the 50mm rectangular indentor at $5*10^{-3}$ mm/s with 2x2 Gaussian integration.

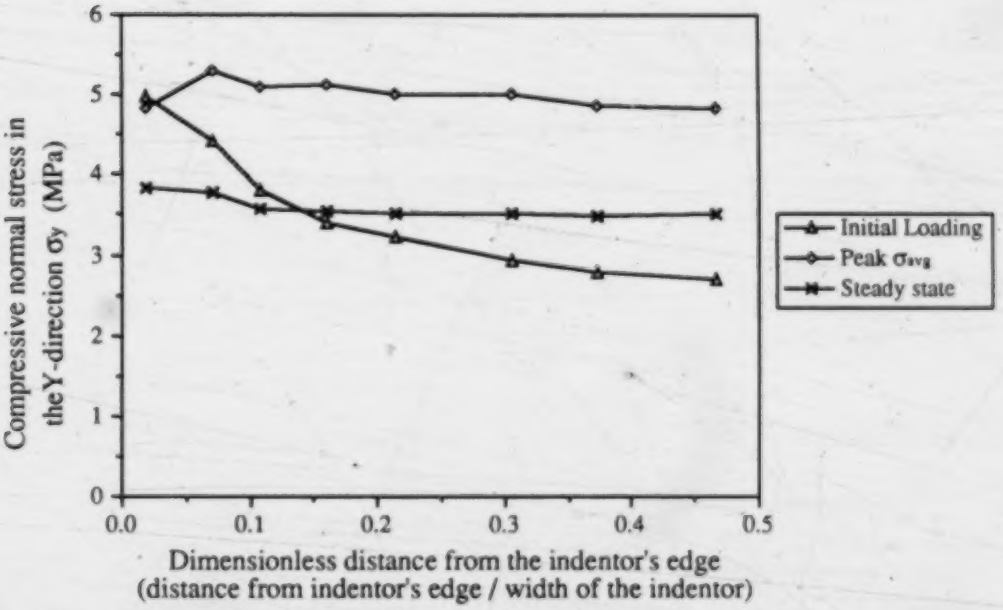
Compressive normal stress in the Y-direction σy (MPa)
Dimensionless distance from the indentor's edge
(distance from indentor's edge / width of the indentor)
Initial Loading
Peak σavg
Steady state

Figure 5.38 Normal stress σ_y along the 50mm rectangular indentor at $5*10^{-4}$ mm/s with 2x2 Gaussian integration.

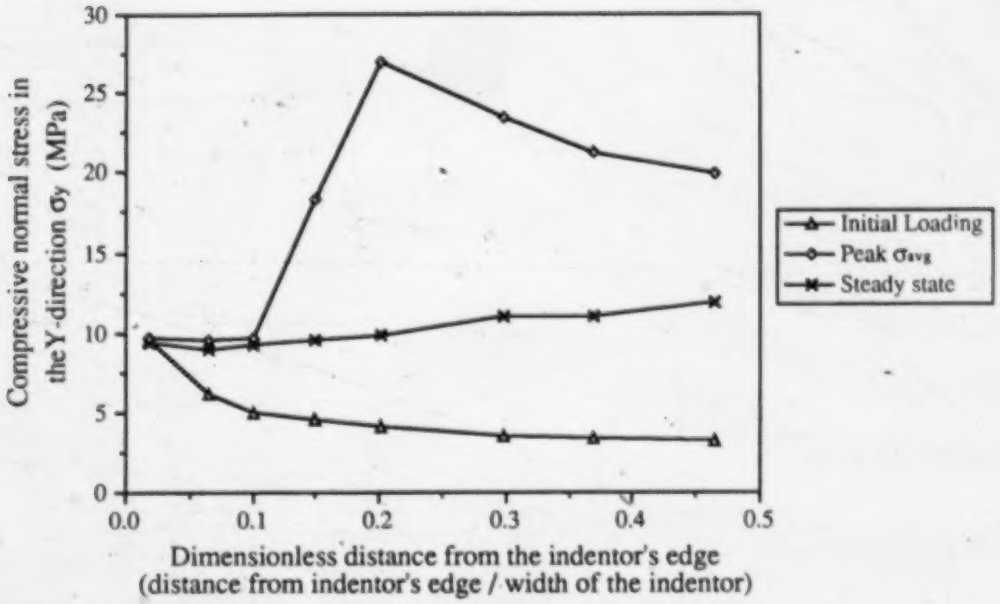

Figure 5.39 Normal stress σ_y along the 150mm rectangular indentor at $5*10^{-1}$ mm/s with 2x2 Gaussian integration.

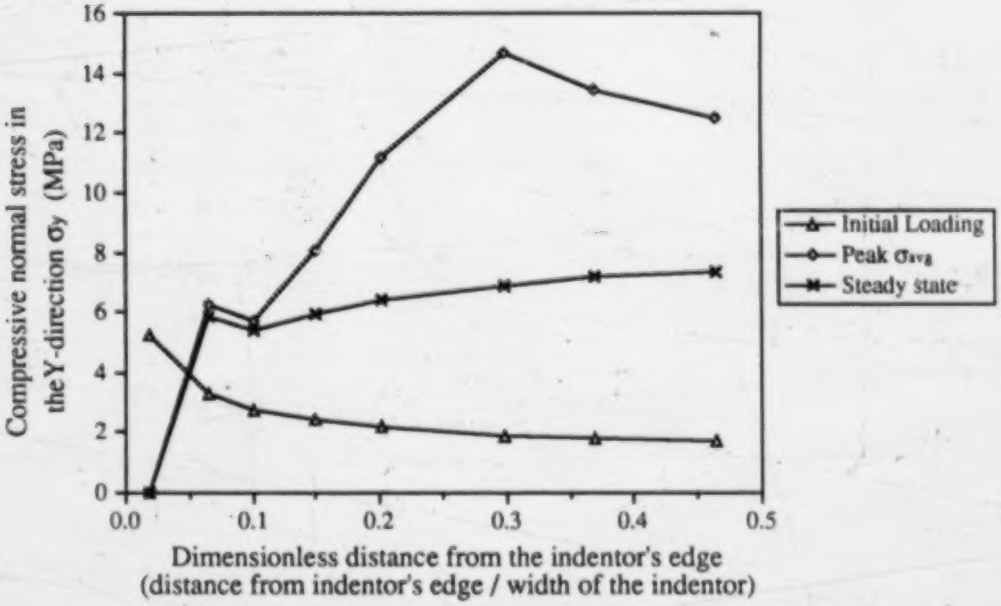

Figure 5.40 Normal stress σ_y along the 150mm rectangular indentor at $5*10^{-2}$ mm/s with 2x2 Gaussian integration.

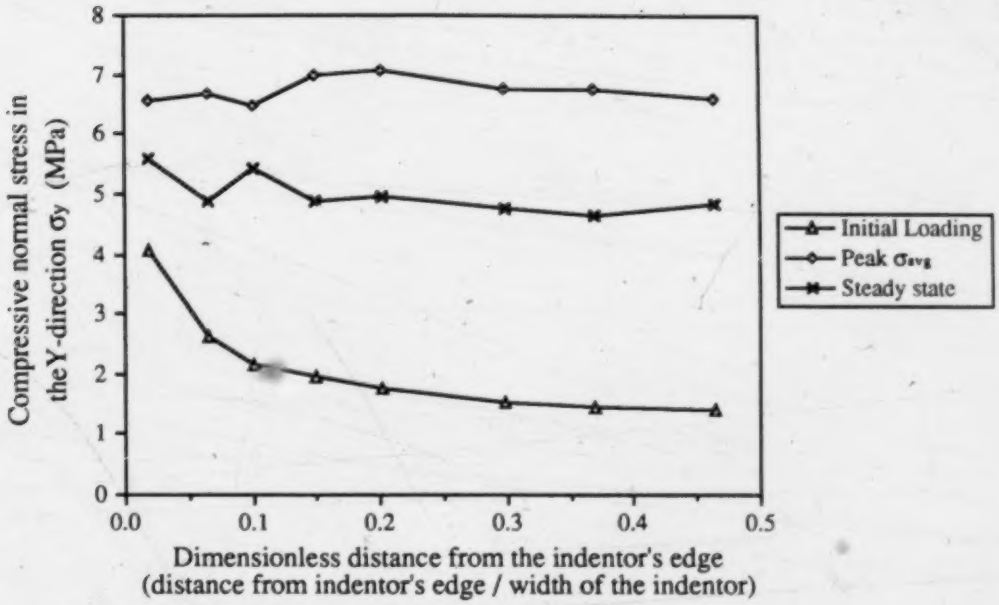
Compressive normal stress in the Y-direction σy (MPa)
Dimensionless distance from the indentor's edge
(distance from indentor's edge / width of the indentor)
Initial Loading
Peak σavg
Steady state

Figure 5.41 Normal stress σ_y along the 150mm rectangular indentor at $5*10^{-3}$ mm/s with 2x2 Gaussian integration.

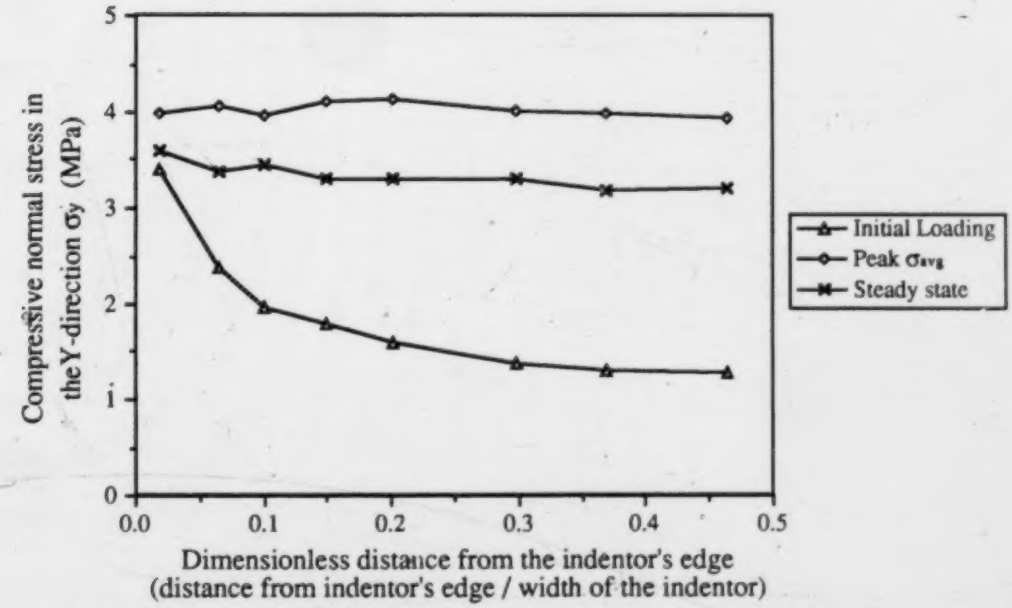
Compressive normal stress in the Y-direction σy (MPa)
Dimensionless distance from the indentor's edge
(distance from indentor's edge / width of the indentor)
Initial Loading
Peak σavg
Steady state

Figure 5.42 Normal stress σ_y along the 150mm rectangular indentor at $5*10^{-4}$ mm/s with 2x2 Gaussian integration.

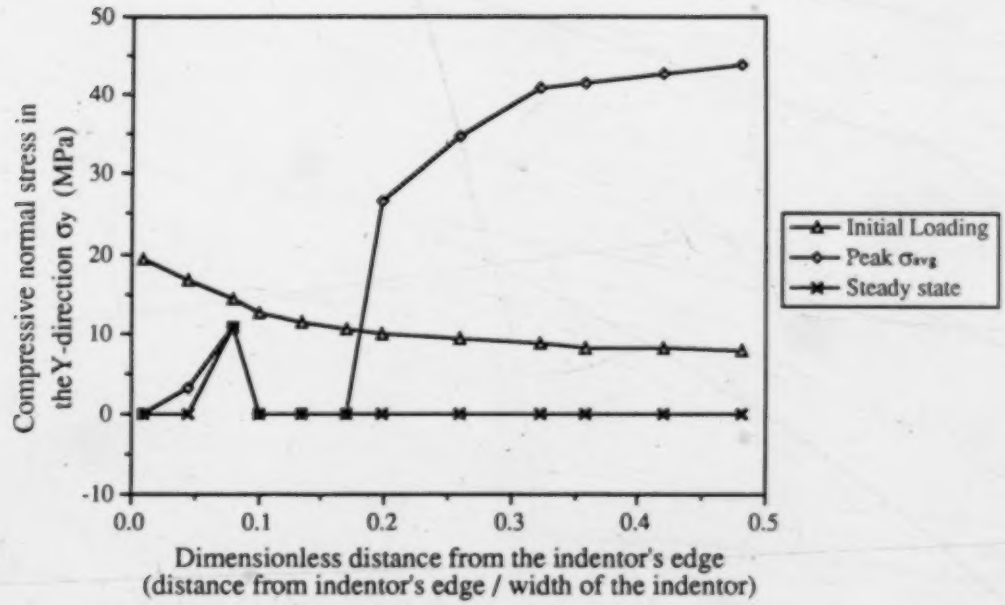

Figure 5.43 Normal stress σ_y along the 50mm rectangular indentor at 5mm/s with 3x3 Gaussian integration.

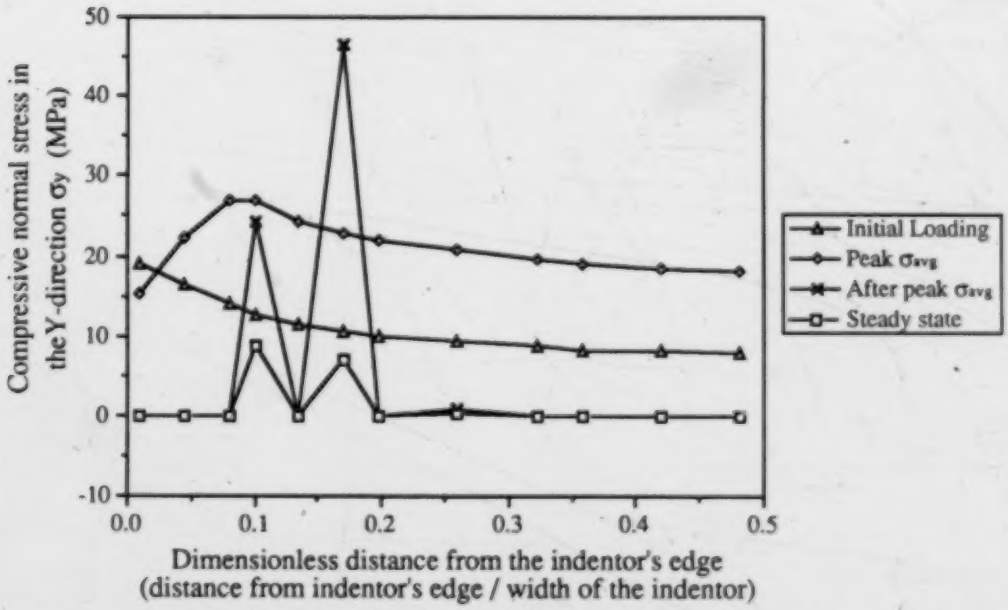

Figure 5.44 Normal stress σ_y along the 50mm rectangular indentor at $5*10^{-1}$ mm/s with 3x3 Gaussian integration.

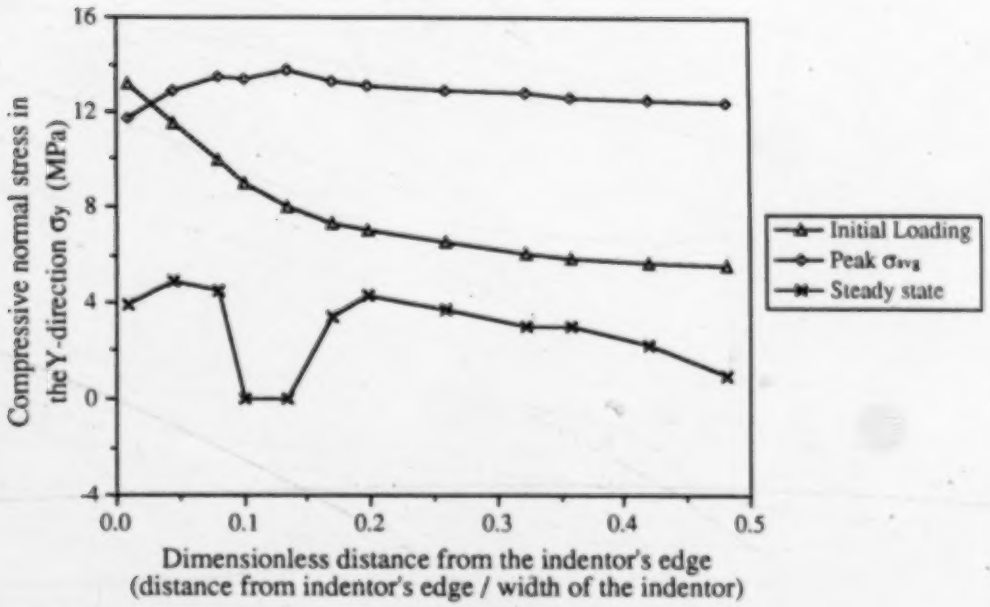

Figure 5.45 Normal stress σ_y along the 50mm rectangular indentor at $5*10^{-2}$ mm/s with 3x3 Gaussian integration.

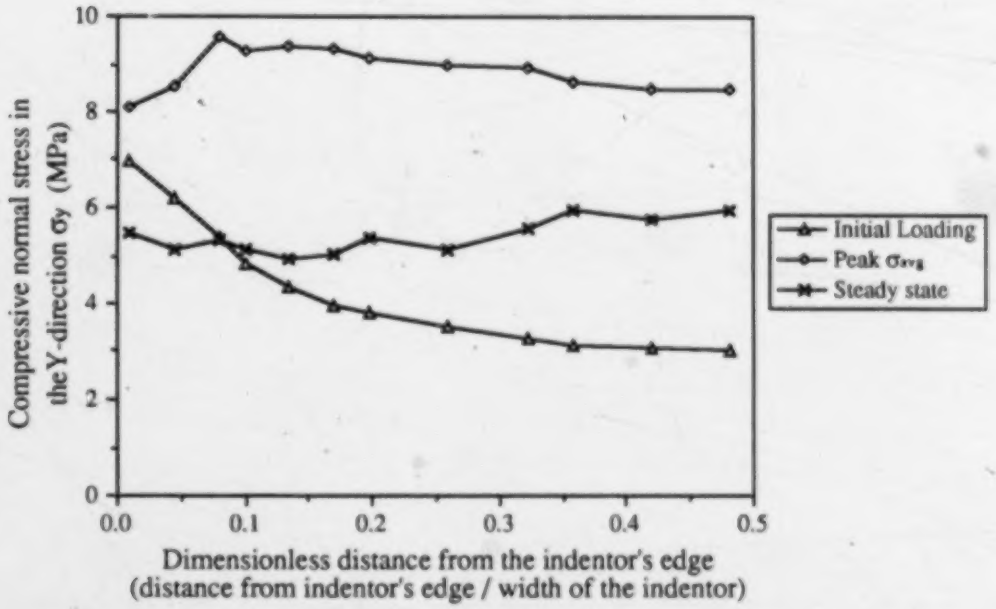

Figure 5.46 Normal stress σ_y along the 50mm rectangular indentor at $5*10^{-3}$ mm/s with 3x3 Gaussian integration.

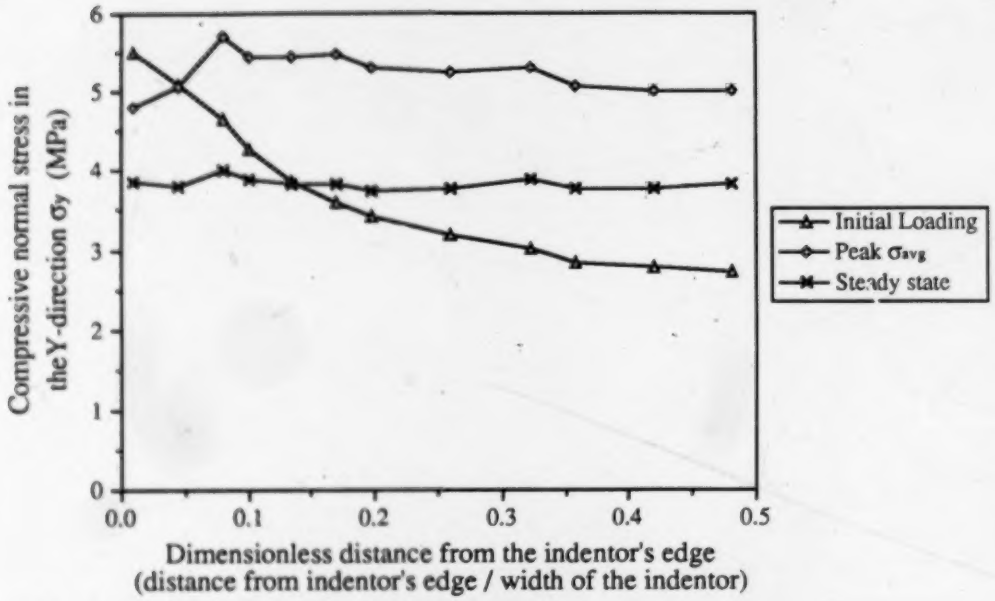
Compressive normal stress in the Y-direction σy (MPa)
Dimensionless distance from the indentor's edge
(distance from indentor's edge / width of the indentor)
Initial Loading
Peak σavg
Steady state

Figure 5.47 Normal stress σ_y along the 50mm rectangular indentor at $5*10^{-4}$ mm/s with 3x3 Gaussian integration.

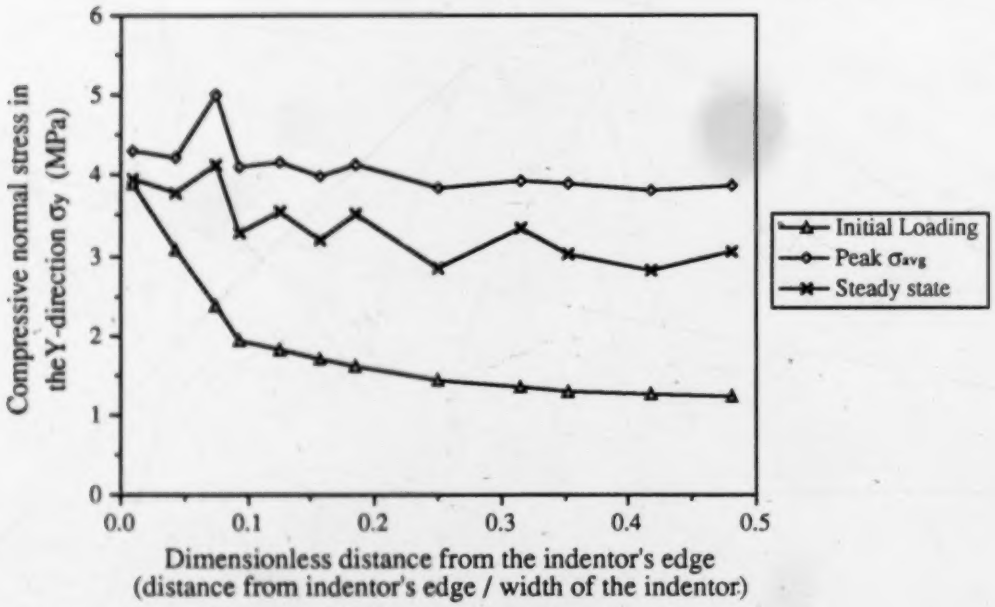
Compressive normal stress in the Y-direction σy (MPa)
Dimensionless distance from the indentor's edge
(distance from indentor's edge / width of the indentor)
Initial Loading
Peak σavg
Steady state

Figure 5.48 Normal stress σ_y along the 150mm rectangular indentor at $5*10^{-4}$ mm/s with 3x3 Gaussian integration.

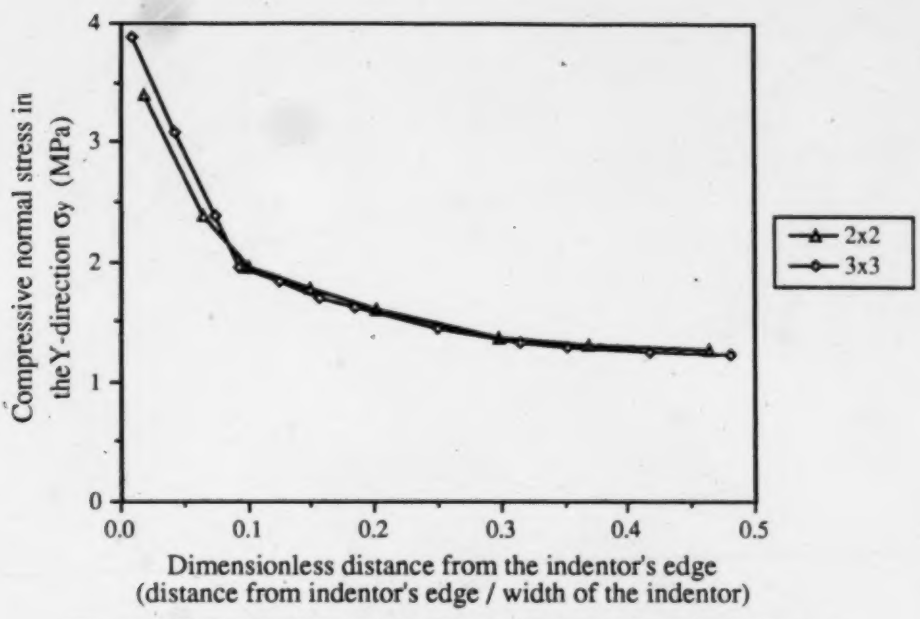

Figure 5.49 Comparison of the normal stress σ_y along the 150mm rectangular indentor at $5*10^{-4}$ mm/s with different Gaussian integration at initial loading.

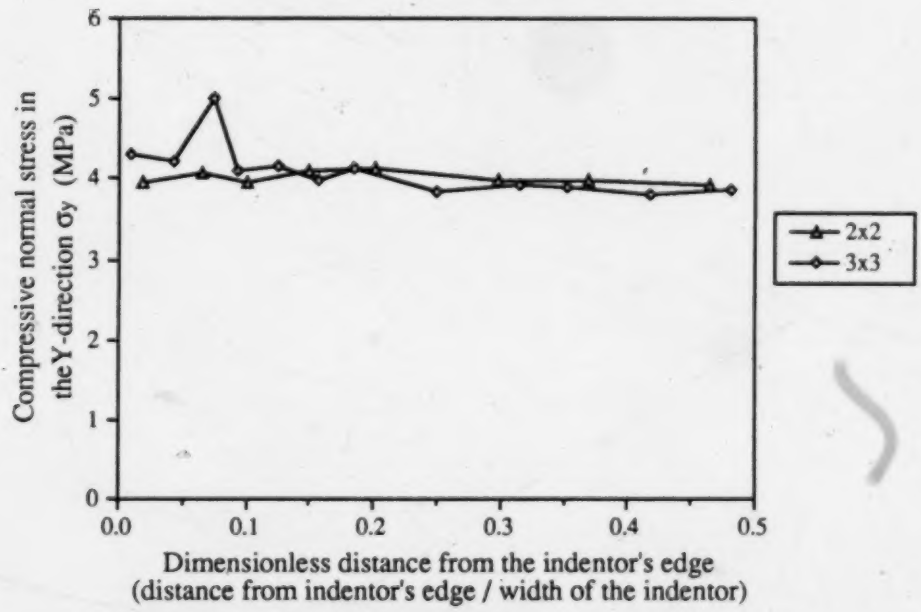

Figure 5.50 Comparison of the normal stress σ_y along the 150mm rectangular indentor at $5*10^{-4}$ mm/s with different Gaussian integration at peak σ_{avg}.

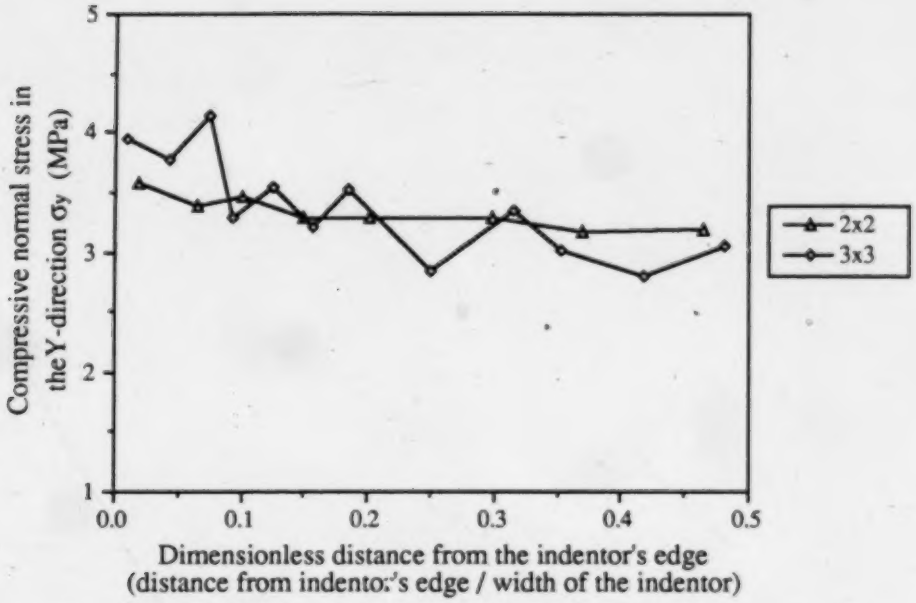

Figure 5.51 Comparison of the normal stress σ_y along the 150mm rectangular indentor at $5*10^{-4}$ mm/s with different Gaussian integration at steady state.

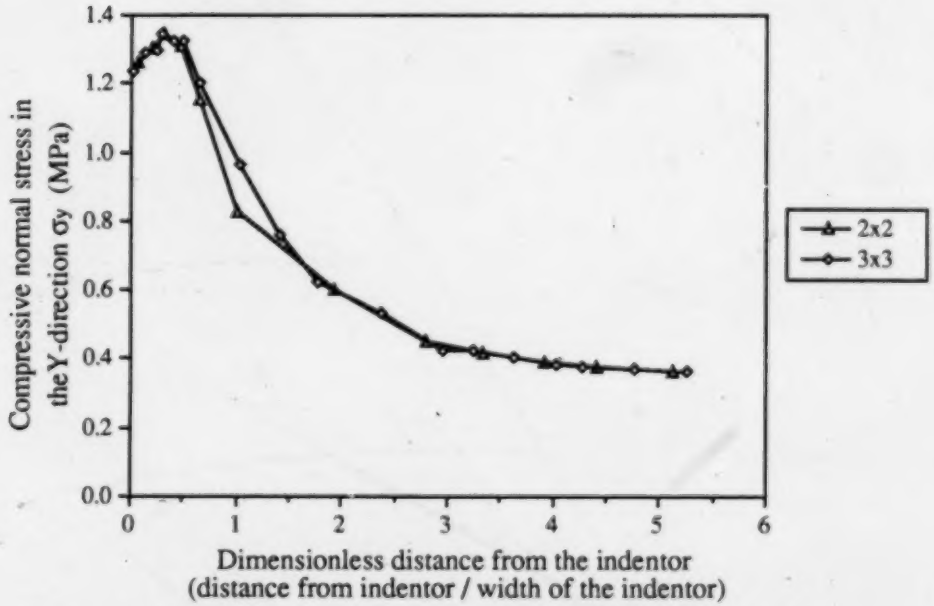

Figure 5.52 Comparison of the normal stress σ_y along Y-axis for the 150mm rectangular indentor at $5*10^{-4}$ mm/s with different Gaussian integration at initial loading.

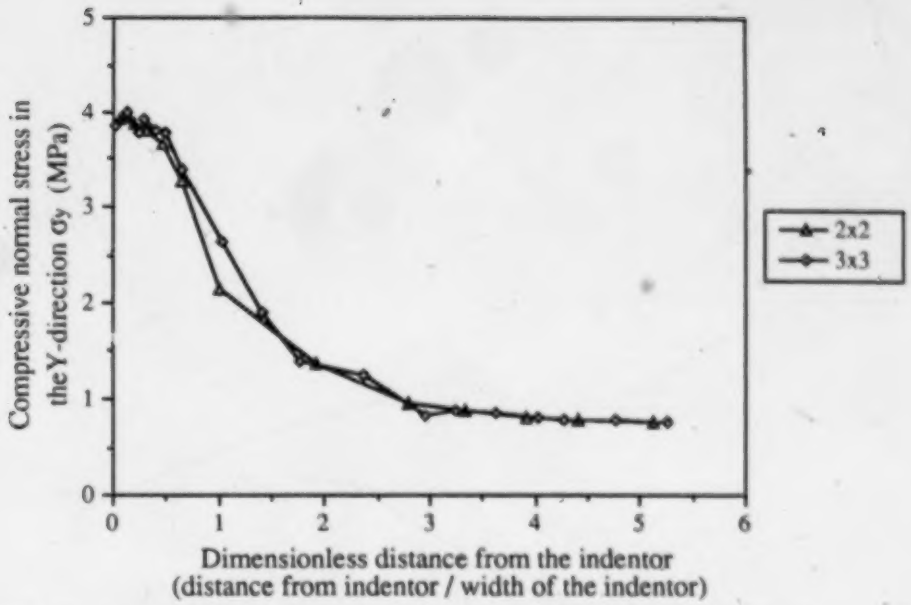
Compressive normal stress in the Y-direction σy (MPa)
Dimensionless distance from the indentor
(distance from indentor / width of the indentor)
2x2
3x3

Figure 5.53 Comparison of the normal stress σ_y along Y-axis for the 150mm rectangular indentor at $5*10^{-4}$ mm/s with different Gaussian integration at peak σ_{avg}.

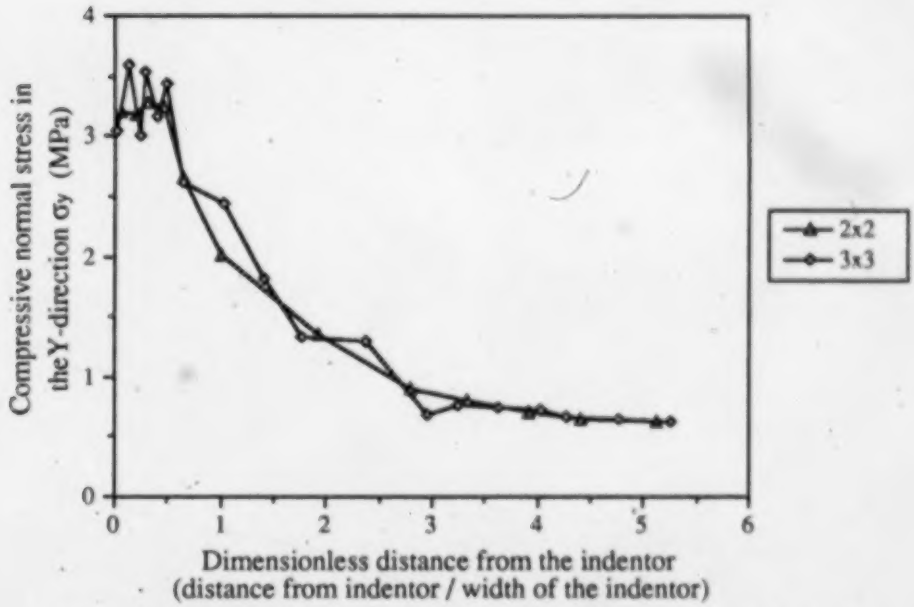
Compressive normal stress in the Y-direction σy (MPa)
Dimensionless distance from the indentor
(distance from indentor / width of the indentor)
2x2
3x3

Figure 5.54 Comparison of the normal stress σ_y along Y-axis for the 150mm rectangular indentor at $5*10^{-4}$ mm/s with different Gaussian integration at steady state.

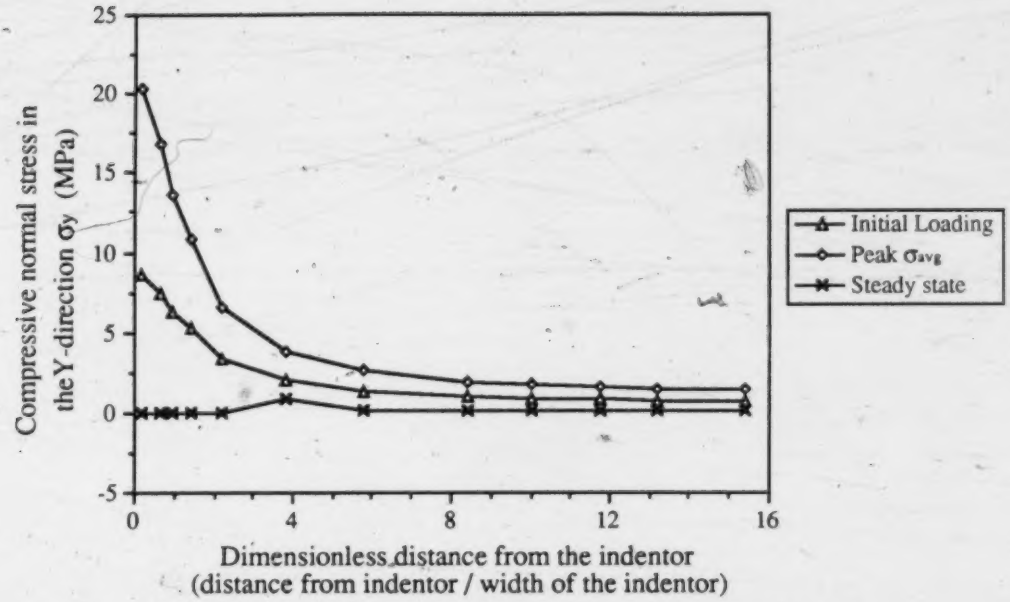

Figure 5.55 Normal stress σ_y along Y-axis for the 50mm rectangular indentor at $5*10^{-1}$ mm/s with 2x2 Gaussian integration.

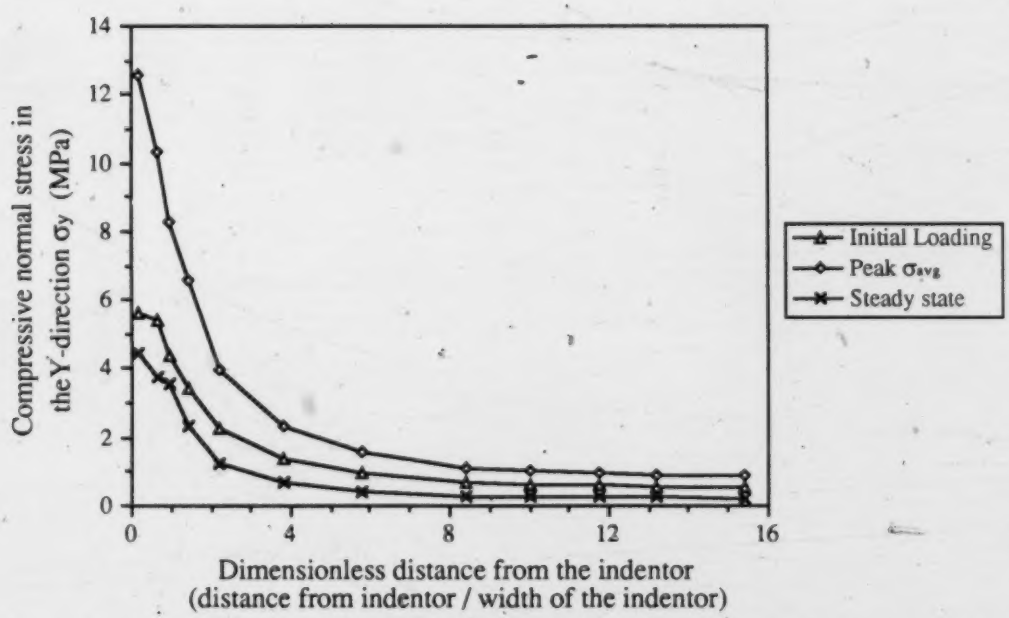

Figure 5.56 Normal stress σ_y along Y-axis for the 50mm rectangular indentor at $5*10^{-2}$ mm/s with 2x2 Gaussian integration.

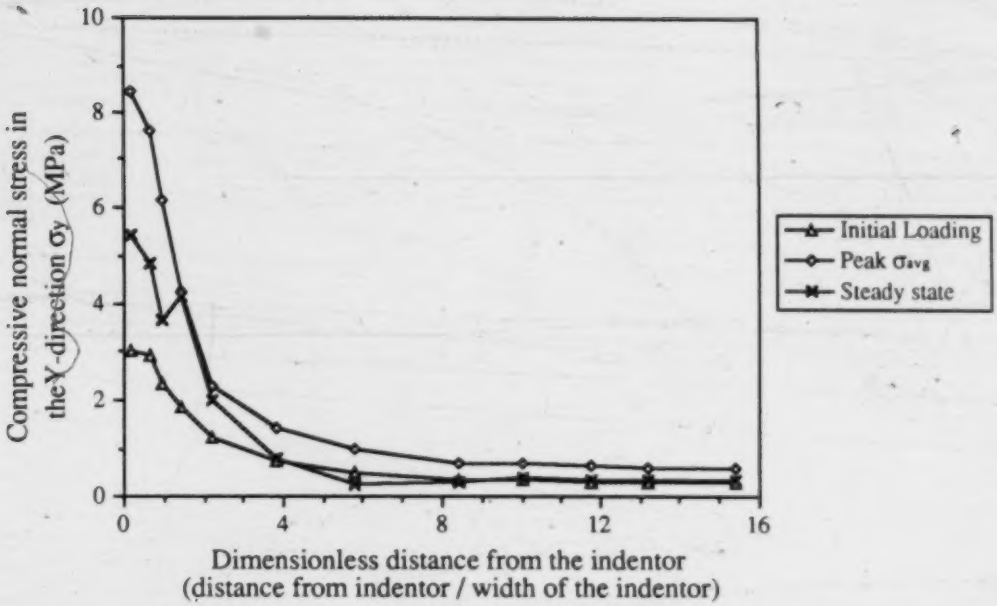

Figure 5.57 Normal stress σ_y along Y-axis for the 50mm rectangular indentor at $5*10^{-3}$ mm/s with 2x2 Gaussian integration.

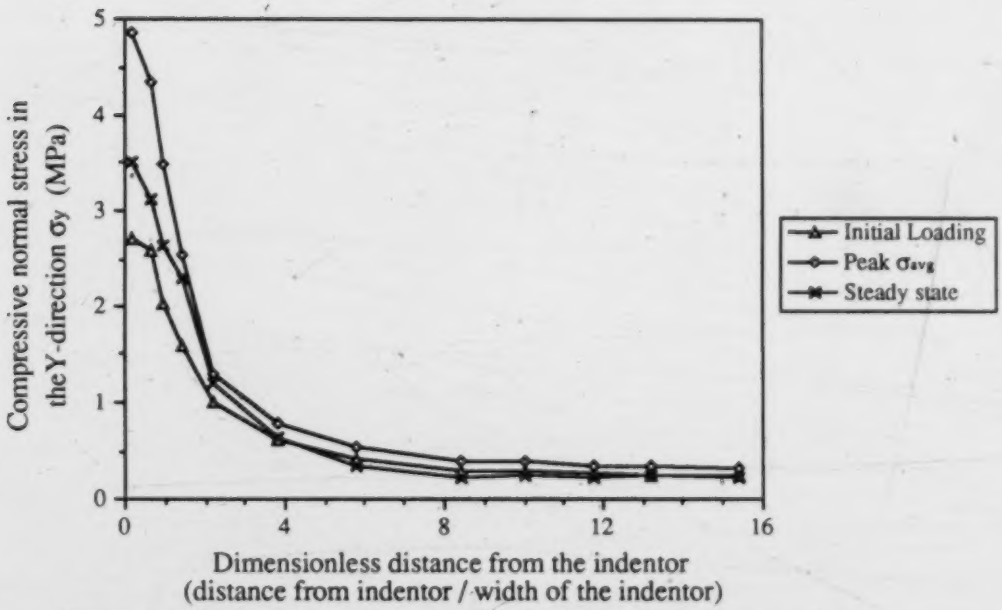

Figure 5.58 Normal stress σ_y along Y-axis for the 50mm rectangular indentor at $5*10^{-4}$ mm/s with 2x2 Gaussian integration.

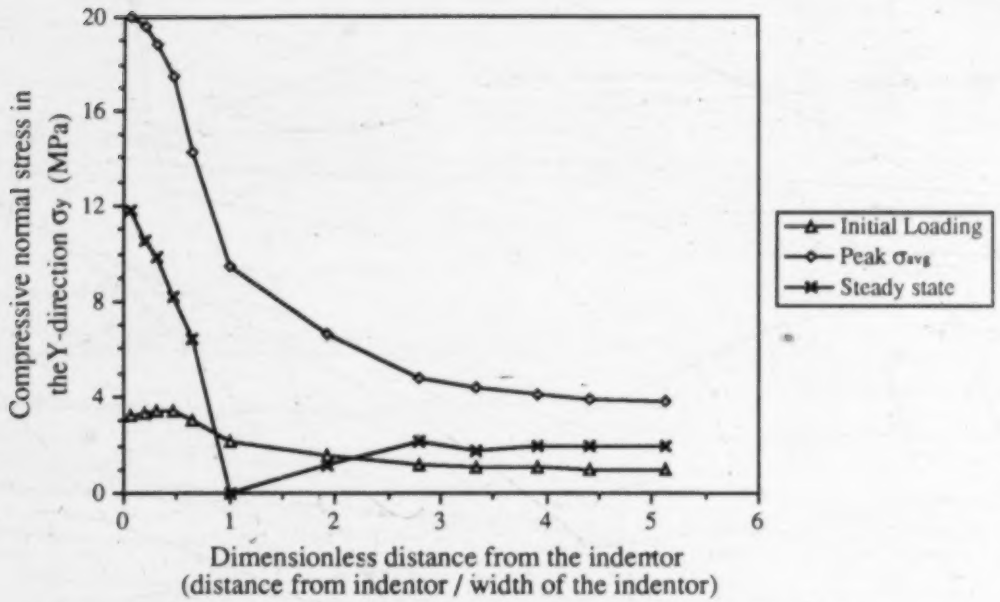

Figure 5.59 Normal stress σ_y along Y-axis for the 150mm rectangular indentor at $5*10^{-1}$ mm/s with 2x2 Gaussian integration.

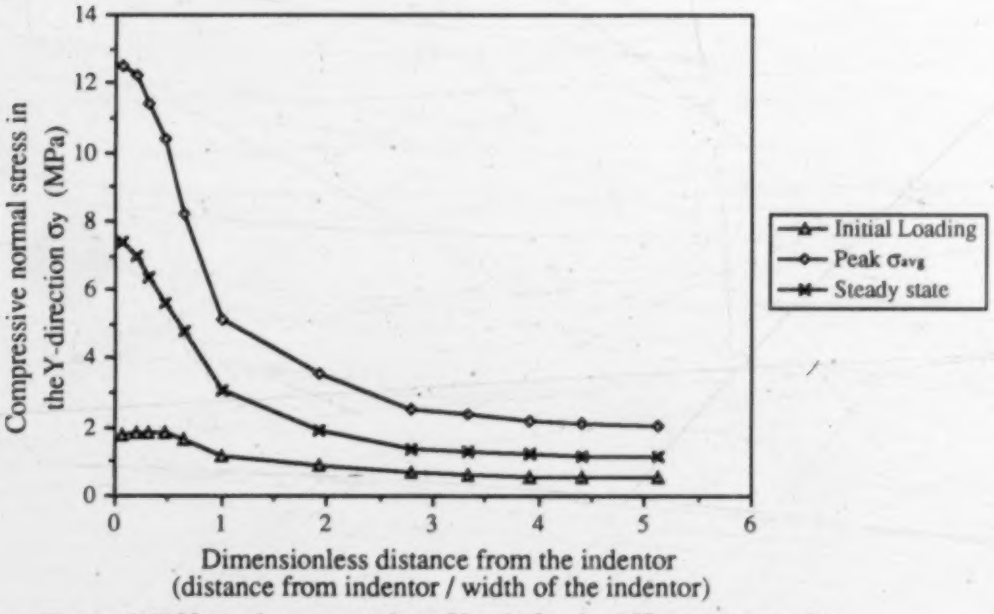

Figure 5.60 Normal stress σ_y along Y-axis for the 150mm rectangular indentor at $5*10^{-2}$ mm/s with 2x2 Gaussian integration.

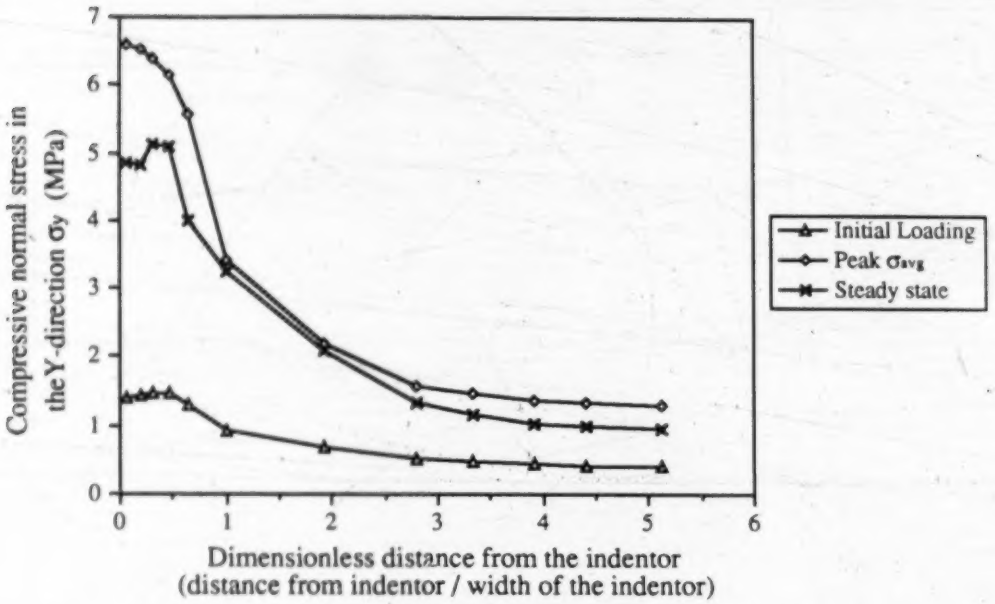
Compressive normal stress in the Y-direction σy (MPa)
Dimensionless distance from the indentor
(distance from indentor / width of the indentor)
Initial Loading
Peak σavg
Steady state

Figure 5.61 Normal stress σ_y along Y-axis for the 150mm rectangular indentor at $5*10^{-3}$ mm/s with 2x2 Gaussian integration.

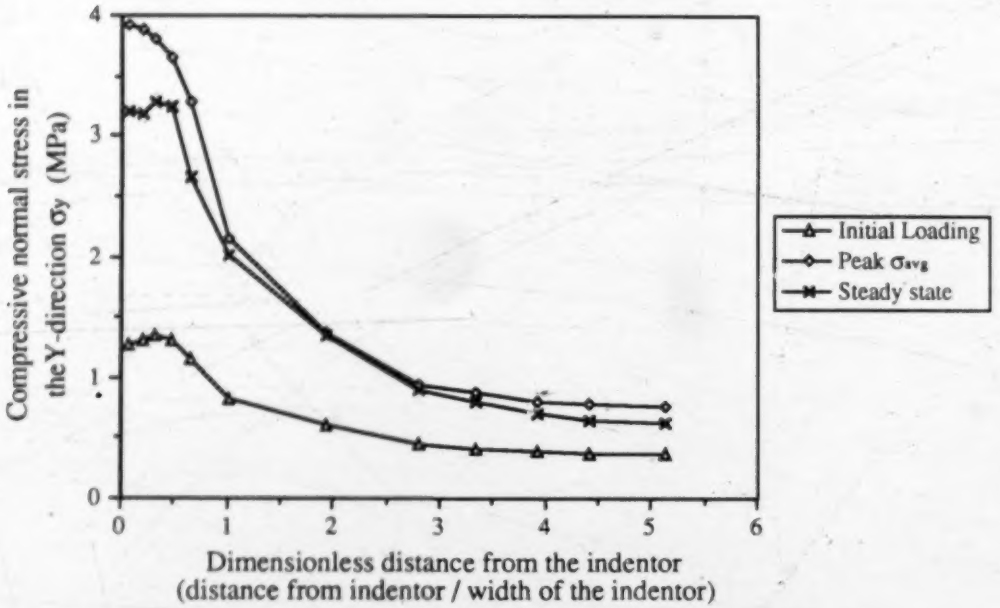
Compressive normal stress in the Y-direction σy (MPa)
Dimensionless distance from the indentor
(distance from indentor / width of the indentor)
Initial Loading
Peak σavg
Steady state

Figure 5.62 Normal stress σ_y along Y-axis for the 150mm rectangular indentor at $5*10^{-4}$ mm/s with 2x2 Gaussian integration.

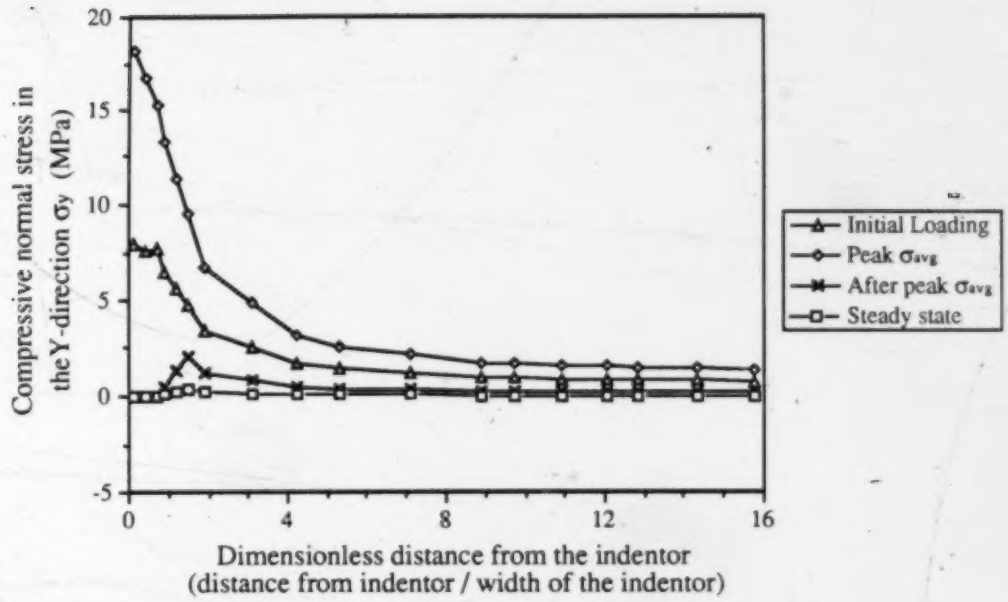

Figure 5.63 Normal stress σ_y along Y-axis for the 50mm rectangular indentor at $5*10^{-1}$ mm/s with 3x3 Gaussian integration.

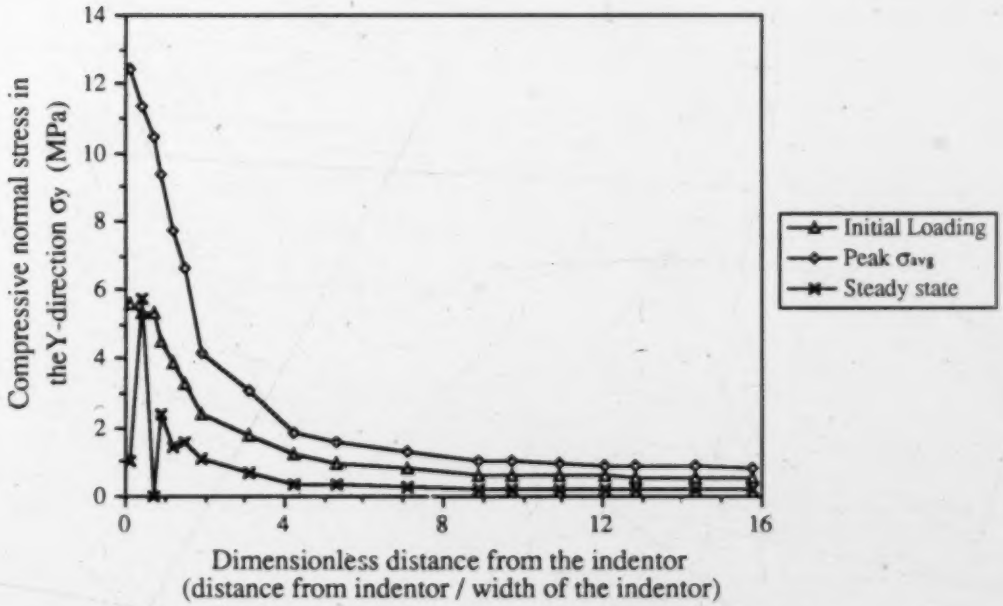

Figure 5.64 Normal stress σ_y along Y-axis for the 50mm rectangular indentor at $5*10^{-2}$ mm/s with 3x3 Gaussian integration.

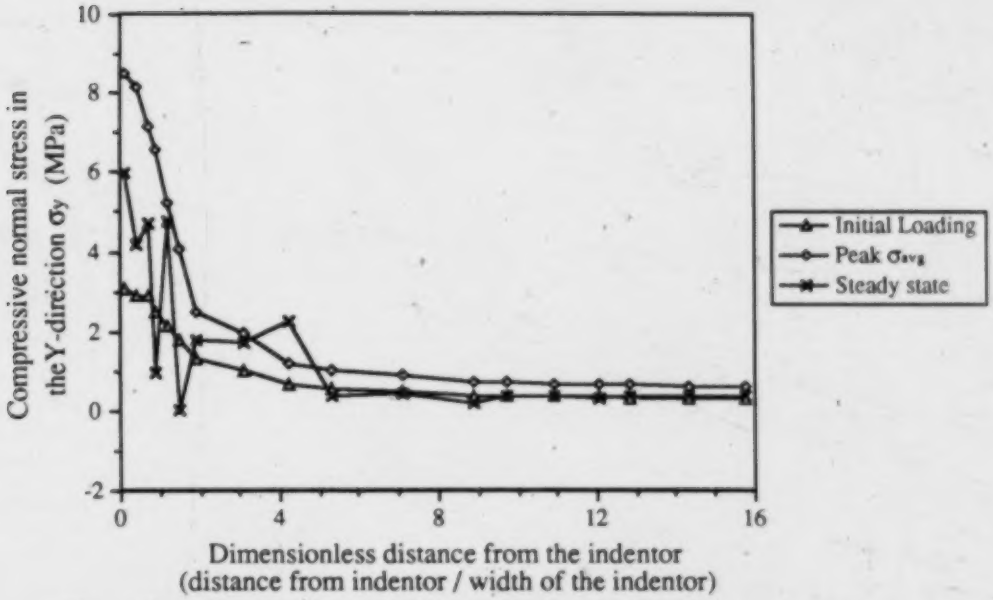

Figure 5.65 Normal stress σ_y along Y-axis for the 50mm rectangular indentor at $5*10^{-3}$ mm/s with 3x3 Gaussian integration.

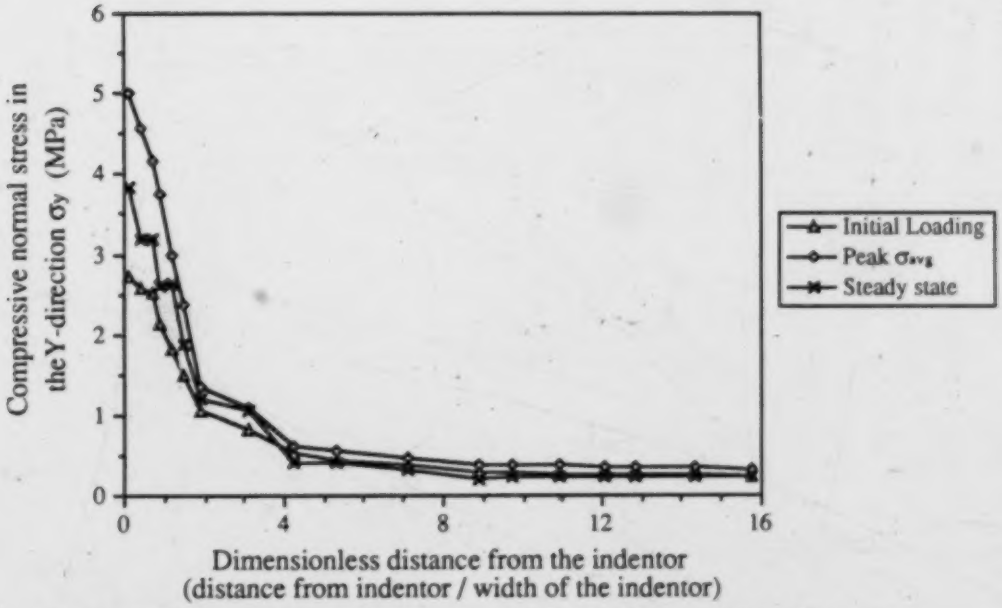

Figure 5.66 Normal stress σ_y along Y-axis for the 50mm rectangular indentor at $5*10^{-4}$ mm/s with 3x3 Gaussian integration.

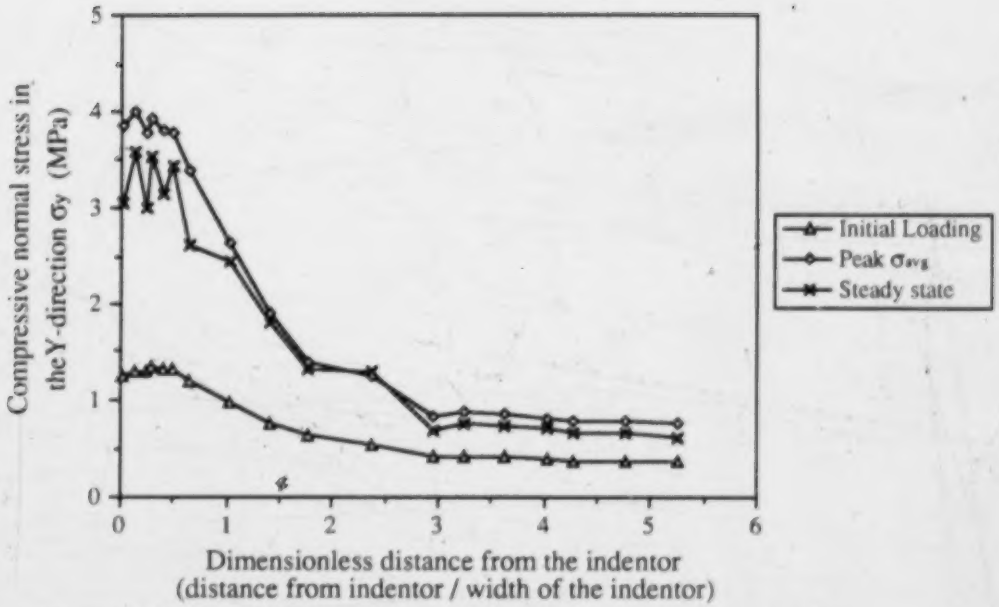

Figure 5.67 Normal stress σ_y along Y-axis for the 150mm rectangular indentor at $5*10^{-4}$ mm/s with 3x3 Gaussian integration.

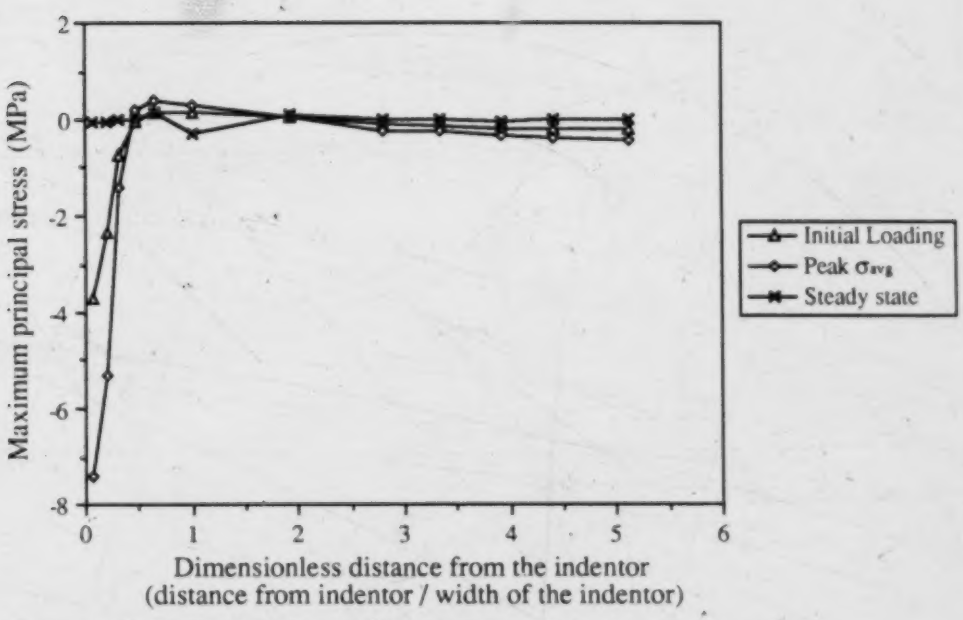

Figure 5.68 Maximum principal stress along Y-axis for the 50mm rectangular indentor at $5*10^{-1}$ mm/s with 2x2 Gaussian integration.

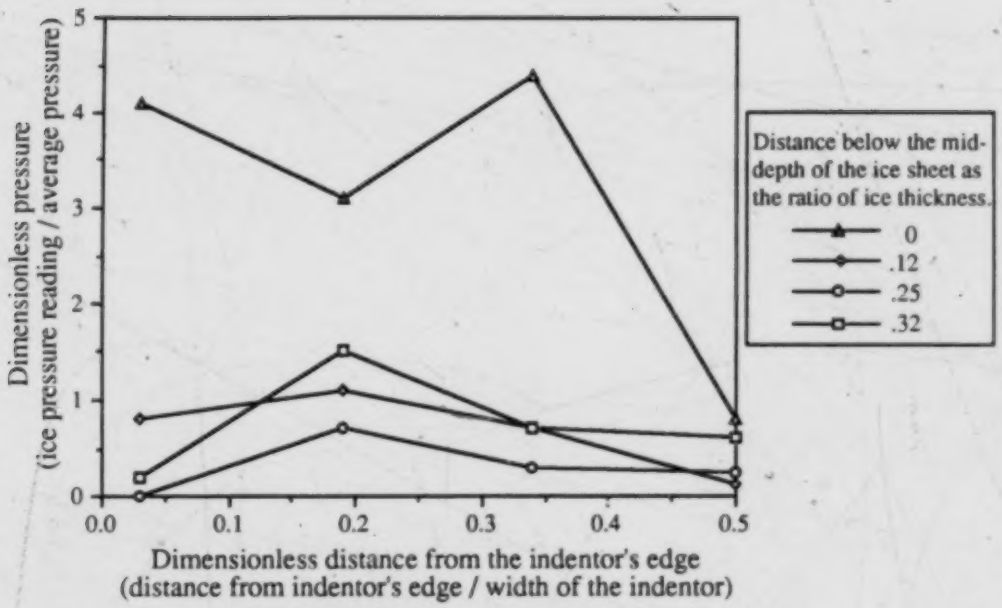

Figure 5.69 The distribution of normal stress on the indentor of Saeki et al.'s test for b/h=4.14 and $v/4b=0.610\times10^{-3}s^{-1}$ (Modified from Saeki et al., 1984)

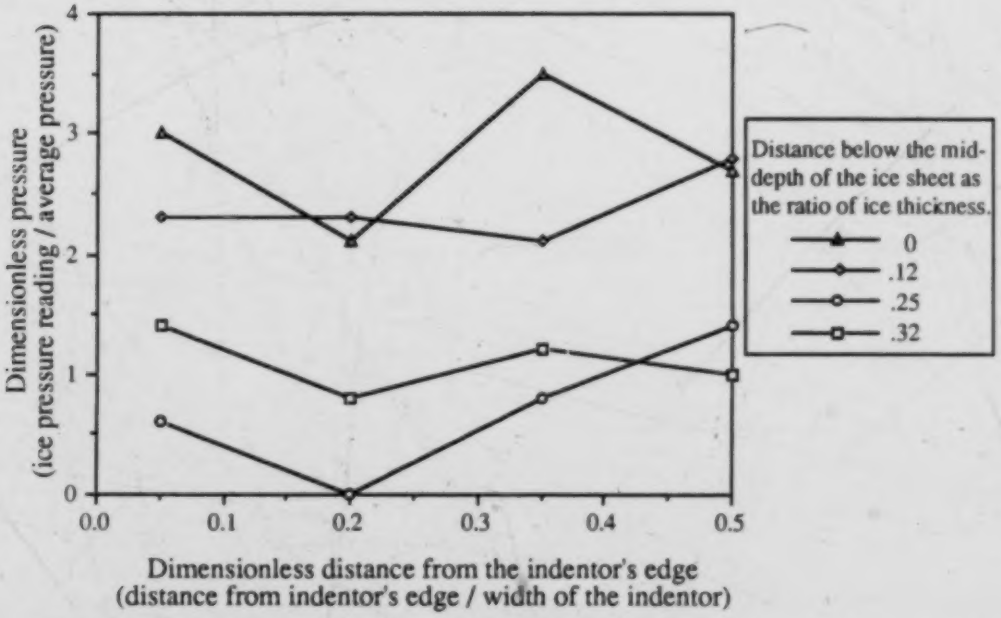

Figure 5.70 The distribution of normal stress on the indentor of Saeki et al.'s test for b/h=2.76 and $v/4b=0.667\times10^{-3}s^{-1}$ (Modified from Saeki et al., 1984)

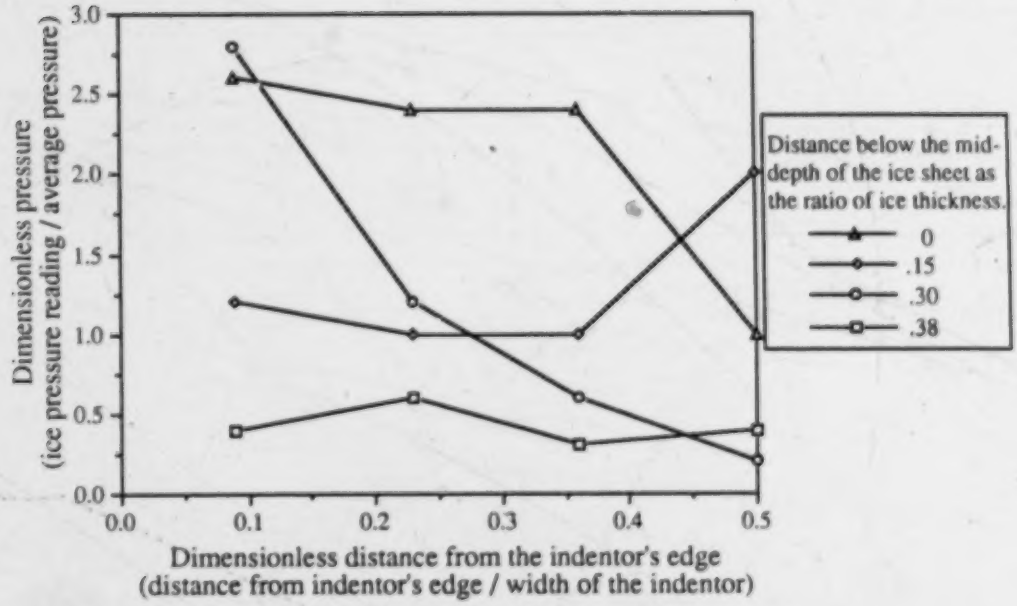

Figure 5.71 The distribution of normal stress on the indentor of Saeki et al.'s test for b/h=1.67 and $v/4b=0.815\times10^{-3}s^{-1}$ (Modified from Saeki et al., 1984)

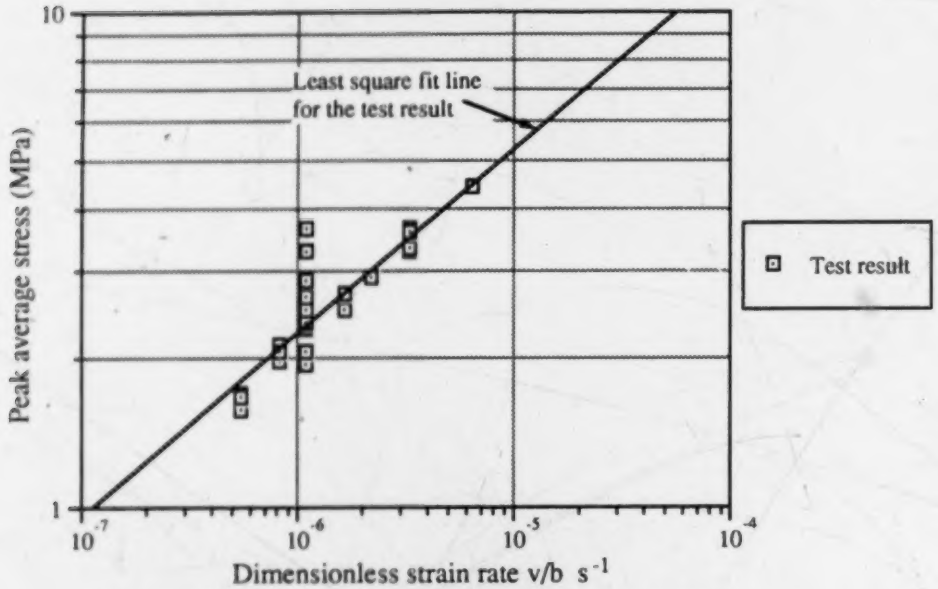

Figure 5.72 The peak average stress at different v/b from Frederking and Gold's test. (Modified from Frederking and Gold, 1975)

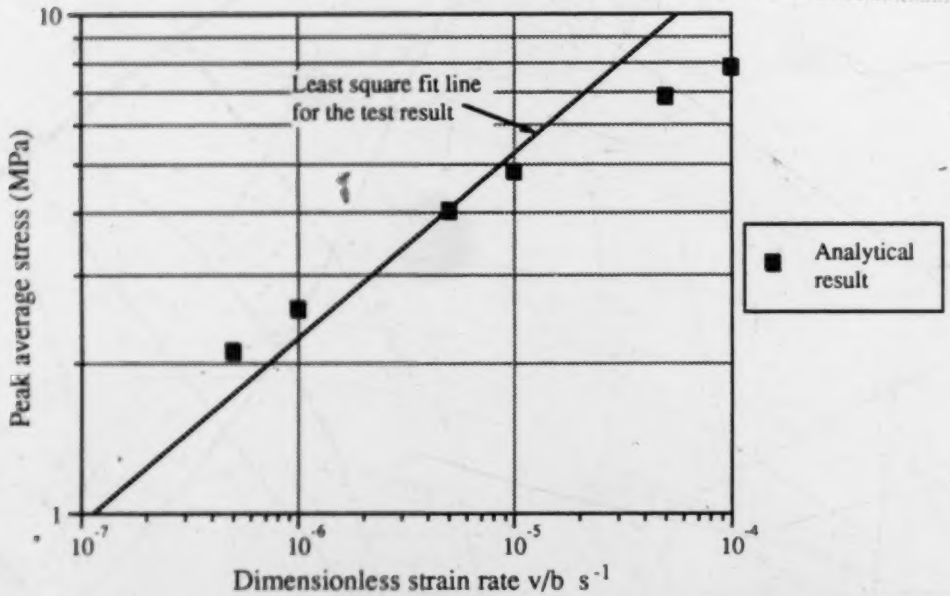

Figure 5.73 The analytical peak average stress at different v/b for Frederking and Gold's test. (Modified from Frederking and Gold, 1975)

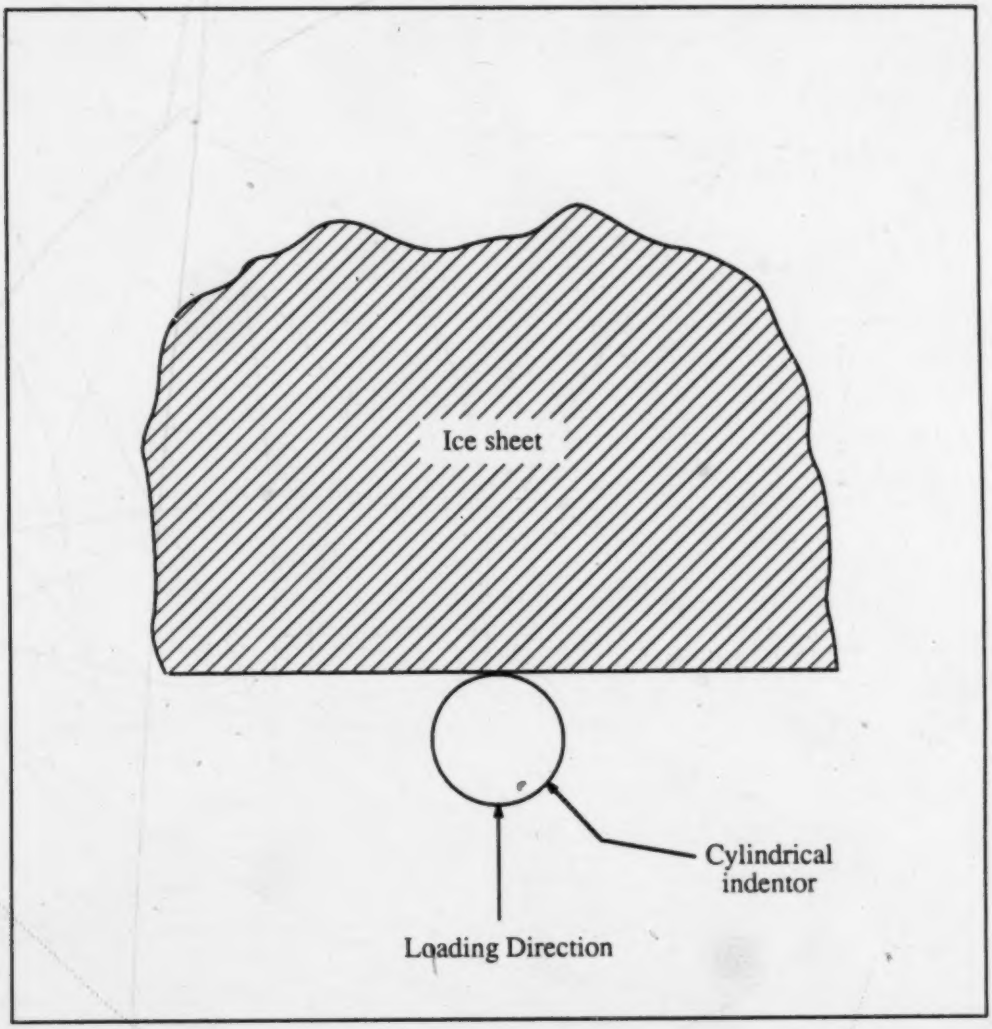

Figure 5.74 Position of the ice plate and the indentor at the start of penetration test.

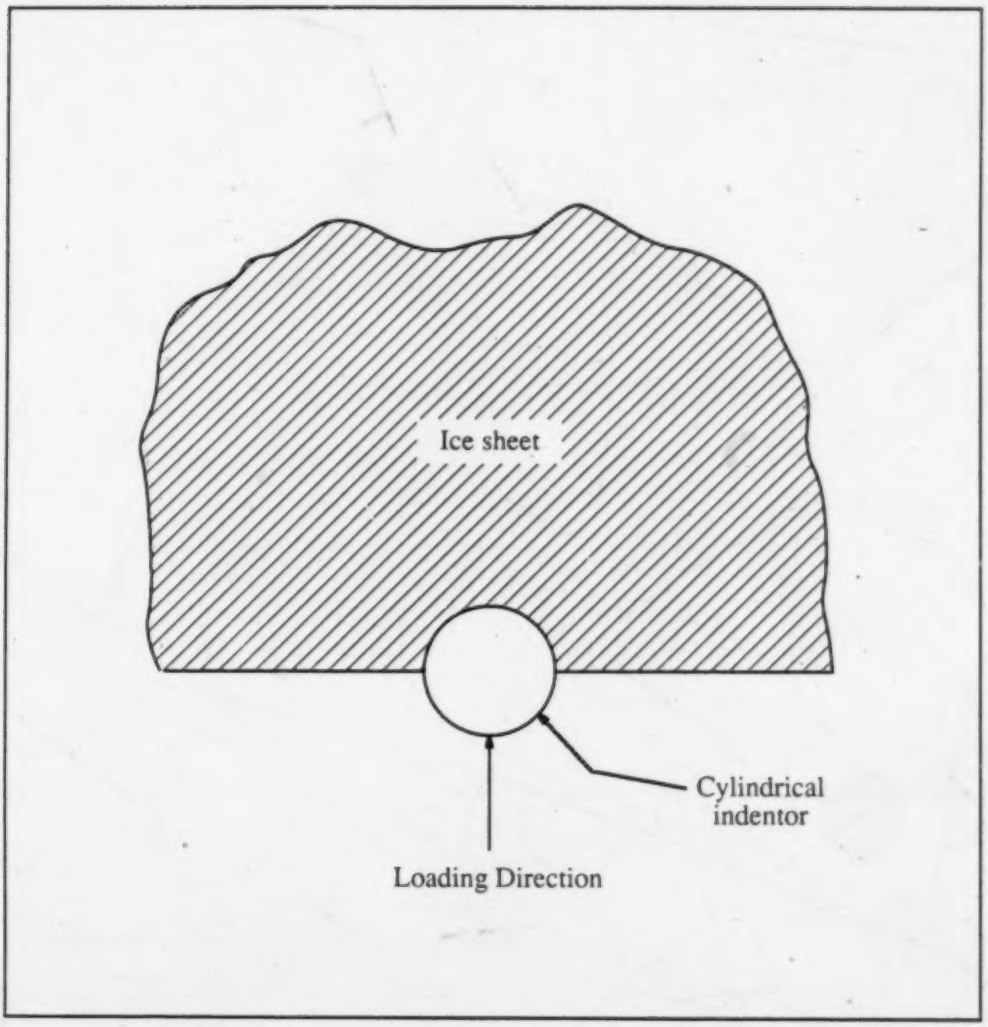

Figure 5.75 Position of the ice plate and the indentor at the start of indentation test.

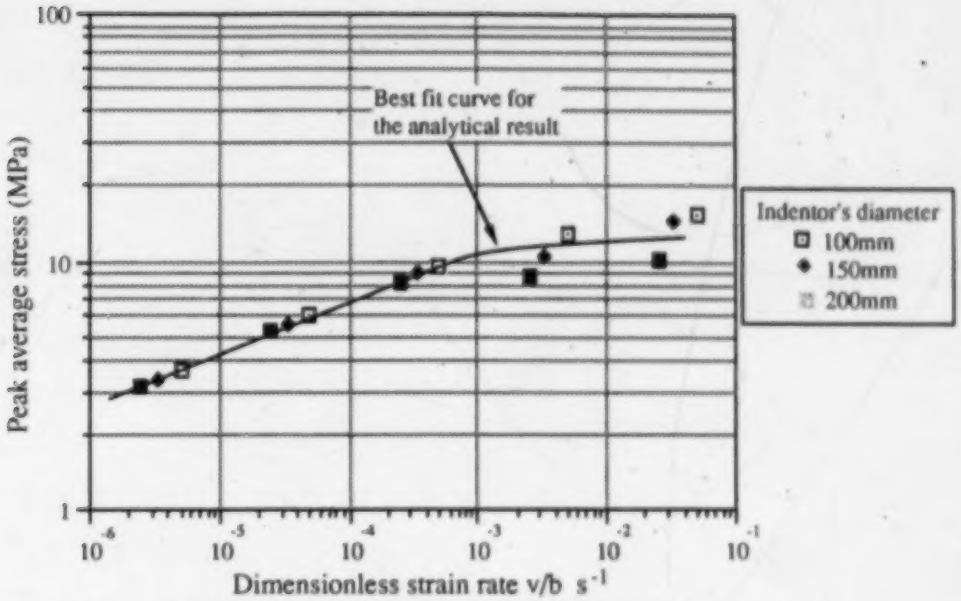

Figure 5.76 The analytical peak average stress at different v/b for the cylindrical indentor.

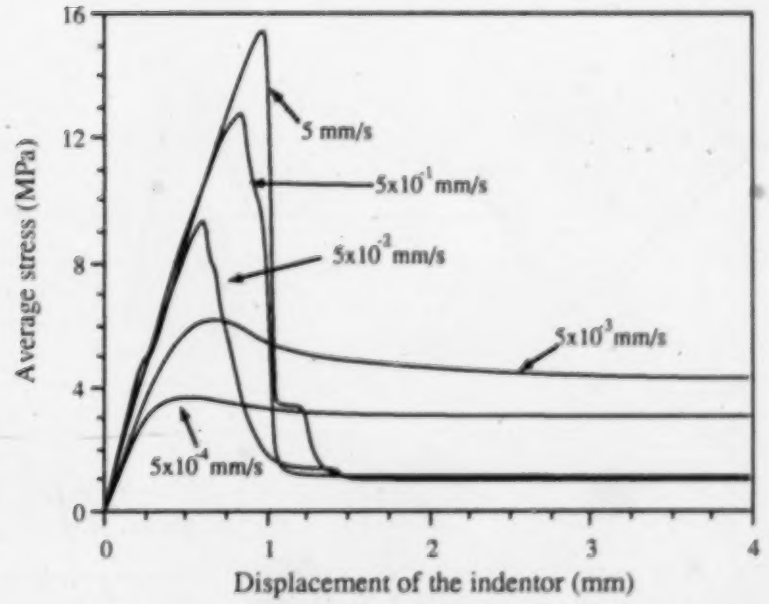

Figure 5.77 The analytical average stress versus indentor displacement with 100mm cylindrical indentor.

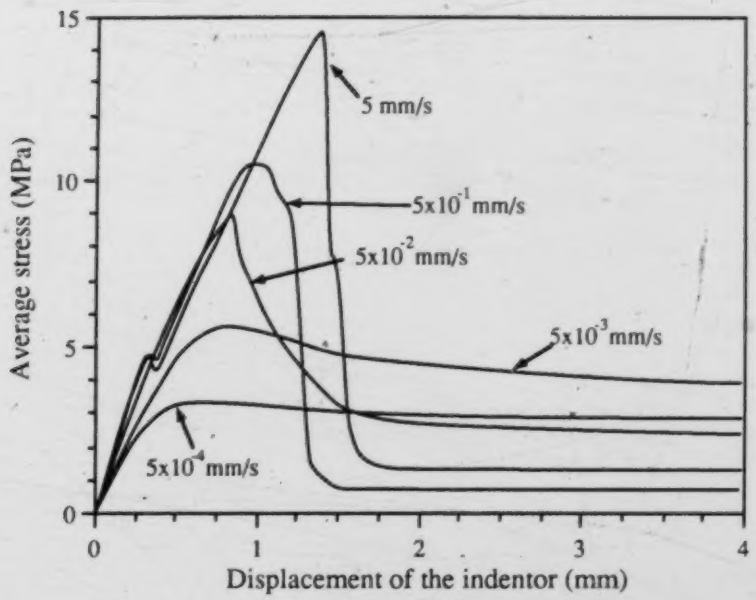

Figure 5.78 The analytical average stress versus indentor displacement with 150mm cylindrical indentor.

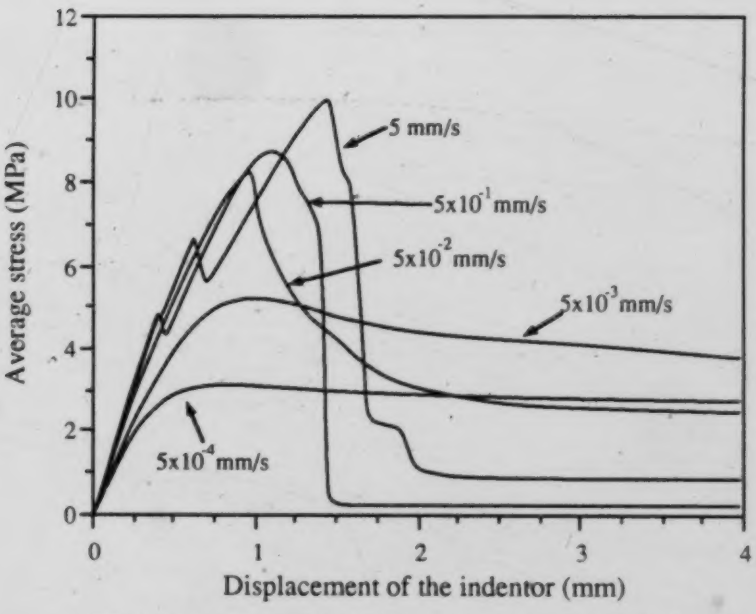

Figure 5.79 The analytical average stress versus indentor displacement with 150mm cylindrical indentor.

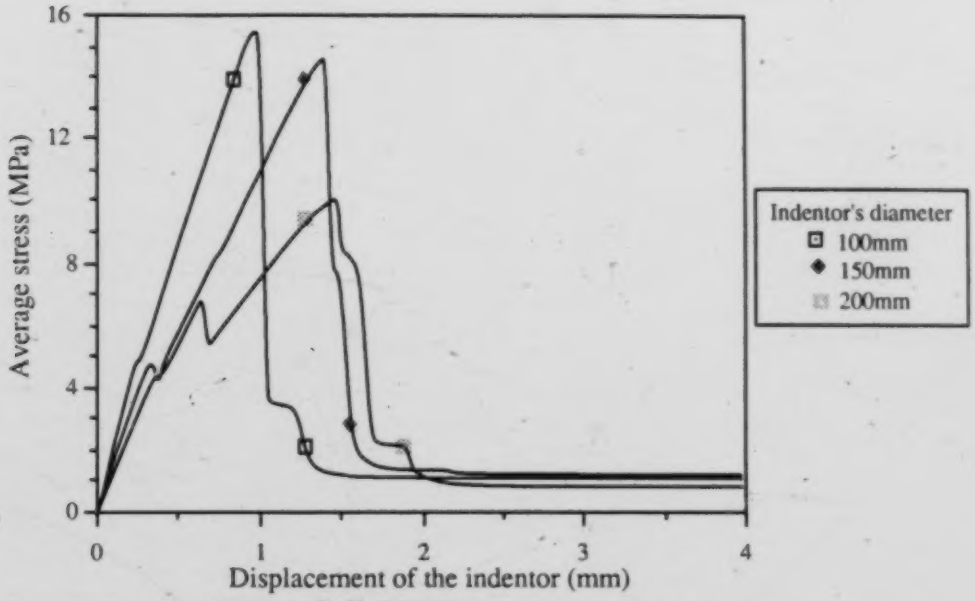

Figure 5.80 The analytical average stress versus indentor displacement for cylindrical indentor at 5 mm/s.

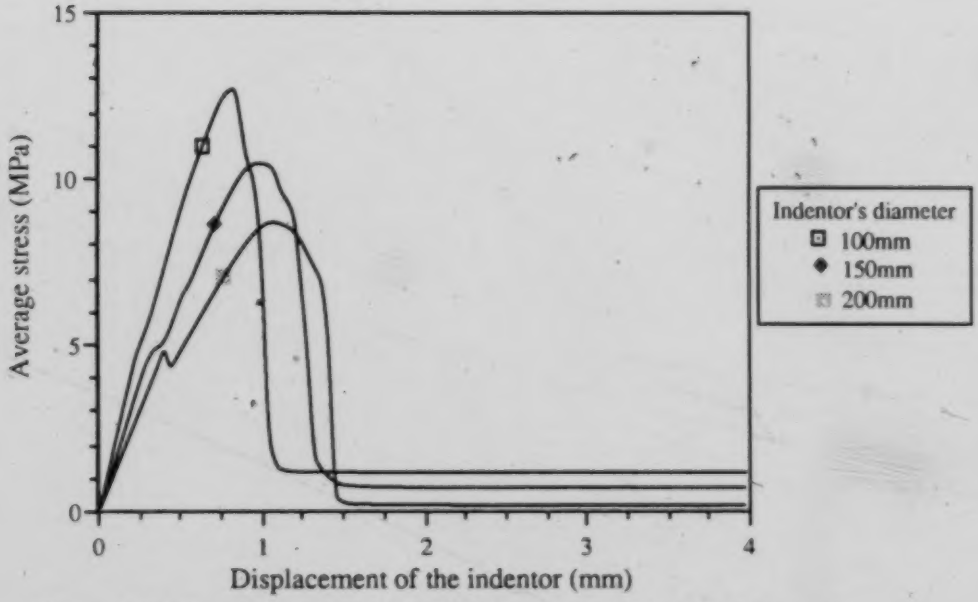

Figure 5.81 The analytical average stress versus indentor displacement for cylindrical indentor at 5×10^{-1} mm/s.

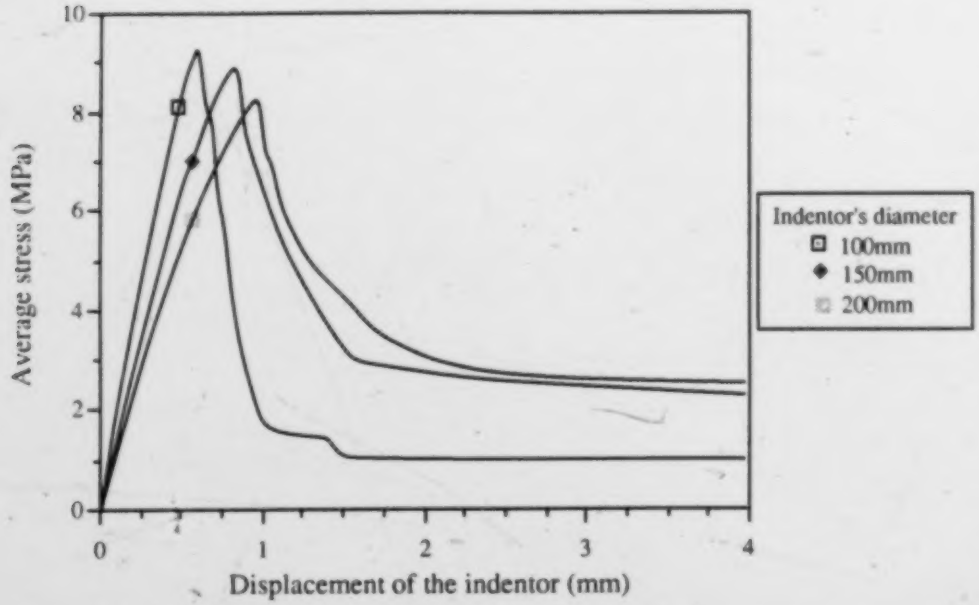

Figure 5.82 The analytical average stress versus indentor displacement for cylindrical indentor at $5x10^{-2}$ mm/s.

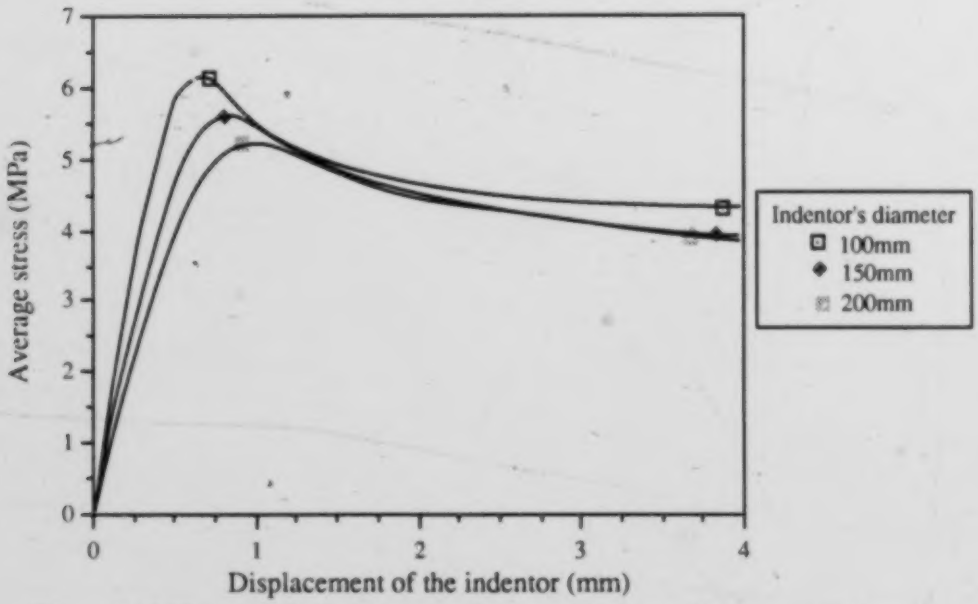

Figure 5.83 The analytical average stress versus indentor displacement for cylindrical indentor at $5x10^{-3}$ mm/s.

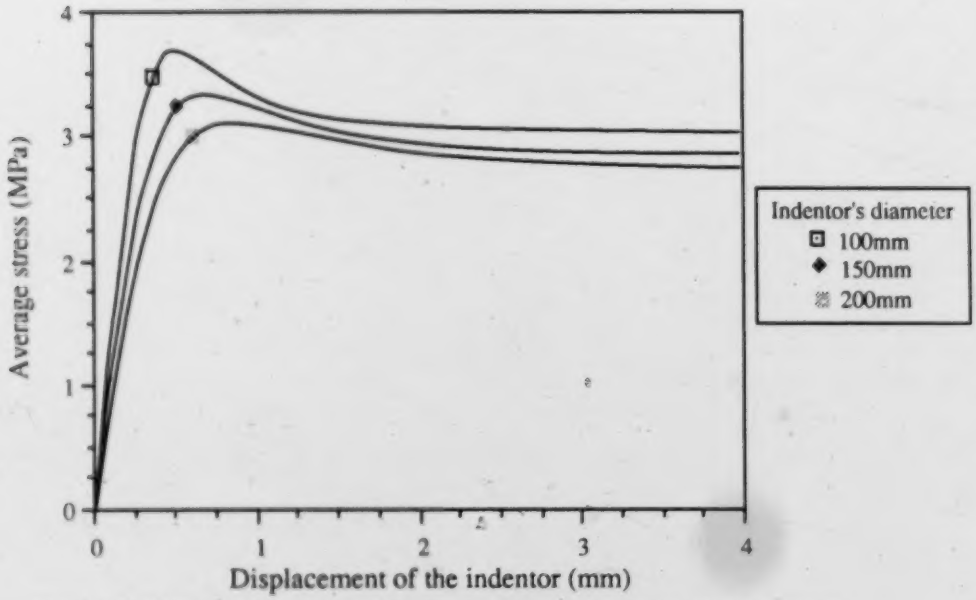

Figure 5.84 The analytical average stress versus indentor displacement for cylindrical indentor at $5x10^{-4}$ mm/s.

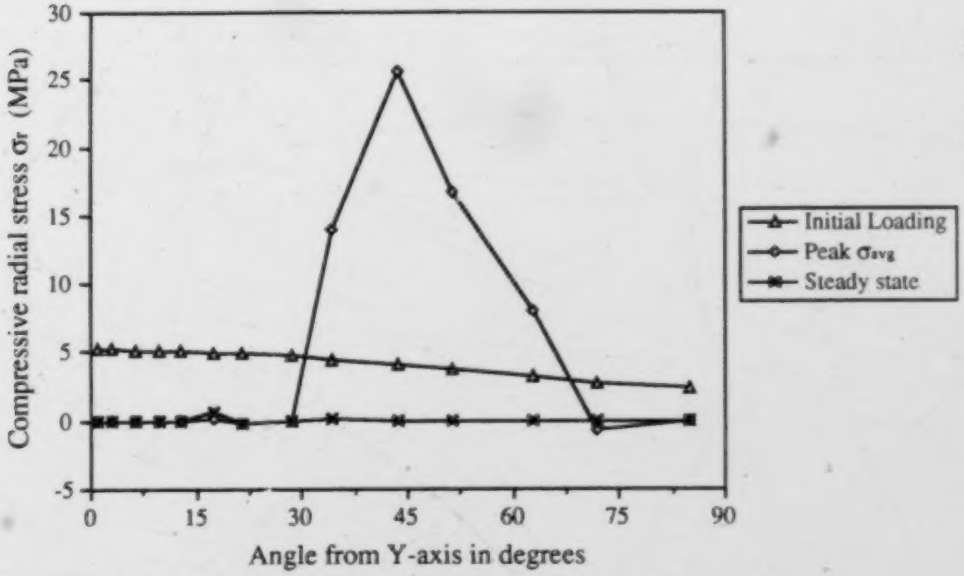

Figure 5.85 Radial stress σ_r along the 100mm cylindrical indentor at $5*10^{-1}$ mm/s with 2x2 Gaussian integration.

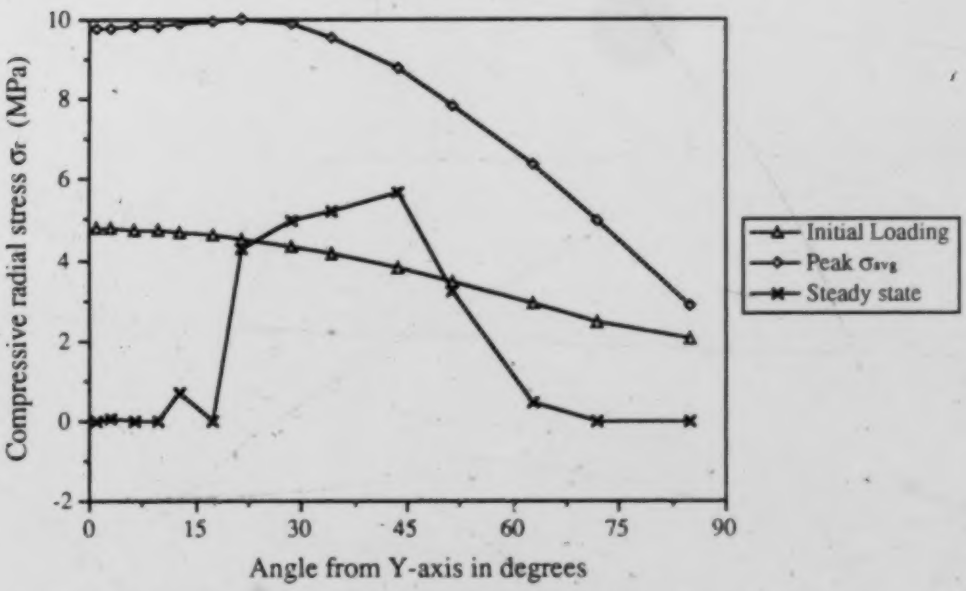

Figure 5.86 Radial stress σ_r along the 100mm cylindrical indentor at $5*10^{-2}$ mm/s with 2x2 Gaussian integration.

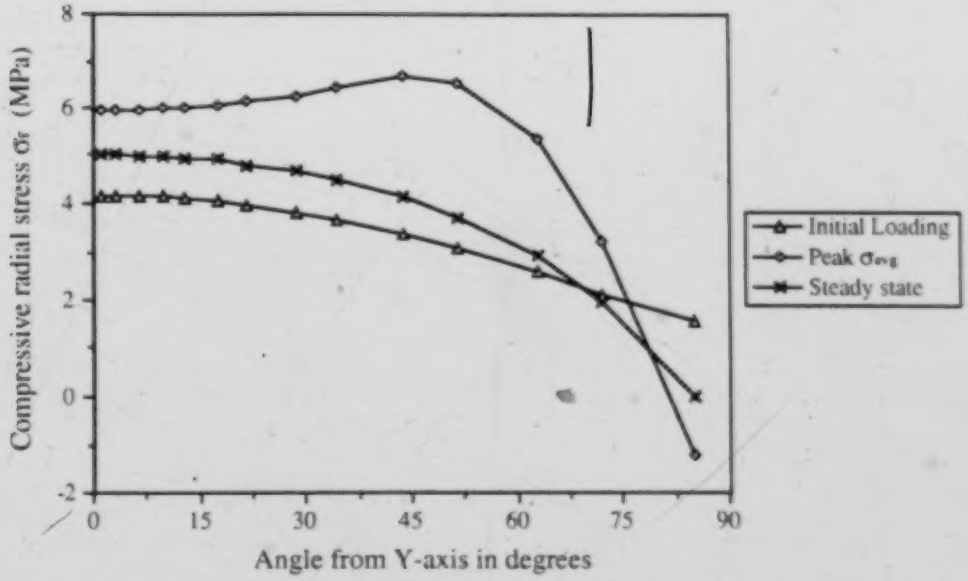

Figure 5.87 Radial stress σ_r along the 100mm cylindrical indentor at $5*10^{-3}$ mm/s with 2x2 Gaussian integration.

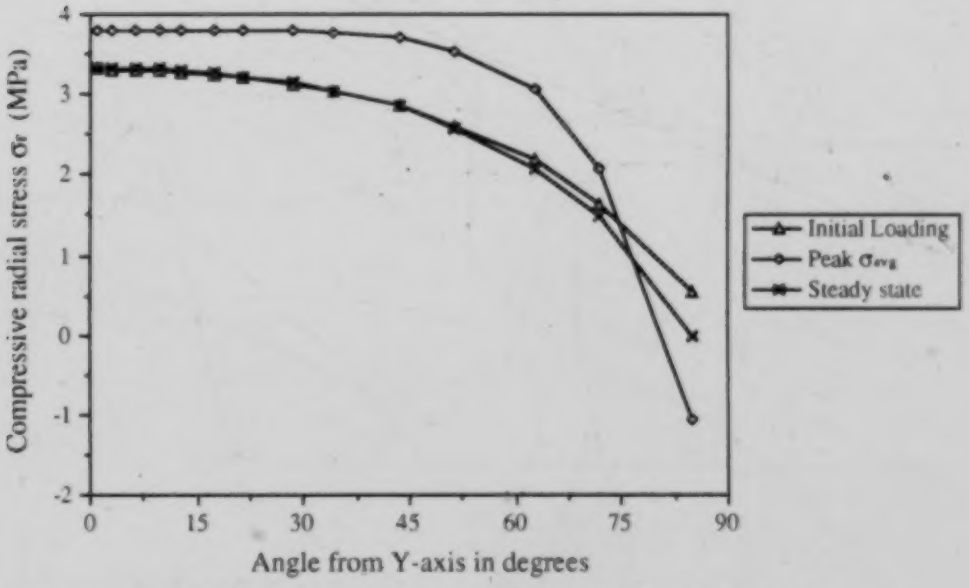

Figure 5.88 Radial stress σ_r along the 100mm cylindrical indentor at $5*10^{-4}$ mm/s with 2x2 Gaussian integration.

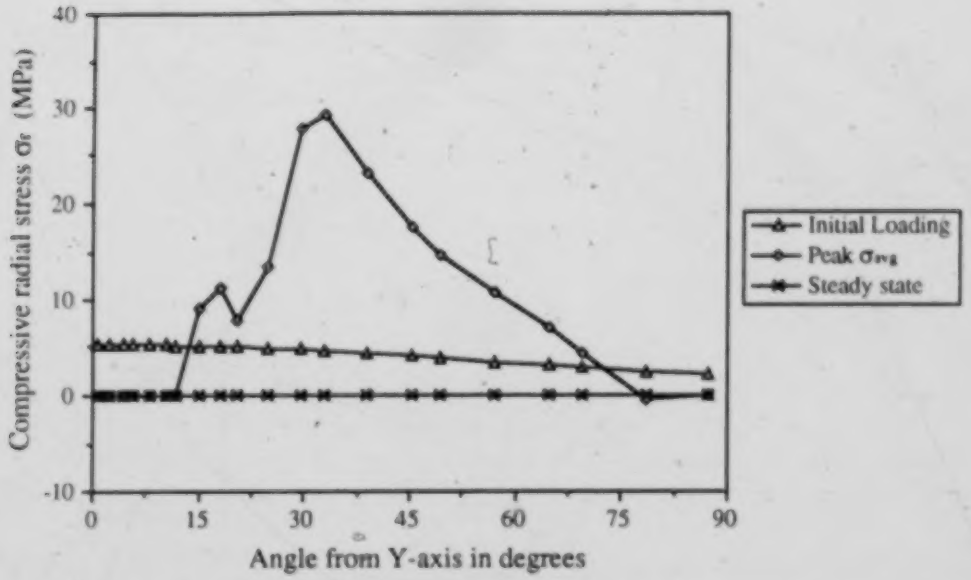

Figure 5.89 Radial stress σ_r along the 100mm cylindrical indentor at $5*10^{-1}$ mm/s with 3x3 Gaussian integration.

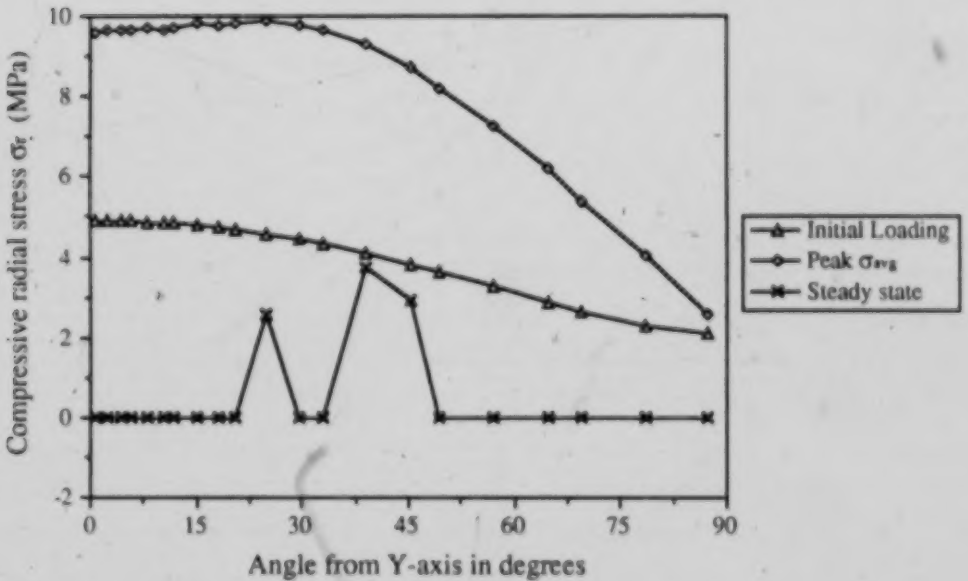

Figure 5.90 Radial stress σ_r along the 100mm cylindrical indentor at $5*10^{-2}$ mm/s with 3x3 Gaussian integration.

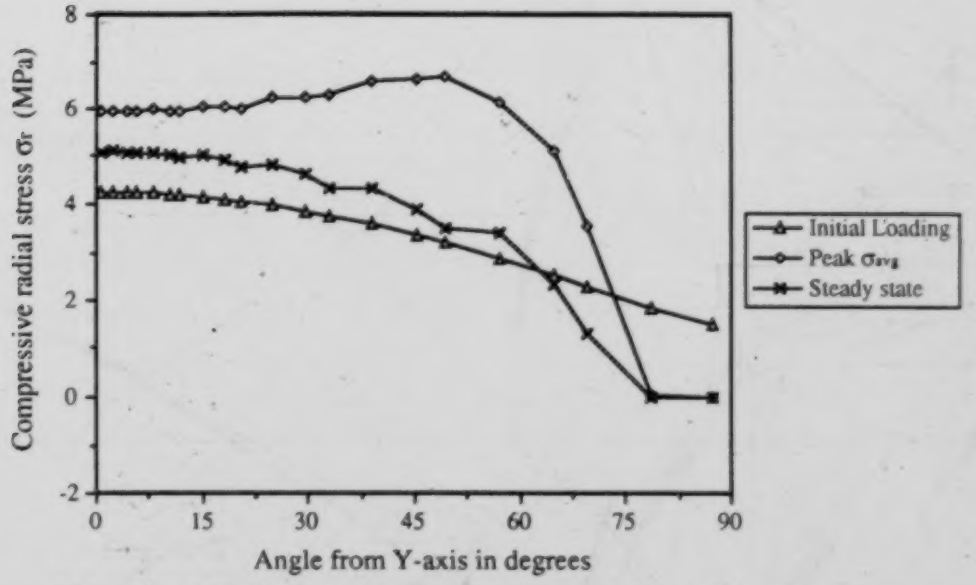

Figure 5.91 Radial stress σ_r along the 100mm cylindrical indentor at $5*10^{-3}$ mm/s with 3x3 Gaussian integration.

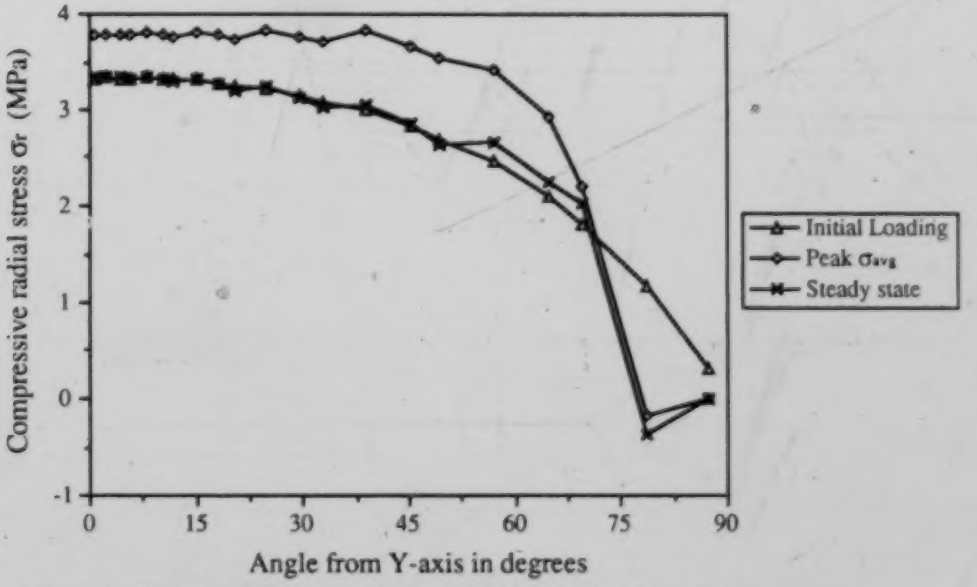

Figure 5.92 Radial stress σ_r along the 100mm cylindrical indentor at $5*10^{-4}$ mm/s with 3x3 Gaussian integration.

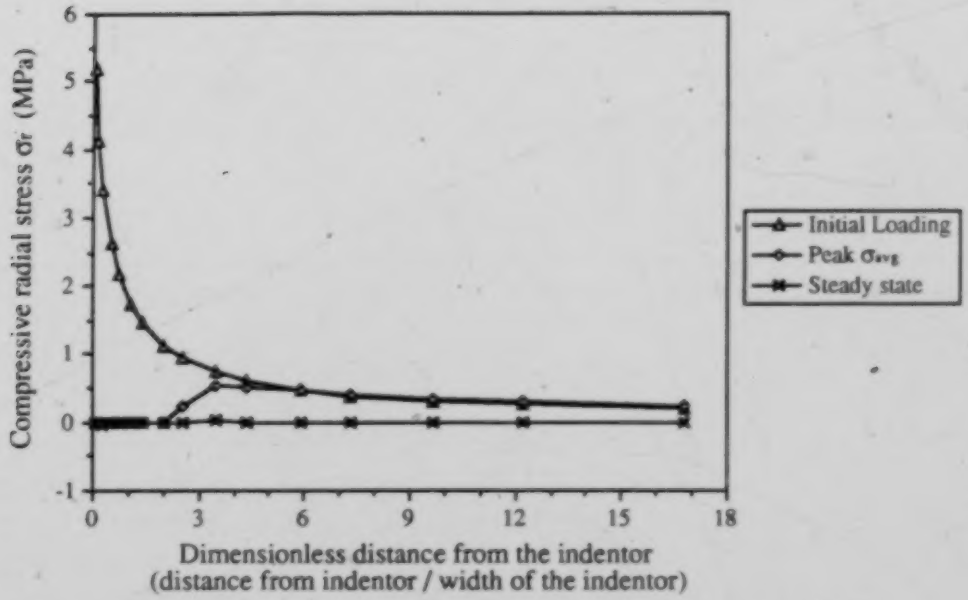

Figure 5.93 Radial stress σ_r along Y-axis for the 100mm cylindrical indentor at $5*10^{-1}$ mm/s with 2x2 Gaussian integration.

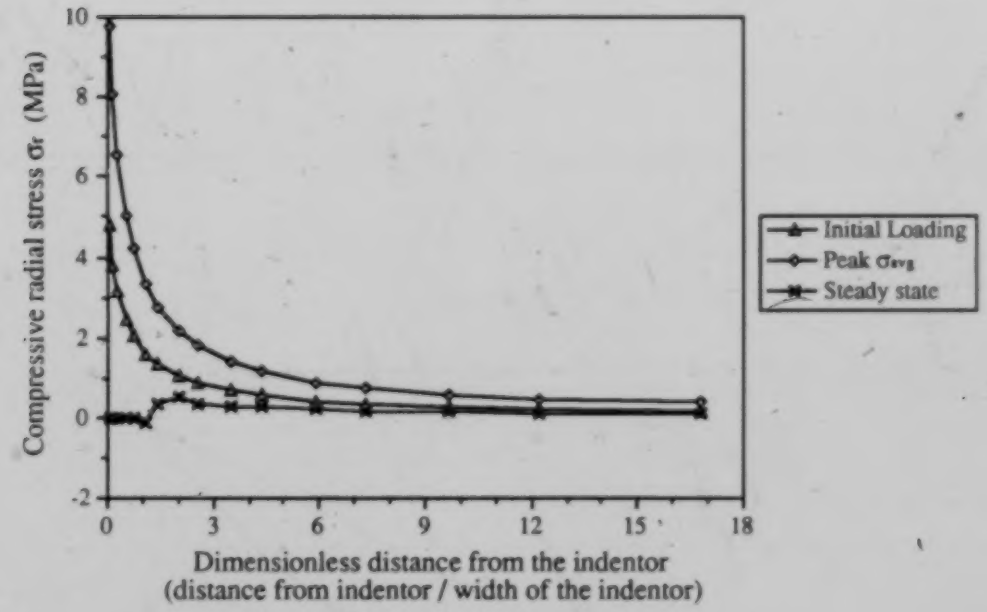

Figure 5.94 Radial stress σ_r along Y-axis for the 100mm cylindrical indentor at $5*10^{-2}$ mm/s with 2x2 Gaussian integration.

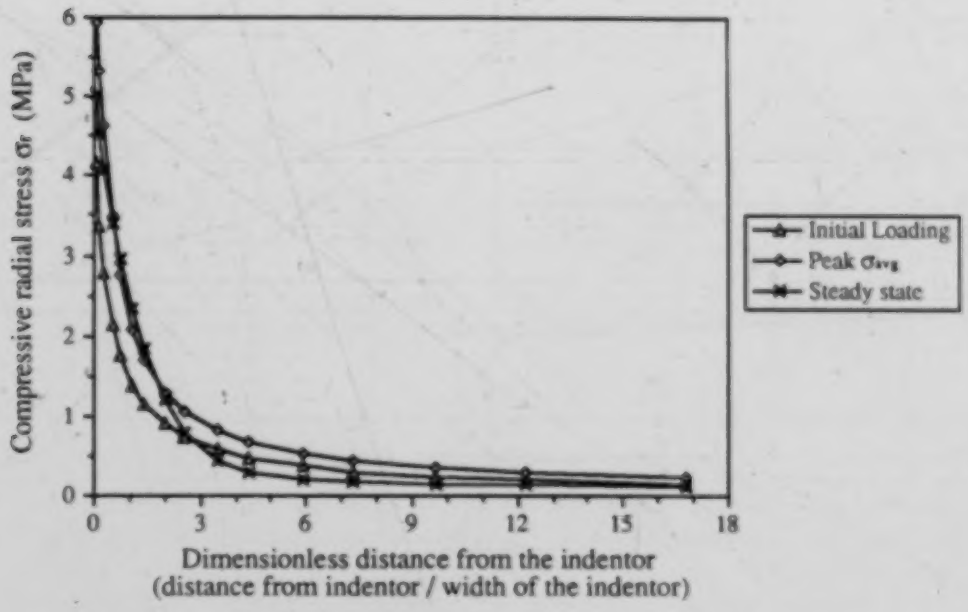
Compressive radial stress σr (MPa)
Dimensionless distance from the indentor
(distance from indentor / width of the indentor)
Initial Loading
Peak σavg
Steady state

Figure 5.95 Radial stress σ_r along Y-axis for the 100mm cylindrical indentor at $5*10^{-3}$ mm/s with 2x2 Gaussian integration.

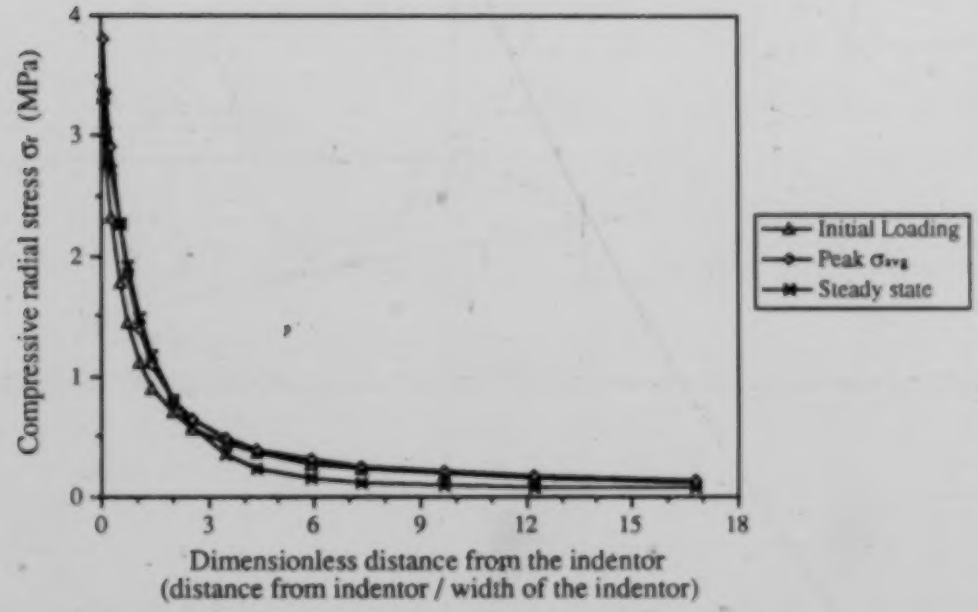
Compressive radial stress σr (MPa)
Dimensionless distance from the indentor
(distance from indentor / width of the indentor)
Initial Loading
Peak σavg
Steady state

Figure 5.96 Radial stress σ_r along Y-axis for the 100mm cylindrical indentor at $5*10^{-4}$ mm/s with 2x2 Gaussian integration.

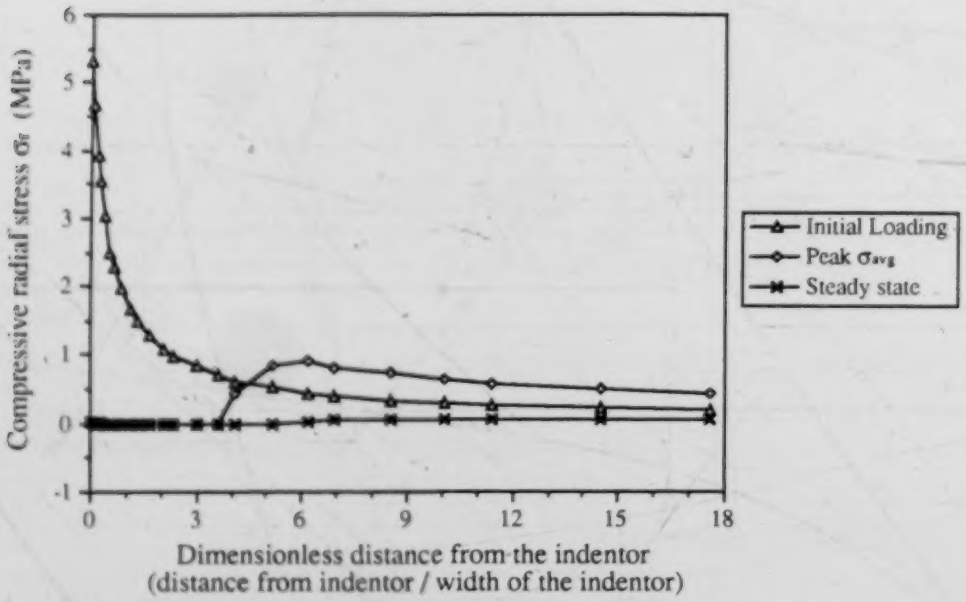
Compressive radial stress σr (MPa)
Dimensionless distance from the indentor
(distance from indentor / width of the indentor)
Initial Loading
Peak σavg
Steady state

Figure 5.97 Radial stress σ_r along Y-axis for the 100mm cylindrical indentor at $5*10^{-1}$ mm/s with 3x3 Gaussian integration.

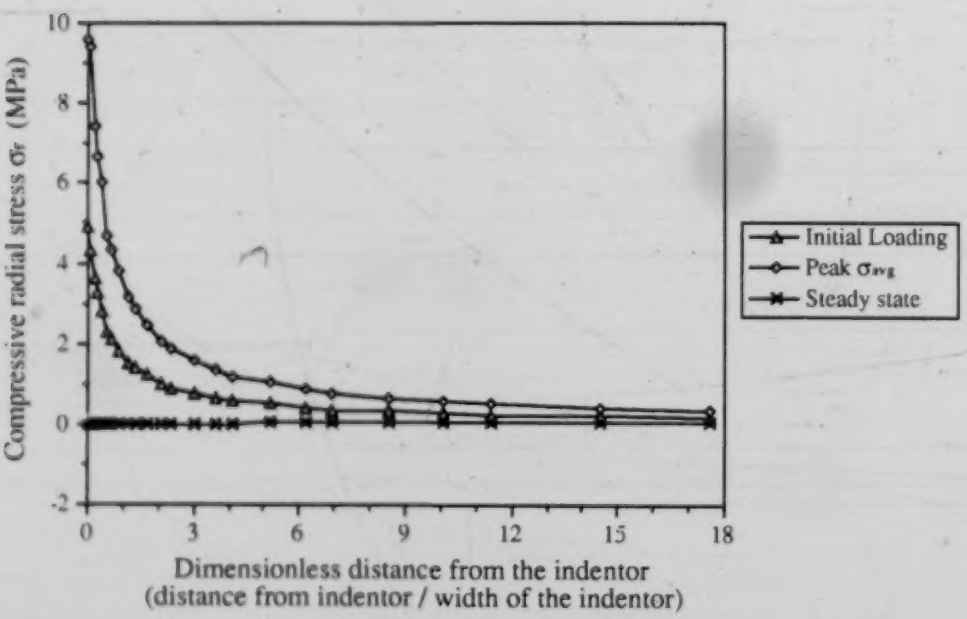
Compressive radial stress σr (MPa)
Dimensionless distance from the indentor
(distance from indentor / width of the indentor)
Initial Loading
Peak σavg
Steady state

Figure 5.98 Radial stress σ_r along Y-axis for the 100mm cylindrical indentor at $5*10^{-2}$ mm/s with 3x3 Gaussian integration.

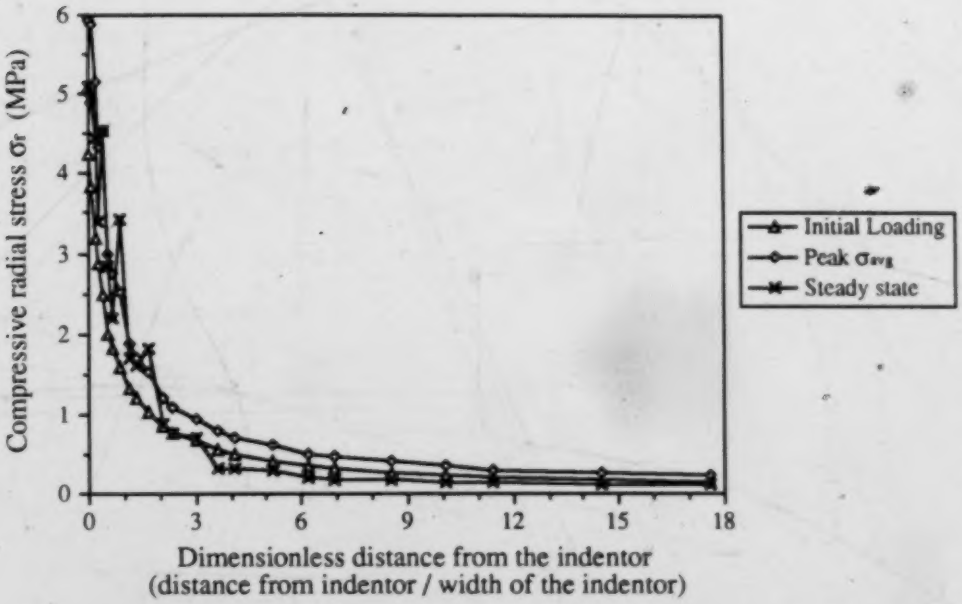

Figure 5.99 Radial stress σ_r along Y-axis for the 100mm cylindrical indentor at $5*10^{-3}$ mm/s with 3x3 Gaussian integration.

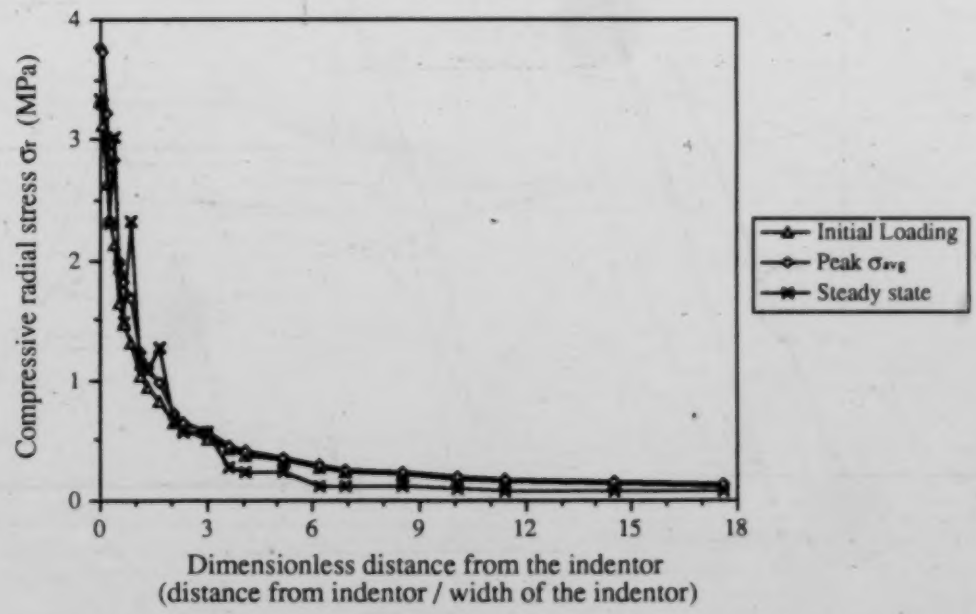

Figure 5.100 Radial stress σ_r along Y-axis for the 100mm cylindrical indentor at $5*10^{-4}$ mm/s with 3x3 Gaussian integration.

6. Summary and Conclusions

A modified combined Kelvin-Voigt and Maxwell unit is used to model ice behaviour in uniaxial compression. To investigate the behaviour of ice in biaxial loading, a plane stress formulation is expanded from the simple one dimensional model. The plane stress model uses a tensile stress cutoff to represent the tensile brittle fracture. Compressive brittle fracture is not considered in the model. The residual strength of ice in constant strain rate compression is modelled by allowing the viscosity in the Maxwell unit to vary with the viscous strain rate after the viscous strain exceeds certain value.

Even though the ice behaviour predicted by the model is dependent on the loading history, the computation involved, requires only the information on the current state of the material. Thus, not much storage memory is required since the loading history of the material does not have to be saved. An iterative scheme is required to obtain the solution for the model. This makes the analysis using the model very tedious. There are two instances where the computation efficiency of the model is significantly reduced: when the parameter m is much bigger than 1, and when tensile brittle fracture occurs. The decline in the convergence rate of the iterative process due to m is a result of the approximation made in the expression for the change in the delayed elastic strain increment with respect to stress. The approximation involves leaving out one of the terms in the expression so that the matrix [W] in section 4.1 is symmetrical. As m gets larger, the value of the omitted term gets bigger , and therefore its omission becomes more significant. The occurrence of tensile brittle fracture forces the calculation to restart at the beginning of the time step. Thus, more iterations have to be performed before convergence is achieved.

The plane strain model is implemented in a finite element program. The program uses a modified Euler method to calculate the stress and strain of the ice. Some of the parameters used in the calculation can be estimated from experimental results reported in the literature; others have to be worked out by trial and error. A few analyses are run using the finite element program, and some of the solutions are compared to the test results. There are three types of loading conditions in the analyses: uniaxial, plane strain and indentation. For uniaxial compression, a number of constant strain rate, constant stess rate and constant stress analyses are performed. As for plane strain and indentation, only constant deformation rate loading is analysed. In both plane strain and indentation, the columnar ice is stress free on the surface normal to the long direction of the ice column. Two indentor shapes used in the indentation analyses are cylindrical and rectangular.

The analytical results from uniaxial compression are plotted against those from Sinha (1982), Frederking (1977), and Mellor and Cole (1982). Besides the uniaxial results, the plane strain analytical solutions are also compared to Frederking's (1977) results. The values of the parameters used in the calculation are different for all three cases. In constant strain rate compression, the model is found to gives a good prediction of the peak stress except at a high loading rate, such as $10^{-3}s^{-1}$ for Mellor and Cole's test. At high loading rate, the model over estimates the strength of the ice because of its inability to account for compressive brittle fracture. The model also over estimates the strain at peak stress at high loading rate due to the same reason. Overall, however, the analytical solutions show good agreement with the experimental stress-strain curve for constant strain rate and constant stress rate compression, and the stress-time curve for constant stress compression.

In the indentation analyses, the value of the parameters are similar to those used in Frederking's test. The ice indentation analyses with a rectangular indentor are investigated under two boundary conditions that match the test setups of Michel and Toussaint (1977), and Frederking and Gold (1974). The peak average stress predicted by the model for both boundary conditions are close to the test results except at high deformation rate. For Michel and Toussaint's test, the model significantly overestimates the peak average stress on the indentor at v/b greater than $10^{-2}s^{-1}$. This is a result of the model's inability to represent compressive brittle facture, similar to the situation encountered in uniaxial compression. At a slightly lower v/b, the model is able to give a reasonable prediction of the peak average stress, but it is unable to give a reliable prediction of the residual strength at steady state. As the average stress approaches the peak value, tensile brittle fracture starts to occur near the edge of the indentor. However, tensile brittle fracture is not extensive at this point After the peak average stress, the zone of tensile brittle fracture continues to propagate and becomes widespread. Since the propagation of tensile brittle fracture is affected by the time step size, the loading rate, and the finite element mesh, it is very difficult to give a consistent and reliable prediction of the residual strength of the ice. For low v/b, the ice plate undergoes ductile deformation without any brittle fracture. These characteristics also show up in the indentation analyses with a cylindrical indentor. The stress distribution from the analyses along the indentor and the centerline of the ice plate at different stage of loading is examined. For both rectangular and cylindrical indentors, the stress along the centerline of the ice plate decreases by more than 80% within a distance of 3b from the indentor. In the analyses, both the 2x2 and 3x3 Gaussian integrations are employed with the second order isoparametric element. A 2x2 Gaussian integration is found to be

more suitable for calculating ice indentation than a 3x3 integration because the stress distribution given by a 3x3 integration fluctuates wildly at steady state.

The proposed model works well for low deformation rate or low stress. As the loading rate increases, the mode of ice failure shifts from ductile to brittle. Consequently, the proposed model, with its inadequacy in representing compressive brittle failure, becomes less effective with a higher loading rate. Thus, further improvement can be made by using a more elaborate brittle failure model that includes both tensile and compressive brittle fracture. In addition to depending on the state of stress, the failure model also has to be strain rate dependent because the maximum peak stress for ice under constant strain rate compression is higher than its compressive brittle fracture strength. For the stress-strain curve to peak at an appropriate strain in a constant strain rate loading, especially at high strain rate, some of the parameters (α_1, α_2, α_3, α_4 and ε_{vc}) that control the deterioration of the ice may have to be varied with the viscous strain rate. There is also a need to have more biaxial and indentation data. More information on the ice behaviour at a different biaxial state of stress and strain rate allows for a better understanding of the material behaviour, and in the process, a better model may be developed. Most indentation tests are performed at the range of loading rate where ice fail in the brittle manner. There is not much information available for indentation in the ductile and the transition from ductile to brittle ranges.

References

1. Afanasev, V.P., Dologopolov, I.V. and Shvayshteyn, Z.I. (1971), "Ice Pressure on Separate Supporting Structures in the Sea", U.S. Army Cold Regions Research and Engineering Laboratory, CRREL Translation TL346.

2. Ashby, M.F., Palmer, A.C., Thouless, M., Goodman, D.J., Howard, M., Hallam, S.D., Murrell, S.A.F., Jones, N., Sanderson, T.J.O. and Ponter, A.R.S. (1986), "Nonsimultaneous Failure and Ice Loads on Arctic Structures", Proceedings of the Eighteenth Offshore Technology Conference, OTC 5127, Houston, Texas, May 1986, pp. 399-404.

3. Brill, R. and Camp,, P.R. (1961), "Properties of Ice", U.S. Army Cold Regions Research and Engineering Laboratory, CRREL Report 68.

4. Carter, D.S. (1972), "Brittle Fracture of Polycrystalline Ice under Compressive Loadings", Proceedings of the International Symposium on Ice, International Association for Hydraulic Research (IAHR), Leningrad, USSR, September 1972, Vol. 1, pp. 62-71.

5. Chen, V.L., Chen, E.S. and Vivatrat, V. (1985), "Constitutive Modeling of Sea Ice", Proceedings of the Seventeenth Offshore Technology Conference, OTC 5057, Houston, Texas, May 1985, pp. 343-351.

6. Cox, G.F.N., Richter-Menge, J.A., Weeks, W.F., Mellor, M. and Bosworth, H. (1984), "Mechanical Properties of Multi-Year Sea Ice, Phase I: Test Results",U.S. Army Cold Regions Research and Engineering Laboratory, CRREL Report 84-9.

7. Cox, G.F.N., Richter-Menge, J.A., Weeks, W.F., Bosworth, H., Perron, N., Mellor, M. and Durell, G.(1985), "Mechanical Properties of Multi-Year Sea Ice, Phase II: Test Results",U.S. Army Cold Regions Research and Engineering Laboratory, CRREL Report 85-16.

8. Frederking, R. (1977), "Plane-Strain Compressive Strength of Columnar-Grained and Granular-Snow Ice", Journal of Glaciology, Vol. 18, No. 80, pp. 505-516.

9. Frederking, R. and Gold, L.W. (1975), "Experimental Study of Edge Loading of Ice Plates", Canadian Geotechnical Journal, Vol. 12, No. 4, pp. 456-463.

10. Glen, J.W. (1955), "The Creep of Polycrystalline Ice", Proceedings of the Royal Society of London, Ser. A, Vol. 228, No. 1175, pp. 519-538.

11. Gold, L.W. (1972), "The Process of Failure of Columnar-Grained Ice", The Philosophical Magazine, Vol. 26, No. 2, pp. 311-328.

12. Hawke, I. and Mellor, M. (1972), "Deformation and Fracture of Ice under Uniaxial Stress", Journal of Glaciology, Vol. 11, No. 61, pp. 103-131.

13. Haynes, F.D. (1973), "Tensile Strength of Ice under Triaxial Stresses", U.S. Army Cold Regions Research and Engineering Laboratory, CRREL Report 312.

14. Haynes, F.D. (1979), "Temperature Effect on the Uniaxial Strength of Ice", Proceedings of the Fifth International Conference on Port and Ocean Engineering under Arctic Condition (POAC 79), Trondheim, Norway, August 1979, pp. 667-681.

15. Hill, R. (1948), "A Theory of the Yielding and Plastic Flow of the Anisotropic Metals", Proceedings of the Royal Society of London, Ser. A, Vol. 193, pp. 281-297.

16. Jones, S.J. (1982), "The Confined Compressive Strength of Polycrystalline Ice", Journal of Glaciology, Vol. 28, No. 98, pp. 171-177.

17. Jones, S.J. and Chew, H.A.M. (1983), "Effect of Sample and Grain Size on the Compressive Strength of Ice", Annals of Glaciology, Vol. 4, pp. 129-132.

18. Karlsson, T. (1971), "A Viscoelastic-Plastic Material Model for Drifting Sea Ice", Proceedings of an International Conference, National Research Council of Iceland, Rejkjavik, Iceland, May 1971, pp. 188-195.

19. Karr, D.G. (1984), "Applications of Continuous Damage Models in Ice Mechanics", Proceedings of the Fourth International Conference on Applied Numerical Modeling, Taiwan, December 1984, pp. 73-77.

20. Karr, D.G. (1985a), "A Damage Mechanics Model for Uniaxial Deformation of Ice", Proceedings of the Fourth International Offshore Mechanics and Arctic Engineering Symposium, Dallas, Texas, February 1985, pp. 227-233.

21. Karr, D.G. (1985b), "Constitutive Equations for Ice as a Damaging Material", Proceedings of the ASCE Specialty Conference: ARCTIC '85 - Civil Engineering in the Arctic Offshore, San Francisco, California, March 1985, pp. 908-916.

22. Korzhavin, K.N. (1962), "Action of Ice on Engineering Structures", U.S. Army Cold Regions Research and Engineering Laboratory, CRREL Translation TL260.

23. Le Gac, H. and Duval, P. (1979), "Constitutive Relations for the Non Elastic Deformation of Polycrystalline Ice", Prceedings of the IUTAM Symposium on the Physics and Mechanics of Ice, Copenhagen, August 1979, Tryde, P. (Ed.), Springer-Verlag, Berlin, 1980, pp. 51-59.

24. Mellor, M. and Cole, D.M. (1982), "Deformation and Failure of Ice under Constant Stress or Constant Strain-Rate", Cold Regions Science and Technology, Vol. 5, pp. 201-219.

25. Mellor, M. and Cole, D.M. (1983), "Stress/Strain/Time Relations for Ice under Uniaxial Compression", Cold Regions Science and Technology, Vol. 6, pp. 207-230.

26. Michel, B. (1977), "A Mechanical Model of Creep of Polycrystalline Ice", Canadian Geotechnical Journal, Vol. 15, pp. 155-170.

27. Michel, B. and Toussaint, N. (1977), "Mechanisms and Theory of Indentation of Ice Plates", Journal of Glaciology, Vol. 19, No. 81, pp. 285-300.

28. Palmer, A.C., Goodman, D.J., Ashby, M.F., Evans, A.G., Hutchinson, J.W. and Ponter, A.R.S. (1983), "Fracture and Its Role in Determining Ice Forces on Offshore Structures", Annals of Glaciology, Vol. 4, pp. 216-221.

29. Ponter, A.R.S., Palmer, A.C., Goodman, D.J., Ashby, M.F., Evan, A.G. and Hutchinson, J.W. (1983), "The Force Exerted by a Moving Ice Sheet on an Offshore Structure: Part I - The Creep Mode", Cold Regions Science and Technology, Vol. 8, pp. 109-118.

30. Ralston, T.D. (1978), "An Analysis of Ice Sheet Indentation", Proceedings of the Fifth International Symposium on Ice Problems, International Association for Hydraulic Research (IAHR), Luded, Sweden, August 1978,Vol. 1, pp. 13-31.

31. Reinicke, K.M. and Ralston, T.D., "Plastic Limit Analysis with an Anisotropic, Parabolic Yield Function", International Journal of Rock Mechanics, Mining Sciences and Geomechanics, Vol. 14, pp. 147-154.

32. Saeki, H., Hamanaka, K. and Ozaki, A. (1977), "Experimental Study on Ice Force on a Pile", Proceedings of the Fourth International Conference on Port and Ocean Engineering under Arctic Condition (POAC 77), St. John's, Newfoundland, September 1977, Vol. 2, pp. 695-706.

33. Saeki, H., Tanaka, S. and Ono, T (1984), "The Distribution of Ice Pressure on Offshore Pile Structure and the Failure Mechanics of Ice Sheet", Proceedings of the Sixteenth Offshore Technology Conference, OTC 4686, Houston, Texas, May 1984, pp.349-356.

34. Sanderson, T.J.O. (1984), "Theoretical and Measured Ice Forces on Wide Structures", Proceedings of the Seventh International Symposium on Ice, International Association for Hydraulic Research (IAHR), Hamburg, August 1984, Vol. 4, pp. 151-207.

35. Sanderson, T.J.O. (1986), "A Pressure Area Curve for Ice", Proceedings of the Eighth International Symposium on Ice, International Association for Hydraulic Research (IAHR), Iowa City, Iowa, August 1986, pp. 361-384.

36. Schulson, E.M. and Cannon, N.P. (1984), "The Effect of Grain Size on the Compressive Strength of Ice", Proceedings of the Seventh International Symposium on Ice, International Association for Hydraulic Research (IAHR), Hamburg, August 1984, Vol. 1, pp. 29-38.

37. Schwarz, J., Hirayama, K. and Wu, H.C. (1974), "Effect of Ice Thickness on Ice Forces", Proceedings of the Sixth Offshore Technology Conference, OTC 2048, Houston, Texas, May 1974, pp.145-155.

38. Sinha, N.K. (1978a), "Short-Term Rheology of Polycrstalline Ice", Journal of Glaciology, Vol. 21, No. 85, pp. 457-473.

39. Sinha, N.K. (1978b), "Rheology of Columnar-Grained Ice", Experimental Mechanics, Vol. 18, No.12, pp. 464-470.

40. Sinha, N.K. (1981), "Deformation Behaviour of Ice-Like Materials in Engineering Applications", Proceedings of the International Symposium on Mechanics of Structured Media, Ottawa, 1981, pp. 419-430.

41. Sinha, N.K. (1982), "Constant Strain- and Stress-Rate Compressive Strength and Deformation of Columnar-Grained ice", Journal of Materials Science, Vol. 17, No. 3, pp. 785-802.

42. Sinha, N.K. (1983), "Field Test 1 of Compessive Strength of First-Year Sea Ice", Annals of Glaciology, Vol. 4, pp. 253-259.

43. Sinha, N.K. (1985), "Confined Strength and Deformation of Second-Year Columnar-Grained Sea Ice in Mould Bay", Proceedings of the Fourth International Offshore Mechanics and Arctic Engineering Symposium, Dallas, Texas, February 1985, Vol II, pp. 209-219.

44. Sodhi, D.S. and Morris, C.E. (1984), "Ice Forces on Rigid, Vertical, Cylindrical Structures", U.S. Army Cold Regions Research and Engineering Laboratory, CRREL Report 84-33.

45. Szyszkowski, V. and Glockner, P.G. (1985), "Modelling the Time-Dependent Behaviour of Ice", Cold Regions Science and Technology, Vol. 11, pp. 3-21.

46. Tanaka, S., Sasaki, K. and Saeki, H. (1987), "The Distribution of Ice Pressure Acting on an Offshore Circular Pile", Proceedings of the Ninth International Conference on Port and Ocean Engineering under Arctic Condition (POAC 87), Fairbanks, Alaska, August 1987, pp. 395-411.

47. Ting, S-K. and Sunder, S.S. (1985), "Constitutive Modelling of Sea Ice with Applications to Indentation Problems", Center for Scientific Excellence in Offshore Engineering Research Report No. 3, Department of Civil Engineering and Department of Ocean Engineering, Massachusetts Institute of Technology, Cambridge, Massachusetts, U.S.A., October 1985.

48. Timco, G.W. and Frederking, R.M.W. (1984), "An Investigation of the Failure Envelope of Granular/Discontinuous Columnar Sea Ice", Cold Regions Science and Technology, Vol. 9, pp. 17-27.

49. Timco, G.W. and Frederking, R.M.W. (1986), "Confined Compression Tests: Outlining the Failure Envelope of Columnar Sea Ice", Cold Regions Science and Technology, Vol. 12, pp. 13-28.

50. Vittoratos, E.S. and Kry, P.R. (1979), "A Comparison of In-situ and Laboratory Uniaxial Fresh Water Ice Strength", Proceedings of the Fifth International Conference on Port and Ocean Engineering under Arctic Condition (POAC 79), Trondheim, Norway, August 1979, pp. 683-695.

51. Vlack, V. (1980), "Elements of Materials Science and Engineering", 4th ed., Addison-Wesley.

52. Wang, Y.S. (1981), "Uniaxial Compression Testing of Arctic Sea Ice", Proceedings of the Sixth International Conference on Port and Ocean Engineering under Arctic Condition (POAC 81), Quebec, Canada, July 1981, pp. 346-355.

53. Wang, Y.S. (1982), "A Rate-Dependent Stress-Strain Relationship for Sea Ice", Proceedings Of the First International Symposium on Offshore Mechanics and Arctic Engineering, ASME, New Orleans, Louisiana, March 1982, pp. 243-248.

54. Weeks, W. and Assur, A. (1967), "The Mechanical Properties of Ice", U.S. Army Cold Regions Research and Engineering Laboratory, CRREL Report II-C3.

55. Zienkiewicz, O.C. (1977), "The Finite Element Method", McGraw-Hill.